STUDY ON VISIBLE LIGHT RESPONSE
OF $La_2(Ti_{1.9998}Fe_{0.0001}Cr_{0.0001})O_{7-n}\ N_n$ PHOTOCATALYST

HUSSANAI LUANGTHANARAK

A Thesis Submitted in Partial Fulfillment of the Requirements for the
Degree of Doctor of Philosophy in Materials Engineering
Suranaree University of Technology
Academic Year 2022

การศึกษาการตอบสนองต่อแสงที่ตามองเห็นของตัวเร่งปฏิกิริยาเชิงแสงชนิด
แลนทานัมไททาเนียมไอรอนโครเมียมออกซีไนไตรด์

นายหัสนัยน์ เหลืองธนารักษ์

วิทยานิพนธ์นี้เป็นส่วนหนึ่งของการศึกษาตามหลักสูตรปริญญาวิศวกรรมศาสตรดุษฎีบัณฑิต
สาขาวิชาวิศวกรรมวัสดุ
มหาวิทยาลัยเทคโนโลยีสุรนารี
ปีการศึกษา 2565

STUDY ON VISIBLE LIGHT RESPONSE
OF $La_2(Ti_{1.9998}Fe_{0.0001}Cr_{0.0001})O_{7-n}$ N_n PHOTOCATALYST

Suranaree University of Technology has approved this thesis submitted in partial fulfillment of the requirements for the Degree of Doctor of Philosophy

Thesis Examining Committee

....

(Dr. Pattanapong Janphuang)

Chair person

....

(Asst. Prof. Dr. Sukasem Watcharamaisakul)

Member (Thesis Advisor)

....

(Assoc. Prof. Dr. Jiratchaya Ayawanna)

Member

....

(Asst. Prof. Dr. Siriwan Chokkha)

Member

....

(Asst. Prof. Dr. Onlamee Kamon-in)

Member

....

(Assoc. Prof. Dr. Chatchai Jothityangkoon)

Vice Rector for Academic Affairs and

Quality Assurance

....

(Assoc. Prof. Dr. Pornsiri Jongkol)

Dean of Institute of Engineering

หัสนัยน์ เหลืองธนารักษ์ : การศึกษาการตอบสนองต่อแสงที่ตามองเห็นของตัวเร่งปฏิกิริยา เชิงแสงชนิดแลนทานัมไททาเนียมไอรอนโครเมียมออกซีไนไตรด์ (STUDY ON VISIBLE LIGHT RESPONSE OF $La_2(Ti_{1.9998}Fe_{0.0001}Cr_{0.0001})O_{7-n} N_n$ PHOTOCATALYST) อาจารย์ที่ปรึกษา : ผู้ช่วยศาสตราจารย์ ดร.สุขเกษม วัชรมัยสกุล, 159 หน้า

คำสำคัญ: ตัวเร่งปฏิกิริยาเชิงแสง, แลนทานัมไททาเนียมออกไซด์, เจือสารคู่ไอรอนโครเมียม, เจือสารไนโตรเจน, ออกซีไนไตรด์, ซินโครตรอน

ไททาเนียมไดออกไซด์ (TiO_2) ถูกใช้กันอย่างแพร่หลายสำหรับโฟโตแคตะลิสต์ โดยการใช้ พลังงานแสงอาทิตย์เพื่อให้เกิดปฏิกิริยา ซึ่งโฟโตแคตะลิสต์ ยังสามารถประยุกต์ใช้ในอีกหลายๆ อย่าง เช่น เม็ดสี สีทาบ้าน เคลือบผิวป้องกันแบคทีเรีย และอื่นๆ อีกมากมาย อย่างไรก็ตาม ไททาเนียม ไดออกไซด์สามารถทำปฏิกิริยาในย่านอัลตราไวโอเลต (UV) ดังนั้น นักวิจัยพยายามที่จะปรับปรุง สมบัติของไททาเนียมไดออกไซด์ ทำให้เกิดปฏิกิริยาในย่านแสงปกติ (Visible light) การเจือสารแคทไอออนสามารถเพิ่มประสิทธิภาพได้ และการเจือสารไนโตรเจน ก็สามารถเพิ่ม ประสิทธิภาพในการเกิดปฏิกิริยาในย่านแสงปกติได้มากกว่า ซึ่งในทางกลับกัน การใช้สารเจือร่วมคู่ สามารถเพิ่มประสิทธิภาพได้เช่นเดียวกัน ดังนั้นการรวมตัวของเหล็ก (Fe) โครเมียม (Cr) แลนทานัม (La) และไนโตรเจน (N) สามารถปรับปรุงสมบัติของไททาเนียมไดออกไซด์ ทำให้มีค่าโฟโตแคตะไลติก สูง นักวิจัยพยายามที่จะเพิ่มค่าโฟโตแคตะไลติกของแลนทานัมไททาเนียมออกไซด์ ($La_2Ti_2O_7$, LTO) ให้เกิดปฏิกิริยาในย่านแสงปกติ ซึ่งการปรับปรุงข้อจำกัดโดยการใช้สารเจือร่วมคู่บนแลนทานัม ไททาเนียมออกไซด์และการใช้สารเจือไนโตรเจน ซึ่งสามารถลดแถบพลังงาน (Band gap enegy, Eg) ทำให้เพิ่มประสิทธิภาพของโฟโตแคตะไลติกได้ ในงานวิจัยนี้เตรียมการใช้สารเจือร่วม คู่เหล็กและ โครเมียมด้วยวิธีการโซลเจล (Sol-gel) สารประกอบเหล็กและโครเมียมบนแลนทานัมไททาเนียม ออกไซด์ ((Fe,Cr) $La_2Ti_2O_7$) เผาที่อุณภูมิที่แตกต่างกัน ภายใต้บรรยากาศไนโตรเจน ผลที่ได้เหล็กและ โครเมียมบนแลนทานัมไททาเนียมออกไซด์ เผาที่อุณหภูมิที่ 1250 องศาเซลเซียส เป็นเวลา 24 ชั่วโมง ในการทดสอบการสลายเมทิลีนบลู (Methylene Blue, MB) ในการฉายแสงปกติเป็นเวลา 180 นาที การใช้ลำแสงซินโครตรอนในการบ่งบอกถึงการมีอยู่ของเหล็กและโครเมียมเข้าไปอยู่ในที่ ของอะตอมไททาเนียม (Ti) ในโครงสร้างการแทนที่ของโลหะแทรนซิชัน ทำให้เกิดถ่ายโอนอิเล็กตรอน และทำให้เกิดความปั่นป่วนของ พี-ดี ไฮบริดไดเซชัน (p-d hybridization) ทำให้เกิดโครงสร้าง อิเล็กทรอนิกส์รอบบริเวณอะตอมออกซิเจนและโลหะแทรนซิชัน ทำให้ลดแถบพลังงานและทำให้เพิ่ม ประสิทธิภาพโฟโตแคตะไลติก การเจือไนโตรเจนสามารถเกิดผลอย่างโดดเด่น ในการวิเคราะห์ด้วย เอ็กซ์พีเอส (XPS) พบว่าเกิดพันธะ Ti-O-N และ Ti-N ด้วยการวิเคราะห์ทั้งเอ็กซ์พีเอสและพีอีเอส (PES) ซึ่งอะตอมไนโตรเจนจะเข้าไปแทนที่ตำแหน่งของออกซิเจนในมุมของไททาเนียมออกไซด์ (TiO_6) ในออกตะฮีดรอล (Octahedral site) การที่เจือไนโตรเจนพบว่ามีค่าโฟโตแคตะไลติกสูง

เนื่องมาจากการผสมกันของชั้น N2p และ O2p ทำให้แถบพลังงานลดลงและขยายการดูดกลืนแสง (Optical absorption) ซึ่งทำให้เกิดการเพิ่มอิเล็กตรอนและโฮล
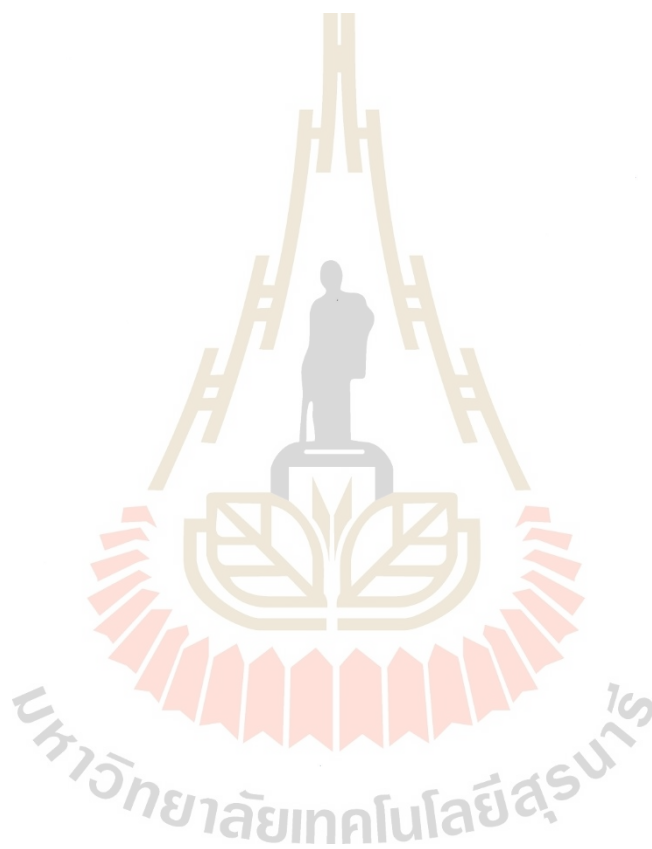
สาขาวิชา <u>วิศวกรรมเซรามิก</u>   ลายมือชื่อนักศึกษา ....

ปีการศึกษา <u>2565</u>   ลายมือชื่ออาจารย์ที่ปรึกษา ....

Titanium dioxide, TiO_2, is widely used for photocatalyst by using solar energy becoming reaction, for the photocatalyst which used in many applications such as pigment, painting, antibacterial coating, etc. However, TiO_2 can be active in Ultra-Violet region, therefore, many researchers would like to improve TiO_2 in visible light region. Doping both cation and anion in TiO_2 have been considered to improve TiO_2 active in visible light. Moreover, nitrogen efficiently improve TiO_2 in visible light more than cation. On the other hand, co-doping cation can be effective as well. Thus, the combination of Fe, Cr, La and nitrogen modifying TiO_2 can obtain high photocatalysis phenomenon. Extensive research has been conducted on enhancing the photocatalytic activity of Lanthanum titanium oxide ($La_2Ti_2O_7$) based photocatalysts. However, these photocatalysts were found to be inactive under visible light. To consider the limitation, a modification was developed by co-doping Fe and Cr on $La_2Ti_2O_7$ to enable visible light driven photocatalytic response. Apart from that, the doping with nitrogen ions (N), a non-metallic element, enhances the decreasing of band gap energy, leading to improve photocatalytic efficiency. In this work, Fe and Cr co-doped $La_2Ti_2O_7$ was prepared by sol-gel method. In addition, (Fe, Cr) $La_2Ti_2O_7$ was calcined with various temperatures under nitrogen atmosphere. Result revealed that, the (Fe,Cr) $La_2Ti_2O_7$ calcined at 1250°C under nitrogen atmosphere for 24h exhibited the maximum of methylene blue degradation under visible light. The results showed that, the (Fe,Cr)-$La_2Ti_2O_7$ calcined at 1250°C for 24h exhibited the highest methylene blue degradation under visible light for 180 min. Synchrotron X-ray absorption spectroscopy indicated that Fe and Cr were substitutionally located adjacent to the Ti atom within the $La_2Ti_2O_7$ structure. This transition metal substitutionally facilitated electron transfer and perturbed the p-d hybridization by modifying the local electronic structure of the surrounding oxygen atoms and transition metal ions, thereby reducing the band gap energy and enhancing the photocatalytic capability. Especially, the strongly effect for photocatalytic activity was shown nitrogen doping that the XPS indicated the bonding structure which was Ti-O-N and Ti-N exhibiting XPS and PES

analysis. The nitrogen atoms was substitution by took place oxygen site sharing corner TiO_6 in octahedral site. The photocatalytic activity was high efficiency corresponding to nitrogen with a narrow band gap caused by mixing N2p states with O2p states and extended the optical absorption, thereby resulting in the generation of more electrons and holes
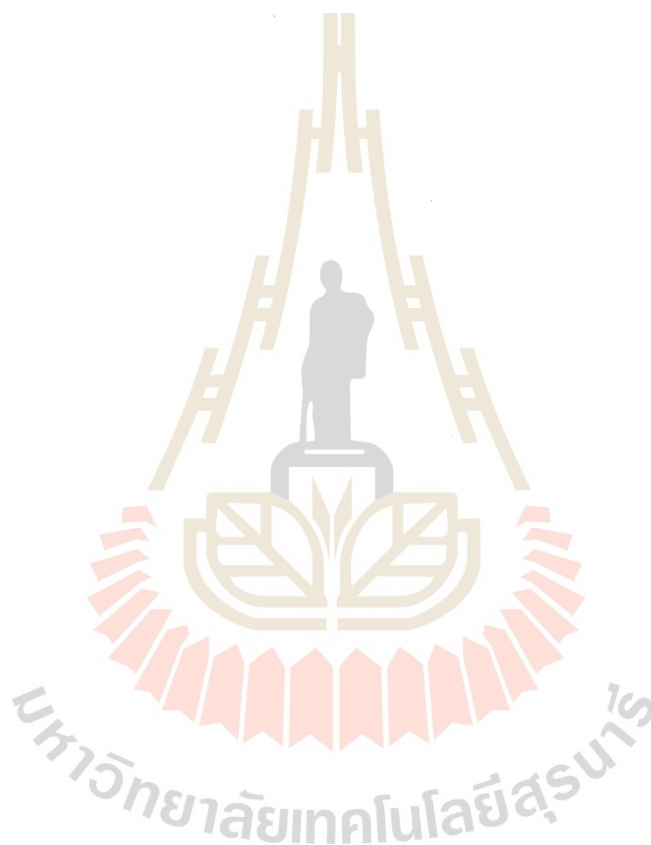
School of <u>Ceramic Engineering</u>   Student's Signature ....

Academic Year <u>2022</u>   Advisor's Signature ....

ACKNOWLEDGMENTS

TABLE OF CONTENTS

TABLE OF CONTENTS (Continues)

TABLE OF CONTENTS (Continued)

LIST OF TABLES

Table   **Page**

LIST OF FIGURES

LIST OF FIGURES (Continued)

LIST OF FIGURES (Continued)

LIST OF FIGURES (Continued)

Figure **Page**

LIST OF FIGURES (Continued)

CHAPTER I
INTRODUCTION TO TiO$_2$ PHOTOCATALYST

1.1   Overview of Titanium Dioxide

Recently, environmental pollution has become a major concern, particularly the contamination of organic and inorganic dyes, heavy metals, and infectious waste. These pollutants can cause severe diseases, with many of them being caused by pathogenic bacteria which is harmful to human beings not only to human health but also to the environment and animals. Various methods have been employed to solve these problems, including thermal, chemical, physical, and photocatalytic treatments. Among these treatments, photocatalytic treatment using the photocatalytic phenomenon has gained widespread acceptance.

The photocatalytic activity is a critical mechanism in the inactivation of bacteria. This phenomenon destroys the inner and outer membranes of bacteria, leading to the death cell due to the action of various radicals. It can also destroy DNA and RNA. The predominant semiconductor used for photocatalytic activity is titanium dioxide (TiO$_2$), which possessed high photocatalytic activity when exposed by solar irradiation, particularly sunlight. TiO$_2$ possesses several desirable properties, including being non-toxic, stable, and environmentally benign. As a result, it finds applications in various fields, such as water and air purification for inactivating bacteria and eliminating heavy metals. It is also used in medical equipment for sterilization, producing radicals such as hydroxyl (OH$^-$), superoxide (O$_2^-$) and hydrogen (H$^+$) radicals for inactivating bacteria.

Solar energy is one of the most promising renewable energy sources, as it is abundant and widely available. The amount of solar energy that reaches the Earth's surface is enormous, with an estimated 89,300 TW of solar irradiation. This solar radiation is composed of different wavelengths of light, with the UV, visible and IR regions being the most significant.

The UV region is composed of wavelengths below 400 nm. and accounts for about 3-5% of the solar irradiation that reaches the Earth's surface. The visible light region, which is responsible for the colors that we see, accounts for about 47% of solar irradiation and has wavelengths between 400-700 nm. The IR region, which includes the heat that we feel from the sun, accounts for about 53% of solar irradiation and has wavelengths above 700 nm.

In the field of renewable energy, solar energy has gained significant attention due to its potential to be converted into electricity through various technologies, such as photovoltaics and concentrated solar power. However, there are also other applications of solar energy, such as solar water heating and solar-powered desalination, which can have a significant impact on energy and water sustainability.

One of the challenges of using solar energy is to increase its efficiency and reduce its cost. Photocatalysis, which is the process of using a catalyst and light to accelerate a chemical reaction, has been proposed as a potential solution for enhancing the efficiency

of solar energy conversion. However, photocatalytic efficiency is typically more active under the UV region of solar irradiation due to its high energy. Therefore, researchers are developing new photocatalytic materials and strategies to improve the efficiency of solar energy conversion under visible light and IR regions as well.

In general, the photocatalytic efficiency of materials is most active under the UV region due to the high energy present in this wavelength range. This energy excites electrons to move from the valence band toward the conduction band, triggering reactions on both sides. Excited electrons (e_{CB}) in the conduction band react with oxygen (O_2) to produce various active species, such as hydroxyl radical (OH), hydrogen peroxide, superoxide (O_2^-), and others. The valence band, on the other hand, is left with positive holes (h^+_{VB}) resulting in water oxidation.
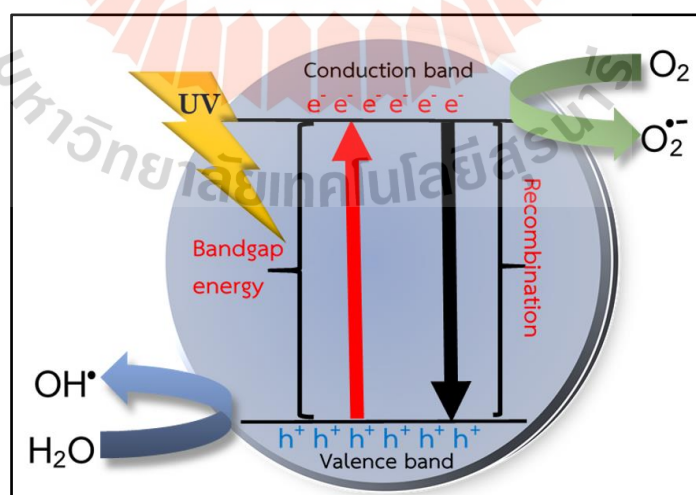
Figure 1.1 Scheme photocatalytic reaction

The layered perovskite structure, $A_2B_2O_7$, with its highly donor-doped state, exhibits photocatalytic performance due to separated electrons and holes, in addition to high stability and redox reaction. $La_2Ti_2O_7$, a member of this structure, is particularly noteworthy for its high photocatalytic water splitting capability, producing H_2 and O_2. It is also efficient under UV region due to its large band gap energy of approximately 3.8 eV.

Band gap energy plays a significant role in exhibiting efficient photocatalysts since the visible light spectrum has insufficient energy to excite electrons to migrate from the valance band to the conduction band, unlike the UV region. This poses a challenge to achieving high photocatalytic activity. Researchers have attempted to improve $La_2Ti_2O_7$'s efficiency by working on the visible light region, such as doping with a transition metal or cation doping. Cation doping is effective in extending the band-edge photoresponse towards visible light irradiation as narrow band gap energy. However, monodoping, which involves doping with a single cation in the microstructure, has limitations due to an unoccupied impurity state that decreases band gap energy. The solution is the co-doping system, where two cations are doped in the microstructure to obtain photocatalytic desirability since it maintains charge balance and has high-evacuated carriers and high degree band gap.

Fe and Cr co-doping are promising candidates for visible light-driven $La_2Ti_2O_7$ as cation doping, and the co-doping system is more effective than mono-doping and undoping. For anion doping, elements like N, C and S decrease the band gap energy. However, nitrogen (N) is remarkable in obtaining high photocatalytic activity working on visible light.

The present work investigates the influence of nitrogen-doped (Fe, Cr) $La_2Ti_2O_7$ and its photocatalytic activity under visible light as methylene blue degradation. $La_2Ti_2O_7$ was prepared by the sol-gel method to obtain high purity $La_2Ti_2O_7$, and doping with Fe and Cr was carried out during the first preparation as cation doping. As for anion doping, calcination was done at different temperatures under a nitrogen atmosphere.

1.2   Research objective

1.2.1   Study the effect N_2 dope on the photocatalytic activity of (Fe, Cr) $La_2Ti_2O_7$ (N) under visible light irradiation.

1.2.2   Study the effect of calcination parameter such as temperature and time on the photocatalytic activity of synthesized (Fe,Cr) $La_2Ti_2O_7$ (N), confirmed by methylene blue (MB) degradation.

1.2.3   Study the sol gel process for preparation of (Fe,Cr) $La_2Ti_2O_7$ base for synthesized (Fe, Cr) $La_2Ti_2O_7$ (N) photocatalyst.

1.3   Research hypothesis

Co-doping, which involves the simultaneous introduction of two or more dopants into a photocatalytic material has been found to be a promising strategy for improving photocatalytic efficiency. This is because co-doping can create additional electronic states within the band gap of the material which can facilitate the separation of photo-generated charge carriers leading to improved photocatalytic activity. Transition metals, such as Fe and Cr, are commonly used as co-dopants due to their ability to create new energy states within the band gap of the photocatalytic material. This, in turn, enhances the absorption of light and promotes the separation of electron-hole pairs, leading to higher photocatalytic efficiency. Nonmetal co-dopants, such as nitrogen, fluorine, and sulfur, can also improve photocatalytic activity by introducing additional energy levels within the band gap of the photocatalyst. Nitrogen, in particular, has been shown to be an effective co-dopant due to its ability to reduce the band gap energy of the photocatalytic material, making it more efficient in absorbing visible light. Furthermore, the combination of transition metals and nonmetals as co-dopants can lead to synergistic effects, resulting in even higher photocatalytic activity. In summary, co-doping with both transition metals and nonmetals can be an effective approach for improving the photocatalytic performance of materials. This strategy can create new energy levels within the band gap, enhance light absorption, and promote charge carrier separation, ultimately leading to higher photocatalytic efficiency.

CHAPTER II
LITERATURE REVIEW

2.1   Overview TiO₂ base photocatalyst

Photocatalysis has been combined two words together that it consists of photochemistry and catalysis and relates to light irradiation and catalysis reaction which accelerate chemical reaction and transformation. Some of words are likely same as catalysis, such as catalyzed, assisted, induced, accelerated, promoted, and stimulated, makes it confusing. The term of catalysis, in the sixteenth century, the word used catalysis from the chemist A. Libavius in his book Alchymia so the original word that was from the Greek and mean "decomposition" or "dissolution" Next, in nineteenth century, applying this about the occurred reaction was not directly to chemical transformation, according to Berzelius, and Ostward defined catalyst as kinetic phenomenon that changed the rate of reaction neither changing chemical product nor changing chemical equilibrium. Until modifying of the definition of catalyst in the reaction rate theory was explained "A catalyst is a compound that are lower the free activation energy enthalpy of the reaction."
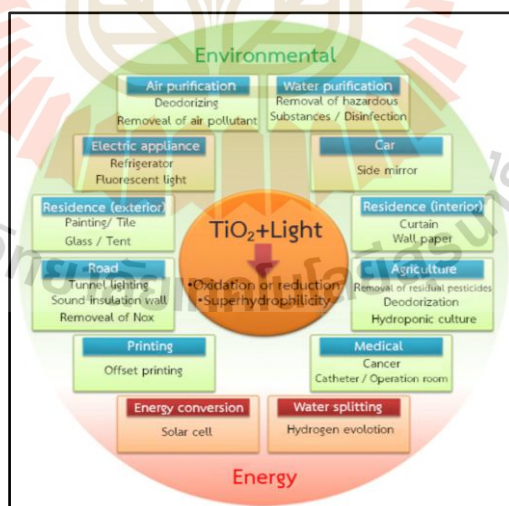
Figure 2.1 The various applications in solving pollution (Nakata, K., &Fujishima, A., 2012).

Titanium dioxide, also known as TiO₂, has gained widespread usage in various applications due to its unique properties, such as photocatalysis (Figure 2.1). This

property has made it an essential component in many fields, particularly in the environmental and energy sectors. TiO$_2$ is not only stable and low-cost but also environmentally friendly and biocompatible, making it highly desirable for many applications. The interest in utilizing the photocatalytic phenomenon to solve current problems has been on the rise for several years. This can be seen in the continuous increase in the number of publications on the subject, which is currently over 1000 peer-reviewed publications per year (Figure 2.2). Scientists from different fields are working tirelessly to develop new technologies that can take advantage of this property and solve pressing environmental issues.

One of the significant environmental problems that TiO$_2$ photocatalysis can help solve is water pollution. Researchers are developing new methods to improve photocatalytic reactions for sanitization and cleansing of water, as well as various techniques for increasing renewal water to clean wastewater. These developments can have a significant impact on the environment and help to make water safer and more readily available for various uses.
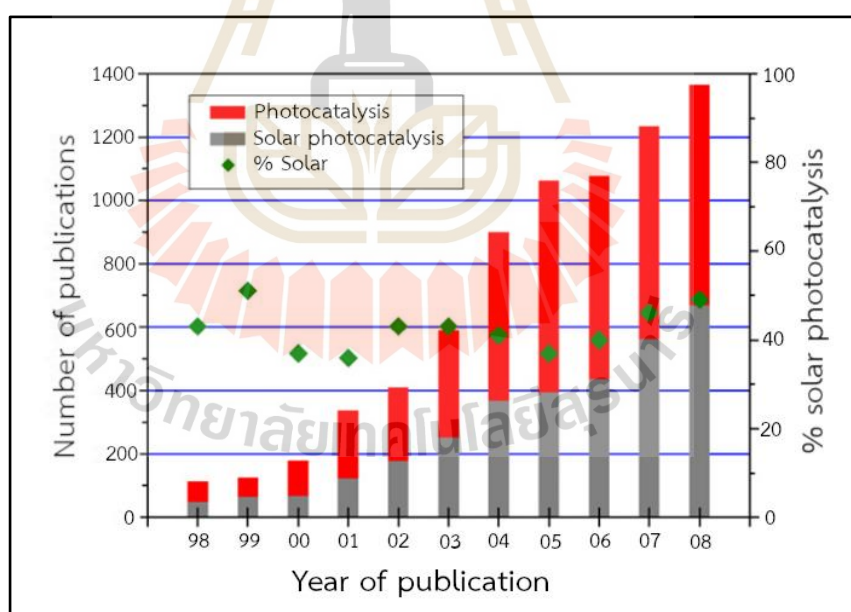
Figure 2.2 The number of publications tend (Spasiano, D. et al., 2015)

2.2   Explored photocatalysis

The phenomenon of water splitting photocatalyst of TiO_2 under Ultraviolet (UV) region by Fujishima and Honda represents a significant milestone in the field of heterogeneous photocatalysis. This finding challenged existing notions within electrochemistry and catalysis and has since become an important area of research and development for many scientists across multiple disciplines.

Despite facing initial resistance and skepticism from some electrochemists, extensive research has been conducted to be more understand how to enhance the efficient photocatalyst of TiO_2. This has been approached to the development of numerous applications for TiO_2 photocatalysts, such as the decontaminated-organic compounds in air pollution and wastewater. As consequence, TiO_2 photocatalysts are considered to approach for environmental remediation, clean energy, and energy harvesting.

Fujishima emphasis on the importance of sharing the benefits of science and technology with everyone is a commendable perspective. Fujishima belief that the significant key of modern science is being a healthy society, comfortable, and wellness lives and is an aspirational goal that many in the scientific community share. Fujishima's work, specifically his utilization of the photocatalyst discovery, exemplifies a commitment to contribute to the creation of such a society.

The water-splitting photocatalytic exploration of TiO_2 under Ultra violet (UV) region by Fujishima and Honda is a significant breakthrough in the field of heterogeneous photocatalysis. This discovery has spurred extensive research, leading to the development
of new applications for TiO_2-based photocatalysts. Fujishima's focus on utilizing scientific discoveries to create a better society highlights of scientific research and the favorable influence it can have on society as entireness.

2.3   Photocatalysis definition

Photocatalysis is the remarkable process that utilizes both harvesting light and catalysis reaction to facilitate or accelerate a chemical reaction. The term "photocatalysis" is speculated from the ancient-Greek language and is separated into 2 words; "photo" meaning light, and "catalysis" referring to the process whereby a substance change the chemical transformation rate of reactants being stable itself. Catalysts reduce the activation energy required for a reaction to occur, effecting in an increased reaction rate. Photocatalysts can be classified as homogeneous or

heterogeneous. Homogeneous photocatalytic processes mainly use metal complexes as catalysts which produce hydroxyl radicals with responded organic matter to toxic-substances destruction.

Heterogeneous photocatalysis, on the other hand, is a technically sophisticated method that uses a solid catalyst, typically a semiconductor material such as titanium dioxide (TiO_2), to degrade various organic pollutants in wastewater. When exposed by light, semiconductors occur electron-hole pairs that are reacted with water or oxygen to form reactive species capable of breaking down organic pollutants into less harmful substances. The advantages of heterogeneous photocatalysis include ease of operation, low energy consumption, environmental friendliness, and the ability to separate the catalyst from treated water for easy reuse. Ongoing research in this area is focused on developing new and more efficient catalysts, optimizing reaction conditions, and scaling up the process for commercial use. Heterogeneous photocatalysis has numerous applications in environmental systems: the decontaminated wastewater, generated hydrogen, purified air, and disinfection. Photocatalysis has gained attraction of wastewater treatment due to its cost-effectiveness and efficiency to acquire complete mineralization of pollutants.

Currently, photocatalytic TiO_2 are considered to promote an approach for the total decontamination of polluted air and wastewater destructing organic compound. One of the pioneers, Fujishima, in the field of photocatalysis, emphasizes the importance of sharing the benefits of science and technology with everyone. According to Fujishima, the crucial role of developing new concepts is perform to various products and services. By utilizing his discovery of the photocatalyst, Fujishima prospect to contribute to the creation of such a society. The field of photocatalysis has immense potential for developing environmentally friendly and sustainable solutions for wastewater treatment and the degradation of organic pollutants. As researchers continue to explore and develop new photocatalysts and optimize reaction conditions, the practical applications of photocatalysis are probable to expand and improve.

2.4   Photocatalysis mechanism

The process of photocatalysis involves the utilization of a suitable catalyst and the interaction of light energy to facilitate redox reactions that lead to the degradation of pollutants. Semiconductor materials are commonly employed as photocatalysts due to their electronic structure, which comprises a filled electron in the valence band and an unoccupied electron in the conduction band. This allows for the transfer of electrons and holes, resulting in the aforementioned redox reactions. Before the occurred redox reaction becomes with electrons and holes, it takes more steps reaction. The steps involved in semiconductor photocatalysis; when photons from light irradiation with equivalent energy or greater than the bandgap energy of the semiconductor material are absorbed, valence band electrons are excited and migrate to the conduction band, leaving holes in the valence band. The left holes can react with water molecules to generate hydroxyl radicals, while the excited electrons in the conduction band react with dissolved oxygen species to form superoxide ions. Both the hydroxyl radicals and superoxide ions possess strong oxidizing power, which accompanies the decontaminated pollutants. In addition, the electrons and holes can endure successive oxidation and reduction reactions with any adsorbed species to form attainable products (Figure 2.3).
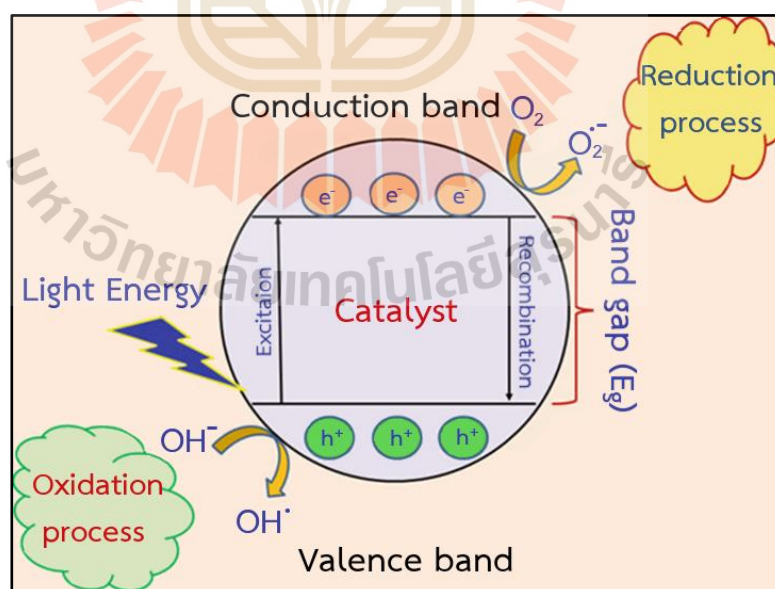
Figure 2.3 Photocatalytic mechanisms scheme (Khan et al., 2017)

Accordingly, all mentioned above, it can write relative equations by:

$$TiO_2 + h\nu \longrightarrow e^- + h^+ \hspace{3cm} (eq\ 2.1)$$

For equation below, occurrence of H_2O_2.

$$O_2 + e^- \longrightarrow O_2^-\bullet \hspace{3cm} (eq\ 2.2)$$

$$O_2^-\bullet + H^+ \longrightarrow HOO\bullet \hspace{3cm} (eq\ 2.3)$$

$$H_2O \longrightarrow OH^- + H^+ \hspace{3cm} (eq\ 2.4)$$

$$HOO\bullet + e^- \longrightarrow HO_2^- \hspace{3cm} (eq\ 2.5)$$

$$HO_2^- + H^+ \longrightarrow H_2O_2 \hspace{3cm} (eq\ 2.6)$$

$$H_2O_2 + e^- \longrightarrow OH^- + OH\bullet \hspace{3cm} (eq\ 2.7)$$

$$H_2O + h^+ \longrightarrow H^+ + OH\bullet \hspace{3cm} (eq\ 2.8)$$
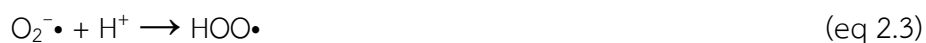
2.4.1 Description of oxidation mechanism

The presence of absorbed water on the photocatalyst surface can furtherenhance the photocatalytic activity. This water can be oxidized by the positive holes in the valence band to form hydroxyl (OH·) radicals which have strong oxidizing power and can react with organic matter present in the pollutants. In the presence of oxygen, these intermediate radicals can undergo radical chain reactions, ultimately decomposing the organic matter into carbon dioxide and water (Figure 2.4).
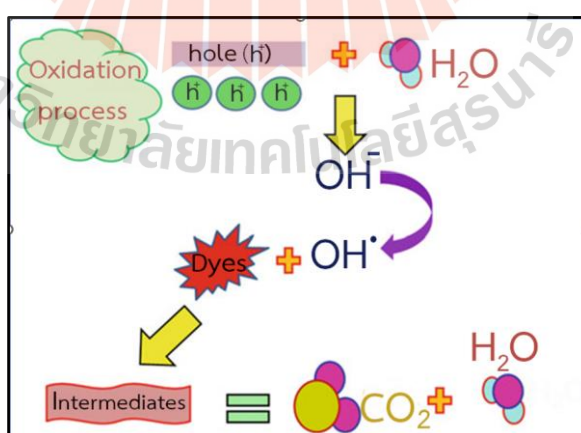
Figure 2.4 Oxidation reaction scheme (Khan et al., 2017)

2.4.2   Description of reduction mechanism

Reduction of oxygen contained in the air also occurs during the photocatalytic process. The conduction band electrons react with dissolved oxygen species to form superoxide anions, which can attach to the intermediate products in the oxidative reaction, forming peroxide or converting to hydrogen peroxide and then water. Reduction is more likely to occur in organic matter than in water, leading to an increase in the number of positive holes, reducing carrier recombination, and enhancing photocatalytic activity (Figure 2.5).
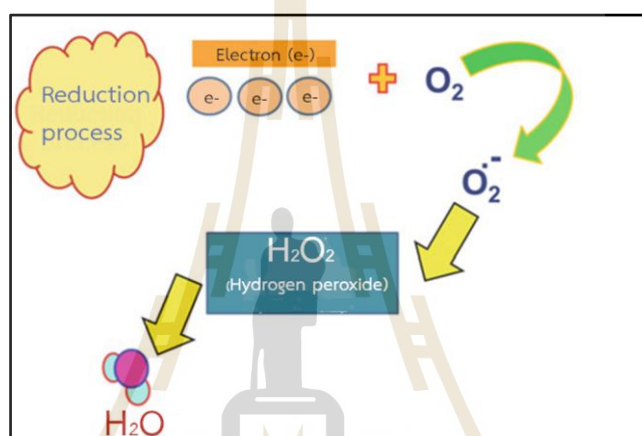
Figure 2.5 Reduction reaction scheme (Khan et al., 2017)

2.5   Limitation of TiO_2 for photocatalyst

The number of researchers reported that TiO_2 can adsorb Ultra violet region, UV, so this range that it is enough energy to excite an electron to excited state, electrons from valence band to conduction band, but it has only 5% out of solar radiation. TiO_2 cannot absorb in visible light range, approximately 43% out of solar radiation due to it becomes the reflection of light of the large band gap energy between the occupied valence and empty conduction band and the fact that the light in visible wave range is not absorbed by TiO_2. Others region, near-infrared and infrared region 52% out of solar radiation approximately, do not promoted electronic transition due to it changes in vibrational energy of covalent bond (Spasiano, D., 2015) (Figure2.6).
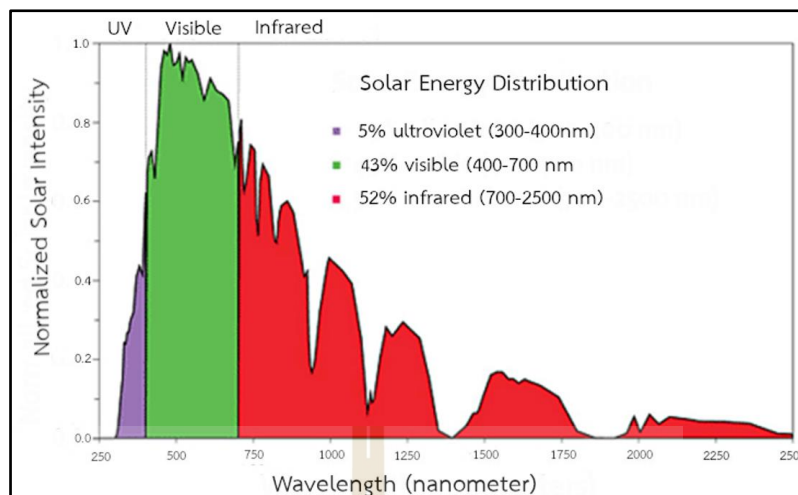
Figure 2.6 Solar energy spectrum (Vu & Kaliaguine, 2019)

2.6   Metal doping

Liqiang et al. (2004) improving TiO_2 is active under visible light, and the doping with transition metals were obtained high photocatalytic activity. One of various transition metal was high efficiency emphasizing Lanthanum (La). The XRD pattern was shown

5 mol% of La doped TiO_2 that the La inhibited phase transformation of TiO_2 comparing with different temperature. At 700°C of La-doped TiO_2 appeared a little rutile peak but undoped TiO_2 translating to rutile structure completely, as shown in Figure 2.7.
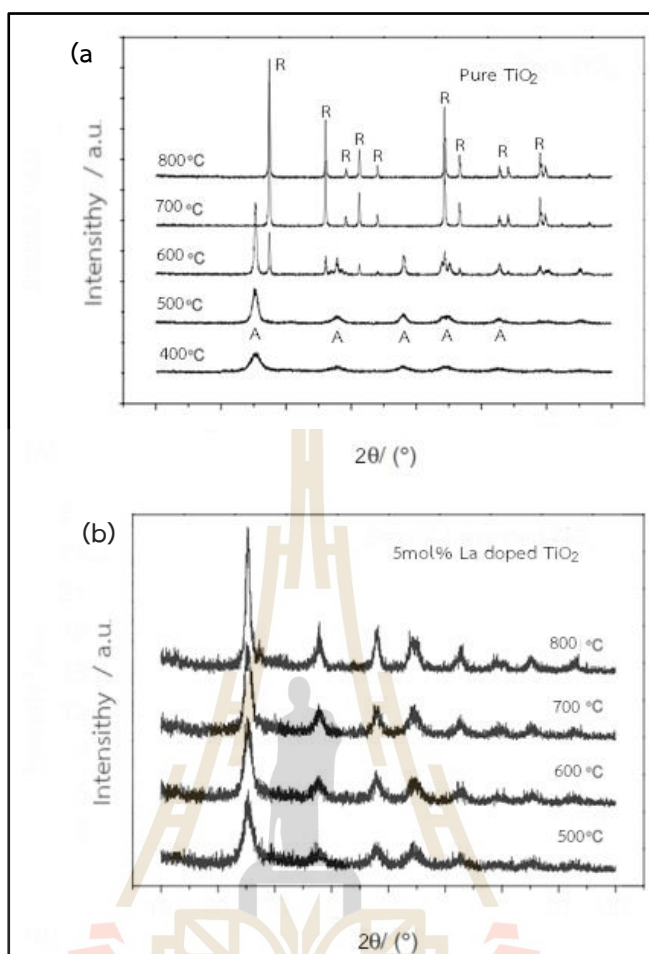
Figure 2.7 XRD pattern (a) pure TiO₂ and (b) the different temperatures
of doping TiO₂ with 5 mol% of La (Liqiang et al., 2004)

Accordingly, XPS spectrum analysis, calcined at 500°C and 600°C, they found
that the increasing of calcination temperature were increased amount of crystal lattice
oxygen, while occurring oxygen vacancies were decreased, the combination of atoms
or groups to become stable. Concentration ratio Ti/La on surface was high that La^{3+}
was diffused to surface with increasing calcination temperature in Figure 2.8.
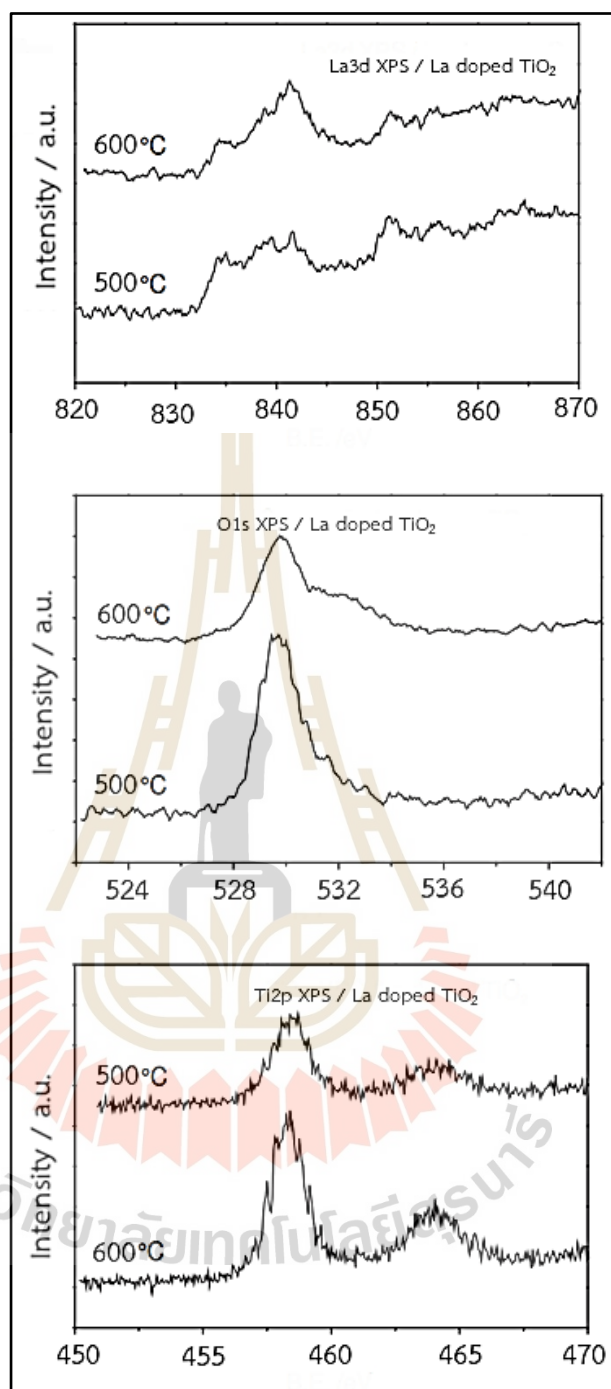
Figure 2.8 Identified elements on the surface by XPS: La, O, and Ti with
doping 5mol% of La on TiO₂ nanoparticles at different
calcination temperature, 500°C and 600°C. (Liqiang et al., 2004)

Importantly, La^{3+} was possible the Ti-O-La formation which effected to inhibit growing of rutile crystal (Figure 2.8). In addition, aspect of photocatalytic activity with 5 mol% of La doped TiO_2 by decreasing phenol appropriate condition was at 600°C (Figure 2.9).
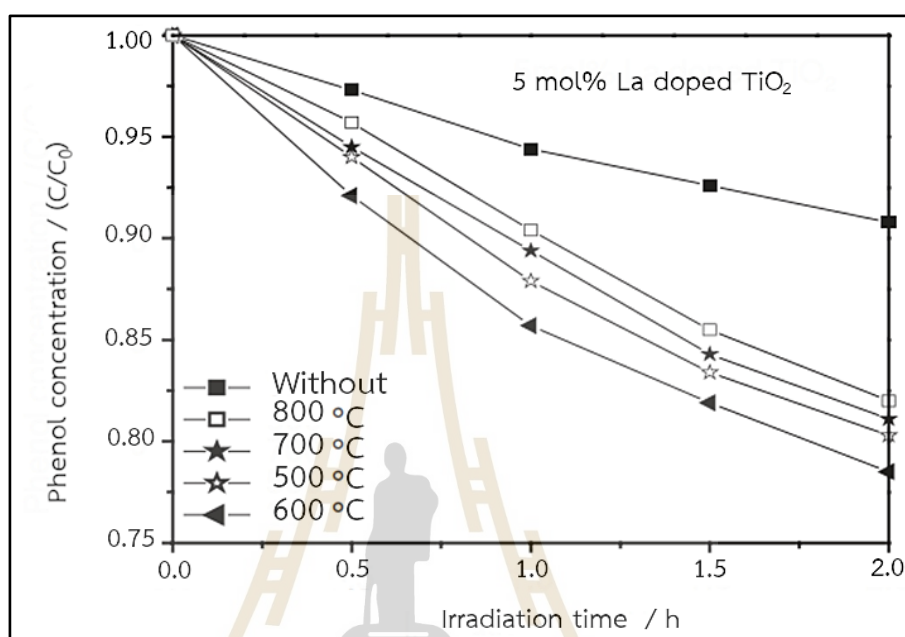
Figure 2.9 The photocatalytic efficiency of phenol degradation with doping 5 mol% La on TiO_2 nanoparticle. (Liqiang et al., 2004)

Zhu, J. et. al. (2006) tried to improve titanium dioxide efficiency, TiO_2, had been extensively researches which was mostly photocatalytic ability to solve environmental pollution because of various useful properties such as high photocatalytic properties, harmless, chemically stable form, and inexpensive cost. However, the limitation of TiO_2 was only active under Ultra Violet (UV), and several-researchers effort developed TiO_2 to be active under visible light using various transition metal doping in TiO_2. Fe^{3+} is one of choices that researchers select to improve photocatalytic activity by doping on TiO_2, modifying a charge carrier, as well as various synthetic techniques used for doping TiO_2. Sol-gel technique is the most processing had been considered to prepare doping ion TiO_2 in nanosized with high purity.
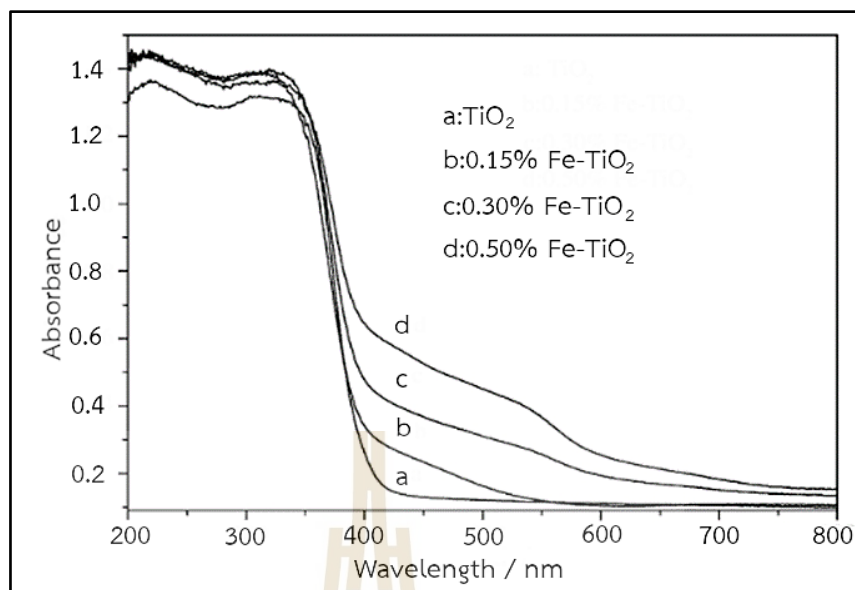
Figure 2.10 UV-Vis measurement (a) pristine TiO_2, (b) TiO_2 with doping 0.15%Fe, (c) TiO_2 with doping 0.30%Fe, and (d) TiO_2 with doping 0.50%Fe. (Zhu, J. et. al., 2006)

Particularly, measuring UV-Vis, Figure 2.10 was shown the consequence of Fe on the wavelength TiO_2 absorption. The absorption range increased from 400 to 650 nm with the Fe contents; it accompanies to change in white to reddish color in which occurs from two factors. The excited electrons on 3d state from Fe^{3+} to conduction band of TiO_2 at 415 nm was charged transition and d-d transition at 500 nm.
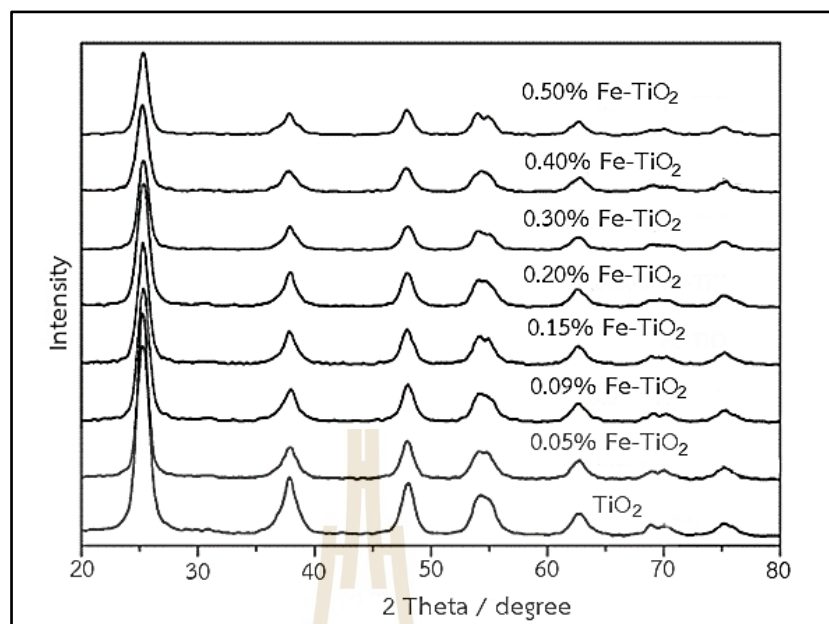
Figure 2.11 XRD pattern of TiO_2 and $Fe\text{-}TiO_2$ (Zhu, J. et. al., 2006)

They found that Fe^{3+} diffuses in C-axis, 0.77 A°, and substitute Ti^{4+} in contributed to Fe^{3+}atomic radius (0.64 A°) was almost equal to Ti^{4+}atomic radius (0.68 A°), For C-axis was possible to be diffusion. Amount content of Fe influencing XRD pattern, it was evident from the result that Fe^{3+} diffuse in C-axis and substituted in TiO_2 structure when the crystal growth of Fe doped TiO_2 that its gain restrained during hydrothermal treatment, which was slightly broadening in XRD peak (Figure 2.11).
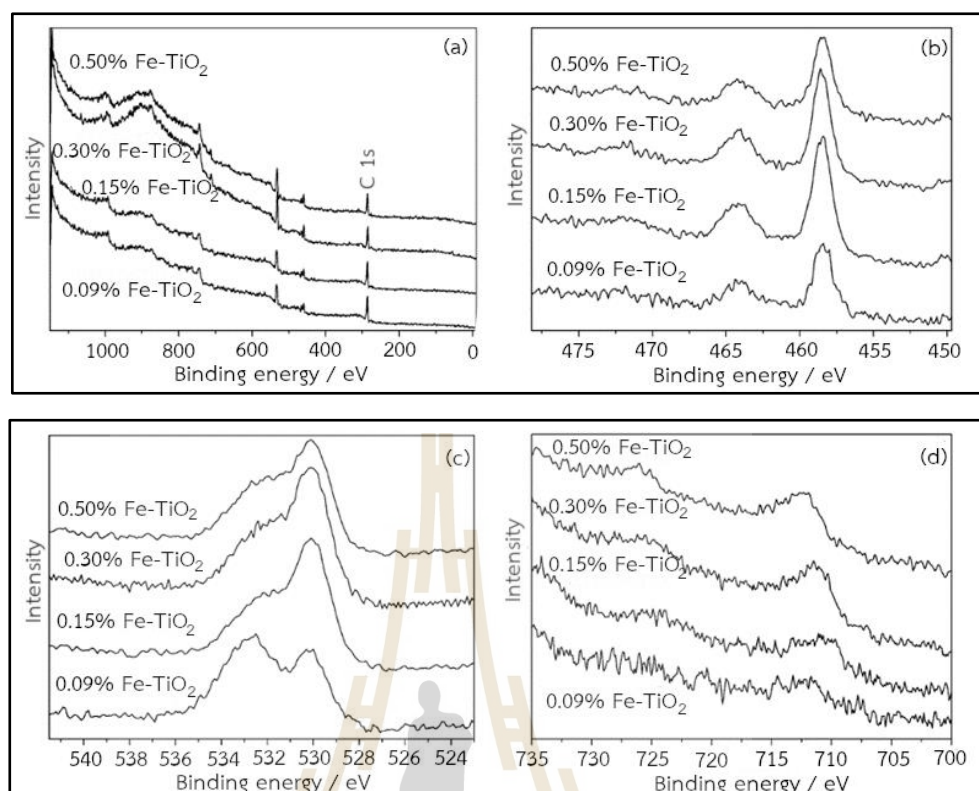
Figure 2.12 Binding energy Fe doped TiO_2 (XPS spectra): (a) all Fe
content, (b) Ti2p state peak, (c) O1s state peak, and
(d) Fe2p state peak. (Zhu, J. et. al., 2006)

The XPS pattern indicated at 464.2 and 458.2 eV respectively, which indicated Ti^{4+}-binding energy in TiO_2 structure, for $2p_{3/2}$ state of Fe_2O_3 at 710.7 eV and $2p_{1/2}$ state at 724.3 eV was shifted, emphasizing Fe^{3+} on surface was more positively charged probably. The Fe2p state was diffused in the TiO_2 lattice and occurring the Fe-O-Ti formation (Figure 2.12).

Prekajski, M. et al. (2016) investigated chromium doped titanium dioxide, Cr-doped TiO_2, with 3 and 6 mol%, calcined in various temperatures; the XRD pattern showed the calcination at 400, 600 and 800°C (Figure 2.13).
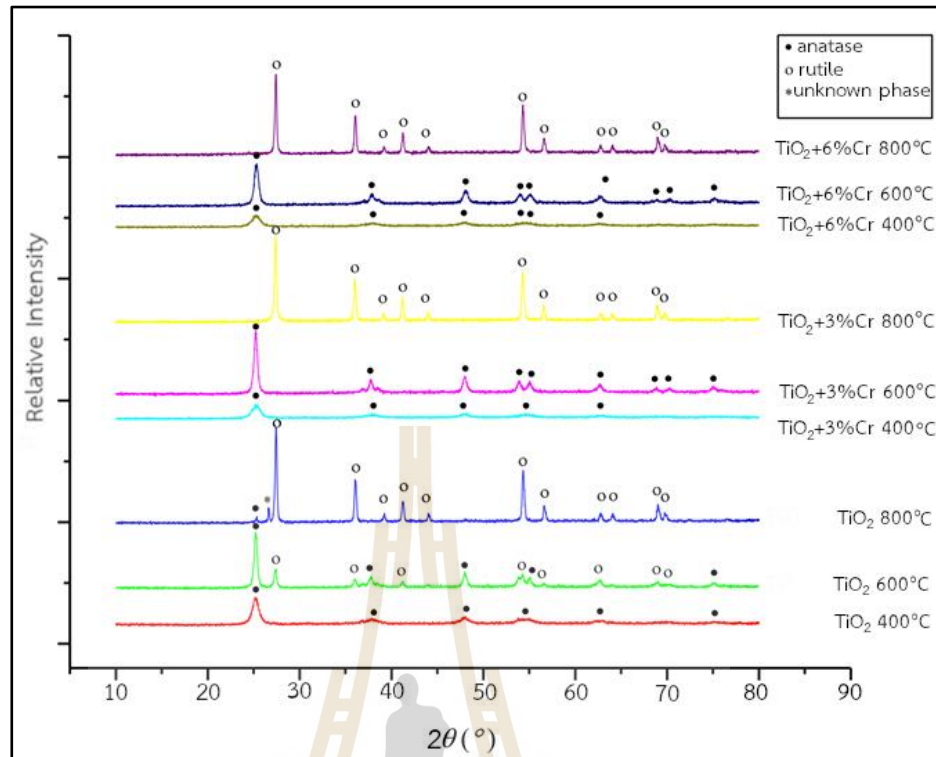
Figure 2.13 XRD pattern TiO_2 and Cr-doped TiO_2, 3 mol% and 6 mol%.
(Prekajski, M. et al., 2016)

Particularly, at 400 °C, all diffraction peaks of Cr-doped TiO_2 which were an anatase structure when temperature rise it up, 600°C that the pure TiO_2 exhibited some peak of rutile structure, but Cr-doped TiO_2 still stabilized in anatase structure. Increasing temperature up to 800°C, pure TiO_2 and Cr-doped TiO_2 promote to rutile structure completely because the kinetic transformation from anatase to rutile was powerfully affected by defecting oxygen degrees when the transformation increased toward oxygen vacancies enhancing. A key effect of phase transformation was oxygen vacancies concentration which caused by two group of dopants: (i) inhibitors and (ii) promoters, in term of the combined effect of both ionic radii and valence.

Apparently, Cr^{3+} as dopant which was strongly promoted anatase to rutile phase transformation that Cr^{3+} was substituted on Ti^{4+} becoming oxygen vacancies increasing mass transport for phase transformation into rutile structure completely.

Table 2.1 Crystal line size with pure and Cr-doped TiO_2, 3 mol% and 6 mol%.
(Prekajski, M. et al., 2016)

	Anatase		Rutile		Anatase crystalline size [nm]	Anatase Microstrain [%]
	a [A°]	b [A°]	a [A°]	b [A°]		
TiO_2 400°C	3.7997	9.512	/	/	4.1	0
TiO_2 600°C	3.7833	9.509	4.5925	2.9585	8.2	0
TiO_2 800°C	3.787	9.504	4.5943	2.9599	27.4	0
TiO_2 + 3%Cr 400°C	3.798	9.491	/	/	4.8	0
TiO_2 + 3%Cr 600°C	3.7833	9.501	/	/	8.51	0
TiO_2 + 3%Cr 800°C	/	/	4.5959	2.9597	26.7	0
TiO_2 + 6%Cr 400°C	3.795	9.497	/	/	5.4	0.5
TiO_2 + 6%Cr 600°C	3.7871	9.5044	/	/	8.5	0.3
TiO_2 + 6%Cr 800°C	/	/	4.5951	2.9594	31.8	0

In addition, when Cr^{3+} replaced on Ti^{4+} in crystal structure, it caused on defecting crystal structure of TiO_2 which occurred microstrain inside (Table 2.1). Furthermore, factor of temperature, the microstrain decreased when temperature increased, depending on concentration of Cr doping. Moreover, Cr-doped TiO_2 exhibited high specific surface area, S_{BET}, greater than pure TiO_2 due to the different charge, in this case lower, led to a different particle packing in contributed to the dopant become to occur unsaturated bond on surface which obtained higher surface energy comparing with pure TiO_2. (Table 2.2), and the concentration of Cr was only 2-3% locating on surface.

Table 2.2 Specific surface area both pure TiO_2 and Cr-doped TiO_2, 3 mol % and 6 mol%. (Prekajski, M. et al., 2016)

Sample	S_{BET} (m^2/g)	S_{meso} (m^2/g)	S_{mic} (m^2/g)	V_{mic} (m^2/g)
TiO_2	70	70	-	-
TiO_2 3% Cr	154	154	-	-
TiO_2 6% Cr	149	149	-	-

Especially, Cr concentration was effective to band gap energy which was reduction when increasing concentration of Cr doping because of oxygen vacancies. The best result of concentration of Cr is 6 mol% with calcination temperature at 400˚C (Figure 2.14).
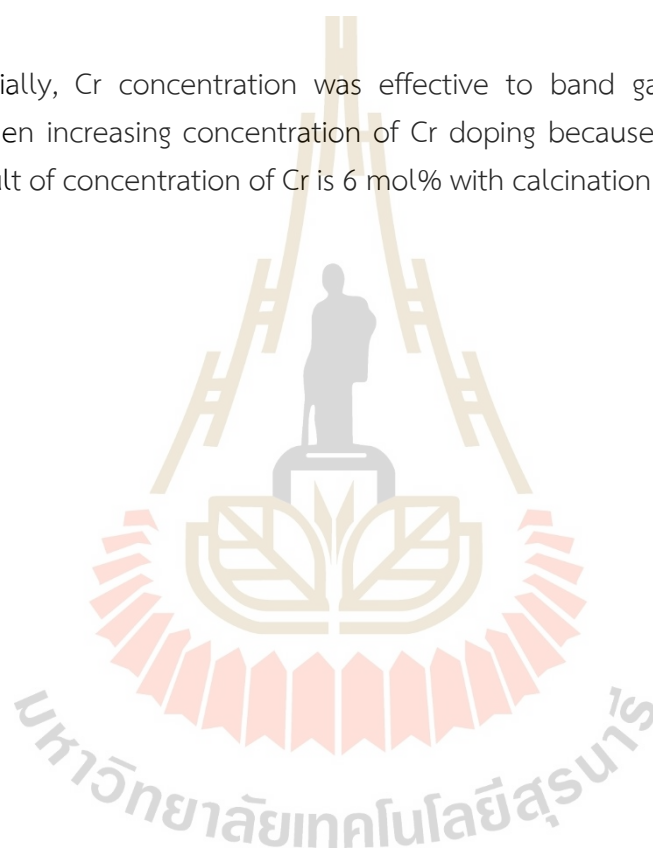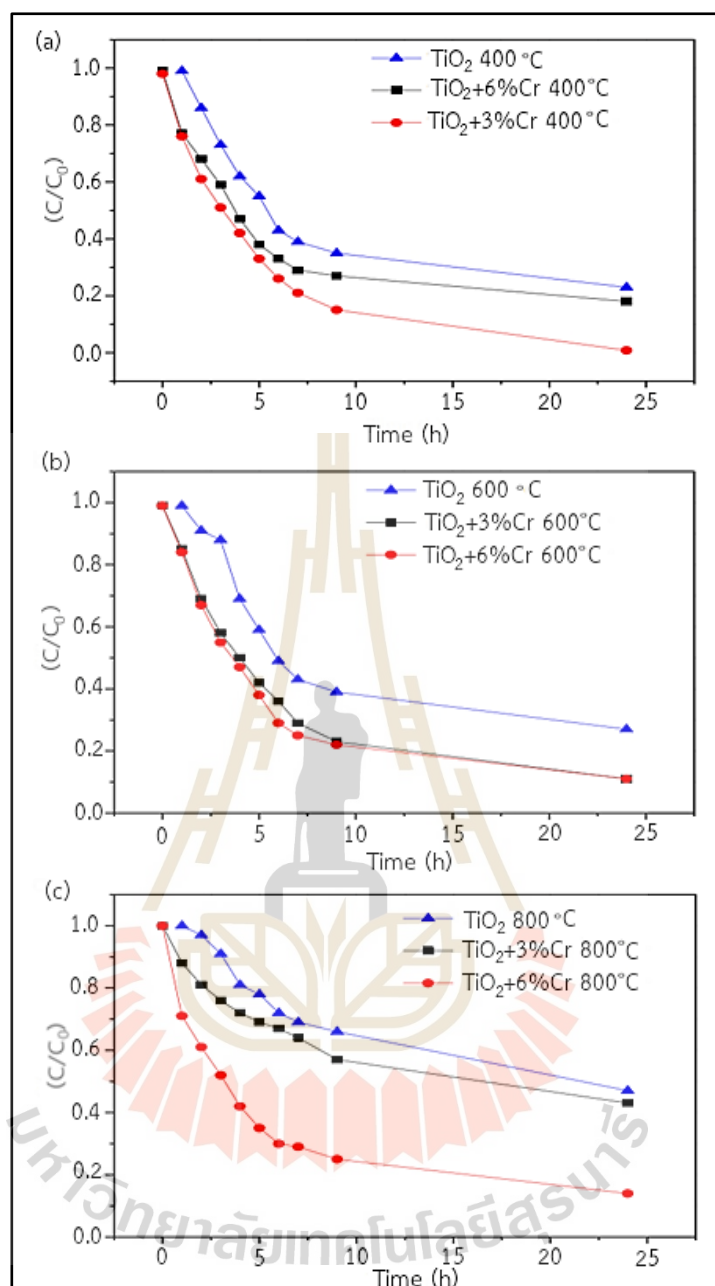
Figure 2.14 Crystal violet (CV) dye degradation by TiO$_2$ sample, pure and
Doping Cr^{3+} , with various concentrations. Different
calcination temperature: (a) 400°C, (b) 600°C, and (c) 800°C.
(Prekajski, M. et al., 2016)

2.7   Non-metal doping

Chen X. and Burda C. (2007) prepared samples for the comparison of doping non-metal, which was nitrogen (N), carbon (C) and sulfur (S), in titanium dioxide (TiO$_2$) to study their properties that it was measurement X-ray diffraction (XRD), X-ray photoelectron spectroscopy (XPS) and UV-Vis, for indicating XRD pattern had four patterns to compare each non-metal doping (Figure 2.15).
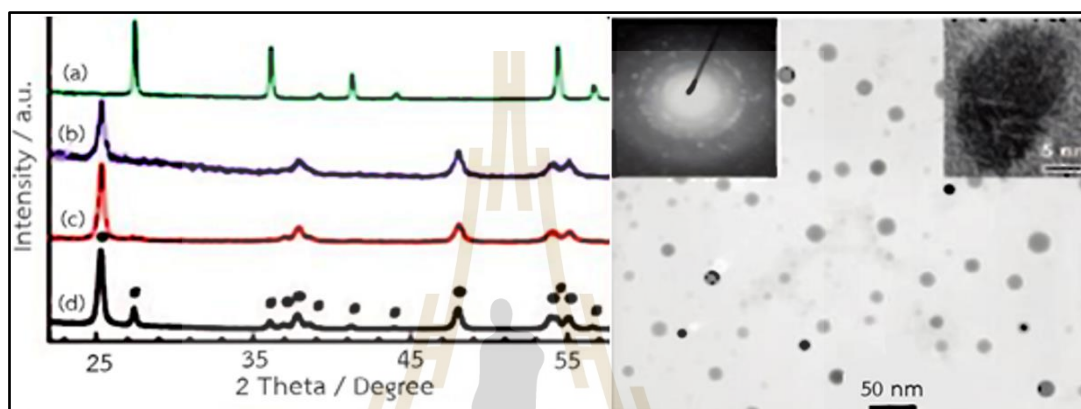
Figure 2.15 XRD pattern (a) pristine TiO$_2$, (b) carbon doped TiO$_2$(C-TiO$_2$), (C)
            sulfur doped TiO$_2$ (S-TiO$_2$) and (d) nitrogen doped TiO$_2$ (N-TiO$_2$)
            below high-resolution TEM (left) and electron diffraction pattern.
            (Chen X. & Burda C., 2007)

The colors of doped TiO$_2$ exhibited a yellow to light yellow which was absorbed under visible light region.
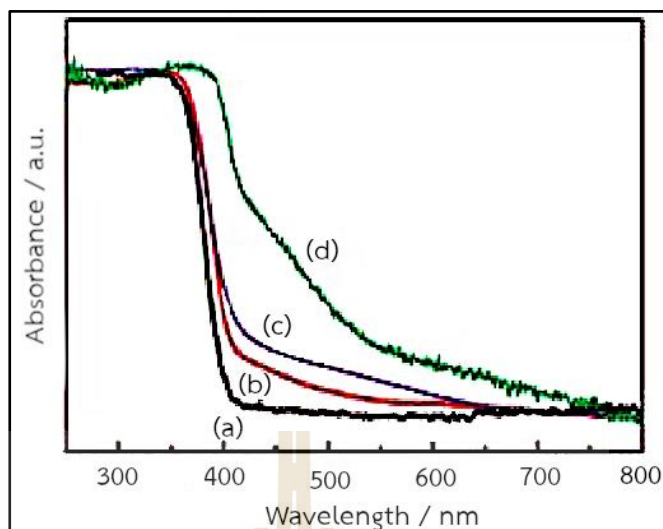
Figure 2.16 UV-Vis (a) pristine TiO_2, (b) C-TiO_2, (c) S-TiO_2 and (d) N-TiO_2.
(Chen X. & Burda C., 2007)

In addition, pure TiO_2, C-, S- and N-doped TiO_2 showed band edge absorption around 390 nm, for N-TiO_2 showed 415 nm, rutile-phase band-edge absorption (Figure 2.16). Furthermore, among three, N-doped TiO_2 obtained largest optical properties, which were high absorption under visible light, $\lambda > 400$ nm.
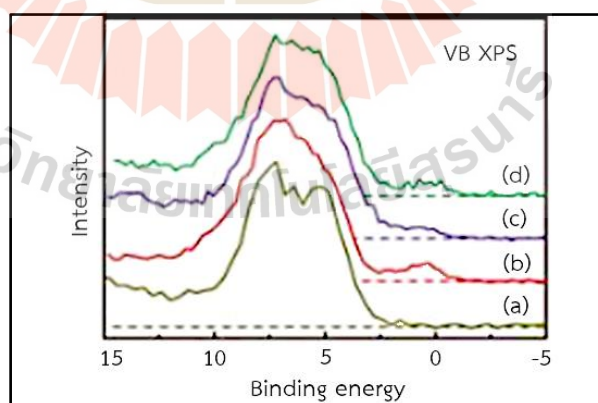
Figure 2.17 VB XPS spectra (a) pure TiO_2, (b) C-TiO_2, (c) S-TiO_2 and
(d) N-TiO_2 (Chen X. & Burda C., 2007)

Analysis by XPS, the XPS spectra was explained how to create a formation structure, binding energy, and another thing that it was explained the total density of state (DOS) of the valence band (VB), for Figure 2.17 TiO_2 was diffused by non-metal that both substitutional and interstitial sites were observed indicting 397.0 eV and 400 eV respectively.

Wang, J. et al. (2009) synthesized Titanate nanotube (TNT) was large band gap energy, 3.3 eV and 3.87 eV which was difficult to transfer electrons from valence band to conduction band as well as UV spectrum transferred electrons due to its enough power energy, but UV region in solar energy was only 4-5% why several researcher was intensively interesting to improve TNTs to be active under visible light, 53% out of solar energy.

Doping non-metal, even nitrogen, on titanium dioxide (TiO_2) was not reduction band gap energy, but it occurred the hybridization of the N 2p state of dopiant with O 2p state valence band of TiO_2 by instread of nitrogen N 2p state above on the maximum valence band of TiO_2.
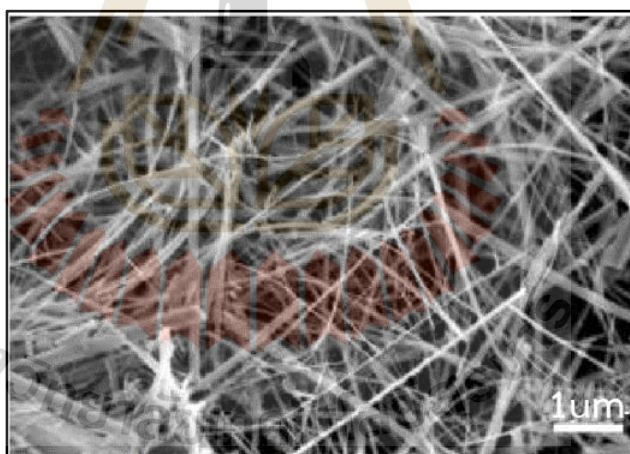
Figure 2.18 TiO_2 nanobelt of SEM image. (Wang, J. et al., 2009)

A structure of undoped TiO_2 nanobelt (Figure 2.18), its phases were analyzed by XRD technique comparing with both undoped and doped TiO_2 which treated them under NH_3 gas in different temperature 525, 550, 575 and 600°C as signified as N525, N550, N575 and N600 respectively, for phases analysis were detected by XRD

technique to discover types of phase in compound. In addition, color of them were different; N525, N550 and N575 were yellow and was a grayish green of N600.
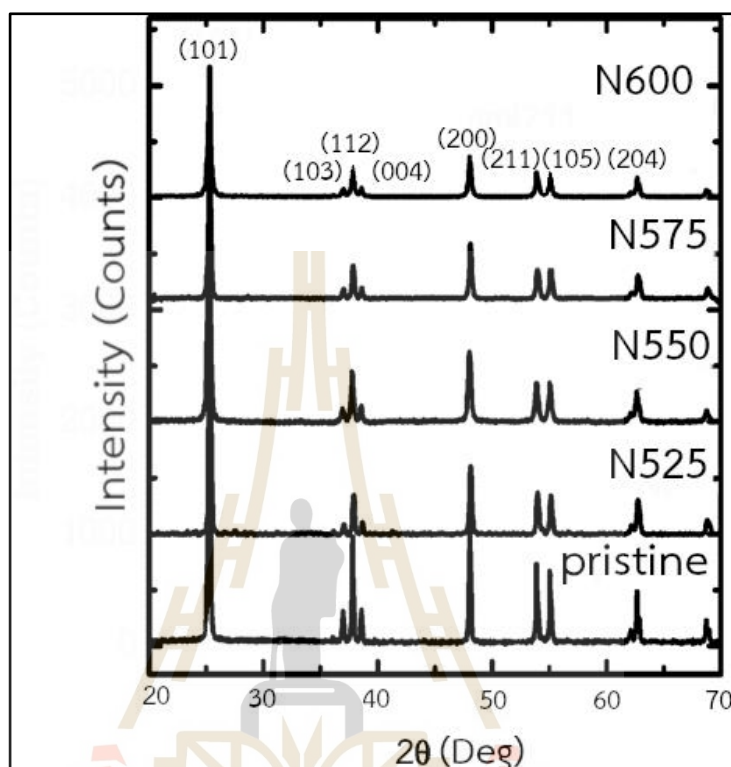
Figure 2.19 XRD pattern pristine TiO_2 and doped TiO_2 at different temperature under NH_3. (Wang, J. et al., 2009)

Accordingly, XRD pattern found that occurring a new peak on there but the intensity of this pattern decreases and become broadening peak in contributed to doping nitrogen (Figure 2.19). As XPS spectra shows binding energy all doped TiO_2 compared with pristine TiO_2 which decreased binding energy when increased temperature, and the doped TiO_2 was decreased N contents (at%) (Table 2.3).

Table 2.3 XPS peak position after treatment TiO$_2$ nanobelt at different temperature.
(Wang, J. et al., 2009)

	Treatment Temperature (°C)	N content (at%)	N 1s peak Position (eV)	Ti 2p3/2 Position (eV)	O 1s peak Position (eV)
Pristine	--	--	--	458.7	530.3
N525	525	0.30	399.6	458.5	529.8
N550	550	1.05	399.5	458.2	529.5
N575	575	1.20	399.7	458.1	529.5
N600	600	1.53	399.6/395.6	458.1	529.5

Figure 2.20 showed a new peak of binding energy at 395.6 eV that its peak appeared to indicate N bonding as TiN, for oxynitride peak at 399.6 eV was ascribed to Ti-O-N or Ti-N-O.
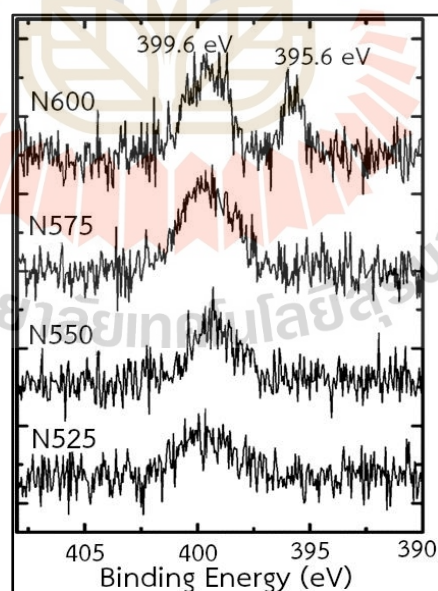
Figure 2.20 XPS spectra N-doped TiO$_2$ at different temperature. (Wang, J. et al., 2009)

Thus, nitrogen as dopant substituted around 400 eV and interstitial site around 396 eV. The valence band spectra showed N-doped TiO$_2$ (N575) that the valence band was increased until around 0.3 eV (Figure 2.21).
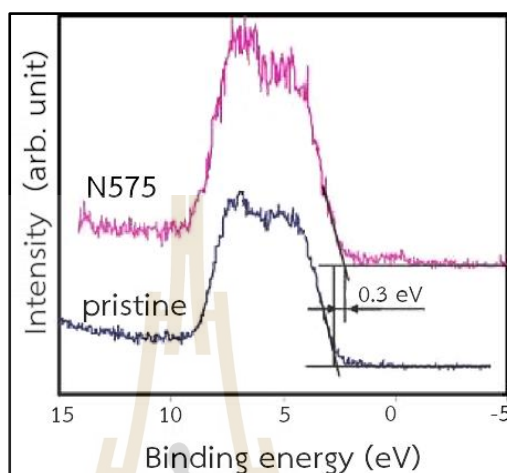
Figure 2.21 XPS spectra, increasing the valence band of N‑doped TiO$_2$ comparing with pristine TiO$_2$ (Wang, J. et al., 2009)

Pristine TiO$_2$ absorbed energy under UV region, which was λ < 400 nm and absorbed under visible light, which was λ > 400 nm, for N-doped TiO$_2$. From Figure 2.22, the N-doped TiO$_2$ increased absorption when their temperature increased.
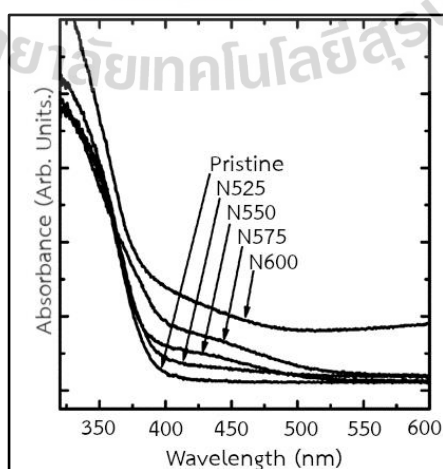
Figure 2.22 UV‑Vis absorption at different temperature. (Wang, J. et al., 2009)

According to measurement of photocatalytic activity, the evaluation of this activity was obtained by decomposing of methylene blue (MB) under visible light and UV irradiation. All samples, undoped and doped TiO_2 that they were the most effective to organic dyes, degrading methyl blue as same both conditions, under visible light. Among them, N550 (treating 550°C, under NH_3) was greater than all samples, for N575 (treating 575°C, under NH_3) was active under UV (Figure 2.23 and 2.24).
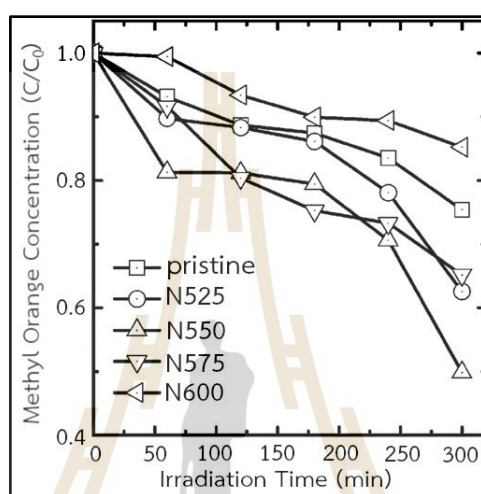
Figure 2.23 Degradation methylene blue under visible light (Wang, J. et al., 2009)
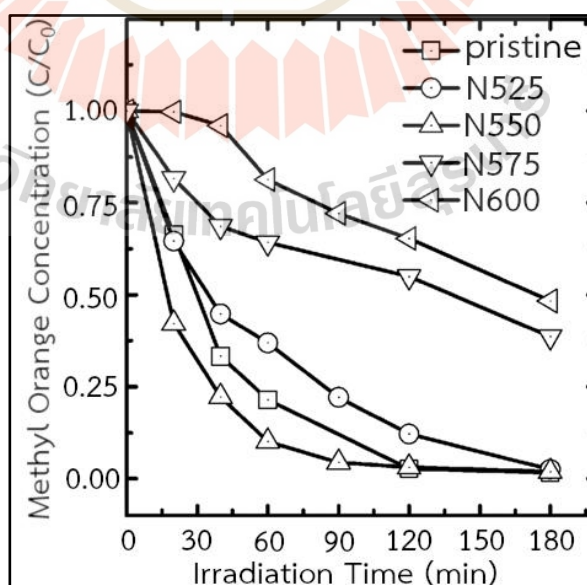
Figure 2.24 Degradation methylene blue under UV (Wang, J. et al., 2009)

Peng, Y.P. et al. (2010) provided microwave to assist N-doped titanate nanotube (N-doped TNTs). Generally, many methods of the doping TNT has been obtained aspect of photocatalytic property and it was satisfactorily synthesized, N-doped TNTs, C-doped TNTs and Ni-doped TNTs, to reduce band gab energy and shifted its absorption under visible light region. N-doped TNTs was efficient greater than other non-metals and transition metals that it mentioned above using microwave -assisted hydrothermal, M-H treatment.
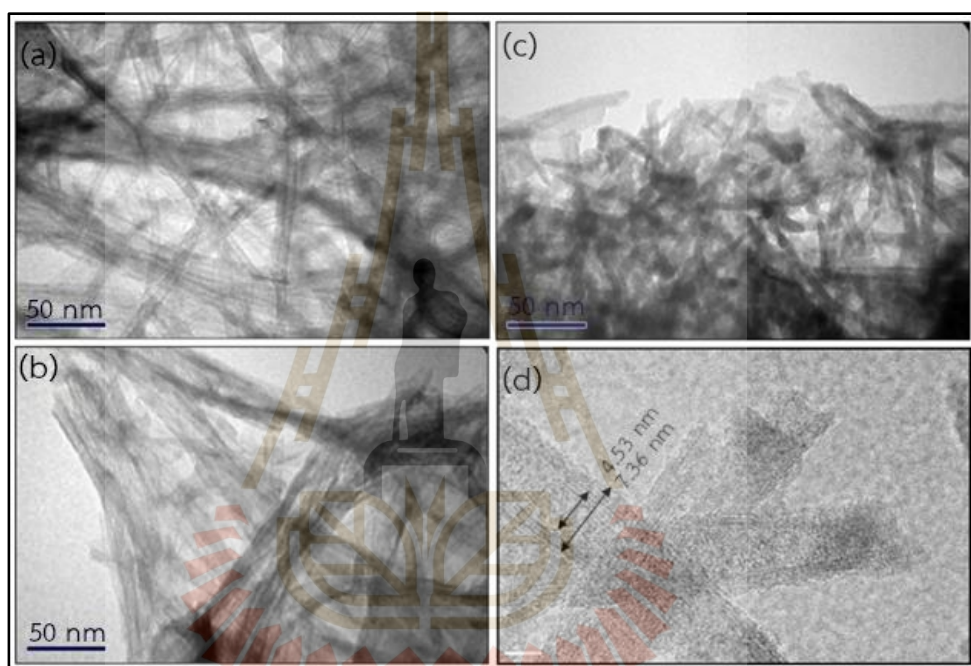
Figure 2.25 TEM images of (a) TNTs, (b) NTNTs-350, (c) NTNTs-450 and
(d) HR-TEM image of NTNTs-350. (Peng, Y.P. et al., 2010)

Apparently, Figure 25 showed structure and morphology of TEM technique, for N-doped TNTs (NTNTs) are analyzed that the image of NTNTs-350 (treatment 350°C) demonstrated a tabular structure after increased treatment temperature at 450°C (NTNTs-400) destroys tabular structure to be tube formation. Even aspect of photocatalytic activity, they found that the NTNTs absorption was under visible light due to doping nitrogen as dopant (Table 2.4 and Figure 2.26).

Table 2.4 S_{BET}, absorbent wavelength and photon energy of TNTs, NTNTs-250, NTNTs-350 and NTNTs-450. (Peng, Y.P. et al., 2010)

	S_{BET}	Absorbent wavelength (nm)	Photon energy (eV)
TNTs	367.0	380	2.85
NTNTs-250	283.4	410	2.57
NTNTs-250 (mild)	283.4	545	1.68
NTNTs-250	218.8	412	2.55
NTNTs-350 (mild)	216.8	570	1.51
NTNTs-450	149.6	405	2.69
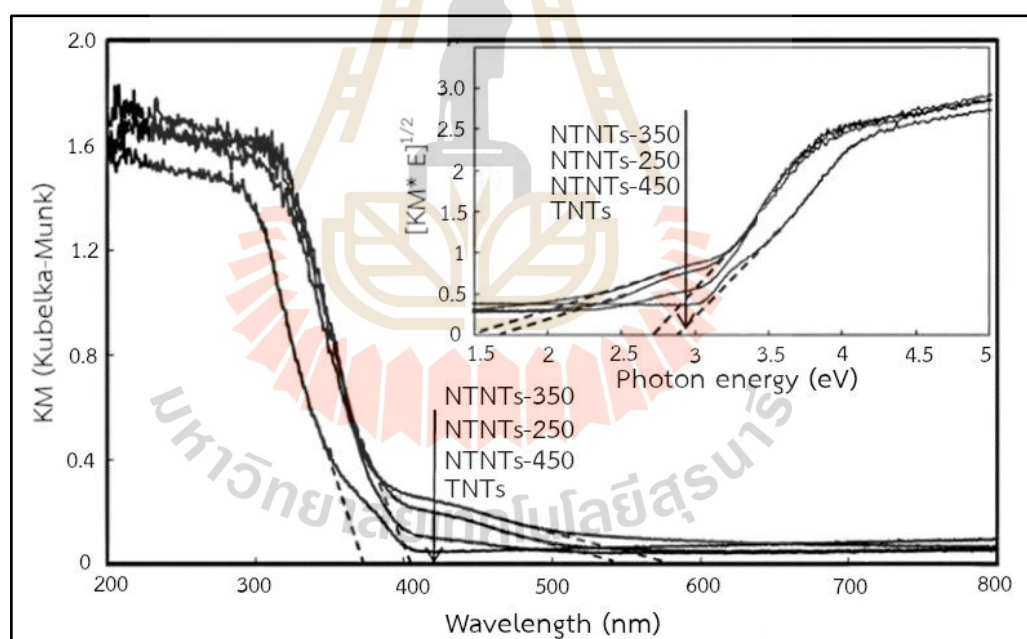
Figure 2.26 UV–vis absorbance of TNTs and NTNTs-250, NTNTs-350 and NTNTs-450. (Peng, Y.P. et al., 2010)

As doped nitrogen, Figure 2.26 demonstrated high absorption at 570 nm, NTNTs-350, and degrade methyl orange, NTNTs-450, that its degradation was 96.3 % with 0.296 min^{-1} for degradation rate.
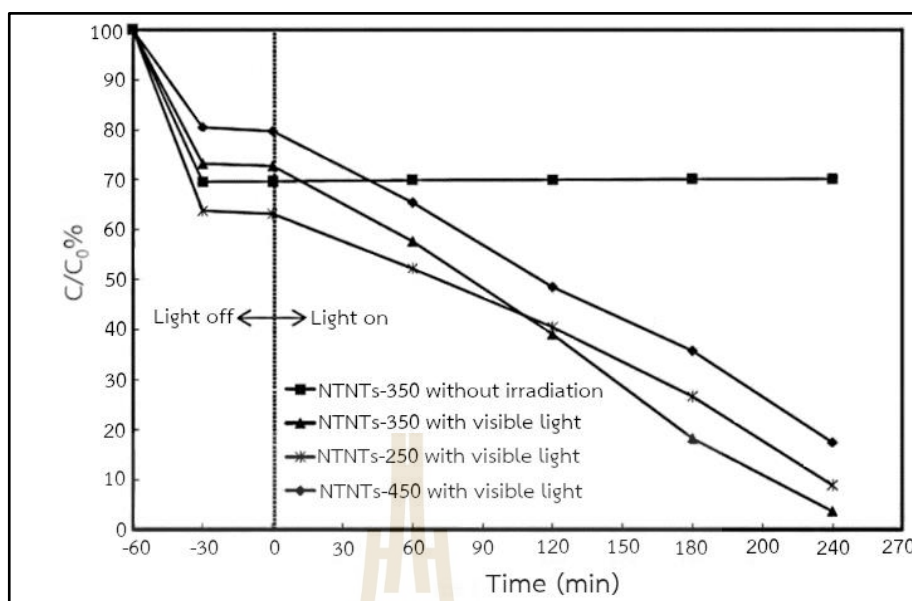
Figure 2.27 Photo-degradation of methyl orange over NTNTs-X with and
without visible Light irradiation. (Peng, Y.P. et al., 2010)

Improving optical properties of titanium dioxide (TiO_2) had been developed by
reducing band gap energy, which was important to exhibit photocatalytic activity when
the band gap energy was narrow so that electrons was transferred from valence band
to conduction band becoming electron hole parried as well, and modifying TiO_2 was
various methods that the one of these method were doped TiO_2 by non-metal such
as nitrogen (N), phosphorus (P) and fluorine (F) as efficient decreasing band gap energy
(Figure 2.27).

Zong, X. et al. (2011) investigated that $CsCaTa_3O_{10}$ was active under visible light
with doped nitrogen via ammonia flowing, as well as nitrogen decreased band gab
energy becoming narrow, which was 2.0 eV from 3.8 eV, pristine $CsCaTa_3O_{10}$. In addition
to diffusing reflectance spectra, both $CsCaTa_3O_{10}$ and N- doped $CsCaTa_3O_{10}$
demonstrated in Figure 2.28.
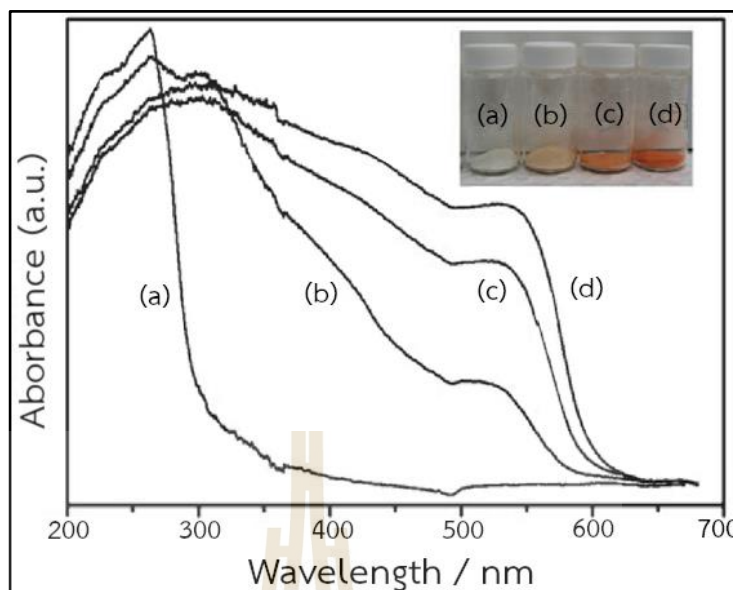
Figure 2.28 Diffuse reflectance spectra of (a) $CsCaTa_3O_{10}$ and (b)–(d)
N-doped $CsCaTa_3O_{10}$. (Zong, X. et al., 2011)

Furthermore, undoped $CsCaTa_3O_{10}$ absorb in UV region, $\lambda < 400$, when it is doped by nitrogen that the absorption apparently increases, $\lambda > 400$, and evaluation of absorption relates to temperature condition when the absorption increases as well. Characterization of binding energy via XPS technique, pristine $CsCaTa_3O_{10}$ was no signal on there after calcination by ammonia (NH_3) appearing new signal when increasing calcination temperature was to obtain high signal, positioned 395.8 eV, due to $CsCaTa_3O_{10}$, for Ta 4f peak was broadened because of Ta-N formation (Figure 2.29).
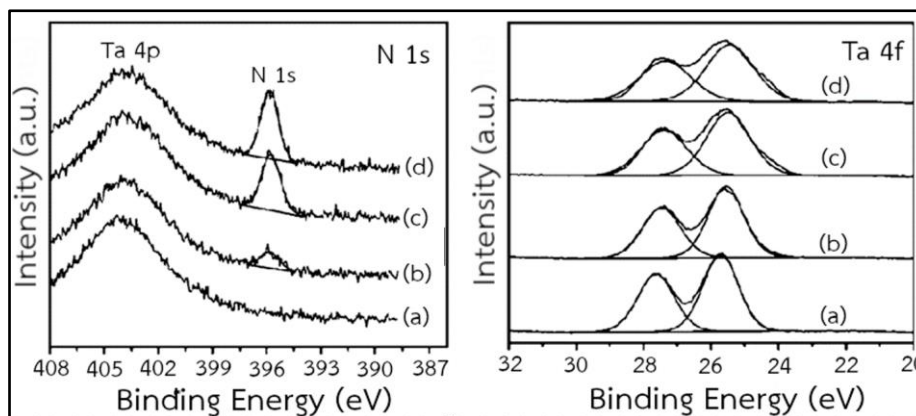
Figure 2.29 High-resolution XPS spectra of N 1s and Ta 4f measured on
(a) $CsCaTa_3O_{10}$ and (b)–(d) N-doped $CsCaTa_3O_{10}$ samples
prepared by calcining $CsCaTa_3O_{10}$ in an ammonia gas flow at
973, 1023 and 1073K, respectively. (Zong, X. et al., 2011)

Chen, S. et al. (2014), decreasing band gap energy was obtained high photocatalytic activity. According to doping TiO_2 with nitrogen active under visible light, TiO_2 was doped by nitrogen but it was weak absorption and a limit extension under visible light that the dopant diffusing from surface to bulk through the interlayer, or tunneled galleries were proposal to be responsive for the homogenous nitrogen doping. A new doping with nitrogen tunneled photocatalyst $MgTa_2O_{6-x}N_x$, its absorption edge was around 570 nm.

Generally, $MgTa_2O_6$ was usually active in UV region with AB_2O_6 structure that it was treated by ammonia gas was obtained doping nitrogen by which occur $MgTa_2O_{6-x}N_x$ showing in XRD pattern (Figure 2.29a).
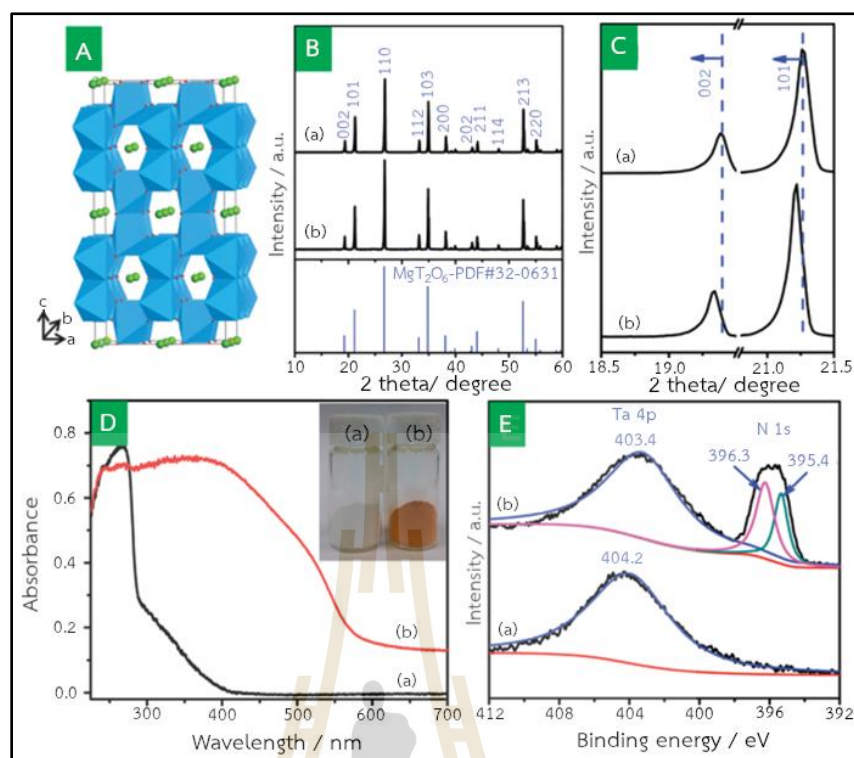
Figure 2.30 Crystal structure of $MgTa_2O_{6-x}N_x$ (A) TaO_6 octahedral, and oxygen and magnesium atoms are illustrated as blue octahedral, and red and green spheres. XRD pattern (B) and enlarged XRD patterns (C), UV-Vis DRS (D), and N 1s and Ta 4p XPS spectra (E) of sample: (a) $MgTa_2O_6$, (b) $MgTa_2O_{6-x}N_x$ (Chen, S. et al., 2014)

In addition to XRD pattern, it exhibited pattern of both $MgTa_2O_6$ and $MgTa_2O_{6-x}N_x$ which were similarity but slightly shifted due to the atomic radius 0.132 nm and 0.124 nm for N^{-3} and O^{-2} ion respectively, for doping nitrogen was less influence on its morphology. Exhibition of photocatalytic activity showed significantly increased absorption under visible light (Figure 2.30D) estimating band gab 2.18 eV, and it also changed color from white to bright orange after thermal ammonia treatment. Consequently, Binding energy at 396 eV considers that the nitrogen was Ta-N formation into the network of Ta-O-Ta.

Rachel Fagan et al. (2016) reported that they used co-doping N, P and F by dividing two methods: method A and method B, for method A used ammonium hexafluorophosphate as reactant, and another one used urea, trifluoroacetic (TFA) and

phosphoric acid (PA). In addition, all methods were analyzed by XRD each temperature (Figure 2.31 and 2.32).
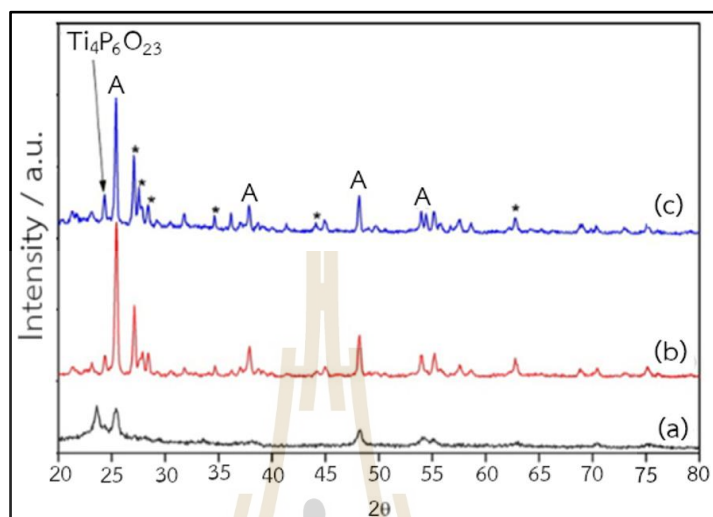
Figure 2.31 XRD pattern for method A, (a) pure TiO_2 and (b) 500°C and 1000°C added dopant, A = antatase. (Rachel Fagan et al., 2016)
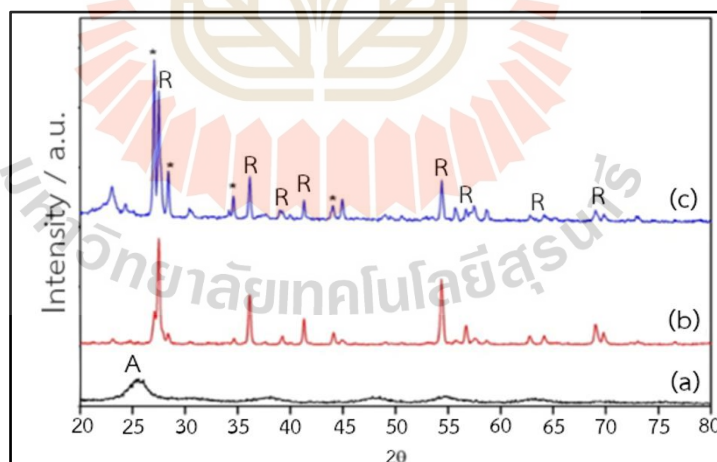
Figure 2.32 XRD pattern for method B, (a) pure TiO_2, (b) 500°C and 1000°C added dopant, R = rutile. (Rachel Fagan et al., 2016)

From XRD pattern, method A still had anatase phase at 1000°C (Figure 2.31), another one, all appearing rutile phase on that (Figure 2.32). Analysis by XPS, at 500 °C,

nitrogen was detected forming O-Ti-O structure that it located peak of XPS at 401.2 eV, but fluorine is absent there. As phosphorus analysis same technique, it expected that phosphorus seemed to effectively replace titanium, Ti, due to atomic radius 0.34 A° and 0.64 A° for phosphorus and titanium respectively, but it bounded to surface of titanium particle, not replaced by P^{+5}, and the peak of XPS of P2p phosphorus was shifted from 134.1 eV (500°C) to 134.7 eV (900°C) and 134.6 eV (1000°C) because of annealing temperature increased. Then, increasing temperature, at 1000°C, there was shifted form 400.24 eV (900°C) down to 397.80 eV indicating N-Ti-N bonding by which it was confirmed by FT-IR as well, for the O-Ti-O peak had been shifted from 454 cm^{-1} (method A) to 513 cm^{-1} (method B) in contributed to the occurrence of N-Ti-N bonding as same temperature 900 °C (Figure 2.33).
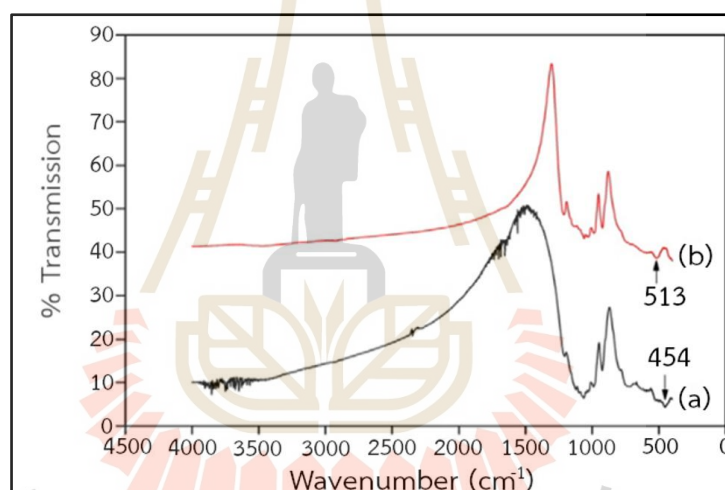
Figure 2.33 FT-IR spectra for (a) method A and (b) method B at 900°C
(Rachel Fagan et al., 2016)
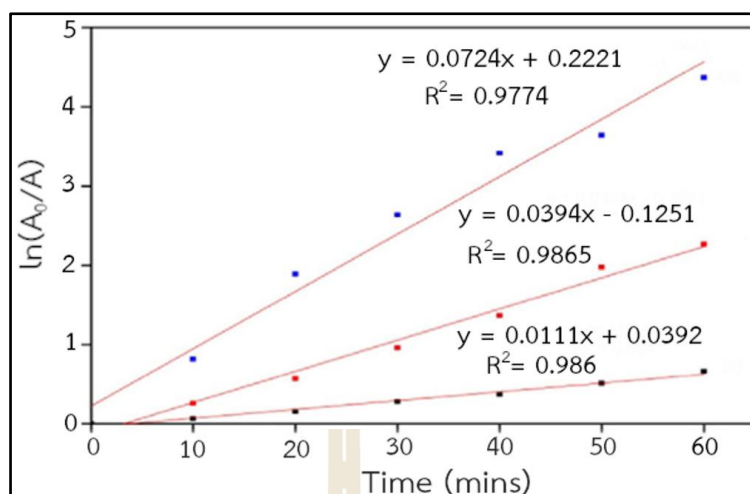
Figure 2.34 Kinetic study for undoped sample comparing with sample preparing by both methods calcined at 900°C, (a) method B, (b) undoped sample, and (c) method A. (Rachel Fagan et al., 2016)

Accordingly, photocatalytic activity of method A at 900°C decomposed rhodamine 6G dye greater than method B as same temperature, less than undoped TiO_2, was attributed to change the anatase form to rutile form completely because of rutile form less photocatalytic activity than anatase, for undoped TiO_2 at 900°C was being both anatase and rutile form (Figure 2.34).

Consequently, formation of nitrogen oxide, NO, occurred both method that the formation was lifted the discrete energy above valence band 0.7 eV which was in midgap state (Figure 2.35).
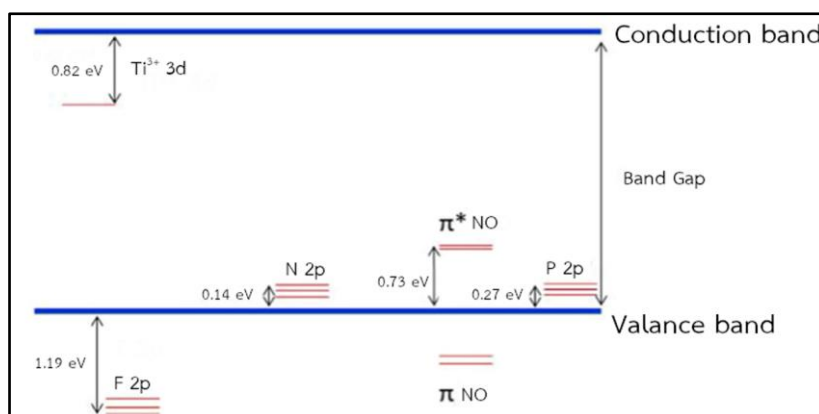
Figure 2.35 Impurity energy state for substitutionally doped TiO_2. (Rachel Fagan et al., 2016)

2.8 TiO_2 antimicrobial

Regmi, C. et al. (2018), the waste water was a big issue which was harmful on social humanity currently, this caused from many factors such as industries, hospital, etc. Apparently, most of the waste water were contaminated with (1) pathogen originate from hospital and biomedical laboratories, (2) different hazardous mineral such as organic dyes, chemicals and excessively used hazardous pesticides, herbicides and plastic. This was harmful to human body becoming severe diseases not only harm to people, but also widely humanity, environment, and ecosystem.

Many industries treated these problems by various methods; physical methods, biological methods, chemical treatment methods. All methods mentioned above, the disadvantages of all these methods were unremoved contaminated products in water completely, and some chemical products occurred formation with that becoming more toxic than parent pollution.

Recently, the novel green technology ids coming famous and benign to environment which was based on advanced oxidation particles (AOPs') in semiconductor materials that it is generated free radical; oxygen radical ($\cdot O_2^-$) and hydroxy radical ($\cdot OH$) treated pollutant including the organic and microbial cells. In addition, the photocatalytic mechanism is developed to desire high photocatalytic activity such as formation of heterojunction, tuning the morphology, doping of metal or nonmetal.

Regmi et al. (2017) developed photocatalytic activity which was active under visible light by doping Fe on $BiVO_4$ as well as it was highly efficient to degrade ibuprofen and Escherichia coli, E. coli, in water.

Then, Li et al. (2017) reported that $BiMoO_6$ on $g\text{-}C_3N_3$ nanosheet increase the efficient photocatalyst by which was under visible light.

Meng et al. (2017), in the same year, synthesized MoS_2 interspersing Bi_2WO_6-heterostructure for disinfection in waste water.

Esfandiari et al. (2014) found that silver (Ag) was used to disinfect as degraded microbial, and Ag further improve photocatalytic activity.

Particularly, Ning et al. (2017) synthezied Ag@AgI landing on BiOI in which exhibited synergistic bacterial mechanism of E. coli under visible light, for Ag doping improving photocatalytic activity, some researchers found that Ag doping enhanced the efficient inactivation of bacteria under visible light in water. Using semiconductor pay an important role inactivation of microbial cells by modified titanium dioxide, TiO_2, which inactivated bacteria and fungi.

Mitoraj et al. (2007) was capable, for E. coli used ZnO-Ag nanoparticles, NPs. In addition, some bacteria were anti-drugs, Staphylococcus aureus (S. aureus), that it uses $\alpha\text{-}NiMoO_4$ to inactivate that bacteria.

Wang et al. (2007), the Semiconductor materials were important key to inactivate various bacteria and microorganism used photocatalytic activity in several applications: bio-imaging, drug delivery, the coating implantable device etc. Moreover, superior photocatalytic property of semiconductor vanished S.aureus bacteria, which was one of the deadliest superbugs bacteria so that it resisted all kind of drugs, such as ZnO, CaO, Fe_3O_4 and TiO_2 inhibiting inactivated bacteria.

Consequently, photocatalytic activity exhibits to generate electron, e^-, and hole, h^+, when energy from solar energy is greater than energy band gap by which the electrons are excited to transit these electrons from valance band to conduction band, e^-_{cb}, remaining holes in valence band, h^+_{vb}, and there are generated charge carriers occurring reactive oxygen radical ($\cdot O_2^-$) and hydroxyl radical ($\cdot OH$)

$$\text{Photocatalyst} + h\nu \longrightarrow e_{cb}^- + h_{vb+} \tag{eq 2.9}$$

$$h_{vb+} + H_2O \longrightarrow \cdot OH^- + H^+ \tag{eq 2.10}$$

$$h_{vb+} + \cdot OH^- \longrightarrow \cdot OH \tag{eq 2.11}$$

$$e_{cb}^- + O_2 \longrightarrow \cdot O_2^- \xrightarrow{2H+} H_2O_2 \xrightarrow{e^-} \cdot OH + \cdot OH^- \tag{eq 2.12}$$

$$\cdot OH + \text{pollutant} + O_2 \longrightarrow \text{simpler products (salt, } CO_2, H_2O \text{ etc.,)} \tag{eq 2.13}$$

$$\cdot OH_{ad} \longrightarrow \cdot OH_{free} + \text{pollutant} \longrightarrow \text{simpler oxidation product} \tag{eq 2.14}$$
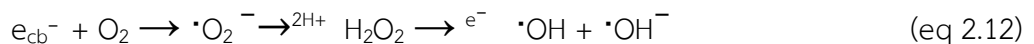
When photocatalytic materials, releasing reactive oxygen species (ROS), contact with cell membrane of bacteria or micro-organism that it experiences different energy and stress there which lead to deconstruct cell membrane, it cannot stay in shape, leaking some cytoplasm out there, then it leads to dead cells. Besides, understanding with the photocatalytic mechanism degrading bacteria is difficult in details, three mechanisms exhibiting with example henceforward (Figure 2.36).

(1) Oxidative stress induction which is oxidation process, producing OH radical, occurring lipid peroxidation

(2) Releasing metal ions can interact with -SH, -NH and -COOH group of nuclei and damage them

(3) Non-oxidative mechanism is inactivated function of cell such as amino acid, carbohydrate metabolism, etc.
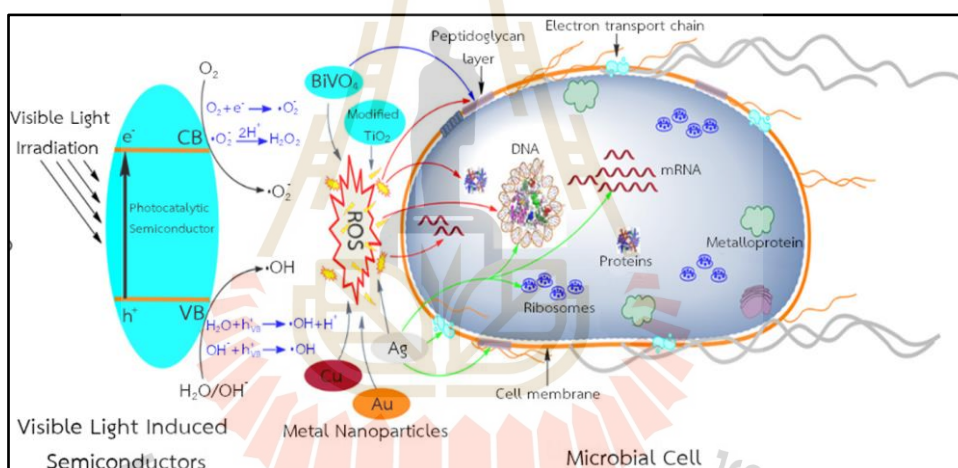
Figure 2.36 Photo-induced process; Photocatalyst destroying cell (Wang et al., 2007)

Consequently, killing bacteria have an ordered attacking to cell with some ROS, stepping degradation, and the ROS destroys indicated cell membrane first then it follows step up along with Figure 2.36.
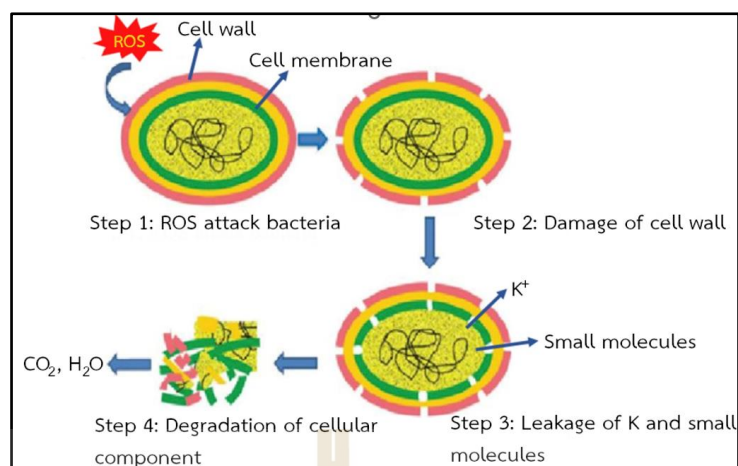
Figure 2.37 Step of destroying cell membrane by ROS radicals (Wang et al., 2007)

Especially, bacteria can be divided two groups: gram-negative and gram-positive, and the gram-negative bacteria is sensitive more than gram-positive for photocatalytic phenomenon. Apparently, the quite different is cell wall, or cell membrane, so that the gram-negative bacteria have triple cell wall structure with a cytoplasmic inner membrane, outer membrane and thin single peptidoglycan in middle layer, for cell membrane of gram-positive bacteria have more thickness than that, so the complex peptidoglycan sheath outside the inner membrane which is more resistant to ROS, reactive oxygen species. The major attacking destroys cell membrane is hydroxyl radical, $\cdot OH$, that it is core mechanism, and H_2O_2 is the most effective on inactivated bacteria, discontinuous function.

2.9   Layered perovskite structure ($La_2Ti_2O_7$, LTO)

Concerning of crystal structure, the layered perovskite structure ($A_2B_2O_7$) as general formula, is the unique structure of electronic configuration because a highly donor-doped state exhibits photocatalytic performance due to separated electrons and holes; in addition, it has high stability and redox reaction. Significantly, $La_2Ti_2O_7$ is that a member of the layered perovskite structure base on this system, obtaining high photocatalytic water splitting: producing H_2 and O_2. In addition, $La_2Ti_2O_7$ reveals that it is hypervalency occurring La atoms on the layered perovskite structure. (Hwang et al., 2003), (Hwang et al., 2000), (Kim et al, 2002), (Ku, Y., Wang, L. C., & Ma, C. M., 2007) (Wang et al., 2011), (Wang et al., 2012)

2.9.1 Doping LTO

J. wang et al. synthesized $La_2Ti_2O_7$ (LTO_NC) which was performed thermal method for doping nitrogen employing under NH_3 atmosphere as nitrogen source and investigated in various temperatures. The XRD pattern was shown doping nitrogen that was absence of impurity that unchanged the crystal structure. The LTO_NC crystal structure was monoclinic phase after NH_3 treatment was low crystallinity due to particle size decreasing, as Figure 2.38 (b)-(e).
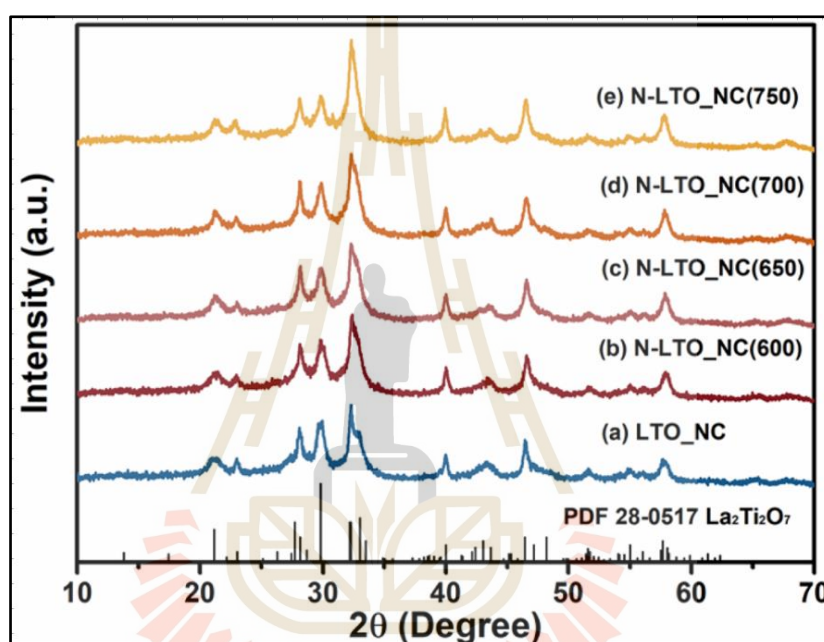
Figure 2. 38 XRD pattern of $La_2Ti_2O_7$ and nitrogen-doped $La_2Ti_2O_7$ with different calcination temperatures (Wang et al., 2021)

Practically, all samples doping nitrogen indicating nitrogen in the structure with NH_3 treatment were characterized by XPS technique for confirmed bonding composition. Morphology was investigated by TEM technique, and $La_2Ti_2O_7$ (LTO) was prepared by thermal method which denoted as LTO_P, without triethanolamine (TEA) controlling as additive and with TEA controlling as LTO_NC. Apart of that, the samples were calcined with different temperatures under NH_3 atmosphere which denoted as N-LTO_NC: N-LTO_NC(600), N-LTO_NC(650), N-LTO_NC(700), N-LTO_NC(750), respectively.
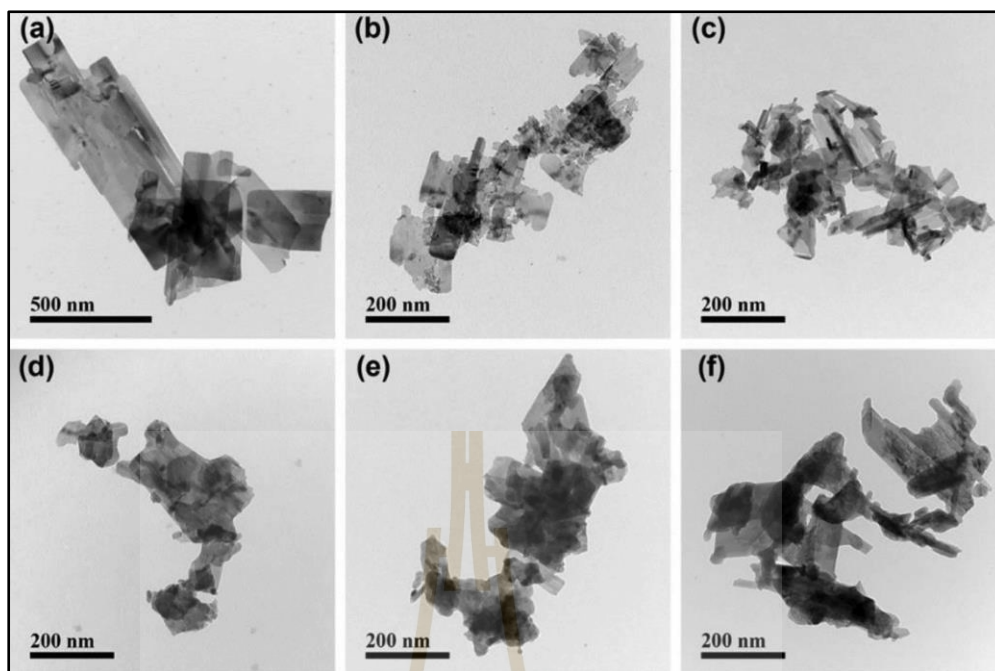
Figure 2.39 TEM images of (a) LTO_P; (b) LTO_NC; (c) N-LTO_NC(600);
(d) N-TO_NC(650); (e) N-LTO_NC(700) and (d) N-LTO_NC(750).
(Wang et al., 2021)

Morphology was investigated by TEM which compared with LTO_P and N-LTO_NC, it obtained an irregular shape and smooth surface, length of LTO_P > 1 μm. Also, the particle size LTO_P was larger than N-LTO_NC(650). Comparing LTO_NC and N-LTO_NC(650) detecting from high-resolution TEM, both were discontinuous atomic lattice because of low crystallinity. The lattice spacing indicated the interplanar distance as (212) and (-122) plane of $La_2Ti_2O_7$ for 0.224 nm and 0.272nm, respectively. Result of $La_2Ti_2O_7$ investigation, the nitrogen doping did not affect morphology and crystal structure. According to optical property, LTO_NC light absorption was below 338nm determining band gap of 3.86eV but nitrogen doping absorbed longer wavelength, and the NH_3 treatment at 600, 650, 700 and 750°C were at 345, 453, 491 and 560nm, respectively. Observation NH_3 treatment, high nitrogen concentration as dopant enhanced absorption edge to longer wavelength, redshift and induced band gap narrowing as an impurity level in mid-gap, see in Figure 3. In addition, the estimated band gap of N-LTO_NC(600) and N_LTO(750) was 3.74 and 2.57, respectively, as shown Figure 2.40(b).
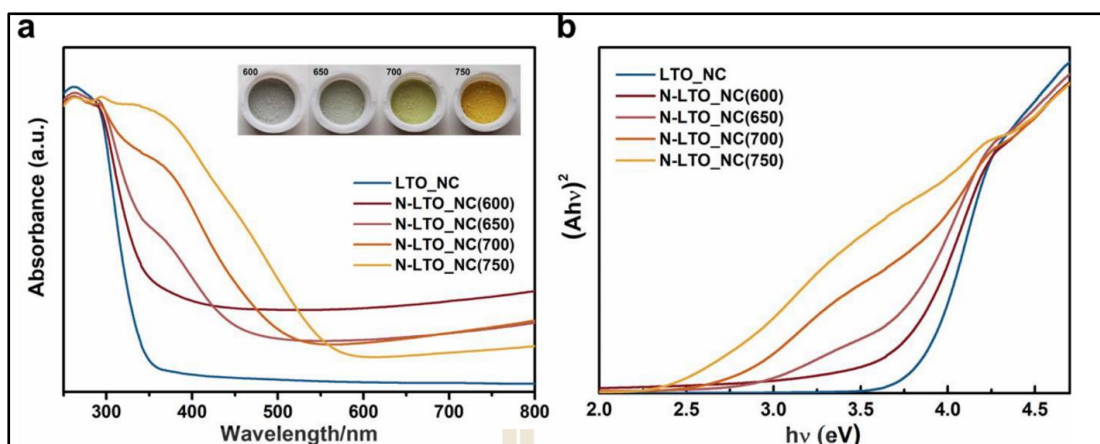
Figure 2.40 (a) UV–vis diffuse reflectance spectra and (b) Tauc plots (b) of
the La$_2$Ti$_2$O$_7$ nanocrystals before and after heat treatment under
NH$_3$ gas flow at different temperatures. (Wang et al., 2021)

Tan et al. investigated Nb and Fe co-doping LTO that the preparation used a sol-gel process for obtaining high purity of LTO and was compared various amount of Fe and Nb co doping. In addition, LTO phase was detected by XRD technique, on XRD pattern no impurity evidence. Besides, Nb and Fe codoping was not detected but it was incorporated in LTO lattice because the ionic radii of Nb and Fe was slightly bigger than Ti which was 0.69, 0.645, and 0.605Å respectively.
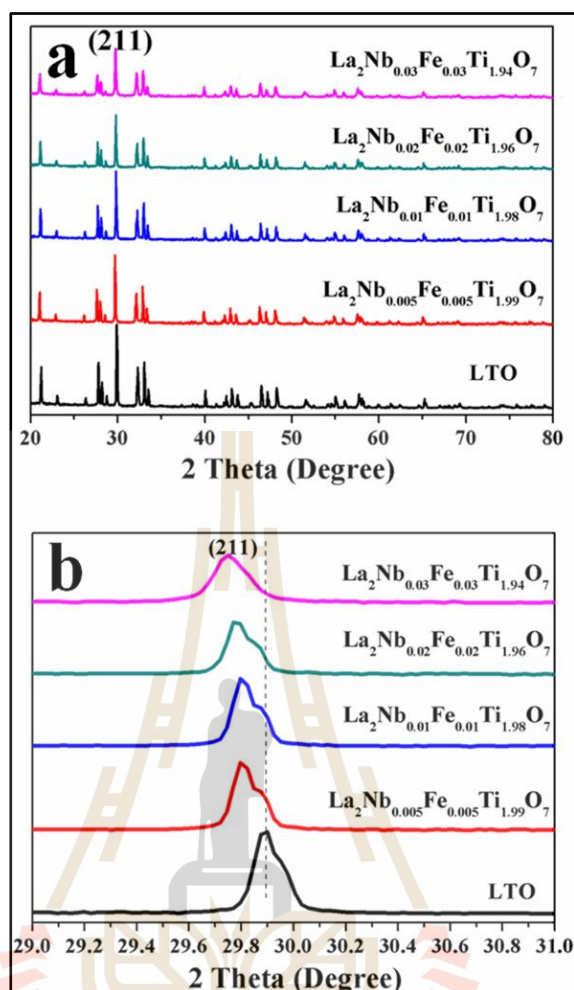
Figure 2.41 XRD pattern of LTO with different doped concentration and
the same calcination temperature (Tan et al., 2017)

The optical property was determined by UV-Vis spectroscopy that the edge absorption of LTO was 350nm when doping Nb and Fe demonstrated redshift absorption to 460nm. Herein, co-doping can extend the light absorption range which was co-doping
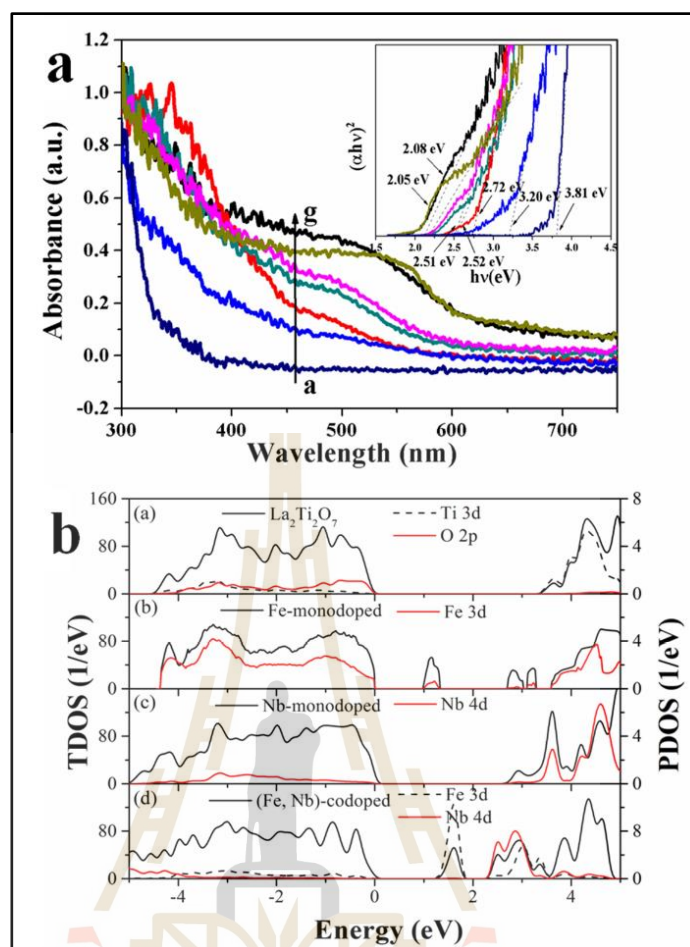
Figure 2.42 (a) UV-vis diffuse reflectance spectra (b) Calculated DOS of
pure, mono-doped and co-doped LTO (Tan et al., 2017)

concentration affected to light absorption strongly and can decrease
bandgap energy due to d-d hybridization. The d-d hybridization of Fe3d located on
the top of valence, for Nb4d orbital govern the bottom of conduction band. (Tan et
al., 2017)

Qian Wang et al. tried to decrease band gap energy of $La_2T_2O_7$ (LTO)
and obtained high hydrogen (H_2) production which employed doping process to be
high photocatalytic efficiency. Generally, LTO was the large band gap (3.8 eV) that it
was difficult to decrease band gap which exhibit high photocatalytic performance, and
Qian Wang et al doped Rh in LTO structure using various method for investigating Rh
doping. Furthermore, the various methods were employed: Polymerized complex (PC),
Molten salt synthesis (MSS) and Solid-state reaction (SSR).
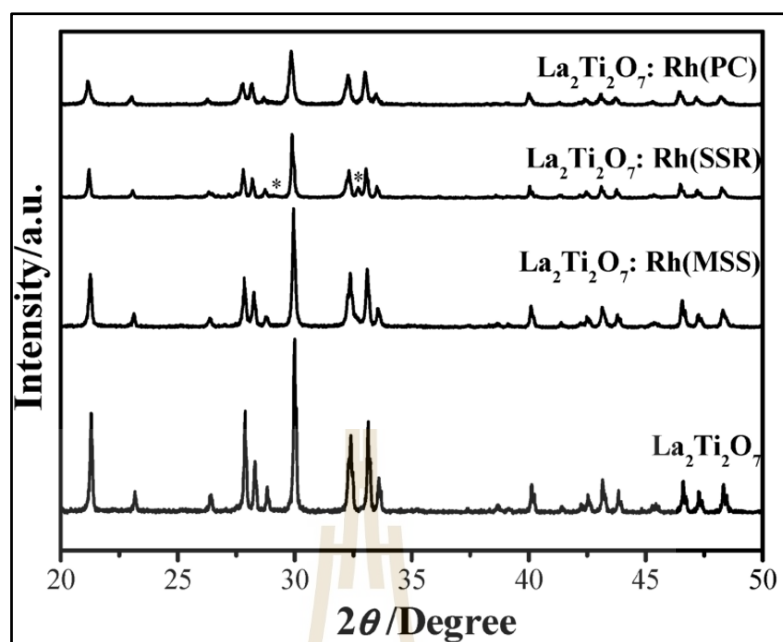
Figure 2.43 XRD patterns for undoped $La_2Ti_2O_7$ (entry 1) and Rh-doped
$La_2Ti_2O_7$ prepared using the MSS method (entry 2), the SSR
method (entry 3), and the PC method (entry 4). The impurity
phase (La0.66TiO2.993) is indicated by asterisks.
(Wang et al., 2013)

The XRD pattern showed doping Rh compared with undoped $La_2Ti_2O_7$
that the MSS and PC methods exhibited monoclinic structure. The determining
crystalline size was 195, 127, 100, and 71 for undoped prepared by MSS method, and
Rh-doped $La_2Ti_2O_7$ prepared by the MSS, SSR, and PC methods, respectively. For
samples of doping Rh with MSS and PC methods, all elemental content analysis
revealed percentage of element which closed agreement with theoretical values. The
MSS method for doping Rh had high surface area using BET surface area exhibiting high
H_2 revolution because molten salt induced lower degree of agglomeration of the
platelet-like particles.
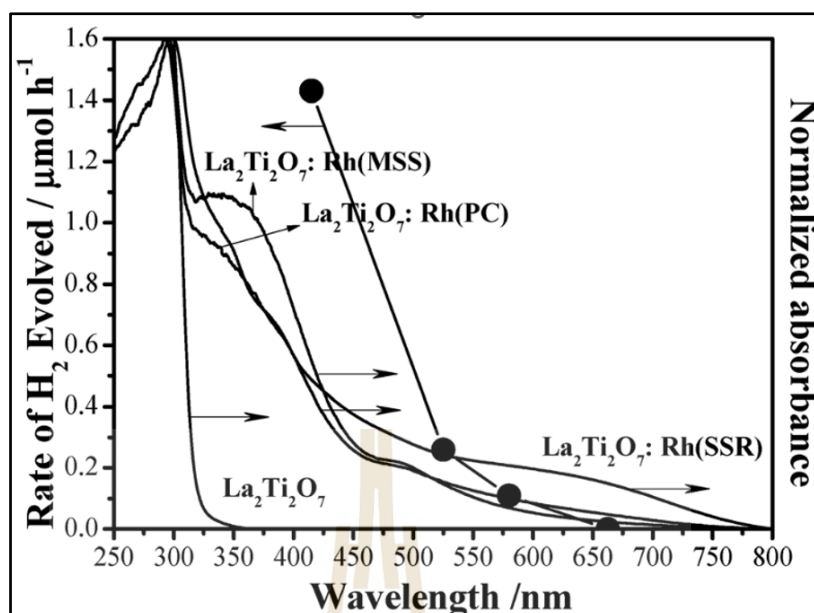
Figure 2.44 Comparison of absorbance and H_2 evolution with Rh doped
$La_2Ti_2O_7$ for various methods

The Rh-doped $La_2Ti_2O_7$ had a steep absorption edge at around 330 nm and a shoulder absorption extending to the visible light region regardless of the preparation method, indicating that Rh doping reduced the energy gap. (Wang et al., 2013)

CHAPTER III

RESEARCH PROCEDURE

3.1   Preparation

3.1.1   Chemical Reactant

Table 3.1 Chemical reactants, Chemical formula and Manufacturers

Chemical reactants	Chemical formula	Manufacturers
Titaniumbutoxide	$C_6H3_6O_4Ti$	ALDICH
Ethylene glycol	$C_2H_6O_2$	QreC

Table 3.2 Chemical reactants, Chemical formula and Manufacturers (Continued)

Citric acid	$C_6H_8O_7$	 ALDICH
Iron (III) nitrate	$Fe(NO_3)_3.9H_2O$	 QreC
Chromium (III) nitrate	$Cr(NO_3)_3.9H_2O$	 SIGMA-ALDICH
Lanthanum (III) nitrate hexahydrate	$La(NO_3)_3.6H_2O$	 ALDICH

3.1.2 Research equipment, materials and analysis

Table 3.3 Research Equipment, Materials and Analysis

Equipment and Materials	
Tube furnace	Nitrogen gas (N_2)
Distilled water	Thermometer
Alumina crucible (boat shape)	Hot plate
LED lamp	Magnetic stirrer
Oven	
Agate mortar and pestle set	

Table 3.4 Analyzed equipment

X-ray Diffractometer (XRD) Model D2 PHASER
Ultra violet-Visible Spectrophotometer (UV-Vis) Model CARY 300
X-ray photoelectron spectroscopy (XPS)
Field emission scanning electron microscopy (FE-SEM)
Energy Dispersive Spectroscopy (EDS)
X-ray absorption spectroscopy (XAS)
Photoemission electron spectroscopy (PES)

3.2   Synthesis powder procedure

```
┌─────────────────────────────────────────────────────────────────────────┐
│  ┌──────────────────┐  ┌──────────────────┐   ┌──────────────┐  ┌──────────────┐
│  │ Titaniumbutoxide │  │ Ethylene glycol  │   │  Citric acid │  │ Distill water│
│  └──────────────────┘  └──────────────────┘   └──────────────┘  └──────────────┘

        ┌──────────────┐      ┌──────────────┐        ┌──────────────┐
        │  Solution A  │      │  Homogenous  │        │  Solution B  │
        └──────────────┘      │   solution   │        └──────────────┘
                              └──────────────┘
                                              ┌────────────────────────┐
                                              │  Stirring 50°C for 2h  │
                                              └────────────────────────┘
   ┌──────────────────┐       ┌──────────────┐
   │  Molar percent   │       │  Solution C  │
   │   (0.005%) of    │       └──────────────┘
   │ Iron (III) nitrate│                             ┌──────────────────────┐
   │      and         │                             │  Lanthanum nitrate   │
   │ Chromium (III) nitrate│                         └──────────────────────┘
   └──────────────────┘     ┌──────────────────────┐
                            │ Metal complex solution│
                            └──────────────────────┘
                                              ┌──────────────┐
                                              │   Stirring   │
                                              └──────────────┘
                              ┌──────────────┐
                              │  Solution D  │
                              └──────────────┘
                                              ┌────────────────────────┐
                                              │  Heating 130°C for 8h  │
                                              └────────────────────────┘
                         ┌──────────────────────┐
                         │  Viscous complex sol │
                         └──────────────────────┘        ┌──────────────────┐
                         ┌──────────────────────┐        │   Calcination    │
                         │ Black precursor powder│       │ temperature at   │
                         └──────────────────────┘        │  350°C for 2h    │
                         ┌──────────────────────┐        │ and increasing   │
                         │   Pink-fate powder   │        │  to 1150°C for 2h│
                         └──────────────────────┘        │ under ambient    │
                    ┌────────────────────────────┐       │  atmosphere      │
                    │ (Fe,Cr) La₂Ti₂O₇ , (FeCrLTO)│      └──────────────────┘
                    │      (Undoping powder)     │
                    └────────────────────────────┘
└─────────────────────────────────────────────────────────────────────────┘
```

Figure 3.1 Flowchart for powder preparation

3.3 Doped nitrogen process
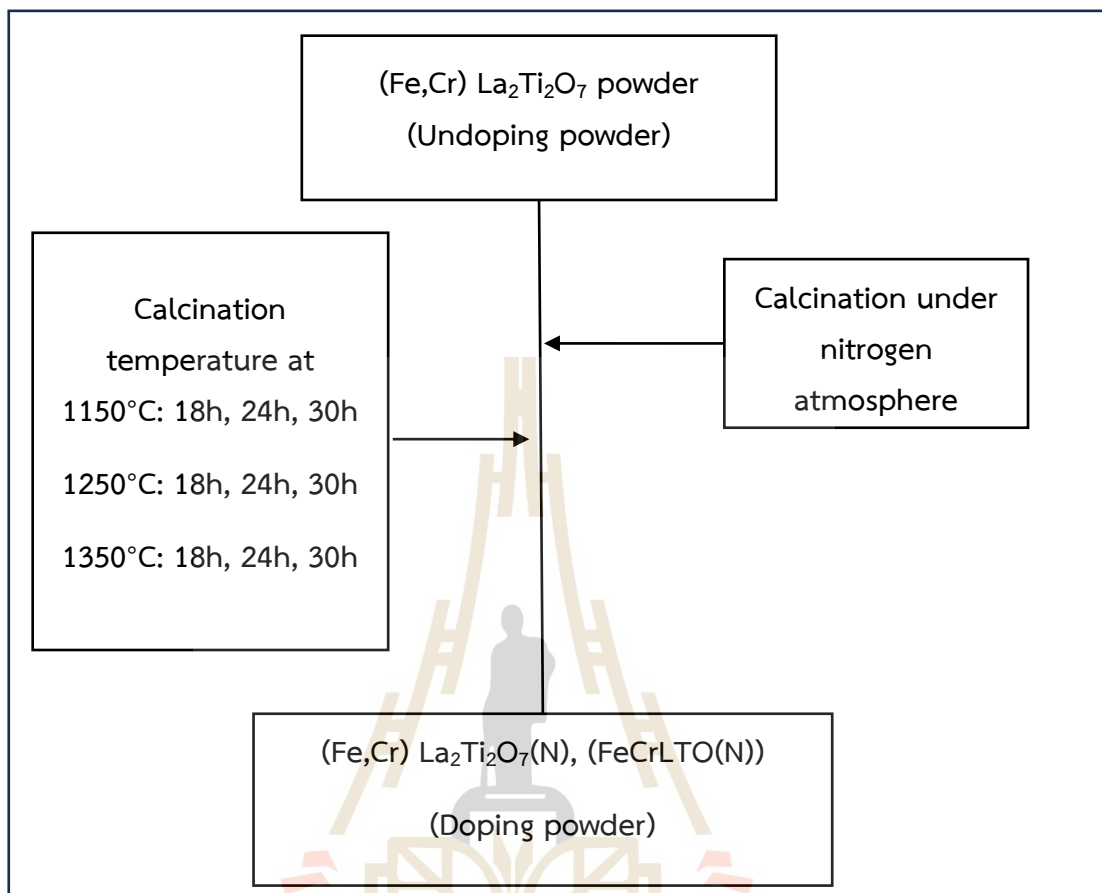
Figure 3.2 Flowchart for doping nitrogen process

3.4   Photocatalytic process
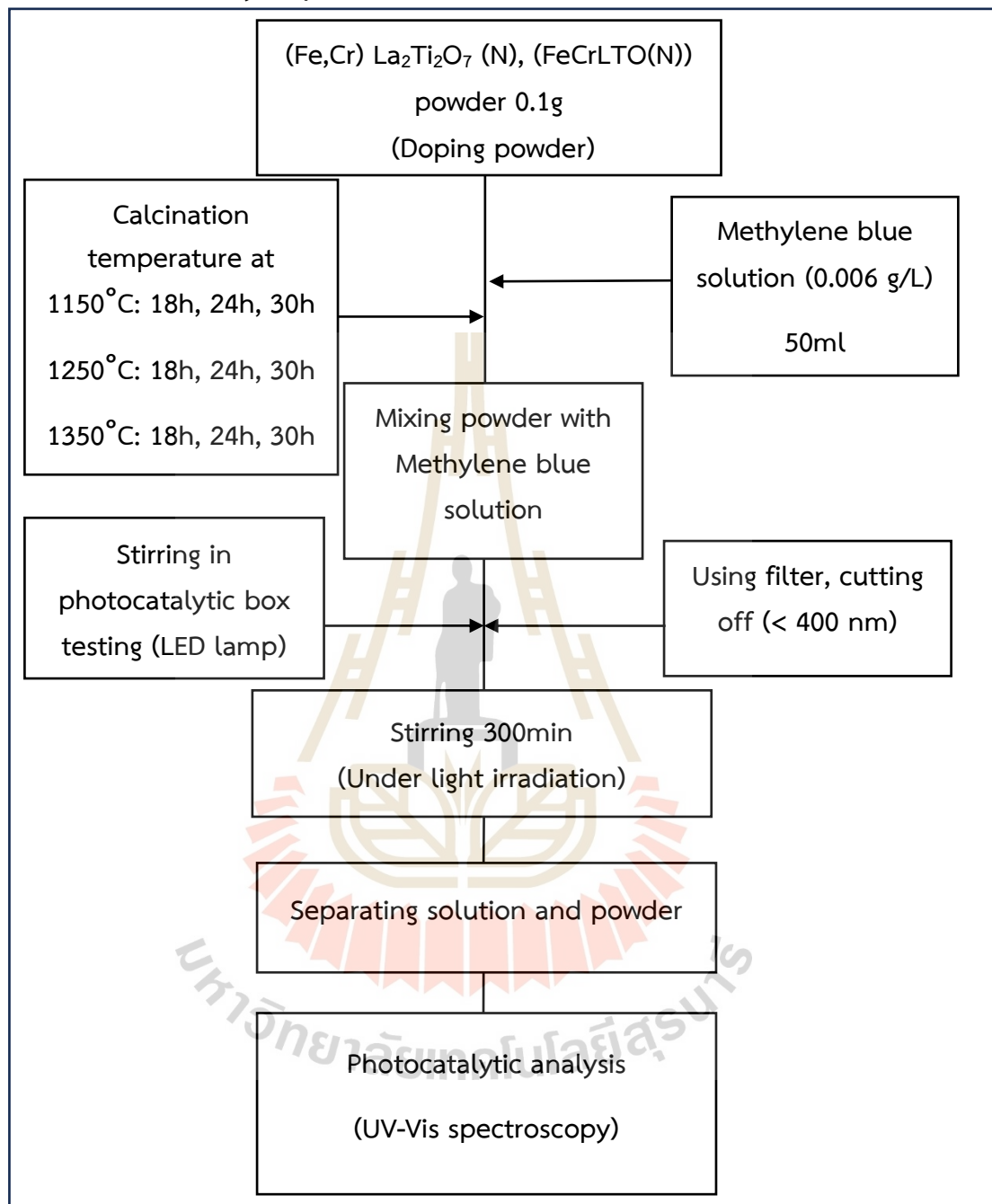
Figure 3.3 Flowchart for photocatalytic testing

3.5 Characterization procedure

3.5.1 Phase analysis
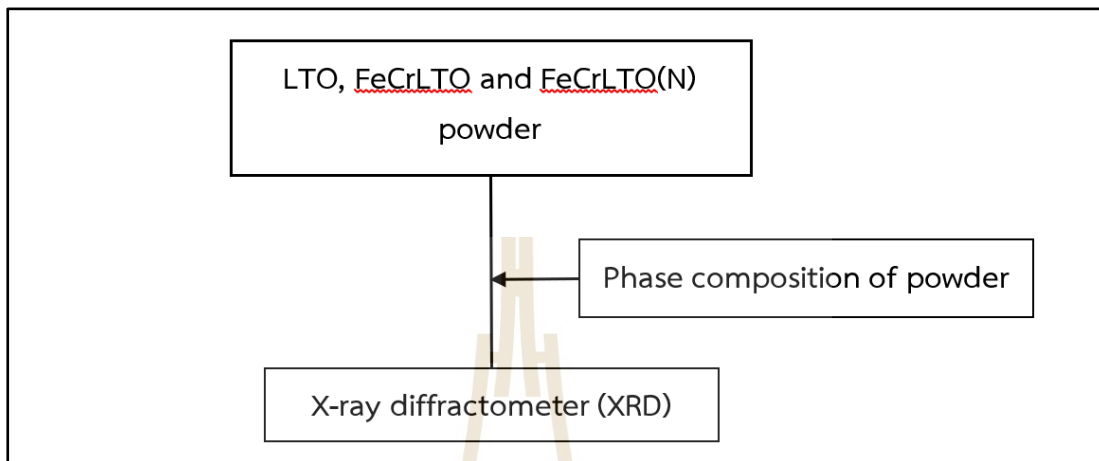
Figure 3.4 Flowchart for phase analysis

3.5.2 Morphology analysis
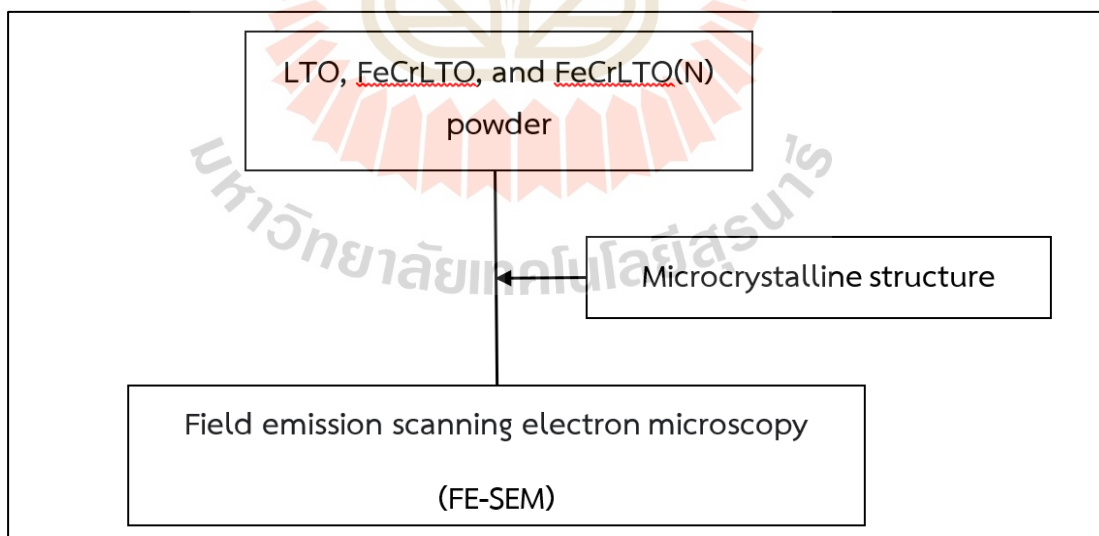
Figure 3.5 Flowchart for Microcrystalline structure Analysis

3.5.3   Elemental composition and X-ray map elements
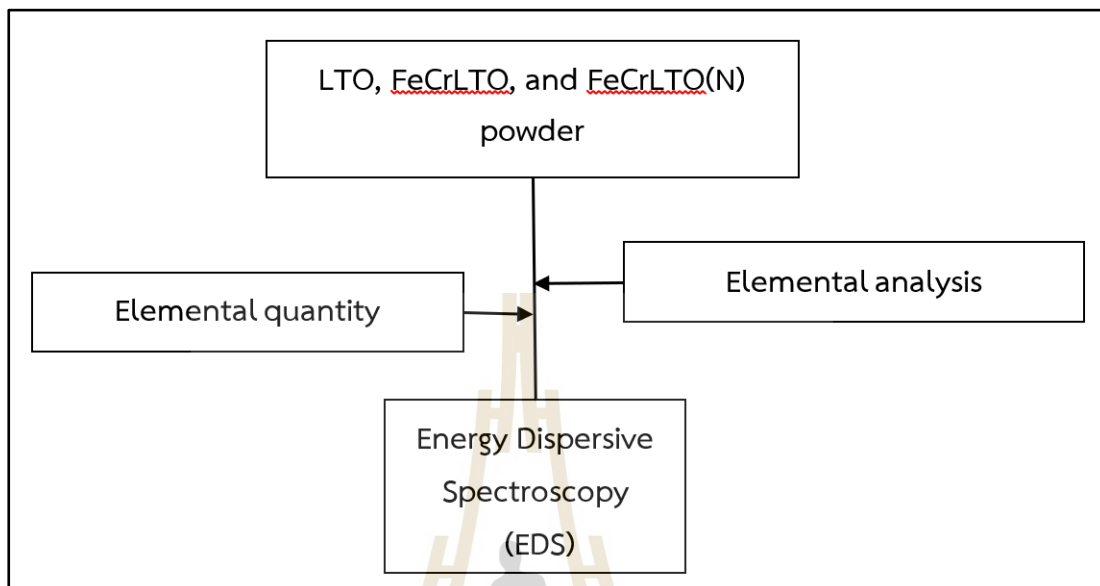
Figure 3.6 Elemental quantity and elemental analysis

3.5.4   Elemental substitution analysis
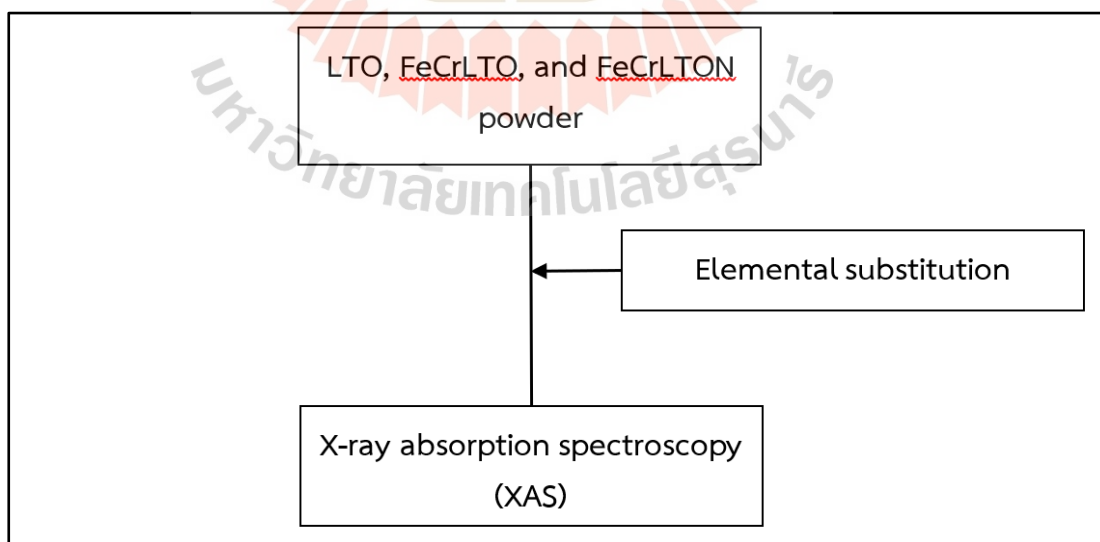
Figure 3.7 Elemental substitution analysis

3.5.5 Nitrogen substitution and elemental bonding
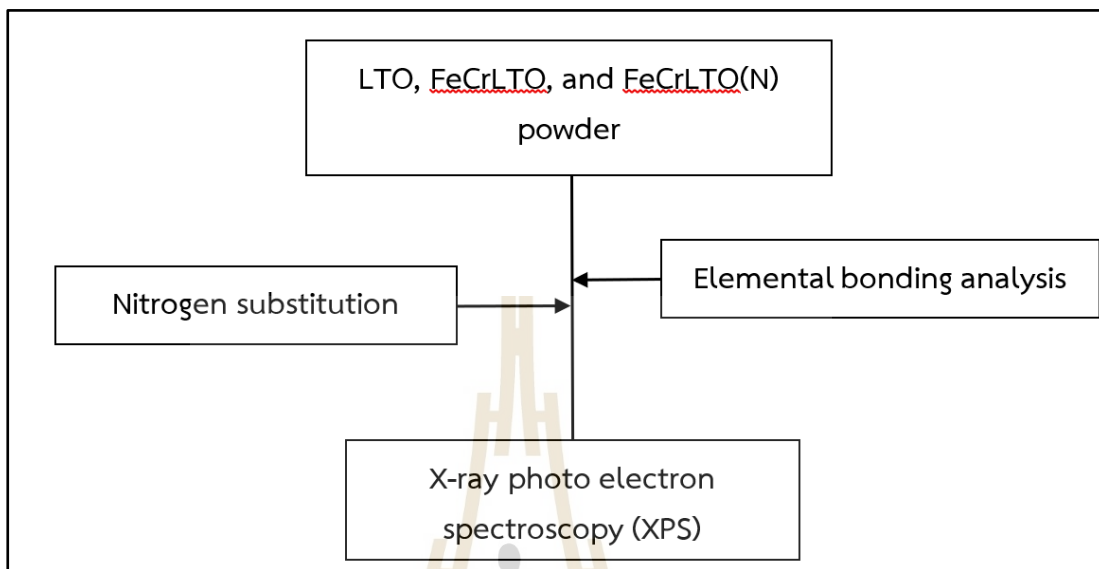
Figure 3.8 Nitrogen substitution and elemental bonding

3.5.6 Nitrogen substitution analysis
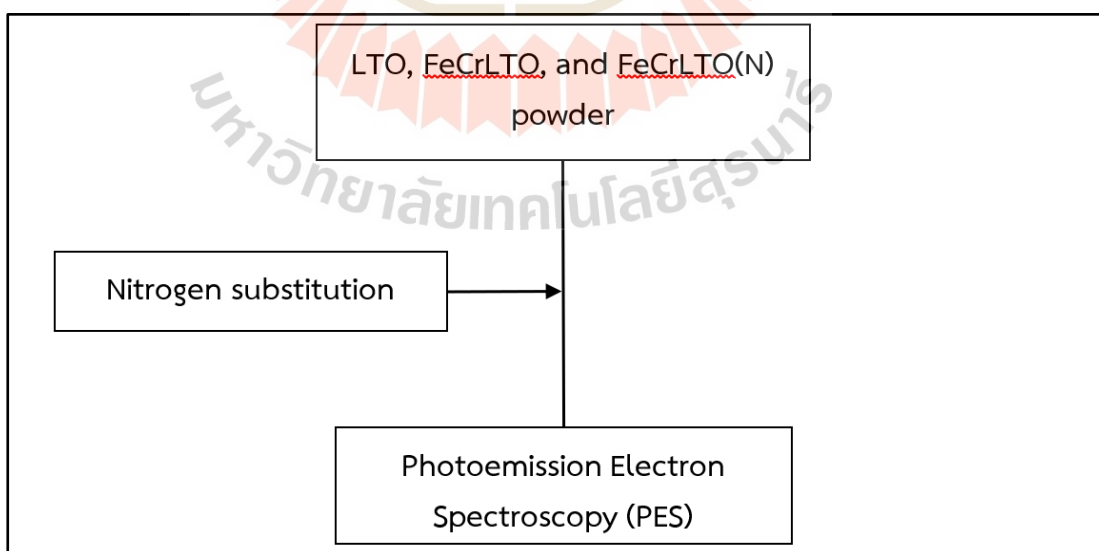
Figure 3.9 Nitrogen substitution analysis

3.6   Details procedure

3.6.1   Powder preparation

La$_2$Ti$_2$O$_7$ powder was prepared sol-gel method, and doping Fe and Cr, which added before making gelation. The solutions prepared in 2 parts. Solution A, the mixing of titaniumbutoxide (C$_6$H$_{36}$O$_4$Ti, 0.476g, 97%, Sigma Aldrich) and ethylene glycol (C$_2$H$_6$O$_2$, 31.002g, 99.5%, QreC) using mole ratio 1:1. Solution B, dissolving citric acid (C$_6$H$_8$O$_7$, 29.283g, 99.5%, Sigma Aldrich) in di-water (28ml)with mole ratio 1:1. Then mixed A and B together to obtain the new solution as solution C, prepared with temperature 50°C for 2h then iron (III) nitrate (Fe(NO$_3$)$_3$.9H$_2$O, 0.0286g, 99.9%, Sigma Aldrich), lanthanum (III) nitrate hexahydrate (La(NO$_3$)$_3$.6H$_2$O, 6.1247g, 99.999%, Sigma Aldrich) and Chromium (III) nitrate (Cr(NO$_3$)$_3$.9H$_2$O, 0.0283g, 99%, Sigma Aldrich) were added into solution C and heated up temperature to 130°C for 8h, resulting in the formation of a gel. The molar percent of Cr and Fe corresponding to Ti presented in the reaction are 0.005% Fe and 0.005% Cr. The calcination temperature of the obtained gel was increased gradually up to 350°C and held for 2h, followed by heating up to 1150°C at a rate of 5°C/min and holding for 2h. In the previous state, the powder was a fate pink color, called FeCrLTO. As doping nitrogen into the structure, calcination temperatures in tube furnace under nitrogen atmosphere of sample powder called FeCrLTO(N).

(1) Dissolving Titaniumbutoxide in Ethylene glycol obtains as solution A.

Figure 3.10 Solution A

(2) Dissolving Citric acid in Distilled water obtains as solution B.

Figure 3.11 Solution B

(3) Mixing Solution A and B and keep stirring.
(4) Until clear solution that is Solution C.

Figure 3.12 Solution C

(5) Weight metal complex powder: Iron nitrate, chromium nitrate and lanthanum nitrate, in Solution C and keep stirring and increasing temperature upto 50 °C for 2h.

(6) Obtaining Solution D

Figure 3.13 Solution D

(7) Then heating at 130°C for 8h dissolving all compound in Solution D.
(8) Formation of viscous gel.

Figure 3.14 Solution D

(9) Calcination at 350°C for volatile of organic compound.

(10) Obtaining black precursor powder after step 9.

Figure 3.15 Black powder after calcination at 350°C

(11) Optimized calcination temperature: was at 1150°C, 2h, without controlling atmosphere.

Figure 3.16 (Fe,Cr) $La_2Ti_2O_7$ powder after calcination at 1150°C for 2h

3.6.2 Doping procedure

To investigate the effect of calcination temperature on the properties of FeCrLTO, the powder was subjected to calcination in a tube furnace under a nitrogen atmosphere (flow rate 1000 ml/min) for 18h, 24h, and 30h at different temperatures: 1150°C (FeCrLTON1150_18h), 1150°C (FeCrLTON1150_24h), 1150°C (FeCrLTON1150_30h), 1250°C

(FeCrLTON1250_18h), 1250℃ (FeCrLTON1250_24h), 1250℃ (FeCrLTON1250_30h), 1350℃ (FeCrLTON1350_18h), 1350℃ (FeCrLTON1350_24h) 1350℃ (FeCrLTON1350_30h). For comparison, control samples were calcined at 1150℃ for 2h under ambient atmosphere, using the same chemical composition as the experimental samples (referred to FeCrLTO1150_2h), and without the addition of iron (III) nitrate and chromium (III) nitrate (referred to as LTO1150_2h).

(12) Taking powder from step 11, calcination in tube furnace at different temperature: 1150, 1250 and 1350˚C and different times: 18h, 24h, 30h under nitrogen atmosphere (N_2)

Figure 3.17 Tube furnace

(13) Flow rate of nitrogen gas (N_2) at 1000 ml/min.
(14) (Fe,Cr) $La_2Ti_2O_7$(N) (FeCrLTON) powder.
(15) Analyzed powder by:

    (15.1) Phase analysis (X-ray Diffractometer (XRD))

    (15.2) Detection of bonding compound (X-ray photoelectron spectroscopy (XPS))

    (15.3) Microstructure of powder (Field emission scanning electron microscopy (FE-SEM))

    (15.4) Analysis of absorption of light (Ultra violet-Visible Spectrophotometer (UV-Vis))

    (15.5) Elemental composition and elemental quantity (Energy Dispersive Spectroscopy (EDS))

(15.6) Elemental substitution (X-ray absorption spectroscopy (XAS))

(15.6) Nitrogen substitution (Photoemission Electron Spectroscopy (PES))

3.6.3   Photocatalytic activity

The degradation of photocatalytic activity was analyzed using methylene blue (MB). The MB solution was prepared at a concentration of 1.8×10^{-4} M (57.57 ppm). For each measurement, 0.01 g of the synthesized photocatalysts powder was added to 50ml of the MB solution. The reaction was performed in a black box with continuous stirring while exposed to LED light (EVE panel square, 18 W, Kenko L41 super pro (W) filter: light wavelength > 400 nm) for a total of 180 min. The photocatalytic activity was determined by measuring the MB degradation using UV-Vis spectroscopy (UV-Vis, model: CARY 300) equipped with a tungsten lamp as the light source.

(16) (Fe,Cr) $La_2Ti_2O_7$(N) (FeCrLTON) powder from step 14, mixing with MB solution which was concentration at 1.8×10^{-4} M was carried up to photocatalytic box for degraded MB solution, stirring 180 min.
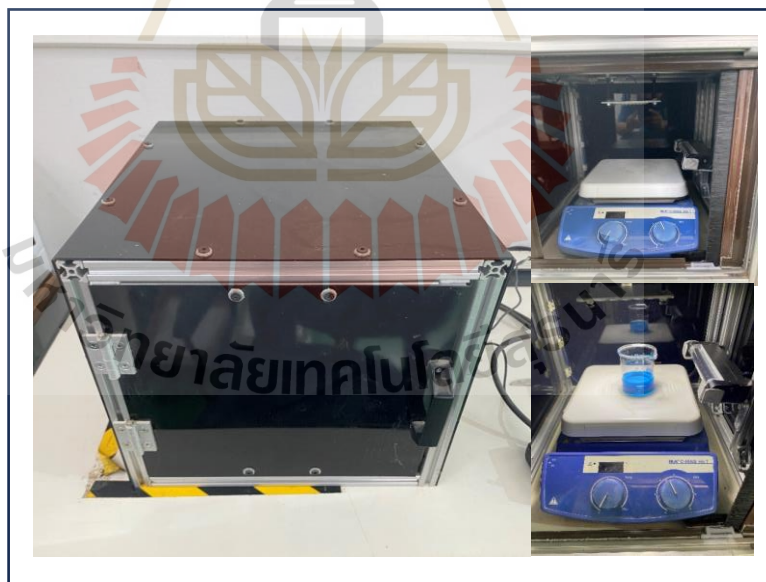
Figure 3.18 photocatalytic box (Dark box)

(17) separating powder and solution after 180 min and carried out to photocatalytic analysis.

3.7   Characterization details

3.7.1   X-Ray Powder Diffraction (XRD)

The crystal structure of the synthesized photocatalysts were determined by X-ray diffraction (XRD, BRUKER D2 PHASER). The characterized conditions used for analysis are as follows: CuKα radiation (λ= 1.5406 Å) at 40 kV, 40 mA, scanning range 20.70° degree (2θ-theta) with 0.02° step size, and a counting time of 0.2 second per step. Data manipulation and XRD pattern fitting were performed using Originpro 2023 version 10.0.0.154 (Learning Edition)

(18) FeCrLTO, FeCrLTON and LTO powder were analyzed a phase composition by XRD
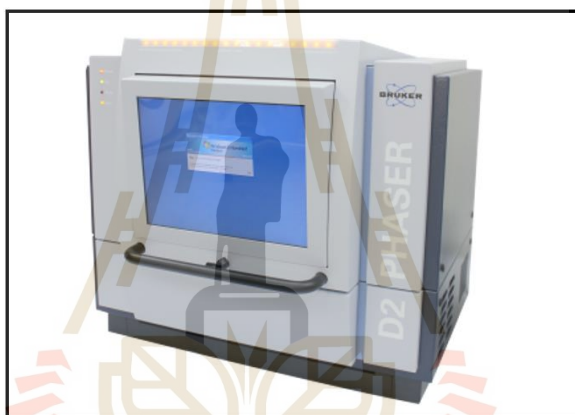
Figure 3.19 X-ray diffraction (XRD, BRUKER D2 PHASER)

3.7.2   UV-Vis spectroscopy (UV-Vis)

The photocatalytic activity was determined by measuring the MB degradation using UV-Vis spectroscopy (UV-Vis, model: CARY 300) equipped with a tungsten lamp as the light source. The wavelength range of the analysis was set between 300 and 700 nm. Measurement was done in a transmittance mode.

(18) After photocatalytic test in step 17, the solution were determined absorption values between 300-700nm by UV-Vis analysis

Figure 3.20 UV-Vis spectroscopy (UV-Vis, model: CARY 300)

3.7.3 Field emission scanning electron microscopy (FE-SEM)

The crystal structure was analyzed by a field-emission scanning electron microscope (FE-SEM) from Carl Zeiss (model: AURIGA). The FE-SEM images revealed the shapes and pores in the crystal structure, and the analysis was performed with an acceleration voltage of 50 kV, a working distance (WD) of 6.5 mm, and a magnification of 30k. The identified elements were analyzed using energy dispersive spectroscopy (EDS).

(19) FeCrLTO, FeCrLTON and LTO powder were analyzed a microcrystalline structure and elemental quantity by FE-SEM and EDS

Figure 3.21 Morphology and elemental quantity analysis by FE-SEM and EDS

3.7.4 X-Ray Absorption Spectroscopy (XAS)

X-ray absorption measurements were carried out at the SUT-NANOTEC-SLRI XAS beamline (BL5.2) of the Synchrotron Light Research Institute (Public Organization) (SLRI), Nakhon Ratchasima, Thailand. The synchrotron light provides electron energy of 1.2 GeV; bending magnet; beam current 80-150 mA. The beam line optics of BL5.2 is equipped with a double crystal, fixed exit, Ge (220) monochromator. The beamline possesses an energy range of 1810-13000 eV, a photon flux of 108-1010 photons/s/100 mA. For Ti K-edge measurement, a Ti foil was used for energy calibration at 4966 eV on a transmission mode. For La L-edge measurement, V foil was used for energy calibration at E0 of 5465 eV in transmission mode. Samples were measured La L-edge XANES and EXAFS in fluorescence-mode at E0 of 5483eV. XANES measurements were performed in the rage of -30 eV to 80 eV of E0, while EXAFS measurement, the photon energy scan was set up in a range of -150 eV, -10 eV, 30 and 12k of E0 with the photon energy step of 5 eV, 0.3 eV and 0.05k. Samples were measured up to 4 scans. The normalized absorption data were processed after background subtraction in the pre-edge and post-edge region, then EXAFS fitting was performed using Athena and Artemis program in Demeter (version 0.9.26) Athena.

(20) FeCrLTO, FeCrLTO(N) and LTO powder were analyzed elemental substitution by XAS

Figure 3.22 Elemental substitution analysis by XAS

3.7.5 X-Ray Photoelectron Spectroscopy (XPS)

The surface elemental composition and oxidation state of samples were analyzed using X-ray photoelectron spectroscopy (XPS), PHI5000 VersaProbe II (ULVAC-PHI, Japan) at the SUT-NANOTEC-SLRI Joint Research Facility, Synchrotron Light Research Institute (SLRI), Thailand. Monochromatized Al-Kα X-ray source (hγ = 1,486.6 eV) was utilized to excite the samples. The XPS spectra were fitted using PHI MultiPak XPS software with a combination of Gaussian–Lorentzian lines. Shirley-type background was used to remove the background from the spectrum before the peak fitting.

The survey spectra were recorded with an energy step of 1.000 eV and a pass energy of 117.4 eV, meanwhile, the high-resolution spectra were recorded with an energy step of 0.05 eV and a pass energy of 46.95 eV. The carbon charging correction refers to the binding energy of adventitious carbon at the binding energy of 284.8 eV

(21) FeCrLTO, FeCrLTON and LTO powder were analyzed nitrogen substitution by XPS

Figure 3.23 Surface elemental composition and oxidation state by XPS

3.7.6 Photoemission spectroscopy (PES)

Photoemission spectroscopy (PES), also known as photoelectron spectroscopy, refers to energy measurement of electrons emitted from solids, gases or liquids by the photoelectric effect, in order to determine the binding energies of electrons in the substance. The term refers to various techniques, depending on whether the ionization energy is provided by X-ray, XUV or UV photons. Regardless of

the incident photon beam, however, all photoelectron spectroscopy revolves around the general theme of surface analysis by measuring the ejected electrons. The PES usually use determine elemental analysis in low energy, low eV, the element can detect low atom weight that is nitrogen, oxygen, boron and etc. the sample was used determined condition: C-ref 281-287 eV, N kedge 390-425eV at the SUT-NANOTEC-SLRI Joint Research Facility, Synchrotron Light Research Institute (SLRI), Thailand.

(22) FeCrLTO, FeCrLTON and LTO powder were analyzed nitrogen substitution by PES

Figure 3.24 Determined nitrogen substitution by PES

CHAPTER IV
RESULT AND DISCUSSION

4.1 Effect of calcination temperature on FeCrLTO

Figure 4.1 was shown (Fe,Cr) $La_2Ti_2O_7$, (FeCrLTO), which was Fe, Cr doped $La_2Ti_2O_7$ calcination temperature at 1150℃ for 2h under ambient temperarure, and comparing (Fe,Cr) $La_2Ti_2O_7$ as Fe, Cr doped $La_2Ti_2O_7$ calcination temperature at 1150℃, (FeCrLTO(N)1150), calcination temperature under nitrogen atmosphere at 1150℃ in different times: 18h, 24h, and 30h.
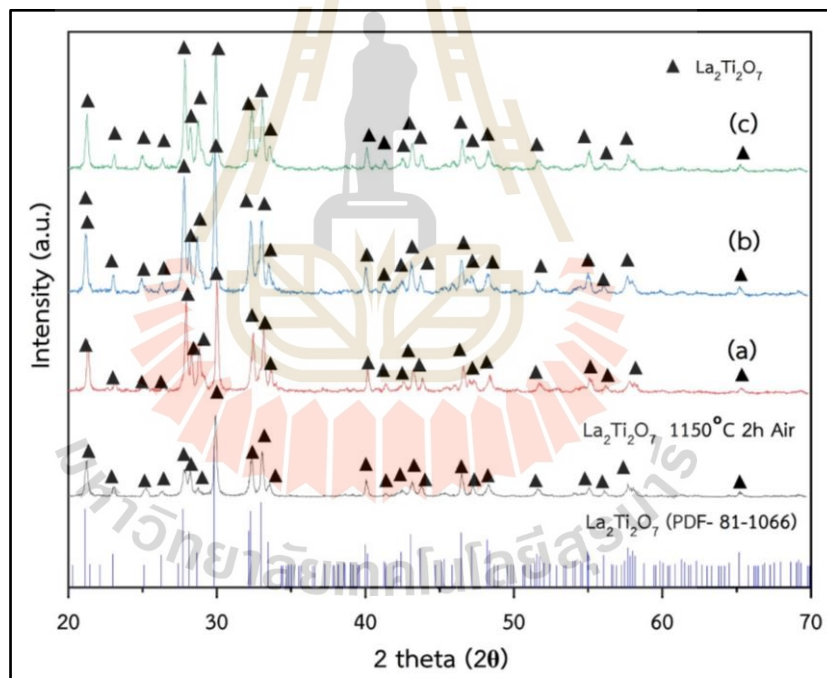
Figure 4.1 XRD pattern of FeCrLTO(N) at 1150℃ with different calcination
times (a) 18h (b) 24h and (c) 30h

Fe and Cr co-doped with $La_2Ti_2O_7$, it disappeared Fe and Cr peaks on XRD pattern because the amount of Fe and Cr was only 0.005mol% which was not on XRD detection and was not appeared Fe and Cr compound on XRD pattern in Figure 4.1 ($La_2Ti_2O_7$, LTO, PDF 81-1066), 1150℃ for 2h under ambient atmosphere which obtained

LTO was monoclinic (P1) of $La_2Ti_2O_7$ corresponding to Hwang et al due to amount of dopant.
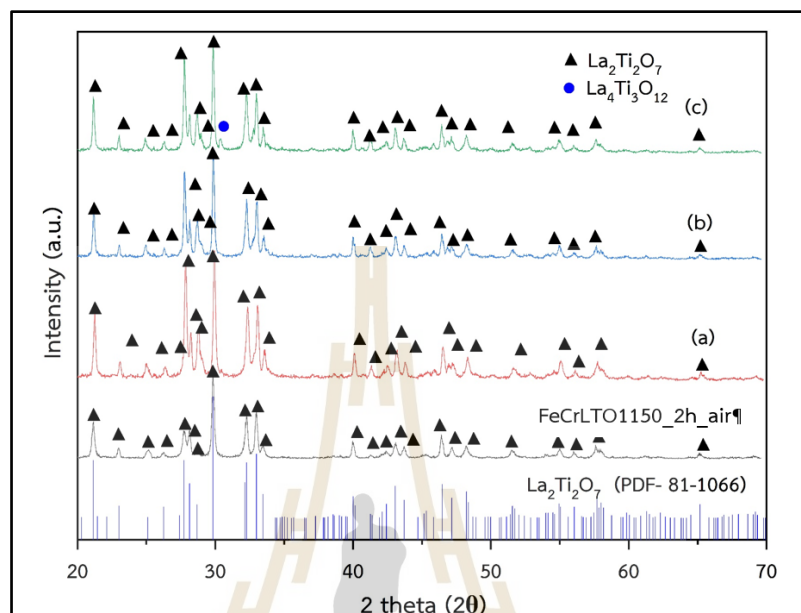
Figure 4. 2 XRD pattern of FeCrLTO at 1250°C with different calcination times (a) 18h (b) 24h and (c) 30h

Hwang et al. investigated Cr or Fe doping in $La_2Ti_2O_7$ that Cr-contents as a dopant were higher than 0.01mol% occurring $LaCrO_3$. For Fe-contents were higher than 0.04mol% which occurred $Fe_3Ti_3O_{10}$. In addition, Ti^{4+} site was substituted by Fe and Cr were not instead of La due to similar cationic size: La^{3+}(1.04Å) Ti^{4+}(0.06Å), Fe^{3+}(0.53Å) and Cr^{3+}(0.53Å) (Hwang et al., 2005).

Obviously, the XRD pattern was almost the same pattern but Fe and Cr were doped on $La_2Ti_2O_7$ (FeCrLTO(N)1150) that FeCrLTO(N)1150 peaks intensity was higher than original FeCrLTO due to high crystallinity with increasing calcination time. Additionally, Myung et al. investigated that the effect of crystalline size was influenced to temperature increasing.

Myung et al. found that TiO_2 nanostructure which calcination temperature was at 170°C for 24h was broad peaks but the calcination times effected to crystallinity when increased to 48h. The crystallinity of TiO_2 nanostructure at 168h was higher than 24h which obtained a high crystallinity when increased calcination times sufficiently (Myung et al., 2011).

Calcination temperature at 1150°C under nitrogen atmosphere as doping nitrogen for 18h, 24h and 30h, FeCrLTO(N)1150_18h, FeCrLTO(N)1150_24h and FeCrLTO(N)1150_30h were similar peak of XRD pattern of FeCrLTO. Previous study, doping nitrogen was employed NH_3 as nitrogen source but result of XRD analysis was not change structure, according to Wang et al.

Wang et al. synthesized doping nitrogen in $La_2Ti_2O_7$ using NH_3 treatment as nitrogen source, and the peak diffraction was not indicated N locate in the host structure. After NH_3 treatment, the XRD pattern was similar peak compared with untreated NH_3. N-doped $La_2Ti_2O_7$ was not largely effected to doping concentration (Wang, Asakura, Hasegawa, & Yin, 2021).
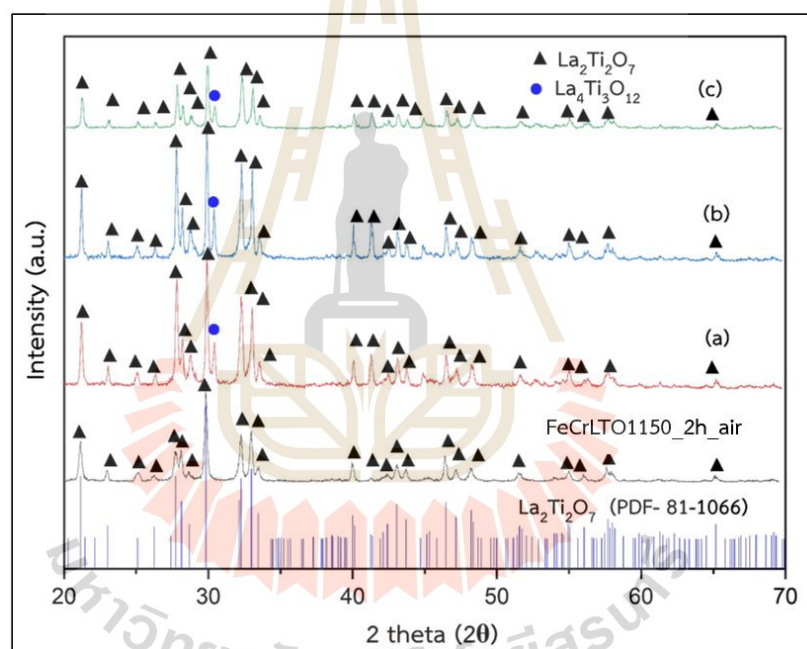
Figure 4.3 XRD pattern of FeCrLTO at 1350°C with different calcination
times (a) 18h (b) 24h and (c) 30h

Calcination temperature at 1250°C in different times: 18h, 24h and 30h was XRD pattern with 1150°C similarly, shown as Figure 4.2, but the increasing calcination time to 30h appeared $La_4Ti_3O_{12}$ peak (PDF 89-4520) which indicated 30.35° of 2θ in Figure 4.2 (c). FeCrLTO(N)1250 was decomposition when increased calcination times and peak observation decreased peak intensity at FeCrLTO(N)1250_30h compared with FeCrLTO(N)1250_18h and FeCrLTO(N)1250_24h. According to the $La_4Ti_3O_{12}$ formation,

Miseki et al. was apparent calcination temperature higher than 1200°C, and Abe and Laine found that the formation of $La_4Ti_3O_{12}$.

Abe and Laine synthesized $La_4Ti_3O_{12}$ which occurred $La_4Ti_3O_{12}$ formation beginning above 1050°C with decreasing $La_2Ti_2O_7$ content, $La_2Ti_2O_7$ decomposition (Abe & Laine, 2020).

Miseki et al. $La_4Ti_3O_{12}$ formation was synthesized via the polymerization complex method after heating at 1200°C for 10 h. In contrast, the solid-state reaction (SSR method) of $La_4Ti_3O_{12}$ formation was obtained at 1400°C. The effective particle shape was influenced to decreasing-calcination temperature due to crystal growth to the direction in a plane parallel to the (-110) plane (Miseki, Kato, & Kudo, 2009).

FeCrLTO(N)1350_18h was $La_4Ti_3O_{12}$ formation, 30.35° of 2θ, until 18h because of high calcination temperature which was higher than 1250°C. The XRD pattern consisted of $La_4Ti_3O_{12}$ and $La_2Ti_2O_7$ as mixing phase and the peak intensity decreased when calcination time to 30h that $La_4Ti_3O_{12}$ was decomposed, shown as Figure 4.3 (c). Therefore, Figure 4.3 (a), (b), and (c) was shown that FeCrLTO(N)1350_18h, FeCrLTO(N)1350_24h and FeCrLTO(N)1350_30h had the $La_4Ti_3O_{12}$ peak appearing on XRD pattern. In addition to $La_4Ti_3O_{12}$ formation, the calcination temperature was higher than 1250°C obtaining $La_4Ti_3O_{12}$ which was obtained $La_4Ti_3O_{12}$ using calcination temperature at 1350°C as well, according to Zhang et al.

Zhang et al. reported that the $La_4Ti_3O_{12}$ preparation was used PC method using calcination temperature 1250°C for 6h and obtained pure $La_4Ti_3O_{12}$ before doping process (Zhang et al., 2019).

4.2   Effect of calcination temperature on FeCrLTO(N)
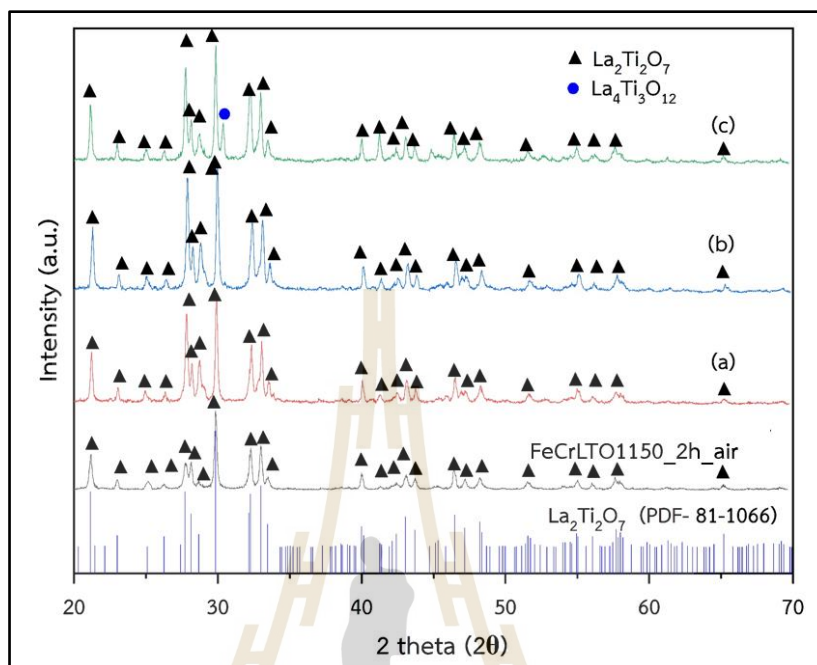
Figure 4.4 XRD pattern of FeCrLTO(N) at 18h with different calcination
temperatures (a) 1150°C, (b) 1250°C and (c) 1350°C

Comparing with calcination time at 18h with different calcination temperatures
was FeCrLTO(N)1150, FeCrLTO(N)1250 and FeCrLTO(N)1350 which was similar XRD
pattern but FeCrLTO(N)1350 indicated $La_4Ti_3O_{12}$, 30.35° of 2θ, that the calcination
temperature was higher than 1250°C occurring $La_4Ti_3O_{12}$ as mentioned above.
Corresponding to crystallinity, the crystallinity was high when increasing temperature,
observed by Phromma et al.

Phromma et al. reported that TiO_2 had a broadened peak in the range of 300°C-
500°C at the same calcination time and increased calcination temperature to 600°C
was more crystallinity due to sharper and narrow peaks of XRD pattern. Besides, the
increasing calcination temperature had an influence on crystalline size, phase
transition, and crystallinity. (Phromma, Wutikhun, Kasamechonchung, Eksangsri, &
Sapcharoenkun, 2020)
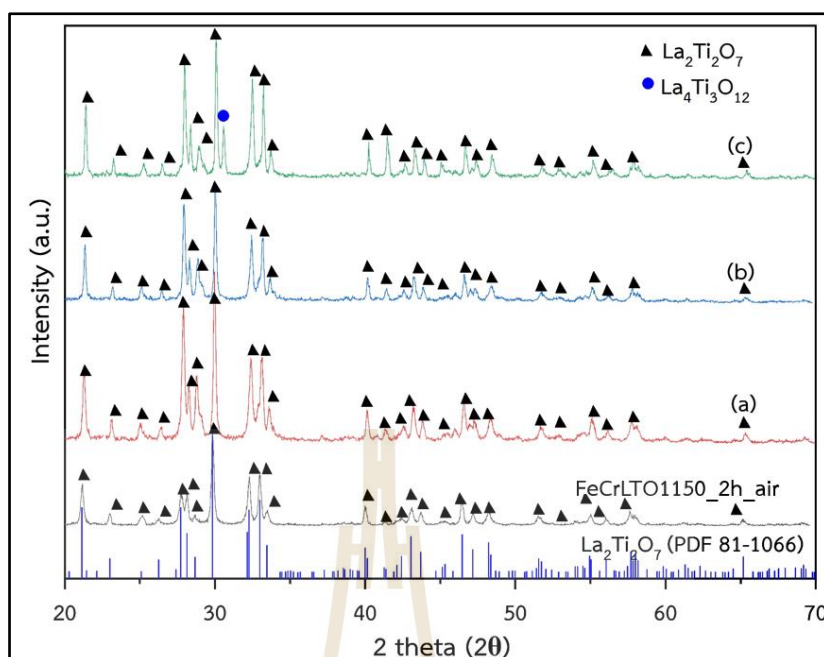
Figure 4.5 XRD pattern of FeCrLTO(N) at 24h with different calcination
temperatures (a) 1150°C, (b) 1250°C and (c) 1350°C

The crystal phases of synthesized photocatalysts was shown in Figure 4.5 revealing that all samples exhibit the $La_2Ti_2O_7$ crystal phase as the dominant phase, and no impurities are detected. It is apparent that the $La_2Ti_2O_7$ crystal started forming after being calcined at 1150°C for 2h under ambient atmosphere. The complete $La_2Ti_2O_7$ crystal was found in FeCrLTO1150(N)_24h and FeCrLTO1250(N)_24h, which obtained monoclinic (P1) of $La_2Ti_2O_7$. However, FeCrLTO1350(N)_24h found an extra peak of $La_4Ti_3O_{12}$ at 2θ of 30.35 degrees, suggesting that higher temperature induced decomposition or phase transformation from $La_2Ti_2O_7$ into mix phase of $La_2Ti_2O_7$ + $La_4Ti_3O_{12}$. In addition, the co-doping of Fe and Cr did not reveal any impurity phases, suggesting that the Fe and Cr cations were possibly integrated into the $La_2Ti_2O_7$ lattice.
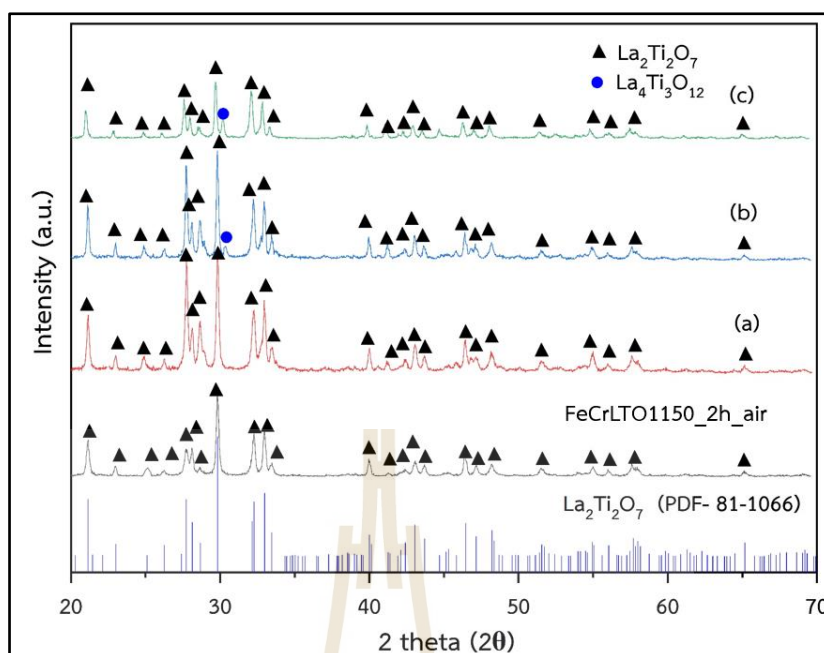
Figure 4.6 XRD pattern of FeCrLTO(N) at 30h with different calcination
temperatures (a) 1150°C, (b) 1250°C and (c) 1350°C

Above FeCrLTO1150_30h, $La_4Ti_3O_{12}$ appeared on XRD pattern but $La_4Ti_3O_{12}$ formation was not imperfect crystal which considered XRD intensity of FeCrLTO1250_30h in Figure 4.6 (c). The $La_4Ti_3O_{12}$ formation was used higher temperature than 1250°C. Fe and Cr disappeared located peal on XRD pattern which was a small amount of that it was not detected.

4.3 Elemental composition analysis

4.3.1 Energy Dispersive X-ray Spectroscopy (EDS)
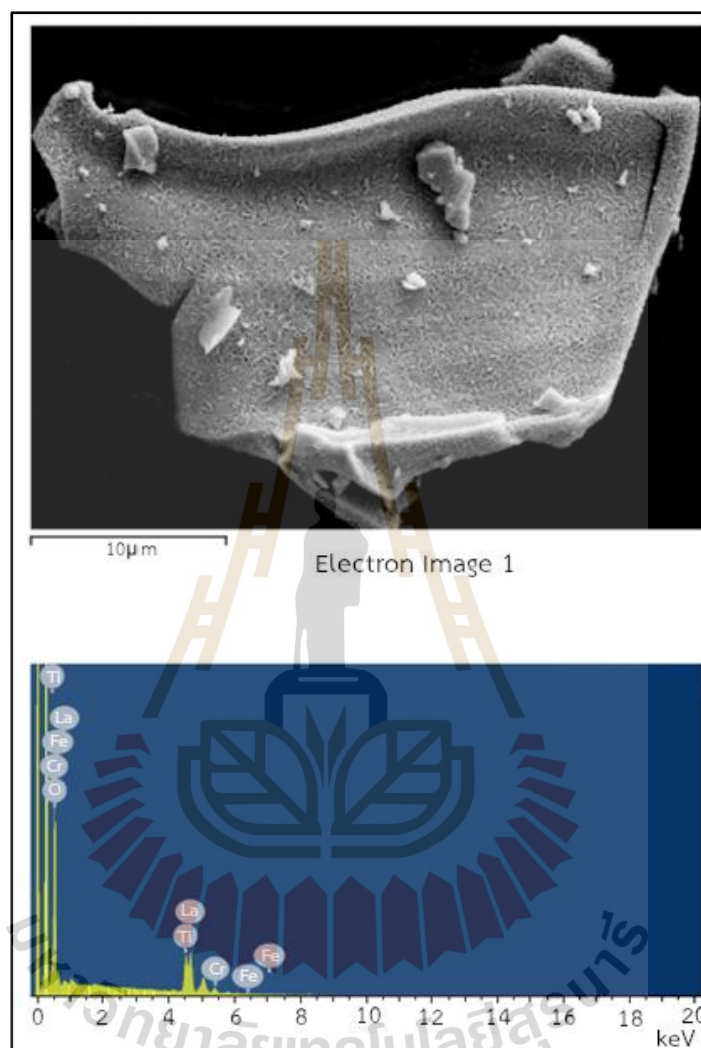
Figure 4.7 FE-SEM using EDS technique of FeCrLTO(N) at 1150°C for 18h
The elemental compositions of synthesized photocatalysts
were analyzed by FE-SEM using Energy-Dispersive X-ray
(EDX) technique. The EDX spectra of FeCrLTO1150_18h

was shown in Figure 4.7, and the percentage of mass relative to each element was summarized in Table 4.1. There was no contamination of the samples with other elements, as indicated by the peaks corresponding to O, Ti, La, Fe, and Cr.

Moreover, the results confirm that Fe and Cr were incorporated into the crystal structure of $La_2Ti_2O_7$. Although the content of O and Ti was similar across all samples, specifically, there were slight variations in the contents of La, Fe, and Cr.

Table 4.1 Elemental composition of FeCr1150(N)_18h

Sample	Elemental composition (%mass relative)				
	O	Ti	La	Fe	Cr
FeCrLTO1150(N)_18h	26.97	10.82	43.01	1.78	17.41

Thus EDS technique was employed to identify the elemental composition and reveal elemental detection: FeCrLTO1150(N)_18h, FeCrLTO1150(N)_24h, FeCrLTO1150(N)_30h, FeCrLTO1250(N)_18h, FeCrLTO1250(N)_24h, FeCrLTO1250(N)_30h, FeCrLTO1350(N)_18h, FeCrLTO1350(N)_24h, and FeCrLTO1350(N)_30h. This section was shown only FeCrLTO(N)1150C_18h. The elemental analysis demonstrated that all samples were found: Ti, La, O, Fe and Cr, and the percent of elements were different in each sample, see in appendix 1. Considering EDS technique was not nitrogen detection which was equipment limitation.

The limited equipment was undetectable nitrogen atoms, which was a light element as uncertain detection. Therefore, the nitrogen atoms in crystal structure was determined with other techniques for insisting that atoms. In addition, X-ray map revealed all elements with the same as EDS technique. Furthermore, absorption in this relatively thick (>7 μm) window prevents analysis of elements with an atomic number below that of sodium (Z < 11). (Williams, 1993)(Malac & Egerton, 1999)
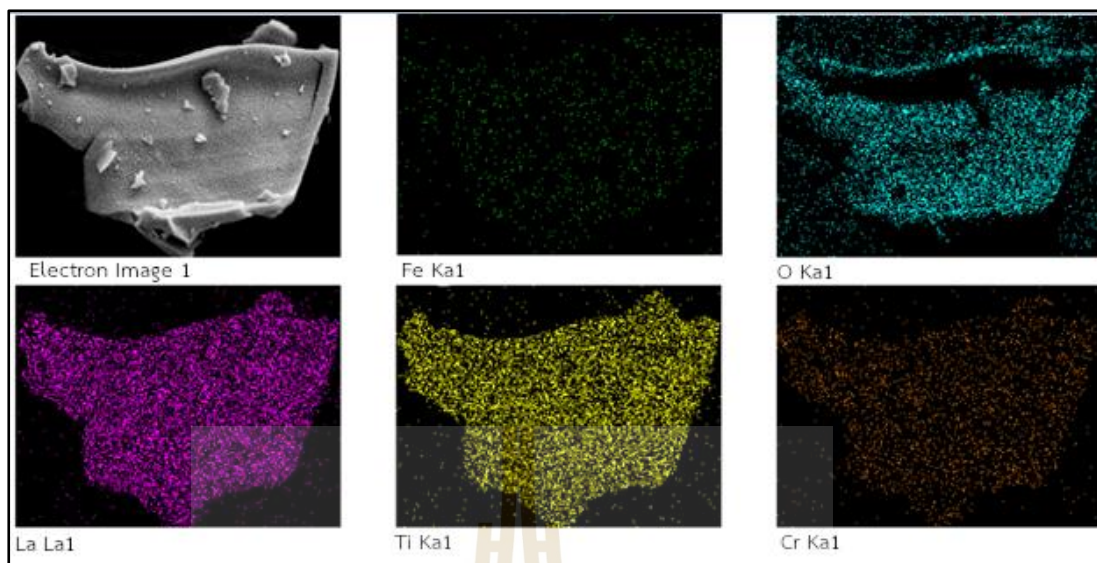
Figure 4.8 X-ray map composition of FeCrLTO(N) at 1150°C for 18h

The detection limit in EDS depends on sample surface conditions, smoother the surface the lower the detection limit. EDS can detect major and minor elements with concentrations higher than 10wt% (major) and minor concentrations (concentrations between 1 and 10wt%). The detection limit for bulk materials is 0.1wt% therefore EDS cannot detect trace elements (concentrations below 0.01wt%) (Goldstein J et al., 2003).

4.4   Morphology and elemental composition

4.4.1   Field Emission Scanning Electron Microscope (FE-SEM)

The crystal morphologies of the synthesized photocatalysts were observed using FE-SEM. The sample calcined at 1150°C (FeCr1150_18h) was found to have the smallest grain size (Figure. 4.9(a)). As the calcination time increased up to 24h (FeCr1150_24h), the crystal structure became larger and the grain edges became sharper comparing with original reference (LTO, 1150°C 2h air).
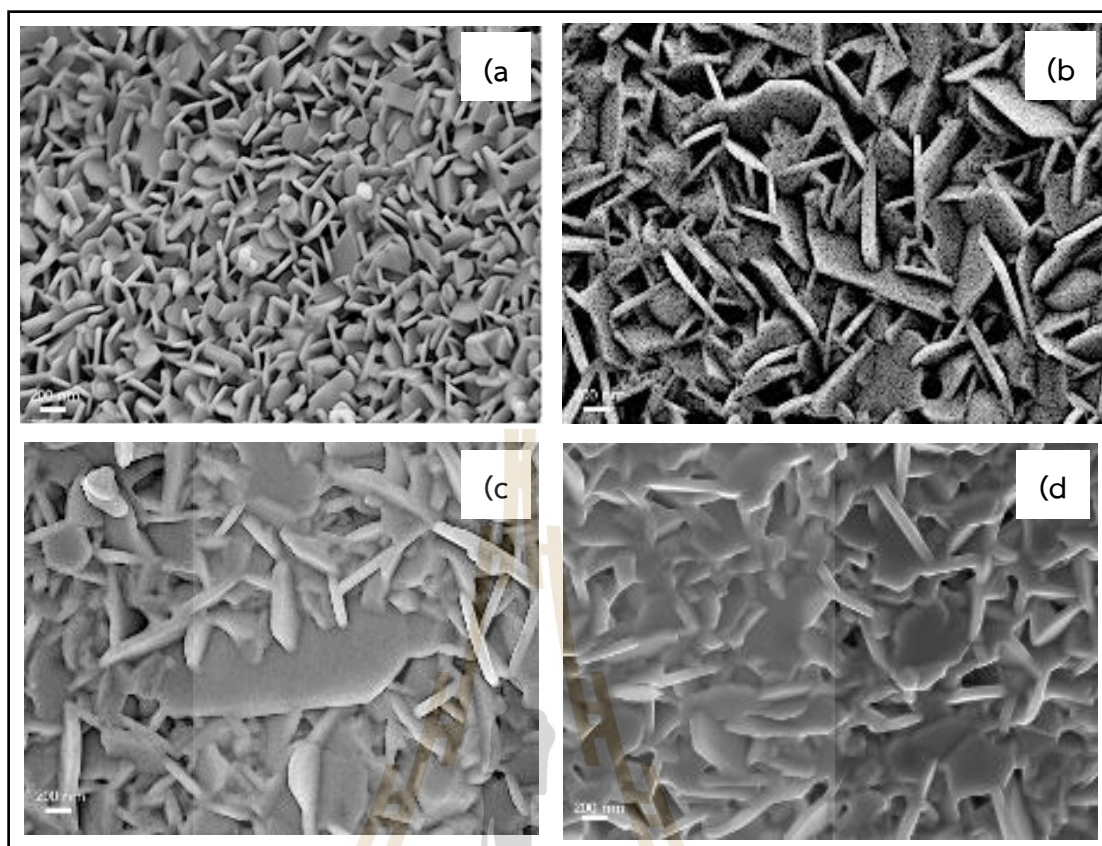
Figure 4.9 FE-SEM image of crystal structure at 1150°C in different
calcination times (a) FeCrLTO 1150°C 2h air (b) FeCrLTO(N)
1150_18h, (c) FeCrLTO(N) 1150_24h and (d) FeCrLTO(N)
1150_30h

Figure 4.9 (c) FeCrLTO(N)1150_24h calcination time increasing to 24h, some
grains were larger than neighbor gains obviously due to the effect of calcination times.

In contrast, the sample calcined at 1150°C (FeCrLTO1150_30h) showed
disappearing gain edges, which resulted in the large grain size connecting with the
adjacent grains, see in Figure 4.9 (d).

The results suggest that changes in the morphology of co-doped
FeCrLTO were induced by the calcination temperature. Although higher temperatures
are more favored for the formation of perovskite-type crystalline grains, but the
temperature should not exceed 1250°C to avoid adverse effects on the crystallinity.
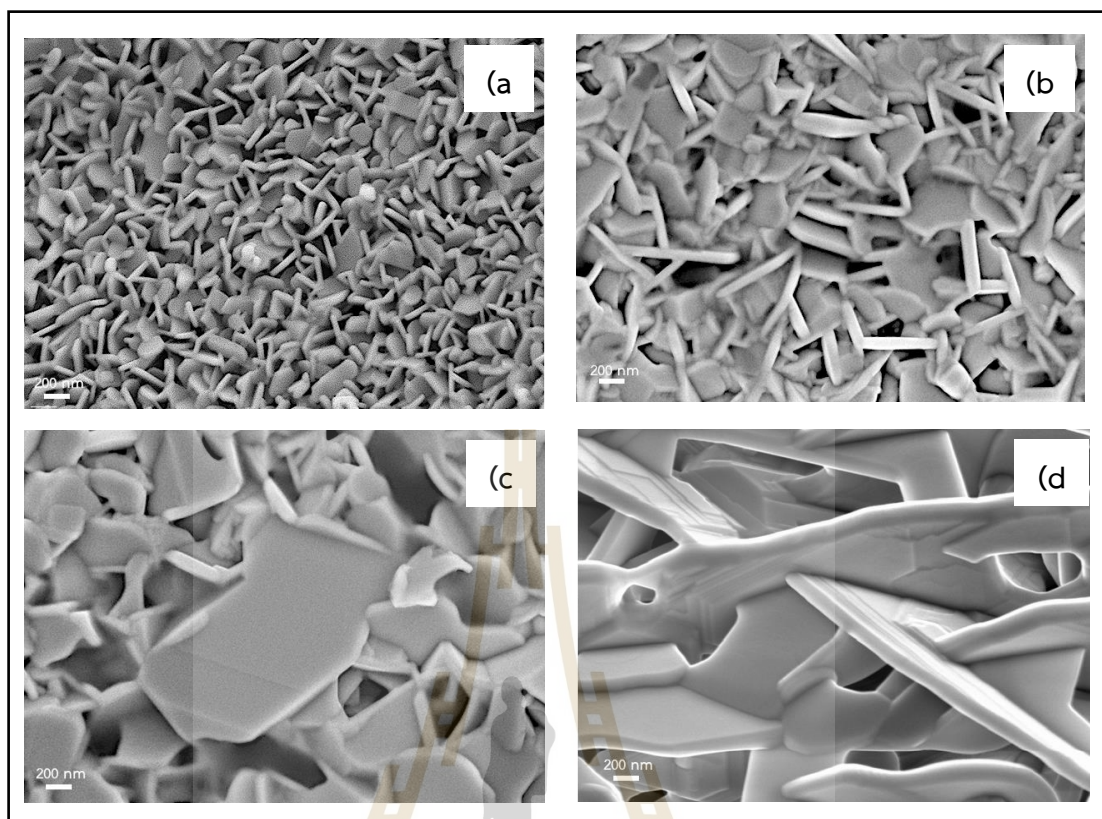
Figure 4.10 FE-SEM image of crystal structure at 1250°C in different
calcination times (a) FeCrLTO 1250°C 2h air (b)
FeCrLTO(N)1250_ 18h, (c) FeCrLTO(N)1250_ 24h and (d)
FeCrLTO(N)1250_30h

The calcination temperature at 1250°C was shown microcrystalline
compared with original reference (LTO, Figure 4.10 (a)) which was found sharpen-gain
edge compared with Figure 4.9 (b) FeCrLTO(N) 1150_18h and was decreased pores
volume, shown as Figure 4.10 (b). The relative of calcination temperature and
calcination time was influence of characteristic pore and crystalline size, according to
Collazzo et al.

Collazzo et al. synthesized nano-TiO$_2$ which was used 150°C and 200°C
for 6, 12, 24 and 36h respectively, they found that the calcination temperature and
calcination time effected to pore size, pore volume, and crystalline size. In addition,
when increasing temperature, pore size was larger but the pore volume decreased.
Pore size observation employing calcination temperature at 150°C for 6h and 36h and
200°C for 6h and 36h obtained 6.3 nm, 8.3 nm, 9.6 nm. and 13.6 nm, respectively. The

pore volume of calcination temperature at 150°C for 6h and 36h and 200°C for 6h and 36h obtained 0.33 cm^3•g^{-1} and 0.29 cm^3•g^{-1}, 0.32 cm^3•g^{-1}, and 0.26cm^3•g^{-1}, respectively. For crystalline size increased when increased calcination temperature, the calcination temperature at 150°C for 6h obtained 8.9 nm for average size when increased temperature up to 200°C for 6h obtaining 12.0 nm for average size. As effective calcination time to crystalline size, the calcination temperature at 150°C for 6h and 36h and 200°C for 6h and 36h obtained 6.3 nm, 8.3 nm, 9.6 nm, and 13.6 nm, respectively. (Collazzo, Jahn, Carreño, & Foletto, 2011)
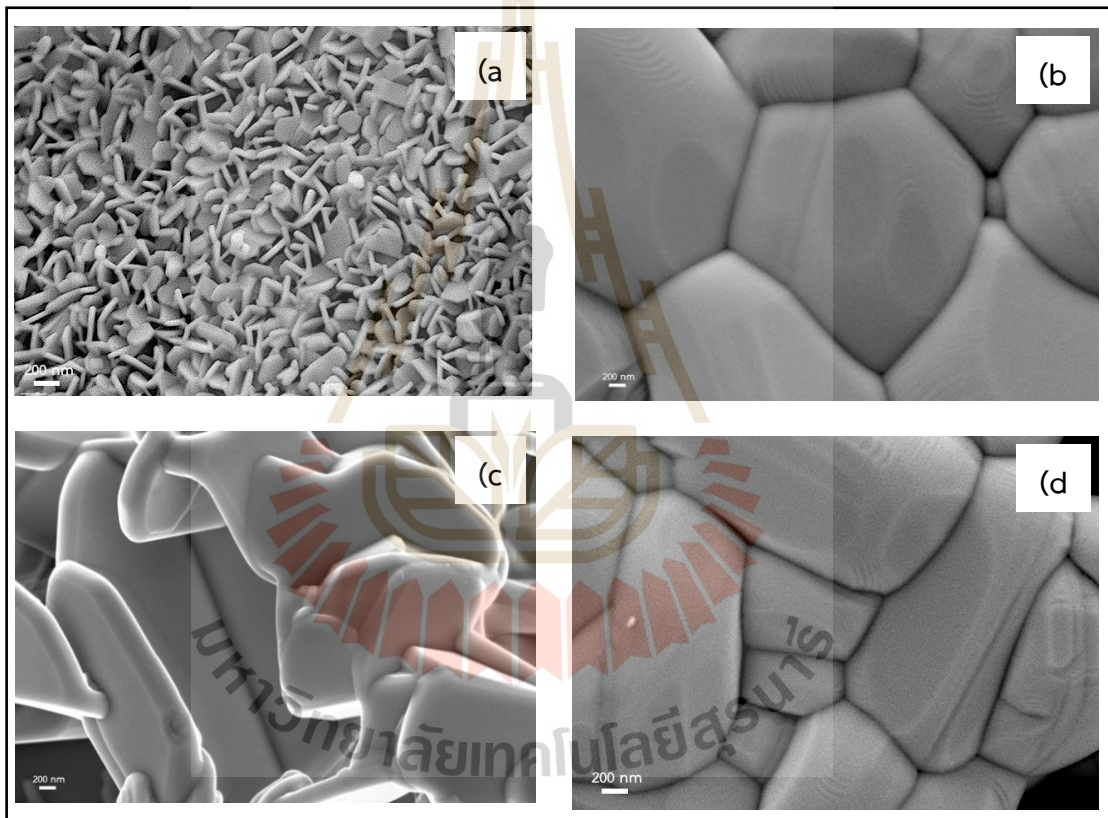
Figure 4.11 FE-SEM image of crystal structure at 1350°C in different calcination
times (a) FeCrLTO 1350°C 2h air (b) FeCrLTO(N) 1350_18h,
(c) FeCrLTO(N)1350_24h and (d) FeCrLTO(N)1350_30h

FE-SEM image of crystal structure at 1350°C was shown the microcrystalline that the grains size was obtained densification due to increasing of calcination time. Apparently, calcination time at 30h occurred grain growth and densification. At 24h,

the grains was connected with neighbor grains as grain boundary diffusion, and the grain shape was changed by effective time.

Grain boundary diffusion and lattice diffusion are important densification mechanisms in metals and ceramics. Plastic flow, by dislocation motion in response to the sintering stress, plays essentially no role in the sintering of ceramics because of the low dislocation density. The occurrence of plastic flow during the sintering of metals is controversial, but most likely dislocations participate in the initial stage of sintering. Finite element analysis (Ogbuji, 1986) and experiments (Morgan, 1973; Brett and Seigle, 1963) indicate that plastic flow by dislocation motion is inactive in the intermediate and final stages of sintering.

4.5   Photocatalytic activity analysis

4.5.1   UV-Vis spectroscopy (UV-Vis)
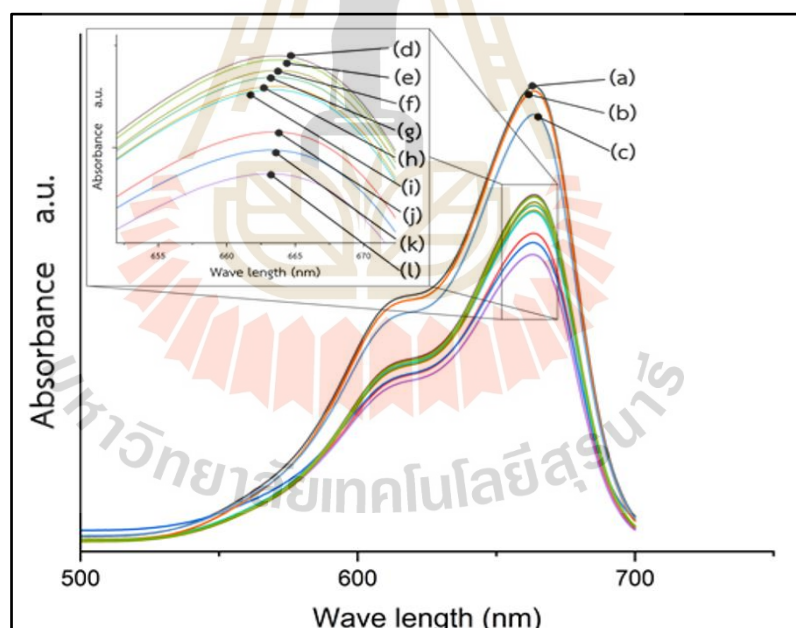
Figure 4.12 (a) Metylene blue (MB), (b) LTO, (c) FeCrLTO, (d) FeCrLTO(N)1350_24h, (e) FeCrLTO(N)1150_18h, (f) FeCrLTO(N)1350_30h, (g) FeCrLTO(N)1250_18h, (h) FeCrLTO(N)1250_30h, (i) FeCrLTO(N)1350_18h, (j) FeCrLTO(N)1150_ 24h (k) FeCrLTO(N)1150_30h, (l) FeCrLTO(N)1250_24h

The photocatalytic activity was observed all samples to degrade methylene blue (MB) (1.8×10^{-4}M) for 180min (Jin, et al., 2008) (Sahoo, Gupta, & Sasidharan Pillai, 2012) under visible light irradiation which was analyzed by UV-Vis spectroscopy. Figure 4.12 revealed photocatalytic activity which was compared to N-doping samples with LTO and FeCrLTO as references. The LTO, Figure 4.12 (b), slightly decreased from original methylene blue (MB), Figure 4.12 (a), because LTO was large band gap energy (3.8eV) (Liu, Nisar, Sa, Pathak, & Ahuja, 2013) which effected to low photocatalytic activity to degrade MB due to inactive photocatalyst under UV region. The large band gap is an obstacle of migration for the excited electrons from valence band to conduction band if the energy is enough or more band gap energy. In addition, UV region has more energy than visible light region. Therefore, LTO was not active under visible light.

Doping process is the one of decreased band gap energy which is high photocatalytic activity. Cation doping can be effective to narrow bandgap obtaining LTO active under visible light, doping with cation induced longer-wavelength absorption.

According to Tan et al., co-doping was investigated the optical property of Nb and Fe co-doping LTO which was determined by UV-Vis spectroscopy that the edge absorption of LTO was 350nm when doping Nb and Fe demonstrated redshift absorption to 460nm. Herein, codoping can extend the light absorption range which was codoping concentration affected to light absorption strongly and can decrease bandgap energy due to d-d hybridization. The d-d hybridization of Fe3d located on the top of valence, for Nb4d orbital governed the bottom of conduction band. (Tan et al., 2017)

4.6 Effect of calcination temperature on FeCrLTO(N)
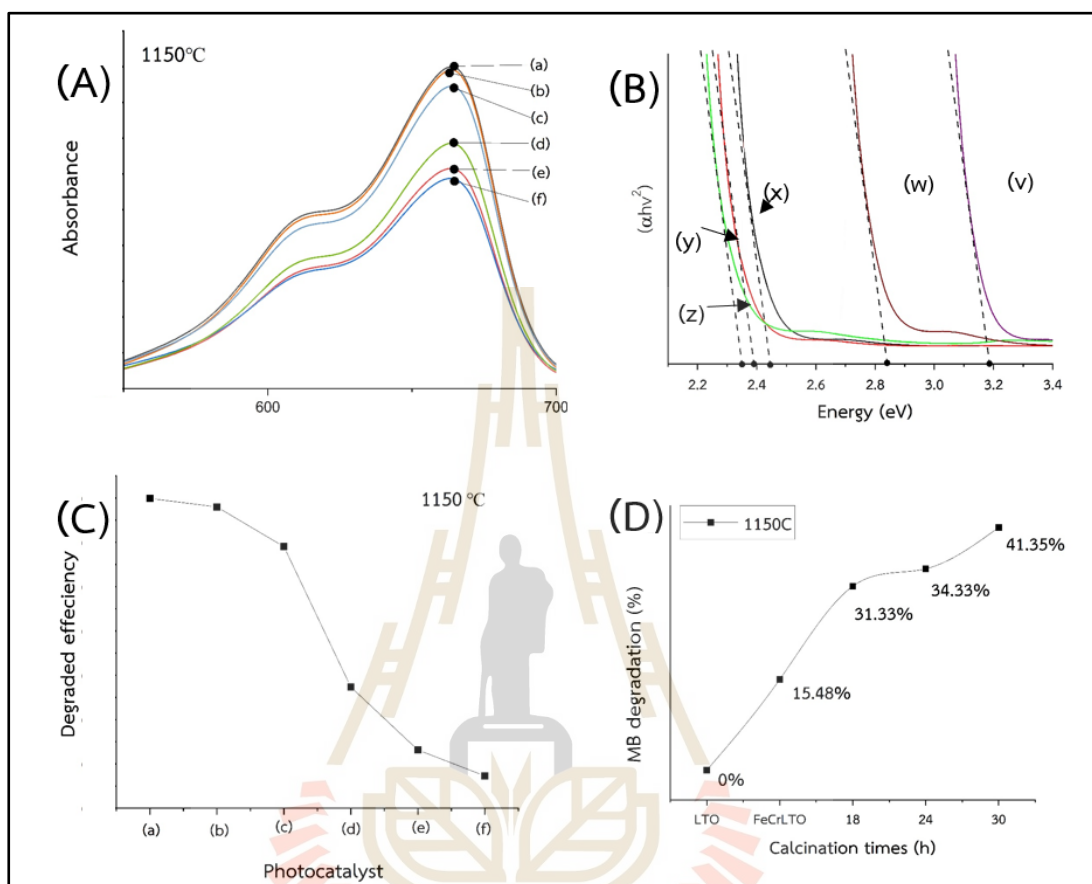
Figure 4.13 Calcination temperature at 1150℃ (A) UV-Vis alnlysis (a) MB,
(b) LTO, (c) FeCrLTO, (d) FeCrLTO(N)1150_18h,
(e) FeCrLTO(N)1150_24h, and (f) FeCrLTO(N)1150_30h,
(B) Estimated band gap energy (v) $Eg_{(LTO)}$,(w) $Eg_{(FeCrLTO)}$,
(x) $Eg_{(FeCrLTO(N)1150\_18h)}$, (y) $Eg_{(FeCrLTO(N)1150\_24h)}$, (z) $Eg_{(FeCrLTO(N)1150\_30h)}$,
(C) Degraded efficiency (a) MB, (b) LTO, (c) FeCrLTO,
(d) FeCrLTO(N)1150_18h,(e) FeCrLTO(N)1150_24h and
(f) FeCrLTO(N)1150_30h, (D) Percentage of methylene blue

The result UV-Vis absorption was detected by the color changing or various concentrations of MB degradation at 180min, for Figure 4.13 was shown FeCrLTO(N)1150 in different-calcination times as 18, 24 and 30h. The MB degradation revealed that FeCrLTO(N)1150_24h was FeCrLTO(N)1150_ 18h which occurred higher

photocatalytic activity. Regarding with crystalline size, the band gap energy was larger when decreasing of crystalline size.

Kim et al. reported that the effect of smaller crystalline size corresponded to more efficient reaction because smaller crystalline size induced a larger band gap. On the other hand, the band gap narrow was the crystalline size increases. (Kim, Han, & Kwak, 2007)

And also cation-cooping influence to obtain high photocatalytic activity, the codoping with cation had d-d or p-d hybridization in the state comparing with LTO and FeCrLTO, shown as Figure 4.13(A): (b)-(c).

Obviously, nitrogen doping strongly affects to photocatalytic efficiency comparing with FeCrLTO and FeCrLTO(N) when doping nitrogen increased MB degradation, see Figure 4.13(A): (c)-(f)

The MB degradation values of FeCrLTO(N)1150_18h, FeCrLTO(N)1150_24h, and FeCrLTO(N)1150_30h were 0.686, 0.6157, and 0.586, respectively. The MB degradation percent was calculated from absorbance values following equation 4.1,

$$\% \text{ MB degradation} = (1-\text{absorbance}) \times 100 \tag{eq 0.1}$$

where absorbance was the highest intensity of UV-Vis analysis at 664nm. (Luangthanarak, et al, 2023)

Additionally, the percentage of MB degradation was 31.66, 34.3 and 41.35%, respectively, see in Figure 4.13(A): (d)-(f). Obviously, FeCrLTO was active under visible light but it degraded MB less than doping nitrogen. Optical properties for photocatalysis were estimated by Tauc's plot which was used to determine the band gap energy (Eg) following equation 4.2,

$$(\alpha h\nu)^2 = K\,(h\nu\text{-}E_g) \tag{eq 0.2}$$

where Eg is estimated energy band gap between conduction band and valence band, α is the absorption coefficient corresponding to Beer-Lambert relation, $h\nu$ is aborption energy: h is Plank constant, ν is incident frequency, and K is the hand tailing parameter. Inaddition to the band gap energy (Eg), Tauc's plot was used to estimated band gap energy, as shown in Figure 4.13 (B) : (v) Eg $_{(LTO)}$ = 3.18 eV, (w) Eg$_{(FeCrLTO)}$ = 2.84 eV , (x) Eg$_{(FeCrLTO(N)1150\_18h)}$

= 2.47 eV, (y) $Eg_{(FeCrLTO(N)1150\_24h)}$ = 2.39 eV, (z) $Eg_{(FeCrLTO(N)1150\_30h}$ = 2.35 eV. The trending of Eg estimation was lower when increasing calcination times. Therefore, influence of increased calcination time effected to decrease Eg due to increasing amount of nitrogen into lattice FeCrLTO. The nitrogen doped FeCrLTO obtained high photocatalytic efficiency.
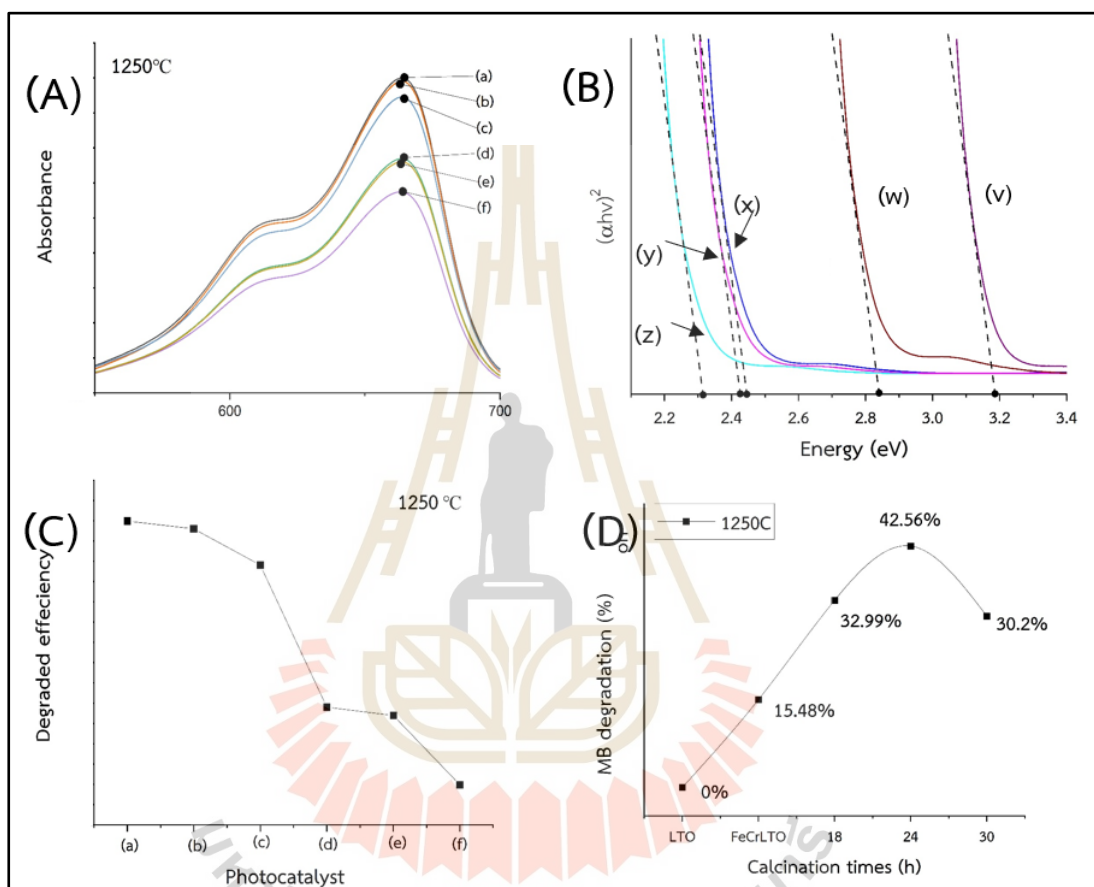
Figure 4.14 Calcination temperature at 1250°C (A) UV-Vis alnlysis (a) MB,
(b) LTO, (c) FeCrLTO, (d) FeCrLTO(N)1250_18h,
(e) FeCrLTO(N)1250_30h, and (f) FeCrLTO(N)1250_24h,
(B) Estimated band gap energy, (v) $Eg_{(LTO)}$, (w) $Eg_{(FeCrLTO)}$,
(x) $Eg_{(FeCrLTO(N)1250\_18h)}$, (y) $Eg_{(FeCrLTO(N)1250\_30h)}$, (z) $Eg_{(FeCrLTO(N)1250\_24h)}$,
(C) Degraded efficiency (a) MB, (b) LTO, (c) FeCrLTO,
(d) FeCrLTO(N)1250_18h,(e) FeCrLTO(N)1250_30h and
(f) FeCrLTO(N)1250_24h, (D) Percentage of methylene blue

Calcination temperature at 1250°C investing at 180min of MB degradation was observed that FeCrLTO(N)1250_18h was lower absorbance than FeCrLTO(N)1250_18h. Both were doped nitrogen at same calcination time but FeCrLTO(N)1250_18h might be nitrogen substitution which was higher than FeCrLTO(N)1150_18h due to calcination temperature. Furthermore, the crystallinity of FeCrLTO(N)1250_18h was higher than FeCrLTO(N)1150_18h when comparing with SEM micrograph, see in Figure (A): (a). Figure 4.14 (B) the estimated Eg was 3.18eV, 2.84eV, 2.44eV, 2.31eV, which was LTO, FeCrLTO, FeCrLTO(N)1250_18h, FeCrLTO(N)1250_30h, FeCrLTO(N)1250_24h, respectively. Comparing with Eg at 1250°C, the lowest of Eg value was FeCrLTO(N)1250_24h because the oxygen was substituted by nitrogen which optimized substitution in this system. For Eg of FeCrLTO(N)1250_30h was higher than FeCrLTO(N)1250_30h, it occurred $La_4Ti_3O_{12}$ formation, see in Figure 4.14. $La_4Ti_3O_{12}$ was mixed phase ($LA_2Ti_2O_7$ and $La_4Ti_3O_{12}$) that the $La_4Ti_3O_{12}$ was high Eg value (4.2eV) and occurred heterojunction.

Hence, this concept of a heterojunction strategy to improve the efficiency of photocatalytic water splitting by combining two or more simple materials that already possessed appreciable visible light absorption, high efficiency and reasonable stability – oxides, nitrides, sulphides and phosphates, and etc. Indeed, there has been some progress in the use of complex oxides and oxynitrides for overall water splitting under visible light. However more research into this emerging family of photocatalyst materials was required, particularly their incorporation into junction architectures, before we can truly assess their impact in this field. (Moniz, Shevlin, Martin, Guo, & Tang, 2015).

Especially, the occurrence of heterojunction could obtain the overlapped band gap energy (Eg) which become narrow Eg but it still had high Eg when compared with FeCrLTO(N)1250_24h leading to strongly effected nitrogen substitution. According to Asahi et al, the substitutional doping of N was then chosen to be the most promising because its p states contribute to the band gap narrowing by mixing with O2p. (Asahi, Morikawa, Ohwaki, Aoki, & Taga, 2001)

Apparently, the percentage of degradation was 32.99, 42.56 and 30.2 of FeCrLTO(N)1250_18h, FeCrLTO(N)1250_24h, FeCrLTO(N)1250_30h, respectively. However, the percentage of FeCrLTO(N)1250_30h decreased because $La_4Ti_3O_{12}$ had large Eg that it overlaps with $La_2Ti_2O_7$ which still was higher Eg than nitrogen substitution. Consequently, FeCrLTO(N)1250_30h, percentage of MB degradation was lowest, see in Figure 4.14 (D):
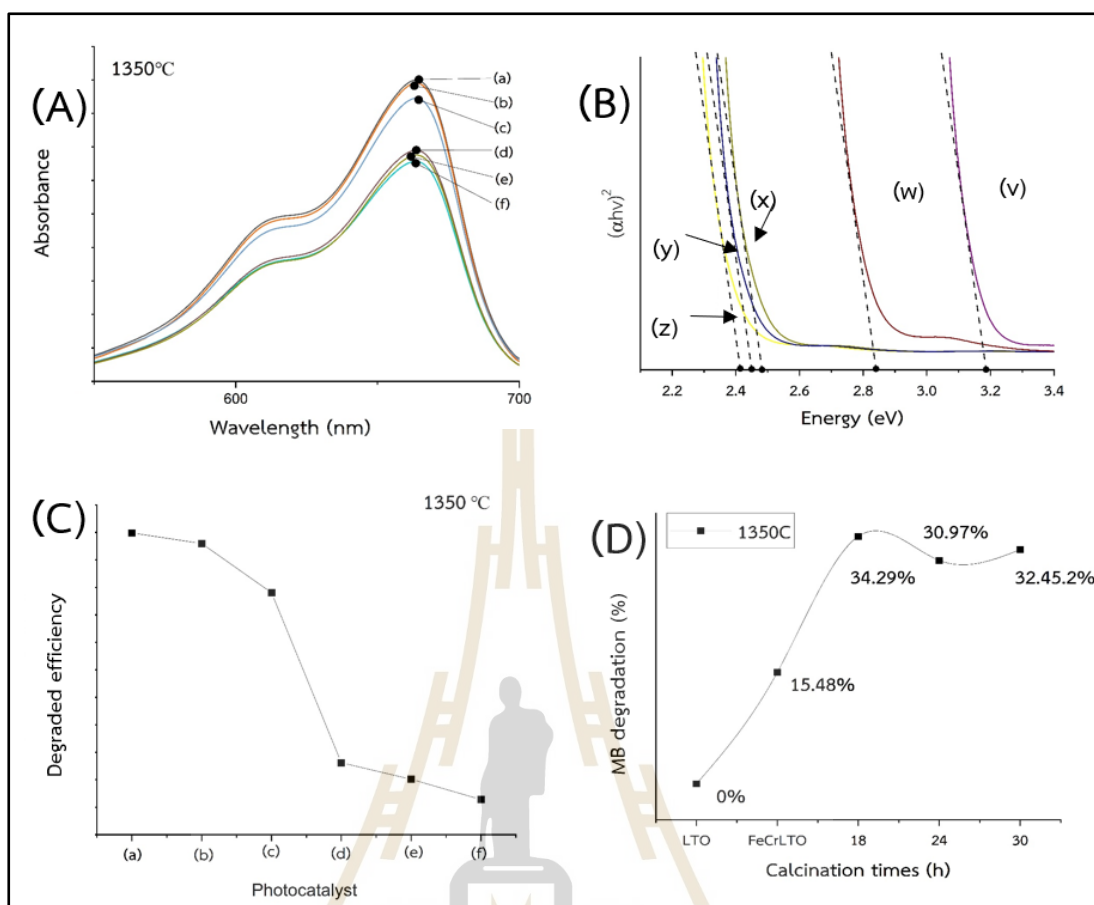
Figure 4.15 Calcination temperature at 1350°C (A) UV-Vis alnlysis (a) MB,
(b) LTO, (c) FeCrLTO, (d) FeCrLTO(N)1350_24h,
(e) FeCrLTO(N)1350_30h, and (f) FeCrLTO(N)1350_18h,
(B) Estimated band gap energy (v) Eg(LTO) ,(w) Eg (FeCrLTO),
(x) Eg(FeCrLTO(N)1350_24h), (y) Eg(FeCrLTO(N)1350_30h),
(z) Eg(FeCrLTO(N)1350_18h), (C) Degraded efficiency (a) MB, (b) LTO,
(c) FeCrLTO, (d) FeCrLTO(N)1350_24h,
(e) FeCrLTO(N)1350_30h and (f) FeCrLTO(N)1350_18h,
(D) Percentage of methylene blue

Figure 4.15 showed the MB degradation of calcination temperature at 1350°C, and when compared with various calcination times that the UV-Vis analysis found that the absorbance value from highest to lowest FeCrLTO(N)1350_24h, FeCrLTO(N)1350_30h, and FeCrLTO(N)1350_18h which were 0.69, 0.67, 0.65 respectively as shown in Figure 4.15(A) : (d)-(f), and also Eg correspondences were 2.48, 2.45,and 2.41eV,respectively, as shown

Figure 4.15(B): (x(-(z). In addition to decreasing Eg, calcination temperature at 1350°C for 18h occurred the oxygen deficiency at high temperature which increase opportunity of nitrogen substitution but it not over reaction, for calcination time 24h was Eg dressing because of bonding reaction with atmosphere occurrence.

According to bonding reaction with atmosphere, Hashizume & Hasegawa found that, annealing AlGaN thin film could be lost nitrogen atoms on surface because the nitrogen atoms reacted with each other or with oxygen atoms (oxidation) to form volatile molecules such as NO_x. (Hashizume & Hasegawa, 2004)

4.7   Effect of calcination times on FeCrLTO(N)
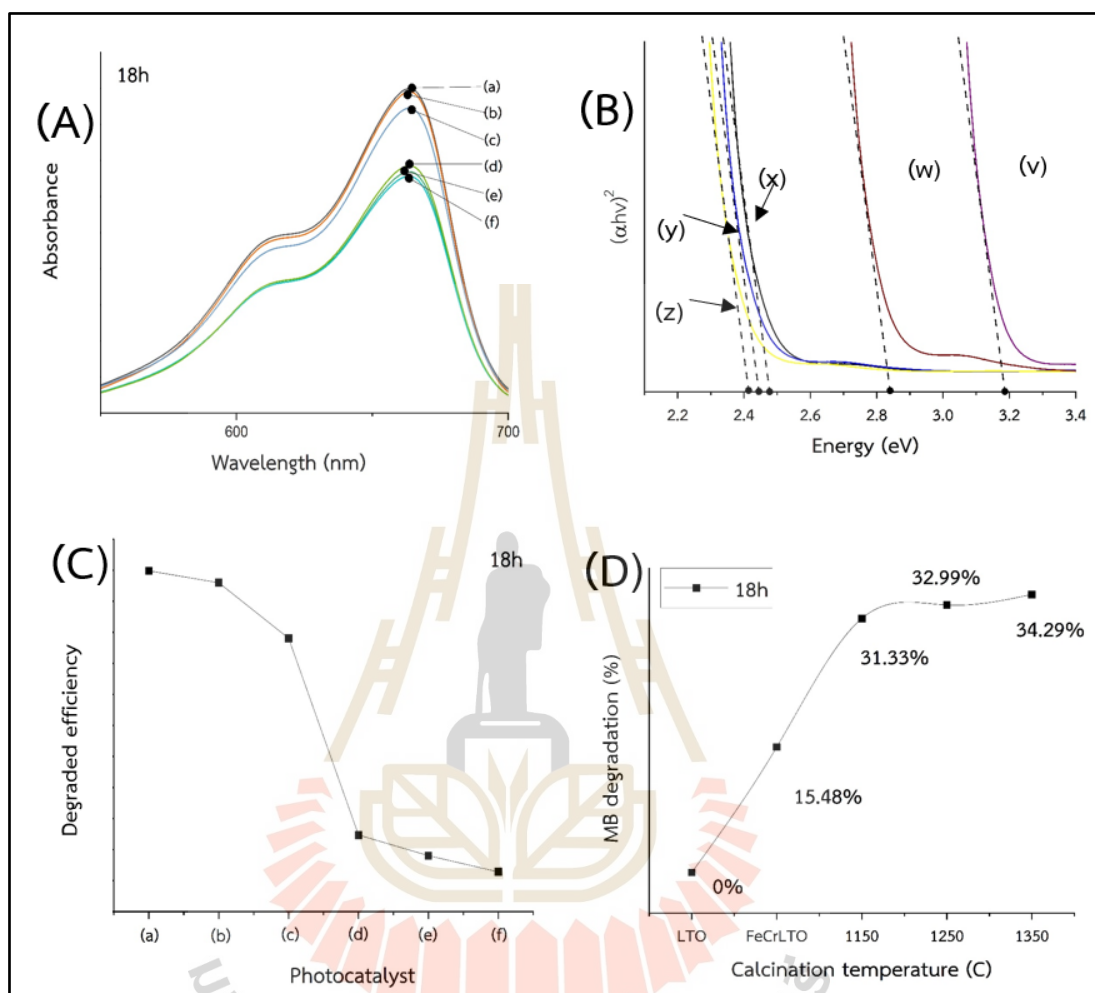
Figure 4.16 Calcination times at 18h (A) UV-Vis alnlysis (a) MB, (b) LTO,
(c) FeCrLTO, (d) FeCrLTO(N)1150_18h, (e) FeCrLTO(N)1250_18h,
and (f) FeCrLTO(N)1350_18h, (B) Estimated band gap energy
(v) $Eg_{(LTO)}$,(w) $Eg_{(FeCrLTO)}$, (x) $Eg_{(FeCrLTO(N)1150\_18h)}$, (y) $Eg_{(FeCrLTO(N)1250\_18h)}$,
(z) $Eg_{(FeCrLTO(N)1350\_18h)}$, (C) Degraded efficiency (a) MB, (b) LTO,
(c) FeCrLTO, (d) FeCrLTO(N)1150_18h, (e) FeCrLTO(N)1250_18h
and (f) FeCrLTO(N)1350_18h, (D) Percentage of methylene blue

Comparing calcination time at 18h with various temperature was 1150, 1250 and
1350℃, for observing doping nitrogen exhibited that, the increasing of calcination
temperature was effected to Eg led to narrow Eg, and the percentage of degradation

was high, as shown Figgure 4.16(B): (x)-(z). Noticeably, the absorption values were 6.8, 6.7, 6.5 of FeCrLTO(N)1150_18h, FeCrLTO(N)1250_18h and FeCrLTO(N)1350_18h, respectively, as shown Figure 4.16(A): (d)-(f), for estimated Eg values were 2.47eV, 2.44eV, and 2.41eV for FeCrLTO(N)1150_18h, FeCrLTO(N)1250_18h, and FeCrLTO(N)1350_18h, respectively. Consequently, increasing temperature might occur oxygen deficiency and incorporated nitrogen atoms in LTO lattice. The nitrogen substitution took place oxygen atoms in TiO_6 octahedral site. (Wang et al., 2013)
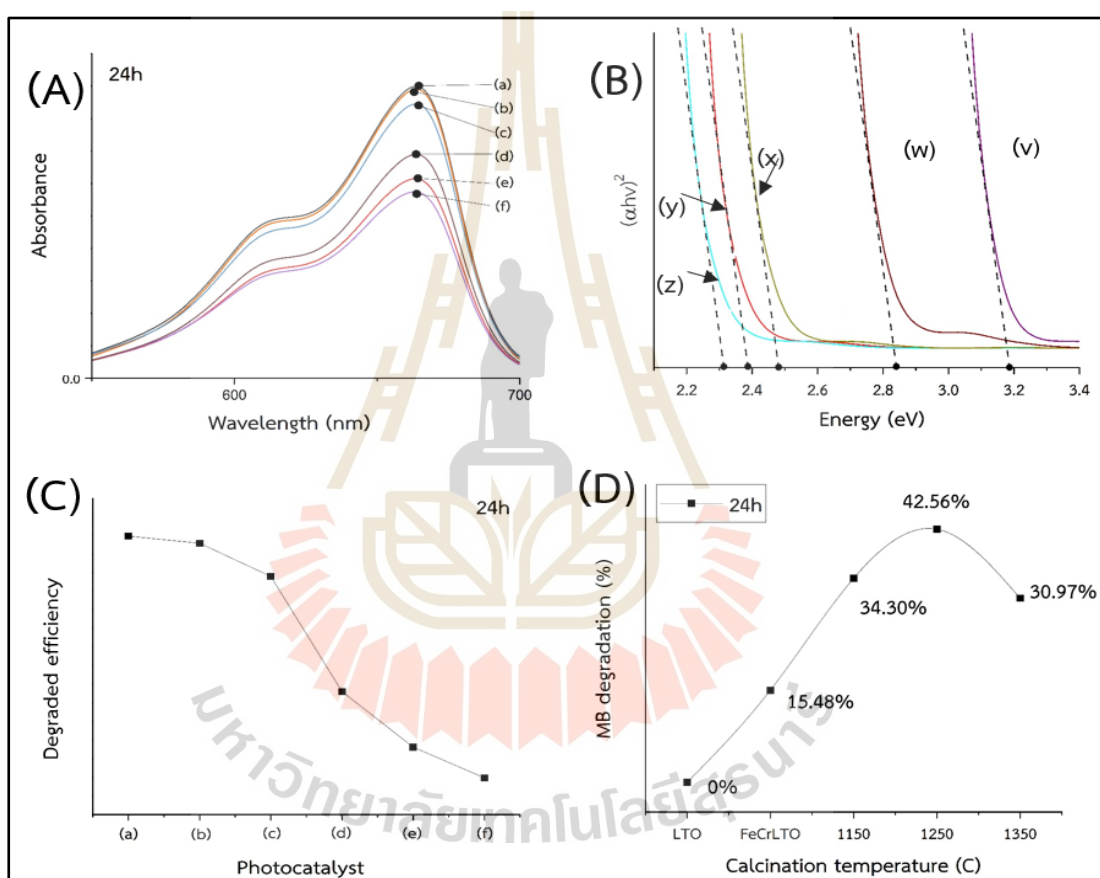
Figure 4.17 Calcination times at 24h (A) UV-Vis alnlysis (a) MB, (b) LTO, (c) FeCrLTO, (d) FeCrLTO(N)1350_24h, (e) FeCrLTO(N)1150_24h, and (f) FeCrLTO(N)1250_24h, (B) Estimated band gap energy, (v) Eg(LTO), (w) Eg(FeCrLTO), (x) Eg(FeCrLTO(N)1350_24h), (y) Eg(FeCrLTO(N)1150_24h), (z) Eg(FeCrLTO(N)1250_24h), (C) Degraded efficiency (a) MB, (b) LTO, (c) FeCrLTO, (d) FeCrLTO(N)1350_24h,(e) FeCrLTO(N)1150_24h and (f) FeCrLTO(N)1250_24h, (D) Percentage of methylene blue

Figure 4.17 showed calcination times at 24h with various temperatures were FeCrLTO(N)1350_24h, FeCrLTO(N)1150_24h and FeCrLTO(N)1250_24h that the absorbance value were 0.69, 0.61, and 0.57, repectively see in Figure 4.17(C) The Eg values of FeCrLTO(N)1350_24h, FeCrLTO(N)1150_24h, and FeCrLTO(N)1250_24h were 2.39, 2.31, 2.48eV, respectively, see in Figure 4.17(B): (w)-(z). Obviously, doping nitrogen of FeCrLTO(N)1250_24h was lowest of Eg obtaining high photocatalytic activity for MB degradation increased to 42.56% because of the optimized nitrogen substitution in this system.
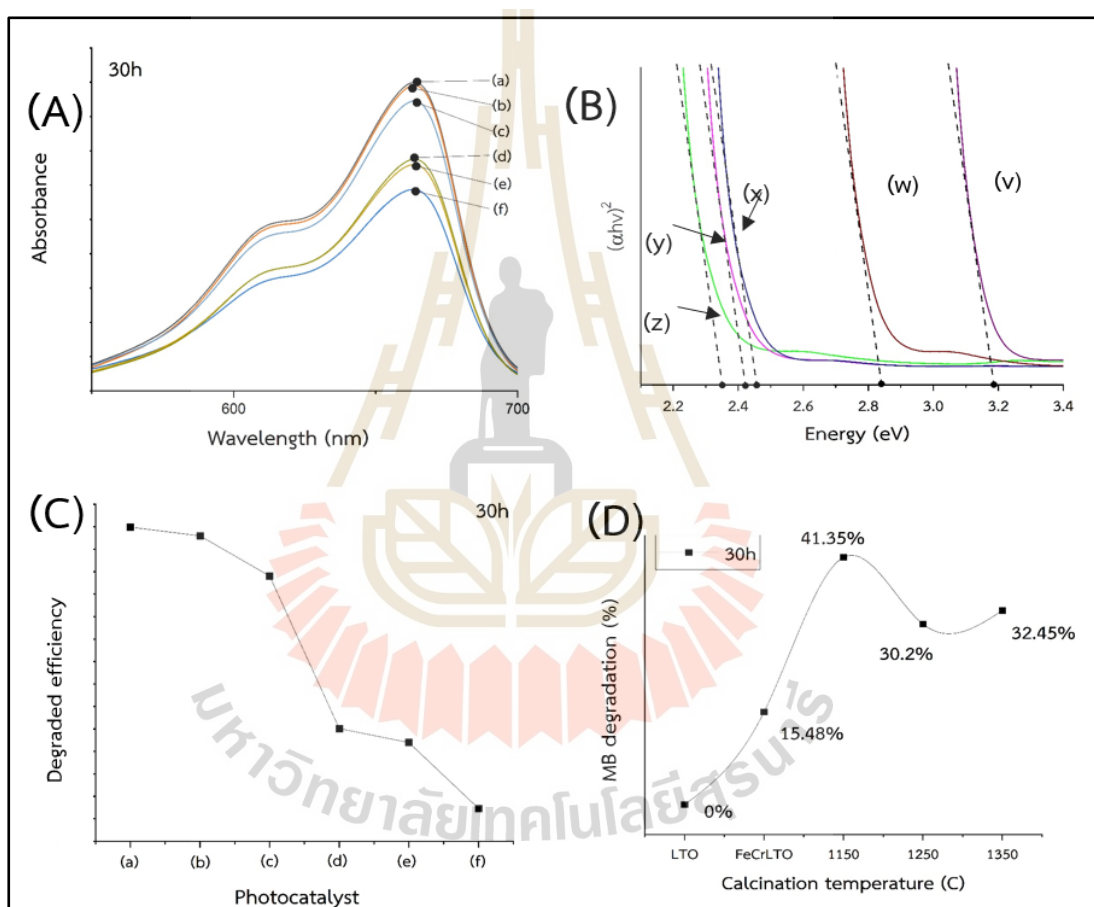
Figure 4.18 Calcination times at 30h **(A)** UV-Vis alnlysis (a) MB, (b) LTO,
(c) FeCrLTO, (d) FeCrLTO(N)1350_30h, (e) FeCrLTO(N)1250_30h,
and (f) FeCrLTO(N)1150_30h, **(B)** Estimated band gap energy (v)
Eg $_{(LTO)}$, (w) Eg $_{(FeCrLTO)}$, (x) Eg $_{(FeCrLTO(N)1350\_30h)}$, (y) Eg $_{(FeCrLTO(N)1250\_30h)}$,
(z) Eg $_{(FeCrLTO(N)1150\_30h)}$, **(C)** Degraded efficiency (a) MB, (b) LTO, (
c) FeCrLTO, (d) FeCrLTO(N)1350_30h, (e) FeCrLTO(N)1250_30h,
and (f) FeCrLTO(N)1150_30h, **(D)** Percentage of methylene blue

For comparing calcination times at 30h with various calcination temperature were FeCrLTO(N)1350_30h, FeCrLTO(N)1250_30h and FeCrLTO(N)1150_30h that the absorbance was 0.67, 0.65, and 0.58, as shown Figure 4.18(A) and (C), respectively. The Eg values were 2.35, 2.42 and 2.41eV for FeCrLTO(N)1350_30h, FeCrLTO(N)1250_30h and FeCrLTO(N)1150_30h, respectively, as shown Figure 4.18(B). Herein, FeCrLTO(N)1150_30h obtained lowest Eg because the calcination temperature at 1150°C for 30h found that the XRD pattern was shown $La_4Ti_3O_{12}$ which obtained heterojunction with $La_2Ti_2O_7$ further the calcination time was increased to 30h enhancing nitrogen substitution as narrow Eg. The percentage of degradation was 41.35, 30.2 and 32.45 for FeCrLTO(N)1150_30h, FeCrLTO(N)1250_30h, and FeCrLTO(N)1350_30h, respectively. The percentage of degradation for FeCrLTO(N)1250_30h decreased from 41.35 to 30.2% that it occurs lost nitrogen in lattice due to high temperature and long calcination time. FeCrLTO(N)1350_30h could increase the percentage of degradation because it was new phase formation on compound which was from decomposition of $La_4Ti_3O_{12}$ and $La_2Ti_2O_7$ but it could not detect from XRD analysis.

4.8 The highest degradation of methylene blue at different times
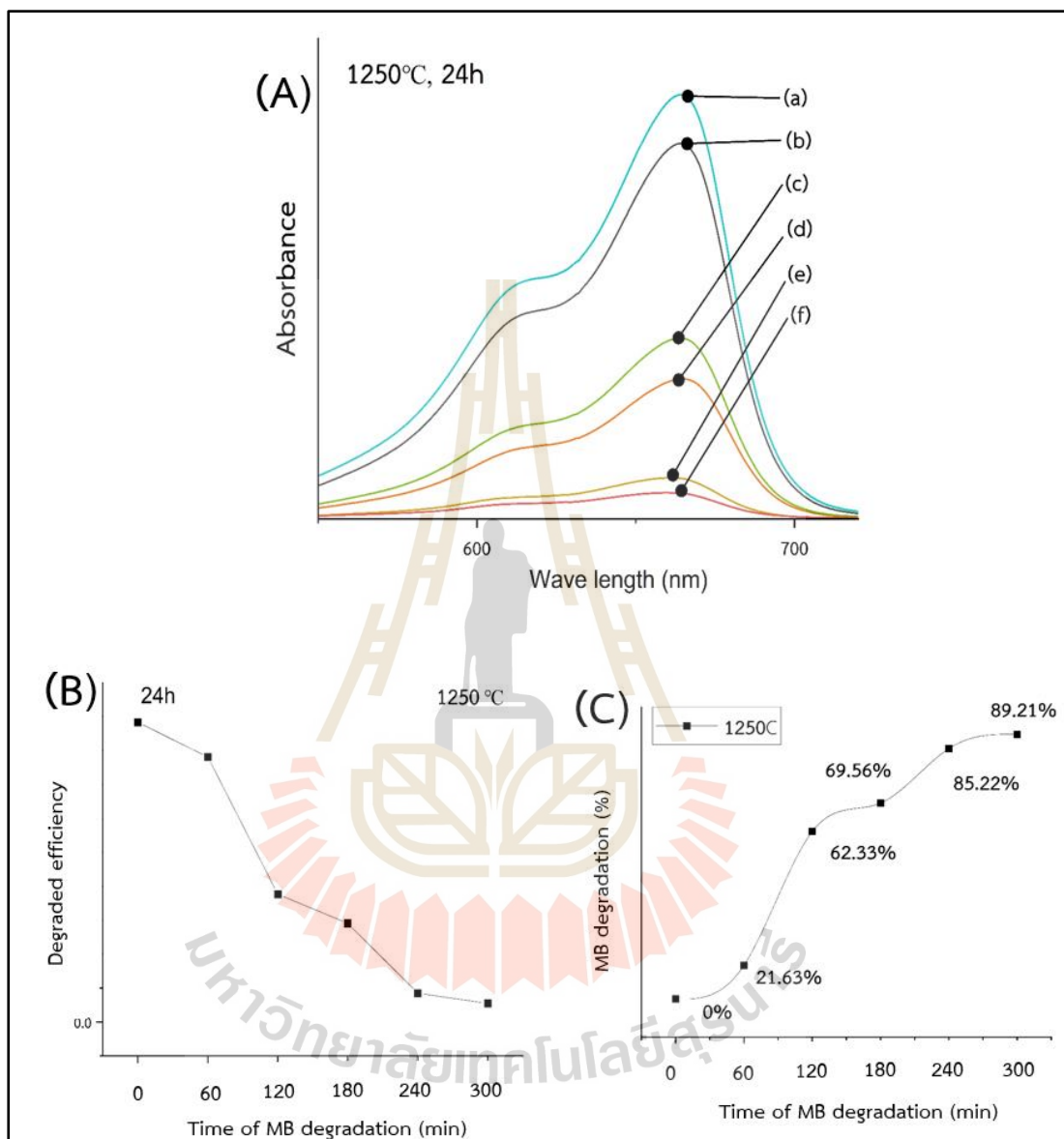
Figure 4.19 FeCrLTO(N)1250_24h for 0.2 g (a) 0 min, (b) 60 min, (c) 120 min,
(d) 180 min, (e) 240 min and (f) 300 min

The highest photocatalytic activity was obtained from FeCrLTO(N)1250_24h, and increasing amount of powder was 0.2 g to test photocatalytic activity. The result of photocatalytic test was appeared increasing photocatalytic more than 89% at

300 min which caused the increased amount of powder employing short time to MB degradation, as shown Figure 4.19 (A)-(C).

4.9 Bonding and compound analysis

Bonding detection was determined by X-ray photo electron (XPS) that this technique could determine the bonding compound and was employed to determine atoms substitution.

The XPS analysis for calcination temperature at 1150°Cfor various calcination times were shown $T2p_{1/2}$ at higher energy, $T2_{3/2}$ at lower energy, O1s, and N1s, as shown Figure 4.20 (A)-(C).

Figure 4.20 (A) for 18h was shown the binding energy was $T2p_{1/2}$ and $T2p_{3/2}$ which was 464.4 and 458.7 eV, respectively, and $T2p_{1/2}$ and $T2p_{3/2}$ of 24h was 465.2 and 459.3 eV occuering Ti-O bonding, for 30h had four different peak which $T2p_{1/2}$ was 465.4, 464.2 and $T2p_{3/2}$ was 459.6, 458.8 eV, respectively. At long calcination time enhanced oxygen deficiency as mentioned above. $T2p_{1/2}$ at 465.4 eV was Ti-O as TiO_{n-x}, oxygen deficiency, as shown Figgure 4.20 (A) 30h. (Pan, Yang, Fu, Zhang, & Xu, 2013)

O1s peak at 18h was shown two peaks 532.3 and 530.4eV which was Ti-O-N formation, the formation Ti-O-N was addition of nitrogen which could incorporated in lattice to become bonding due to nitrogen inside and nitrogen atmosphere reaction but it was small amount of Ti-O-N reaction. And also O1s peak at 24h revealed binging energy at 532.8 and 530.7 eV which was T-O, O1s peak at 30h was La-O at 533 eV and was 532.5 and 530.9 eV as Ti-O. Evidently, N1s counld not detect nitrogen as broad peak.
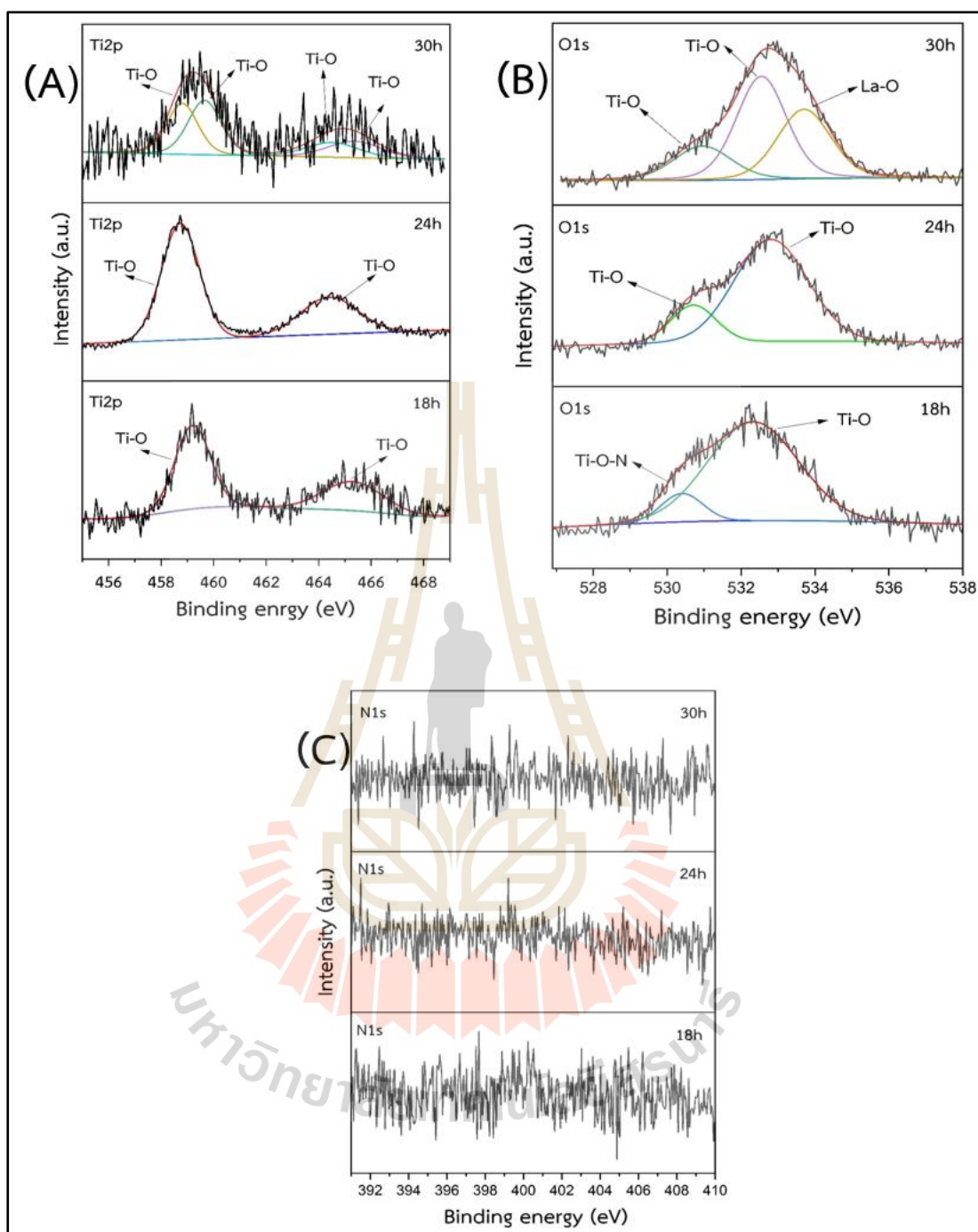
Figure 4.20 XPS analysis of calcination temperature at 1150°C for 18h,
24h and 30h (A) Ti2p (B) O1s (C) N1s

To investigate the calcination temperature at 1250°C with various calcination time, the at calcination time 18h was shown $T2p_{1/2}$ and $T2p_{3/2}$ which were 465.14 and

459.4 eV, respectively. Bonding $T2p_{1/2}$ and $T2p_{3/2}$ were Ti-O which was same bonding as calcination time at 24h: 465.08 and 459.4 eV for $T2p_{1/2}$ and $T2p_{3/2}$ as shown Figure 4.21 (A) and (C).

Additionally, calcination time at 24h found that several bond structures were 464.6 ($T2p_{1/2}$), 461.7 ($T2p_{1/2}$), 458.8 ($T2p_{3/2}$), 457.19 ($T2p_{3/2}$) and 454.5eV ($T2p_{3/2}$) for T-O, Ti-N, Ti-O, Ti-O-N, Ti-N, respectively, as shown Figure 4.21(B).

For binding energy of O1s was 533.5, 531.5, 530.5 eV for La-O, TiO, and Ti-O-N, respectively. Evidently, binding energy at 530.5 eV exhibited Ti-O-N structure but it was not shown in Ti2p that it might be small amount of Ti-O-N occurrence to determine inaccuracy.

Binding energy of N1s was 18 and 30h could not be detected but at 24h exhibited Ti-O-N at 397.09 eV which occurred nitrogen atoms substitution on oxygen atom in TiO_6 sharing on corner octahedral site. (Wang et al., 2021)
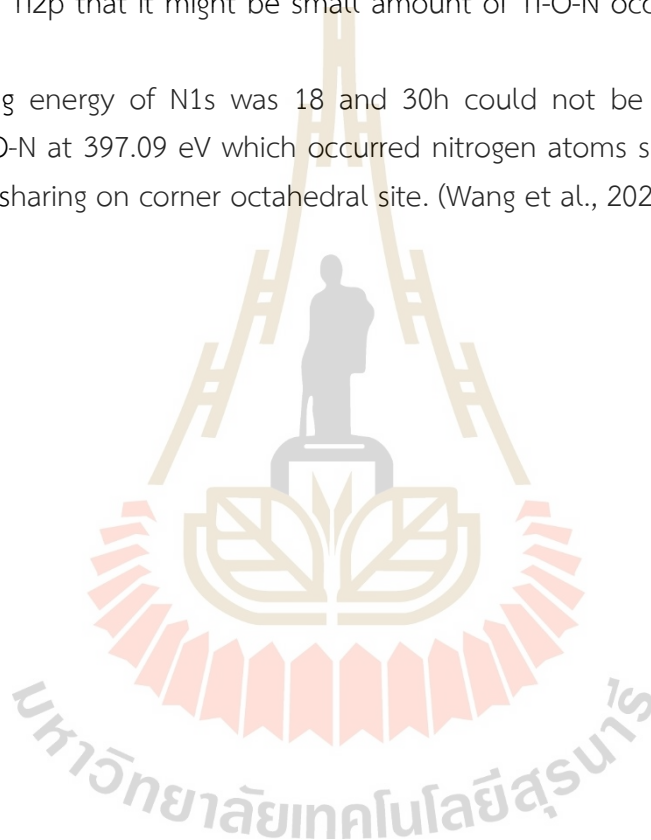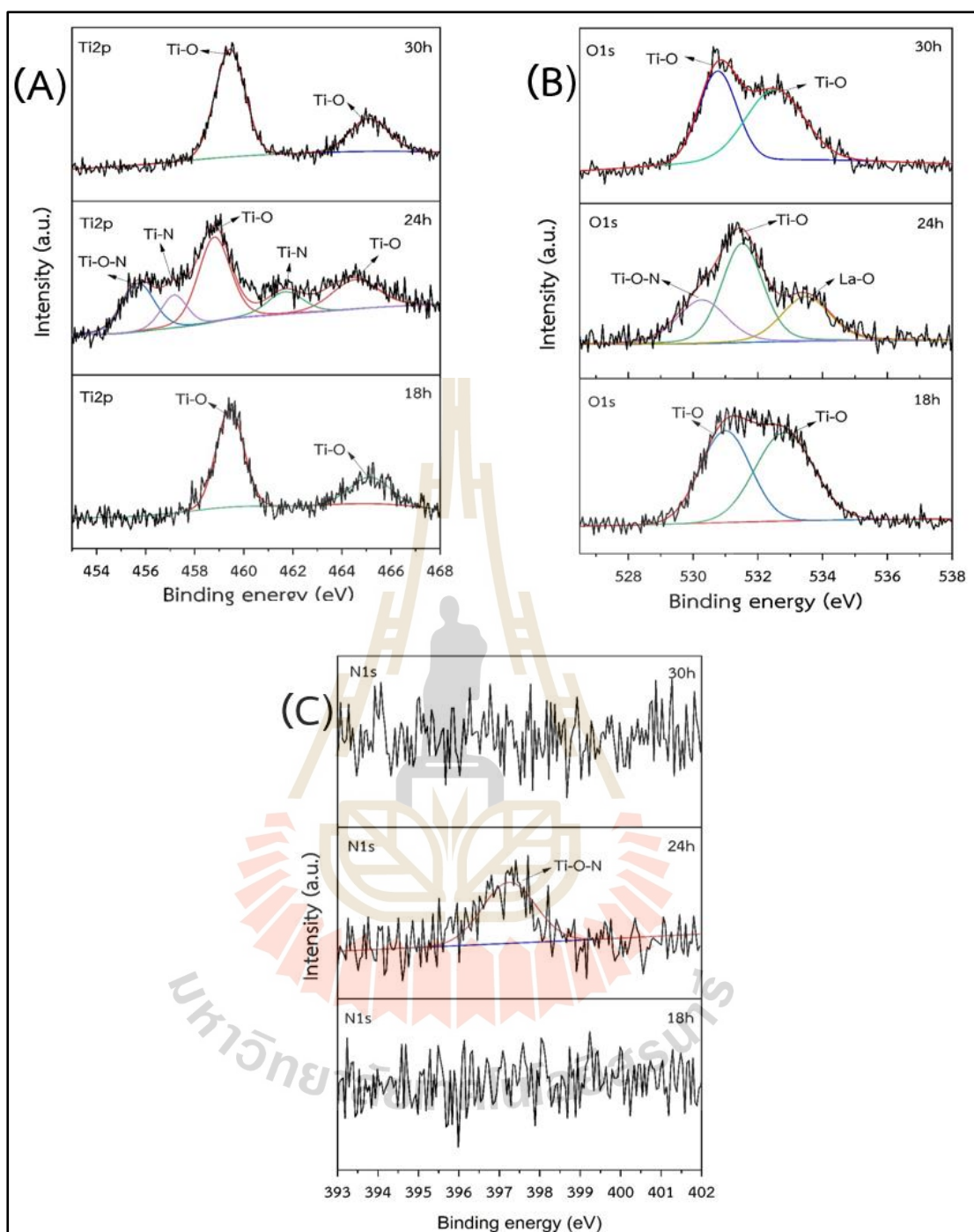
Figure 4.21 XPS analysis of calcination temperature at 1250°C for 18h,

24h and 30h (A) Ti2p (B) O1s (C) N1s
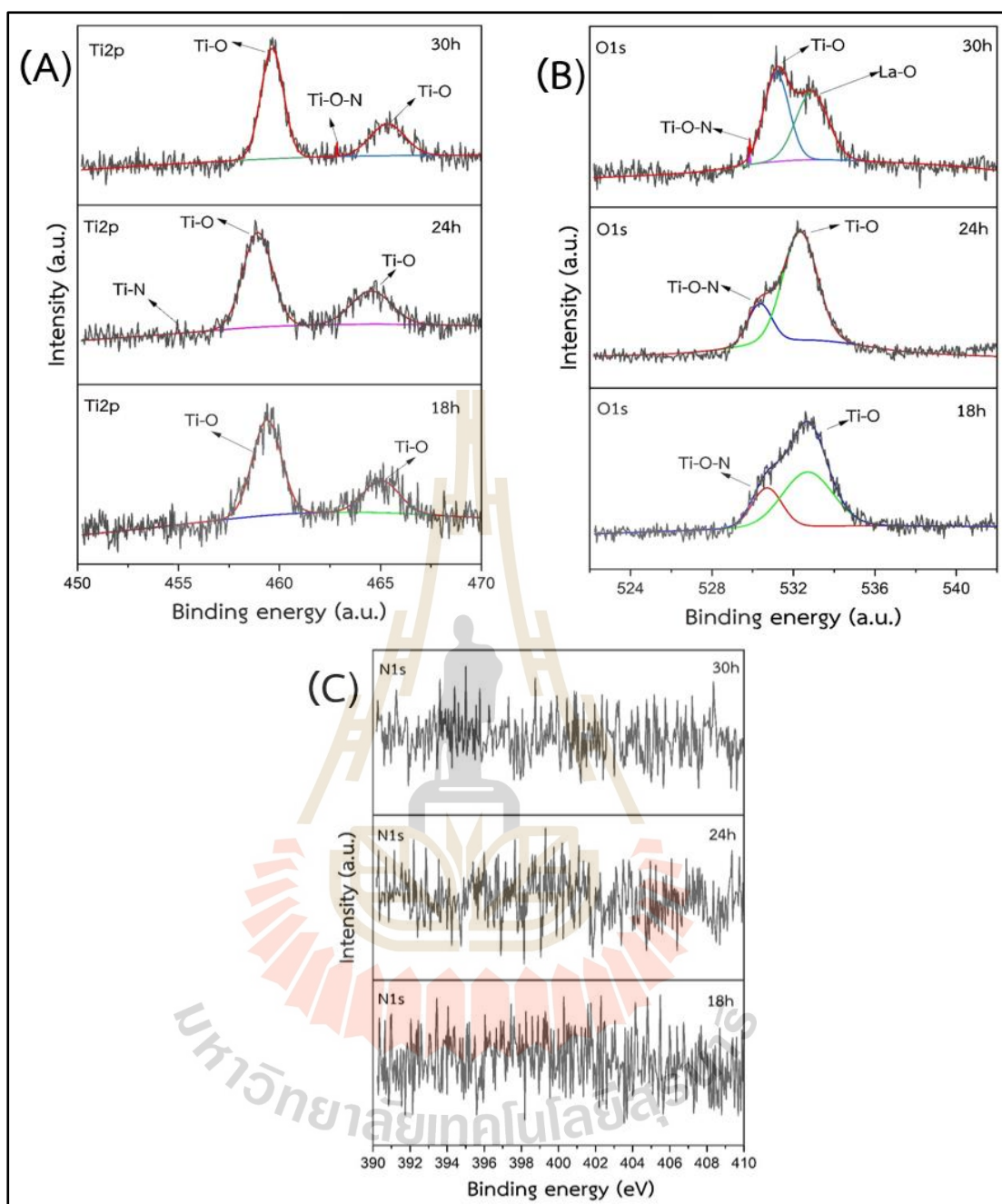
Figure 4.22 XPS analysis of calcination temperature at 1350°C for 18h,
24h and 30h (A) Ti2p (B) O1s (C) N1s

Binding energy of calcination temperature at 1350°C with various temperature, the calcination time at 18h was 465.1 and 459.4 eV for T2p$_{1/2}$ (Ti-O) and T2p$_{3/2}$ (Ti-O), respectively, as shown Figure 4.22 (A). Figure 4.22 (A) at 24 was shown T2p$_{1/2}$, T2p$_{3/2}$ and T2p$_{3/2}$ for 464.5, 458.9 and 454.6 eV that the bonding structure was Ti-O, Ti-O and

Ti-N (residual reaction), respectively. For binding energy Ti2p at 30h showed T2p$_{1/2}$, T2p$_{1/2}$ and T2p$_{3/2}$ which were 465.2, 462.8 and 459.5 eV.

Binding energy of O1s at 18h was shown 532.7 and 530.7 eV for T-O (TiO$_{2-x}$) which was oxygen deficiency, and at 24h was 532.3 and 530.4 eV which was Ti-O-N formation. Binding energy at 30h of O1s was 532.8, 531.1, and 529.8 eV for bonding structure was Ti-O, Ti-O and Ti-O-N, respectively, as shown Figure 4.22 (B)

Binding energy of N1s could not be detected on XPS analysis. Limitation of XPS could not detect on surface that it could not analyze in depth. To solve the problem, Photo emission electrons (PES) was introduced to determine the nitrogen substitution analysis

4.10 Nitrogen substitution analysis

Photo emission electrons (PES) was employed to determine light weight element that the XAS could not be detected because the XAS had high energy which did not detect light weight element. The limitation XAS change to PES for detect light weight element at K edge.

Comparing with nitrogen N-K edge could determine nitrogen in lattice and indicated bond structure, N-K edge was sort of low to high (a) LTO, (b) FeCrLTO, (c) FeCrLTO(N)1350_24h, (d) FeCrLTO(N)1150_18h, (e) FeCrLTO(N)1350_30h, (f) FeCrLTO(N)1250_18h, (g) FeCrLTO(N) 1250C 30h, (h) FeCrLTO(N) 1350_18h, (i) FeCrLTO(N)1150C_24h, (j) FeCrLTO(N) 1150_30h and (k) FeCrLTO(N)1250_24h, as shown 4.23.

Some peaks of N-K edge did not show on pattern but it could employ derivative photon energy for clearly determination, as shown Figure 4.24.

Evaluation N1s by XPS of calcination temperature at 1150°C for 24h, and 30h could not be detected but PES analysis demonstrated that N-K edge determined nitrogen that the bonding structure was N-Ti-O and Tl-(N-O), as shown Figure 4.23 (i) and (j). (Meng et al., 2012)
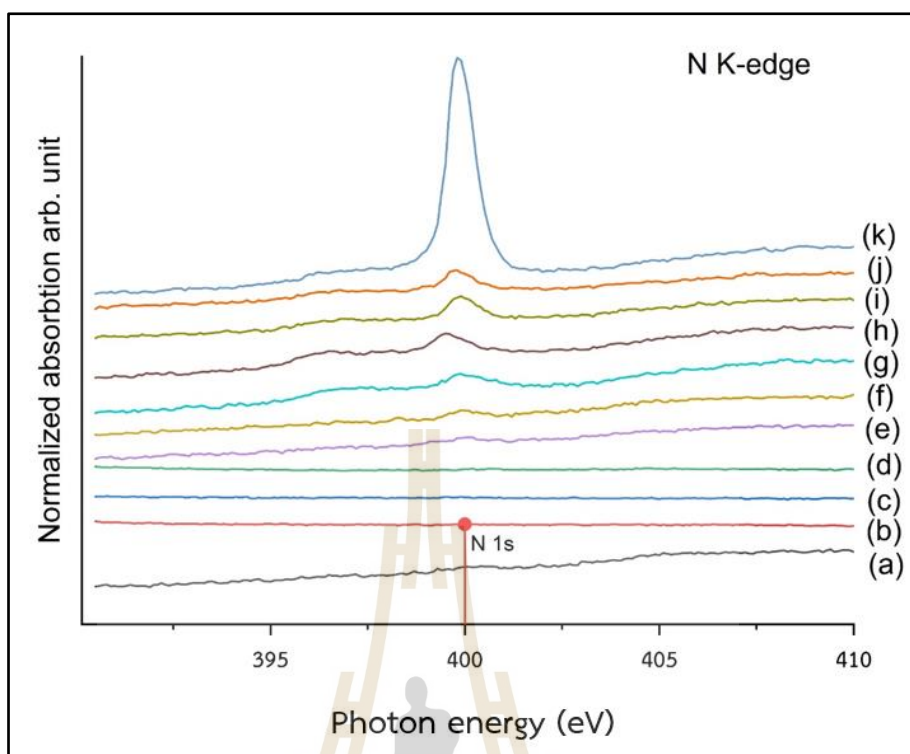
Figure 4.23 PES N-K edge (a) LTO, (b) FeCrLTO, (c) FeCrLTO(N)1350_24h, (d) FeCrLTO(N)1150_18h, (e) FeCrLTO(N)1350_30h, (f) FeCrLTO(N)1250_18h, (g) FeCrLTO(N) 1250C 30h, (h) FeCrLTO(N) 1350_18h, (i) FeCrLTO(N)1150C_24h, (j) FeCrLTO(N) 1150_30h and (k) FeCrLTO(N)1250_24h
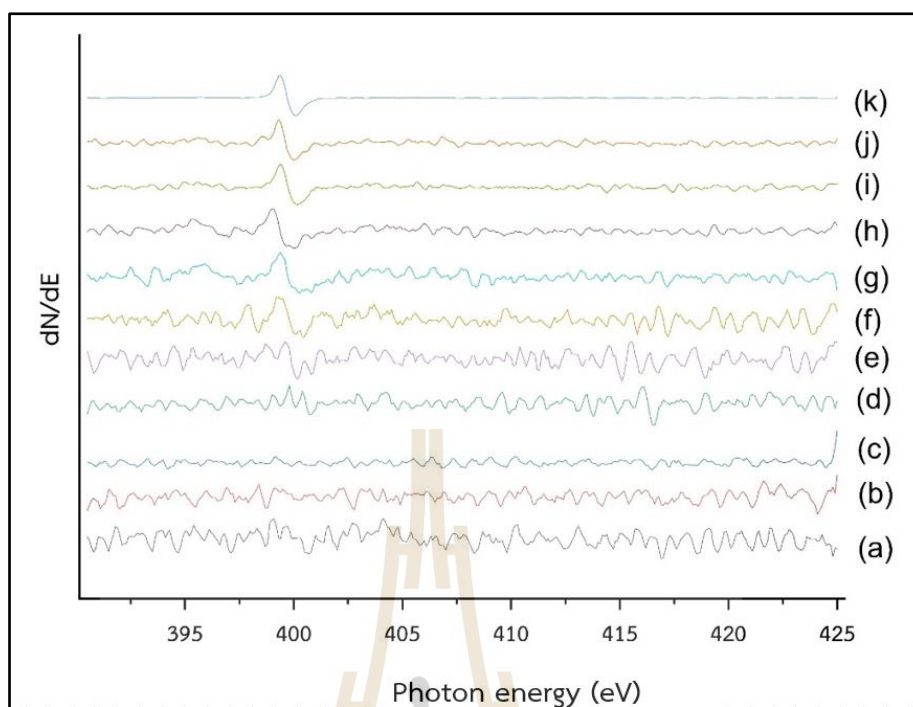
Figure 4.24 Derivative photon energy FeCrLTO(N) (a) LTO, (b) FeCrLTO,
(c) FeCrLTO(N)1350_24h, (d) FeCrLTO(N)1150_18h,
(e) FeCrLTO(N)1350_30h, (f) FeCrLTO(N)1250_18h,
(g) FeCrLTO(N)1250_30h, (h) FeCrLTO(N)1350_18h,
(i) FeCrLTO(N) 1150_24h, (j) FeCrLTO(N)1150_30h and
(k) FeCrLTO(N)1250_24h
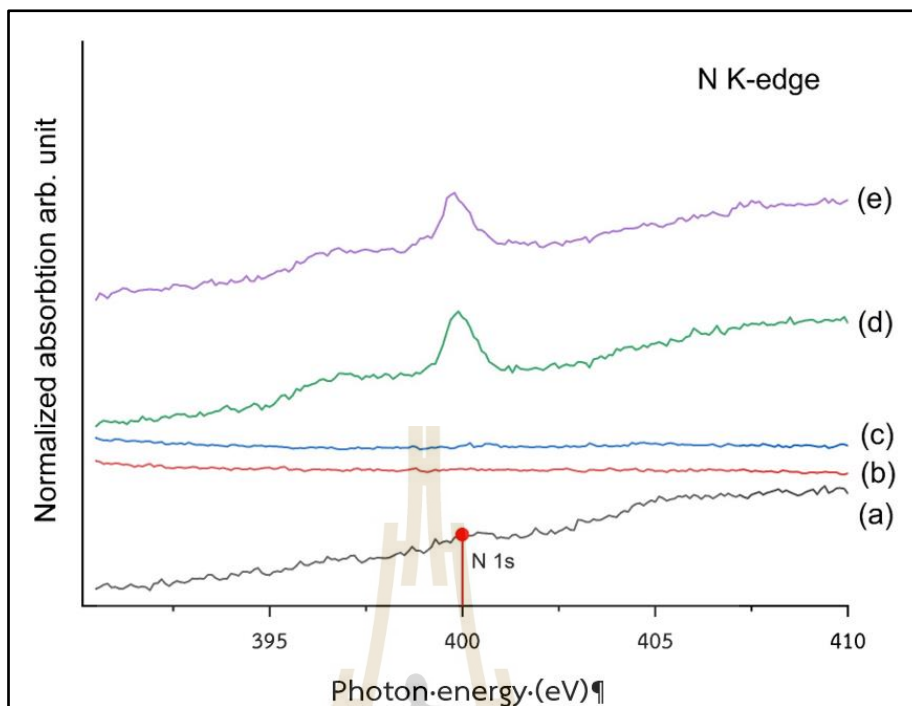
Figure 4.25 (a) LTO, (b) FeCrLTO, (c) FeCrLTO(N) 1150℃ 18h,
(d) FeCrLTO(N)1150_ 24h and (e) FeCrLTO(N)1150_30h

On XPS analysis, calcination temperature at 1150℃ for 18, 24 and 30h exhibited broad peak but PES analysis was shown nitrogen at 24, and 30h as Figure 4.25 (d) and (e). the bonding structure was N-Ti-O and TI-(N-O) for 397.3 and 399.9 eV, respectively.
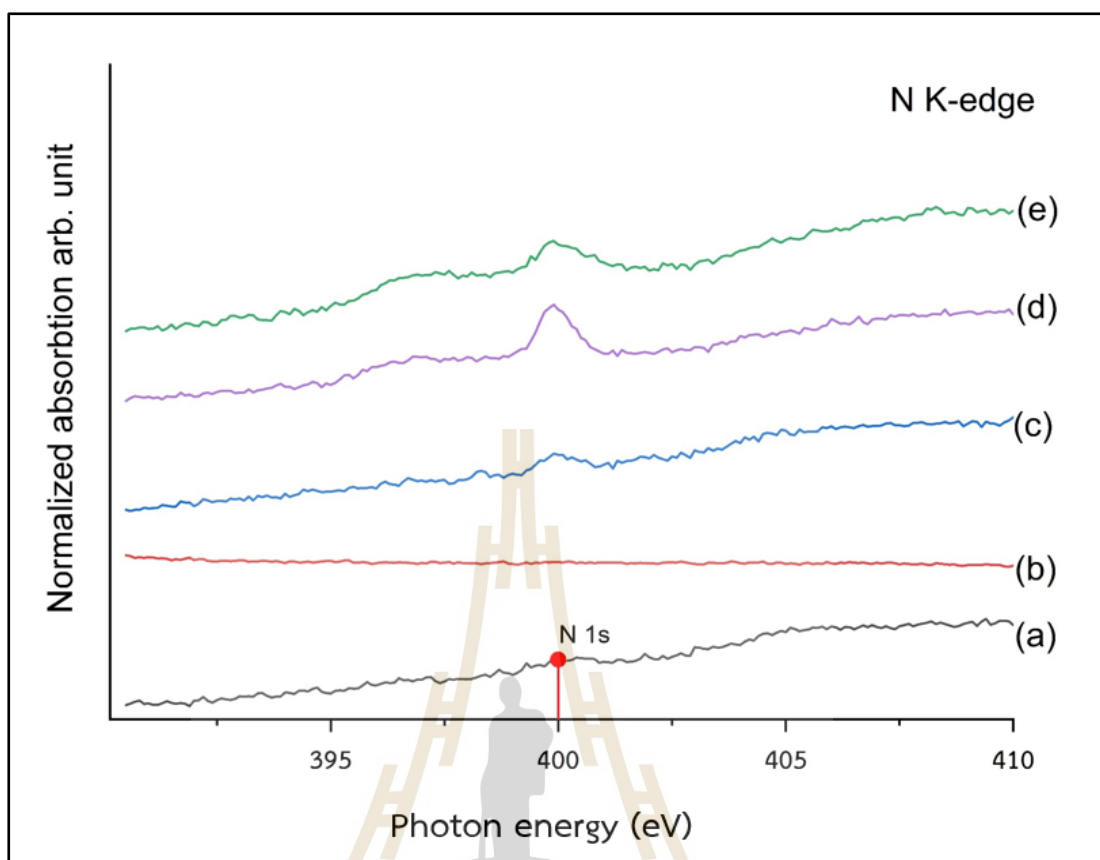
Figure 4.26 (a) LTO, (b) FeCrLTO, (c) FeCrLTO(N)1250_18h,
(d) FeCrLTO(N)1250_24h and (e) FeCrLTO(N)1250_30h

On XPS analysis could detect only FeCrLTO(N)1250_24h for N1s at 397.09 (Ti-O-N), and PES analysis found that FeCrLTO(N)1250_24h had another peak at 399.9 eV for Ti-(N-O). Additionally, FeCrLTO(N)1250_18h and FeCrLTO(N)1250_30h determining by PES analysis exhibited nitrogen which was N-Ti-O and Ti-(N-O) at 397.1 and 399.7.
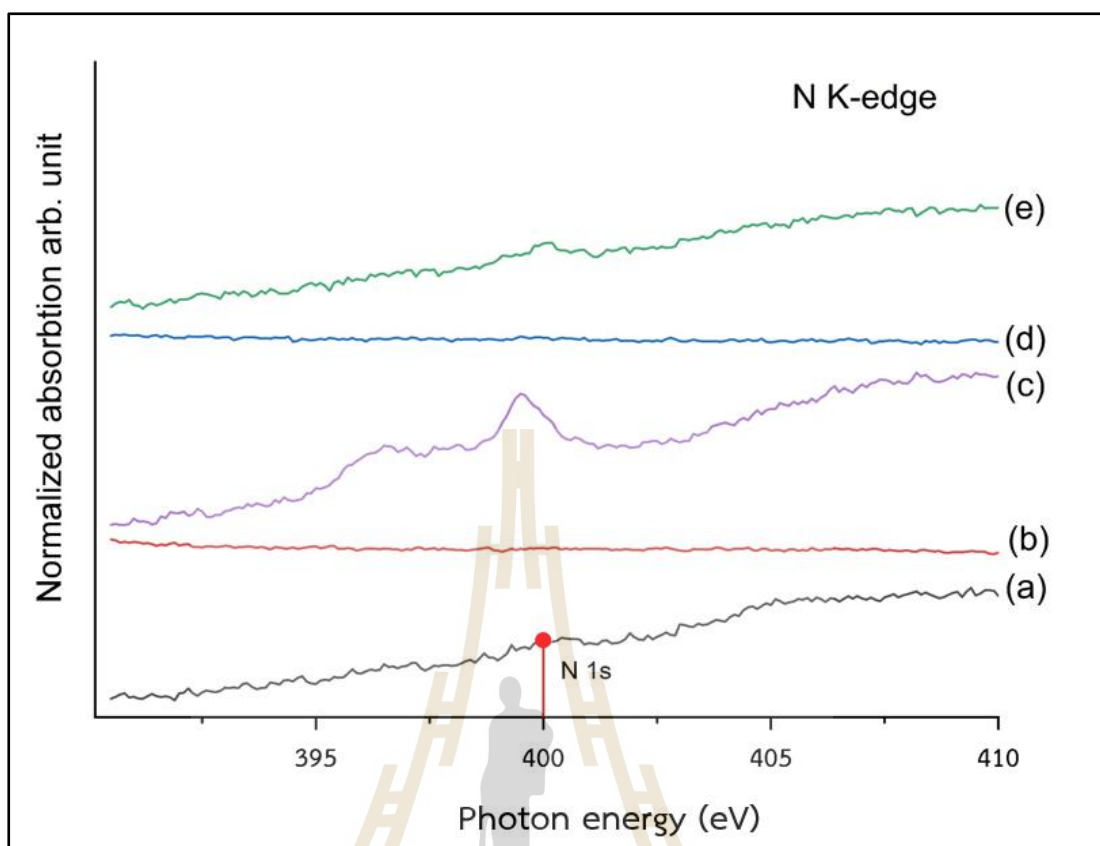
Figure 4.27 (a) LTO, (b) FeCrLTO, (c) FeCrLTO(N)1350_18h, (d) FeCrLTO(N)1350_24h and (e) FeCrLTO(N)1350_30h.

To investigate on XPS for calcination temperature at 1350°C found that, the broad peak on N1s for 18, 24 and 30h, PES analysis could indicate N1s of FeCrLTO(N)1350_18h and FeCrLTO(N)1350_30h but did not find on FeCrLTO(N)1350_24h, as shown Figure 4.27(c)-(e). For FeCrLTO(N)1350_18h assigned 397.2 and 399.8eV which was N-Ti-O and Ti-(N-O), respectively, FeCrLTO(N)1350_30h assigned 399.9eV which was Ti-(N-O).

For investigation, PES analysis of all sample were substitution due to the binding energy were not over 400eV. Binding energy was more than 400eV becoming nitrogen interstitial site in lattice that the binding energy was 399.5-399.9 and 397.0-397.5eV which were N-Ti-O and Ti-(N-O), respectively, and it located substitutional site.
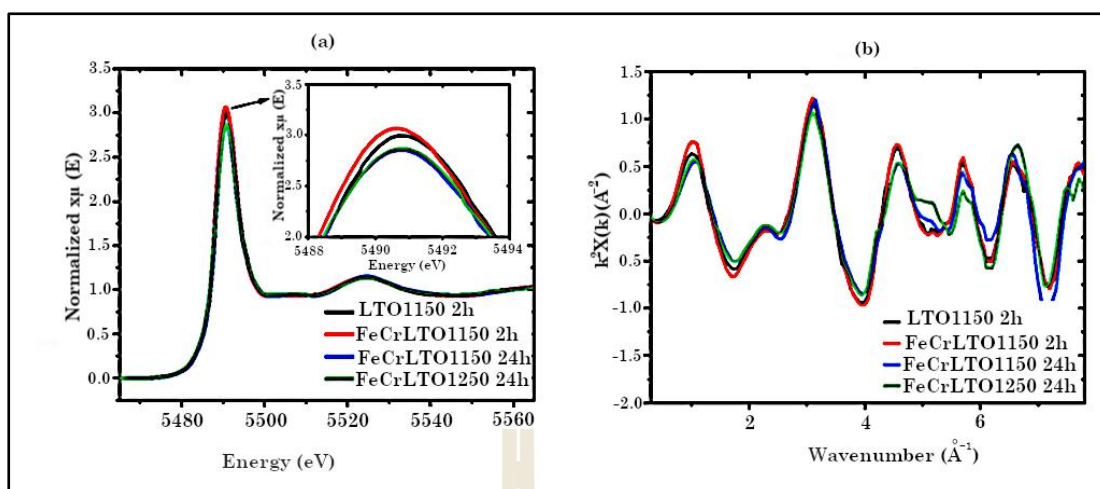
Figure 4.28 La L$_3$-edge XANES spectra of synthesized photocatalysts and
the magnification of the white line region (a). The
unsmoothed k^3-weighted of La L$_3$-edge EXAFS of synthesized
photocatalysts (b).

XAS analysis was performed to investigate the electronic structure and local
structure of synthesized La$_2$Ti$_2$O$_7$ photocatalysts. The XANES spectra of La L$_3$-edge of
all samples were shown similar feature but different in terms of peak height (Figure
4.28). The white line (5490.82 eV) observed in the La L$_3$-edge spectra described the
origin of electric transition of 2p$_{3/2}$ electrons to the 5p or 5d state. The strong and
symmetrical white line indicated that was no deformation of the local structure. The
EXAFS k^2 weight spectra (Figure 4.28(b)) supported the XANES results, demonstrating a
similar k^2 weight patterns. The FeCrLTO1150_2h sample had the highest white line
intensity (Figure 4.28 (b)), while the FeCrLTO1250_24h and FeCrLTO1150_24h had the
lowest intensity. These findings imply that the co-doping of Fe and Cr in the La$_2$Ti$_2$O$_7$
structure in different temperature could impact the p-d hybridization by modifying the
local electronic structure of the surrounding oxygen atoms and transition metal ions.
Ti K-edge spectrum of all synthesized La$_2$Ti$_2$O$_7$ photocatalysts show the similar
spectrum feature. The absorption edge position (4981.91eV) remained unchanged,
signifying that the valence state of Ti did not alter as a consequence of calcination
process. The oxidation state of all samples is in the form of Ti^{4+}. All samples shared
the same white line position of 4985.37 eV attributing to the 1s to 3p (or 4p) states
dipole transitions. The height of this peak was generally related to the unoccupied
orbital. FeCrLTO1150_2h sample showed highest intensity, which means the highest

unoccupied p orbital, while FeCrLTO1250(N)_24h had the lowest intensity. This suggests that doping Fe and Cr into $La_2Ti_2O_7$ at 1250°C in an N_2 atmosphere may have perturbed the occupancy of the electron p orbital (Figure 4.29).
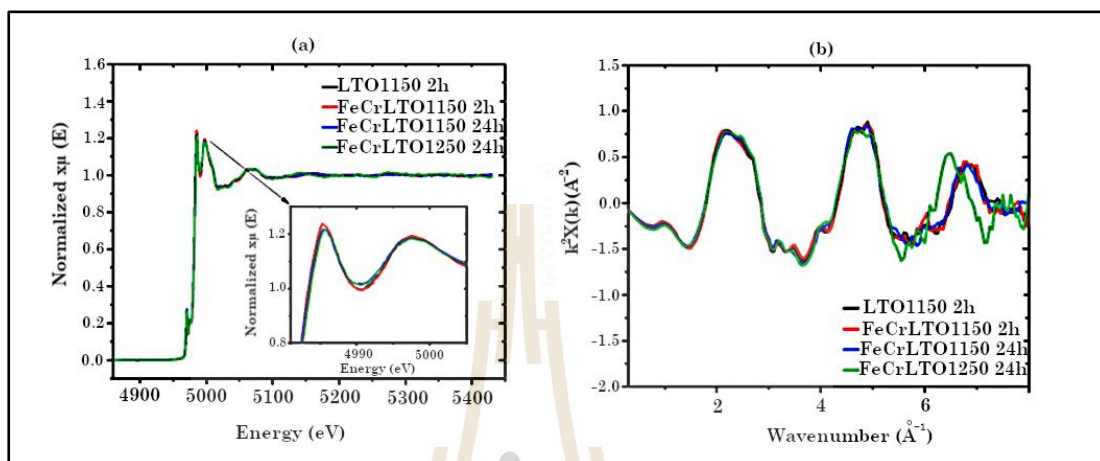
Figure 4.29. Ti K-edge XANES spectra of synthesized photocatalysts (a) and the magnification of the white line region. The unsmoothed k^3-weighted of Ti K-edge EXAFS of synthesized photocatalysts (b).

The Ti K-edge EXAFS functions in the K space and R space of synthesized photocatalysts are mostly aligned at the same position, except FeCrLTO(N)1250_24h which showed peak shift in k^2 weight space (Figure 4.29). These findings demonstrate a transformation of the local structures of Ti atoms in $FeCrLa_2Ti_2O_7$ structure.

Since the XRD patterns of the synthesized photocatalysts predominantly exhibited the $La_2Ti_2O_7$ structure, this structure was employed for the EXAFS fitting. The EXAFS best-fit parameters of LTO samples to $La_2Ti_2O_7$ were listed in Table 4.2.

Table 4.2 The EXAFS best-fit parameters of LTO samples.

Fit parameter			LTO1150 2h	FeCrLTO1150 2 h	FeCrLTO1150 24 h	FeCrLTO1250 24 h
R factor			0.00682	0.0080399	0.0080399	0.0081609
SO_2			0.873	0.873	0.873	0.814
Delta E_0			1.5534	0.978	0.978	2.032
R (A)	Ti-O1	N = 1	1.97097	1.98446	1.98861	2.02939
	Ti-O2	N = 1	2.14025	2.15250	2.12481	1.98773
	Ti-O3	N = 2	1.90673	1.90367	1.89527	1.94938
	Ti-O4	N = 1	2.29333	2.33259	2.33259	2.29319
	Ti-O5	N = 1	2.49690	2.53234	2.53304	2.47567
	Ti-La1	N = 1	3.42331	3.43370	3.46541	3.35690
	Ti-La2	N = 2	3.70544	3.53227	3.55604	3.73304
	Ti-La3	N = 1	3.48902	3.64860	3.67860	3.54595
	Ti-La4	N = 1	3.61854	3.43632	3.41716	3.36572
	Ti-La5	N = 1	3.38770	3.30016	3.28831	3.10888
	Ti-Fe	N=0.372	-	-	-	2.66832
	Ti-Cr	N=0.744	-	-	-	2.63988
$\sigma 2$	Ti-O1	N - 1	0.00286	0.00286	0.00286	0.00200
	Ti-O2	N = 1	0.00634	0.00634	0.00634	0.06340
	Ti-O3	N = 2	0.00554	0.00554	0.00554	0.00554
	Ti-O4	N = 1	0.00554	0.00554	0.00554	0.00554
	Ti-O5	N = 1	0.00443	0.00211	0.00211	0.00780
	Ti-La1	N = 1	0.00228	0.00027	0.00027	0.00340
	Ti-La2	N = 2	0.00645	0.00690	0.00690	0.00137
	Ti-La3	N = 1	0.00144	0.00645	0.00645	0.00399
	Ti-La4	N = 1	0.00690	0.00144	0.00144	0.00183
	Ti-La5	N = 1	0.00576	0.00690	0.00690	0.00003
	Ti-Fe	N=0.372	-	-	-	0.00555
	Ti-Cr	N=0.744	-	-	-	0.00842

The nearest neighbour atom of Ti corresponded to the oxygen in Ti-O shells with 6 coordination. The Ti-La shells also contained 6 coordinated atoms.
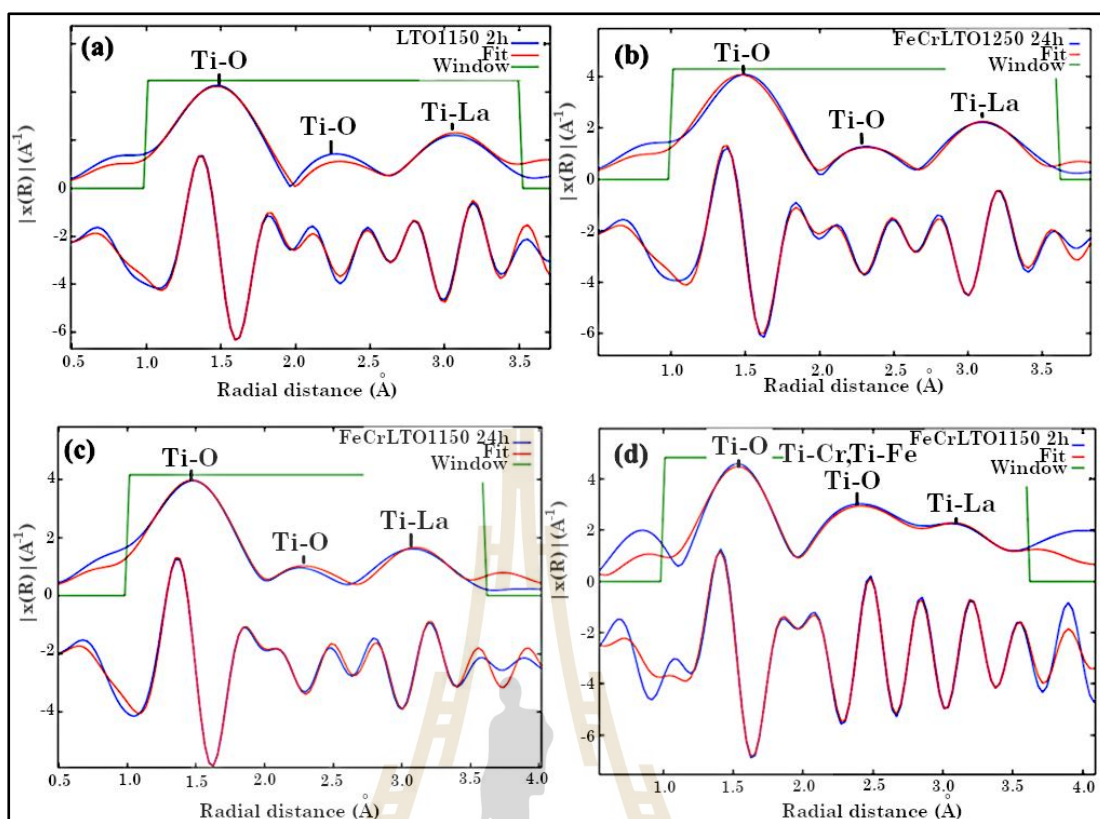
Figure 4.30 Ti K-edge EXAFS of synthesized photocatalysts with fits taken
from the $La_2Ti_2O_7$ model. (a) LTO1150_2h, (b) FeCrLTO1150_2h,
(c) FeCrLTO1150_24h, (d) FeCrLTO1250_24h. Upper graph is the
k^3-weighted EXAFS. Lower graph is the Fourier transforms of the
EXAFS signals in R space. Phase shifts were not corrected.

The R space (Figure 4.30) identified 3 peak positions: (Peak1) Ti-O (1-3) (~2Å),
(Peak 2): Ti-O (4-5) (~2.3-2.5Å), (Peak 3) Ti-La (~3.3-3.7Å). It is noteworthy that, the
intensity of Peak 2 in FeCrLTO1250_24h was higher than that of Peak 3, which differed
from the other samples. Therefore, EXAFS fitting cloud not be wholly matched with
$La_2Ti_2O_7$ structure. The extra paths of Ti-Fe and Ti-Cr were introduced to $La_2Ti_2O_7$
structure for EXAFS fitting. The perfect fitting was exhibited in the Ti-Fe degeneracy of
0.372 and Ti-Cr degeneracy of 0.744. The inter-atomic distance of Ti-Fe and Ti-Cr are
2.67 Å and 2.64 Å, respectively.

The evidence implied that, the substitutional of Fe and Cr atom was positioned
adjacent to the Ti atom in $La_2Ti_2O_7$ structure but not the La atom. In $La_2Ti_2O_7$, the Ti
atom acts as the photoactive center, absorbing photons and promoting electrons to

higher energy levels. The presence of substituted Fe and Cr atoms adjacent to the Ti atom could induce electron transfer from these metal atoms to the Ti atom, thus facilitating the separation of electron-hole pairs and improving the photocatalytic efficiency.

The substituted doping of Cr and Fe in the $La_2Ti_2O_7$ structure can affect the p-d hybridization between the oxygen 2p orbitals and the transition metal 3d orbitals, as indicated by the XANES results. The 3d orbitals of Cr and Fe have partially filled electrons that can interact with the 2p orbitals of the surrounding oxygen atoms, leading to hybridization between these orbitals. This interaction can be changed in the electronic structure of the nearby oxygen atoms and Ti ions, ultimately affecting the p-d hybridization. Therefore, substituted doping of Cr and Fe in the $La_2Ti_2O_7$ structure can lead to changes in their optical and photocatalytic properties. These changes reduce the band gap of the photocatalysts, causing their absorption spectrum to shift and ultimately improve their photocatalytic performance. Extensive research has been conducted on the use of orbital hybridization to regulate the electronic structures and surface chemisorption properties of transition metals in order to enhance the performance of catalysts (Chen, H., et al, 2022).

Moreover, calcination under a N_2 atmosphere can be used to control the oxygen content of the material and to prevent oxidation or reduction reactions that could alter the electronic properties of (Fe,Cr) co-doping $La_2Ti_2O_7$.

The (Fe, Cr) $La_2Ti_2O_7$ (N) mechanism, as shown Figure 4.31.
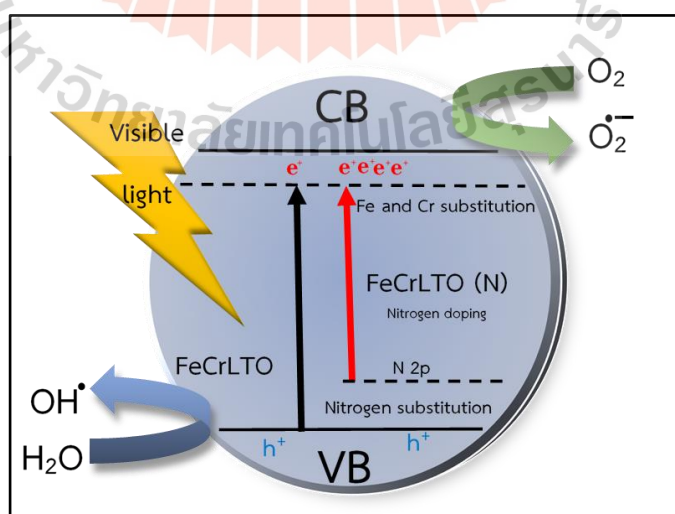
Figure 4.31 (Fe,Cr) $La_2Ti_2O_7$ (N) mechanism of photocatalyst

The Fe and Cr co-doping are effect to band gap energy and lead to formation of oxygen vacancy and Ti^{3+} defects because Fe and Cr built the new band energy below conduction band or incorporated with conduction band. The Cr^{6+} formation could effect to charge balance due to Cr releasing electron more than Ti to $La_2Ti_2O_7$ as electron donor. For Fe and others Cr atoms less releasing electrons than Ti become electron acceptor. If the electrons on the donor levels passivate to the same extent as the holes on the acceptor levels, charge-compensated n-p doping pairs were forming. The Fe and Cr were substituted on Ti site. The red-shift of the optical absorption edge could be ascribed to a d-d transition $^4A_2$-$^4T_2$ in Fe or Cr. Obviously, Fe and Cr ions co-doping had induced a series of impurity states (Fe3d and Cr 3d orbital) in the forbidden gap of $La_2Ti_2O_7$. The electrons of Fe 3d4s and Cr 3d4s were easily excited from the valence band (VB) to the conduction band (CB) over $La_2Ti_2O_7$ under the visible-light irradiation. Doping $La_2Ti_2O_7$ with N produced isolated N2p states and shifted the VB edge upward to narrow the band gap.

CHAPTER V
CONCLUSION AND RECOMMENDATION

5.1   Conclusion

The $La_2Ti_2O_7$ perovskite structure is a member of the oxides with a general formula of $A_2B_2O_7$ which possesses a layered perovskite structure. These layered perovskite materials have unique electronic structure in which either A or B atom has a cation valency greater than +1 (highly donor-doped) The separation of the electrons and holes is more efficient in the highly donor-doped (110) layered perovskite $La_2Ti_2O_7$ than in other semiconductors. Therefore, photocatalysts based on $La_2Ti_2O_7$ have been widely studied for water splitting to generate H_2 and O_2 and is a stable form when using organic pollutant degradation in several times. The sol-gel method is appropriate preparation for $La_2Ti_2O_7$-based photocatalysts that can be activated by visible light, the optimal approach with co-doping of Fe and Cr at the concentration of 0.005 molar percent corresponding to Ti atom. The calcination process was carried out under an N_2 atmosphere to control the oxygen concentration of the material and prevent the oxidation and reduction reactions that could modify the electronic characteristics of the (Fe,Cr) co-doped $La_2Ti_2O_7$. The calcining temperature of 1250°C for 24h was provided the best photocatalytic efficiency. Fe and Cr was found to be substituted into the lattice sites of the photocatalysts. The Fe and Cr substitution leads to the transfer of electrons from Fe and Cr metal atoms to the Ti atom, thus facilitating the separation of electron-hole pairs and improving the photocatalytic efficiency. Additionally, Fe and Cr alter the p-d hybridization within the $La_2Ti_2O_7$ lattice, resulting in a reduction of the band gap and the absorption of lower energy. Especially, the strong effect of photocatalytic activity was nitrogen doping that the XPS confirmed the bonding structure which was Ti-O-N and Ti-N exhibiting XPS and PES analysis. The nitrogen atoms was substitution by took place oxygen site sharing corner TiO_6 in octahedral site. The photocatalytic activity was obtained high efficiency corresponding to nitrogen with a narrow band gap caused by mixing N 2p states with O 2p states and extended the optical absorption, thereby resulting in the generation of more electrons and holes.

5.2   Recommendation

The $La_2Ti_2O_7$ synthesis was used sol-gel process which obtained high purity and nano-crystalline. The sol-gel process was uncomplicated doping process and could use various dopant in sol-gel system. For nitrogen gas was used anion doping as nitrogen doping, nitrogen doping with nitrogen gas completed that was difficult to assign nitrogen in lattice and could not determine nitrogen quantity in $La_2Ti_2O_7$ lattice. Nitrogen doping had to use high pressure which was benefit synthesis. More metal dopants as tri-dopants should be consider to obtain high photocatalytic activity.
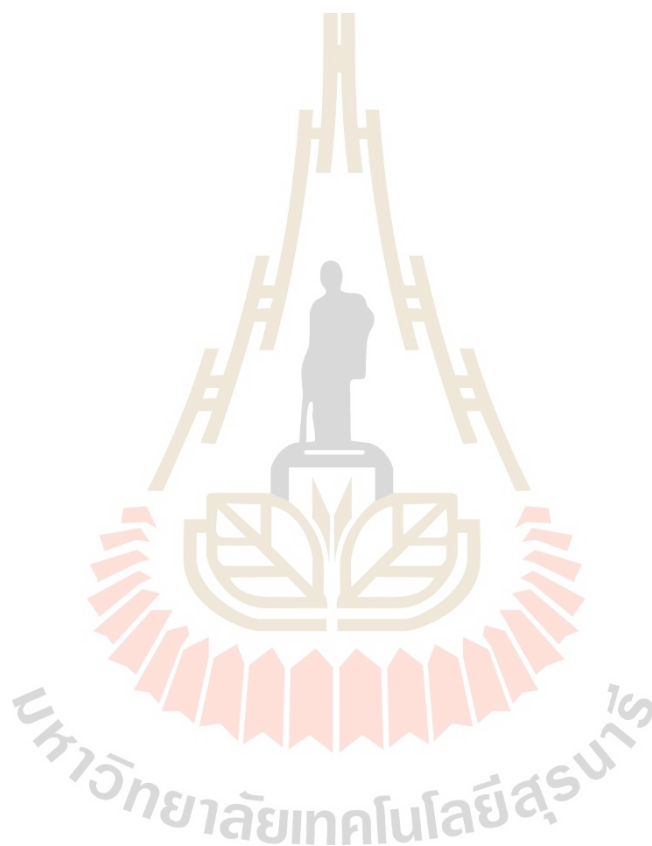
REFERENCES

Abe, Y., & Laine, R. M. (2020). Photocatalytic $La_4Ti_3O_{12}$ nanoparticles fabricated by liquid-feed flame spray pyrolysis. *Ceramics International, 46*(11, Part B), 18656-18660. doi:https://doi.org/10.1016/j.ceramint.2020.04.178

Byrne, C., Subramanian, G., & Pillai, S. C. (2018). Recent advances in photocatalysis for environmental applications. *Journal of Environmental Chemical Engineering, 6*(3), 3531-3555. doi:https://doi.org/10.1016/j.jece.2017.07.080

Chen, X., & Burda, C. (2008). The Electronic Origin of the Visible-Light Absorption Properties of C-, N- and S-Doped TiO_2 Nanomaterials. Journal of the American Chemical Society, 130(15), 5018-5019. doi:10.1021/ja711023z

Chen, S., Qi, Y., Liu, G., Yang, J., Zhang, F., & Li, C. (2014). A wide visible-light-responsive tunneled $MgTa_2O_{6-x}N_x$ photocatalyst for water oxidation and reduction. Chemical Communications, 50(92), 14415-14417. doi:10.1039/C4CC06682K

Collazzo, G. C., Jahn, S. L., Carreño, N. L. V., & Foletto, E. L. (2011). Temperature and reaction time effects on the structural properties of titanium dioxide nanopowders obtained via the hydrothermal method. *Brazilian Journal of Chemical Engineering, 28*.

Esfandiari N., Simchi A., Bagheri R. (2014). Size tuning of Ag-decorated TiO_2 nanotube arrays for improved bactericidal capacity of orthopedic implants. J. Biomed. Mater. Res. A 102, 2625–2635. 10.1002/jbm.a.34934

Fagan, R., McCormack, D. E., Hinder, S., & Pillai, S. C. (2016). Improved high temperature stability of anatase TiO_2 photocatalysts by N, F, P co-doping. Materials & Design, 96, 44-53. doi:https://doi.org/10.1016/j.matdes.2016.01.142

Fujishima A, Honda K. (1972). Electrochemical photolysis of water at a semiconductor electrode. Nature 238(5358):37–38

Fujishima A, Rao TN, Tryk DA. (2000). Titanium dioxide photocatalysis. J Photochem Photobiol C1(1):1–21

Hwang, D. W., Kim, H. G., Kim, J., Cha, K. Y., Kim, Y. G., & Lee, J. S. (2000). Photocatalytic Water Splitting over Highly Donor-Doped (110) Layered Perovskites. Journal of Catalysis, 193(1), 40-48. doi:https://doi.org/10.1006/jcat.2000.2875

Hwang, D. W., Cha, K. Y., Kim, J., Kim, H. G., Bae, S. W., & Lee, J. S. (2003). Photocatalytic Degradation of CH_3Cl over a Nickel-Loaded Layered Perovskite. Industrial & Engineering Chemistry Research, 42(6), 1184-1189. doi:10.1021/ie020457c

Hwang, D. W., Kim, H. G., Lee, J. S., Kim, J., Li, W., & Oh, S. H. (2005). Photocatalytic Hydrogen Production from Water over M-Doped La2Ti2O7 (M = Cr, Fe) under Visible Light Irradiation (λ > 420 nm). *The Journal of Physical Chemistry B, 109*(6), 2093-2102. doi:10.1021/jp0493226

Huang, H.-C., Yang, C.-L., Wang, M.-S., & Ma, X.-G. (2017). Enhanced photocatalytic performance of anatase TiO_2 substitutionally co-doped with La and N. Solar Energy Materials and Solar Cells, 170, 233-238. doi:https://doi.org/10.1016/j.solmat.2017.06.001

Jin, M., Nagaoka, Y., Nishi, K., Ogawa, K., Nagahata, S., Horikawa, T., Hayashi, J. i. (2008). Adsorption properties and photocatalytic activity of TiO_2 and La-doped TiO_2. Adsorption, 14(2), 257-263. DOI:10.1007/s10450-007-9095-4

Kim, D. S., Han, S. J., & Kwak, S.-Y. (2007). Synthesis and photocatalytic activity of mesoporous TiO_2 with the surface area, crystallite size, and pore size. Journal of Colloid and Interface *Science, 316*(1), 85-91. doi:https://doi.org/10.1016/j.jcis.2007.07.037

Kim, J., Hwang, D. W., Kim, H.-G., Bae, S. W., Ji, S. M., & Lee, J. S. (2002). Nickel-loaded $La_2Ti_2O_7$ as a bifunctional photocatalyst. Chemical Communications (21), 2488-2489. doi:10.1039/B208092C

Ku, Y., Wang, L. C., & Ma, C. M. (2007). Photocatalytic Oxidation of Isopropanol in Aqueous Solution Using Perovskite-Structured $La_2Ti_2O_7$. Chemical Engineering & Technology, 30(7), 895-900. doi:https://doi.org/10.1002/ceat.200700071

Lin, J., Liu, X., Zhu, S., Liu, Y., & Chen, X. (2015). Anatase TiO2 nanotube powder film with high crystallinity for enhanced photocatalytic performance. *Nanoscale Research Letters, 10*(1), 110. doi:10.1186/s11671-015-0814-6

Liqiang, J., Xiaojun, S., Baifu, X., Baiqi, W., Weimin, C., & Honggang, F. (2004). The preparation and characterization of La doped TiO_2 nanoparticles and their photocatalytic activity. Journal of Solid State Chemistry, 177(10), 3375-3382. doi:https://doi.org/10.1016/j.jssc.2004.05.064

Liu, P., Nisar, J., Sa, B., Pathak, B., & Ahuja, R. (2013). Anion–Anion Mediated Coupling in Layered Perovskite $La_2Ti_2O_7$ for Visible Light Photocatalysis. The Journal of Physical Chemistry C*, 117*(27), 13845-13852. doi:10.1021/jp402971b

Malac, M., & Egerton, R. F. (1999). Calibration Specimens for Determining Energy-Dispersive X-ray k-Factors of Boron, Nitrogen, Oxygen, and Fluorine. *Microscopy and Microanalysis, 5*(1), 29-38. doi:10.1017/S1431927699000021

Miseki, Y., Kato, H., & Kudo, A. (2009). Water splitting into H_2 and O_2 over niobate and titanate photocatalysts with (111) plane-type layered perovskite structure. *Energy & Environmental Science, 2*(3), 306-314. doi:10.1039/B818922F

Maegli, A. E., Otal, E. H., Hisatomi, T., Yoon, S., Leroy, C. M., Schäuble, N., Weidenkaff, A. (2012). Perovskite-Type $LaTiO_2N$ Oxynitrides for Solar Water Splitting: Influence of the Synthesis Conditions. Energy Procedia, 22, 61-66. doi:https://doi.org/10.1016/j.egypro.2012.05.218

Mitoraj D., Janczyk A., Strus M., Kisch H., Stochel G., Heczko P. B., et al. (2007). Visible light inactivation of bacteria and fungi by modified titanium dioxide. Photochem. Photobiol. Sci. 6, 642–648. 10.1039/B617043A

Myung, S.-T., Takahashi, N., Komaba, S., Yoon, C. S., Sun, Y.-K., Amine, K., & Yashiro, H. (2011). Nanostructured TiO_2 and Its Application in Lithium-Ion Storage. *Advanced Functional Materials, 21*(17), 3231-3241. doi:https://doi.org/10.1002/adfm.201002724

Nakata, K., &Fujishima, A. (2012). TiO_2 photocatalysis: Design and applications. Journal of Photochemistry and Photobiology C: Photochemistry Reviews, 13, 169–189. doi: 10.1016/j.jphotochemrev.2012.06.001

Ning S., Lin H., Tong Y., Zhang X., Lin Q., Zhng Y., et al. (2017). Dual couples Bi metal Depositing and Ag@AgI islanding on BiOI 3D architectures for synergistic bactericidal mechanism of E.coli under visible light. Appl. Catal. B Environ. 204, 1–10. 10.1016/j.apcatb.2016.11.006

Peng, Y.-P., Lo, S.-L., Ou, H.-H., & Lai, S.-W. (2010). Microwave-assisted hydrothermal synthesis of N-doped titanate nanotubes for visible-light-responsive photocatalysis. Journal of Hazardous Materials, 183(1),754-758. doi: https://doi.org/10.1016/j.jhazmat.2010.07.090

Prekajski, M., Zarubica, A., Babić, B., Jokić, B., Pantić, J., Luković, J., & Matović, B. (2016). Synthesis and characterization of Cr^{3+} doped TiO_2 nanometric powders. Ceramics International, 42(1, Part B), 1862-1869. doi:https://doi.org/10.1016/j.ceramint.2015.09.1513

Rajeshwar K, Osugi ME, Chanmanee W, Chenthamarakshan CR, Zanoni M, Kajitvichyanukul P, Krishnan-Ayer R. (2008). Heterogeneous photocatalytic treatment of organic dyes in air and aqueous media. J Photochem Photobiol C 9(4):171–192

Regmi C., Kim T. H., Ray S. C., Yamaguchi T., Lee S. W. (2017). Cobalt-doped $BiVO_4$ (Co-$BiVO_4$) as a visible-light-driven photocatalyst for the degradation of

malachite green and inactivation of harmful microorganisms in wastewater. Res. Chem. Intermed. 43, 5203–5216. 10.1007/s11164-017-3036-y

Regmi, C., Joshi, B., Ray, S. K., Gyawali, G., & Pandey, R. P. (2018). Understanding Mechanism of Photocatalytic Microbial Decontamination of Environmental Wastewater. Frontiers in chemistry, 6, 33-33. doi:10.3389/fchem.2018.00033

Rehman S, Ullah R, Butt AM, Gohar ND. (2009). Strategies of making TiO_2 and ZnO visible light active. J Hazard Mater 170(2–3):560–569

Sahoo, C., Gupta, A. K., & Sasidharan Pillai, I. M. (2012). Photocatalytic degradation of methylene blue dye from aqueous solution using silver ion-doped TiO_2 and its application to the degradation of real textile wastewater. *J Environ Sci Health A Tox Hazard Subst Environ Eng, 47*(10), 1428-1438. doi:10.1080/10934529. 2012.672387

Spasiano, D., Marotta, R., Malato, S., Fernandez-Ibañez, P., & Di Somma, I. (2015). Solar photocatalysis: Materials, reactors, some commercial, and pre-industrialized applications. A comprehensive approach. Applied Catalysis B: Environmental, 170-171, 90-123. doi:https://doi.org/10.1016/j.apcatb.2014.12.050

Steven, L., S. (2013). new and future developments in catalysis, UK: Elsevier publication.

Tan, Y., Li, Z., Tian, Y., Hu, S., Jia, L., Chi, B., Li, J. (2017). Charge-compensated (Nb, Fe)-codoped La2Ti2O7 photocatalyst for photocatalytic H2 production and optical absorption. *Journal of Alloys and Compounds, 709*, 277-284. doi:https://doi.org/10.1016/j.jallcom.2017.03.129

Wang, J., Tafen, D. N., Lewis, J. P., Hong, Z., Manivannan, A., Zhi, M., Wu, N. (2009). Origin of Photocatalytic Activity of Nitrogen-Doped TiO_2 Nanobelts. Journal of the American Chemical Society, 131(34), 12290-12297. doi:10.1021/ja903781h

Wang, Q., An, N., Chen, W., Wang, R., Wang, F., Lei, Z., & Shangguan, W. (2012). Photocatalytic water splitting into hydrogen and research on synergistic of Bi/Sm with solid solution of Bi–Sm–V photocatalyst. International Journal of Hydrogen Energy, 37(17), 12886-12892.

Wang, R., Xu, D., Liu, J., Li, K., & Wang, H. (2011). Preparation and photocatalytic properties of CdS/La2Ti2O7 nanocomposites under visible light. Chemical Engineering Journal, 168(1), 455-460. doi:https://doi.org/10.1016/j.cej.2011.01.035

Wang W., Huang G., Yu J. C., Wong P. K. (2015). Advances in photocatalytic disinfection of bacteria: Development of photocatalysts and mechanisms. J. Environ. Sci. 34, 232–247.Williams DB (1993) Light element microanalysis and imaging. In: Quantitative Microbeam Analysis, Fitzgerald AG, Storey BE, Fabian D. (eds).

Bristol: Institute of Physics, pp 169–177 Goldstein J, Newbury D, Joy D, Lyman C, Echlin P, Lifshin E, et al. Scanning electron microscopy and x-ray microanalysis. 3rd ed. New York: Springer; 2003.

Wu, F., Liu, G., & Xu, X. (2017). Efficient photocatalytic oxygen production over Ca-modified LaTiO$_2$N. Journal of Catalysis, 346, 10-20. doi:https://doi.org/10.1016/j.jcat.2016.11.022

Zhang, G., Zhang, S., Wang, L., Liu, R., Zeng, Y., Xia, X., Luo, S. (2017). Facile synthesis of bird's nest-like TiO2 microstructure with exposed (001) facets for photocatalytic degradation of methylene blue. *Applied Surface Science, 391*, 228-235. doi:https://doi.org/10.1016/j.apsusc.2016.04.095

Zhang, S., Zhang, P., Liu, X., Yang, Z., Huang, Y., & Seo, H. J. (2019). Synthesis, structure, and luminescence of Eu3+-activated La4Ti3O12 nanoparticles with layered perovskite structure. *Journal of the American Ceramic Society, 102*(4), 1784-1793. doi:https://doi.org/10.1111/jace.16011

Zhu, J., Chen, F., Zhang, J., Chen, H., & Anpo, M. (2006). Fe^{3+}TiO$_2$ photocatalysts prepared by combining sol–gel method with hydrothermal treatment and their characterization. Journal of Photochemistry and Photobiology A: Chemistry, 180(1), 196-204. doi:https://doi.org/10.1016/j.jphotochem.2005.10.017

Zhu, Z., Cai, H., & Sun, D.-W. (2018). Titanium dioxide (TiO$_2$) photocatalysis technology for nonthermal inactivation of microorganisms in foods. Trends in Food Science & Technology, 75, 23-35. doi:https://doi.org/10.1016/j.tifs.2018.02.018

APPENDIX A

EDS spectroscopy and Xray Map composition analysis
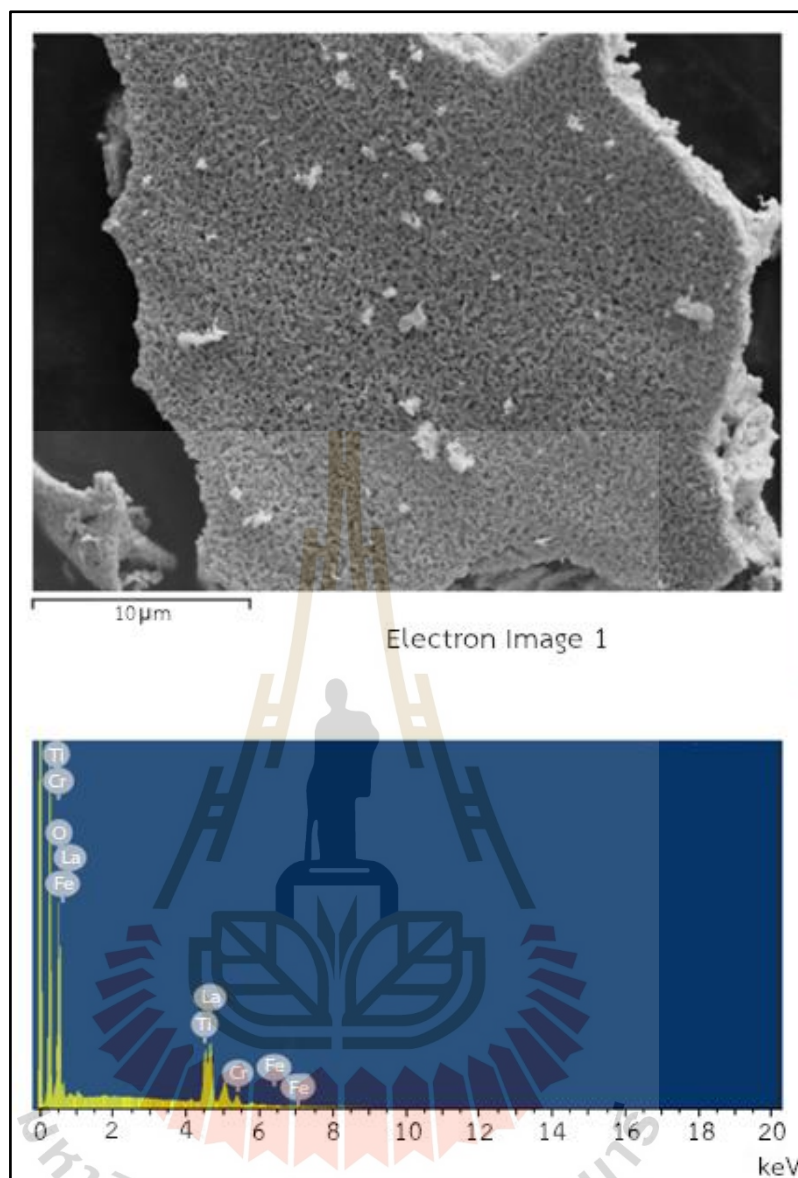
Figure A1 FE-SEM using EDS technique of FeCrLTO(N) at 1150°C for 24h
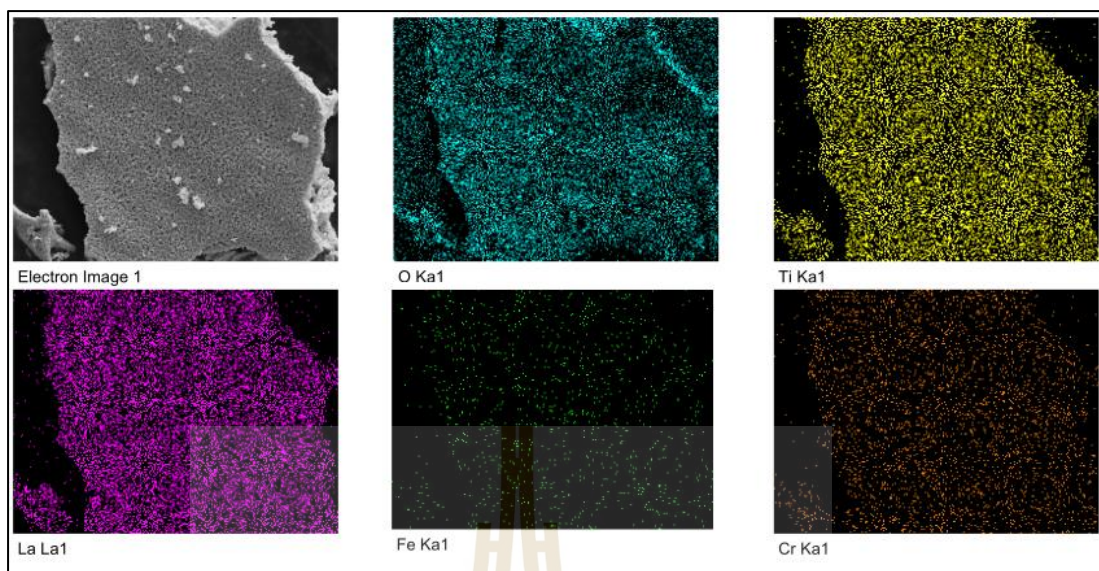
Figure A2 X-ray map composition of FeCrLTO(N) at 1150°C for 24h

Table A1 elemental composition of FeCrLTO1150(N)_24h

Sample	Elemental composition (% mass relative)				
	O	Ti	La	Fe	Cr
FeCrLTO1150(N)_24h	17.84	14.02	53.86	1.71	12.57
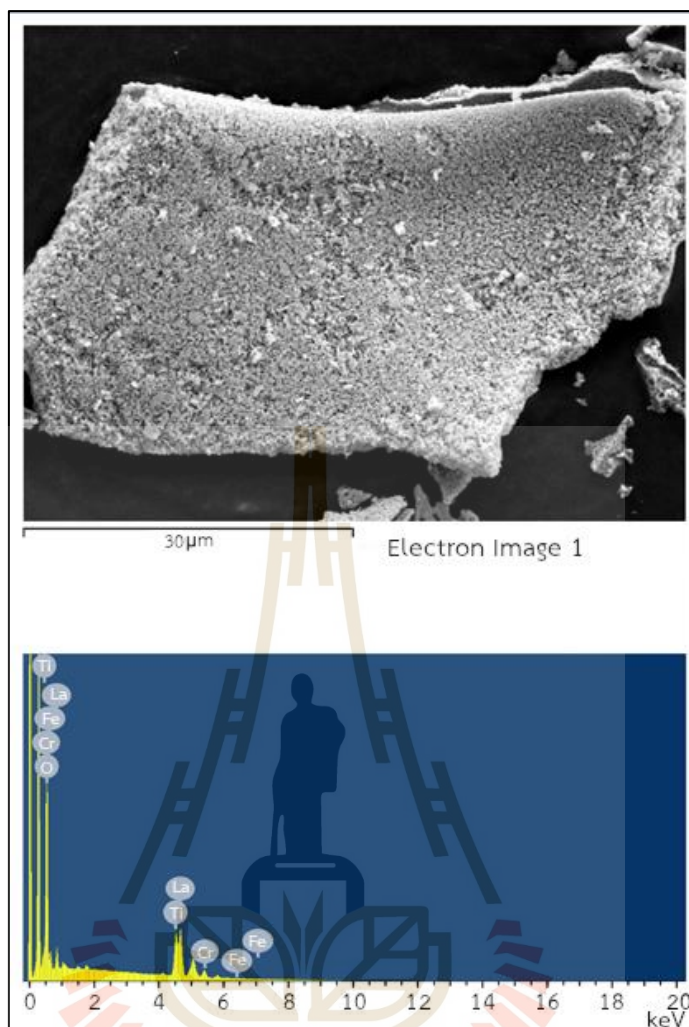
Figure A3 FE-SEM using EDS technique of FeCrLTO(N) at 1150°C for 30h
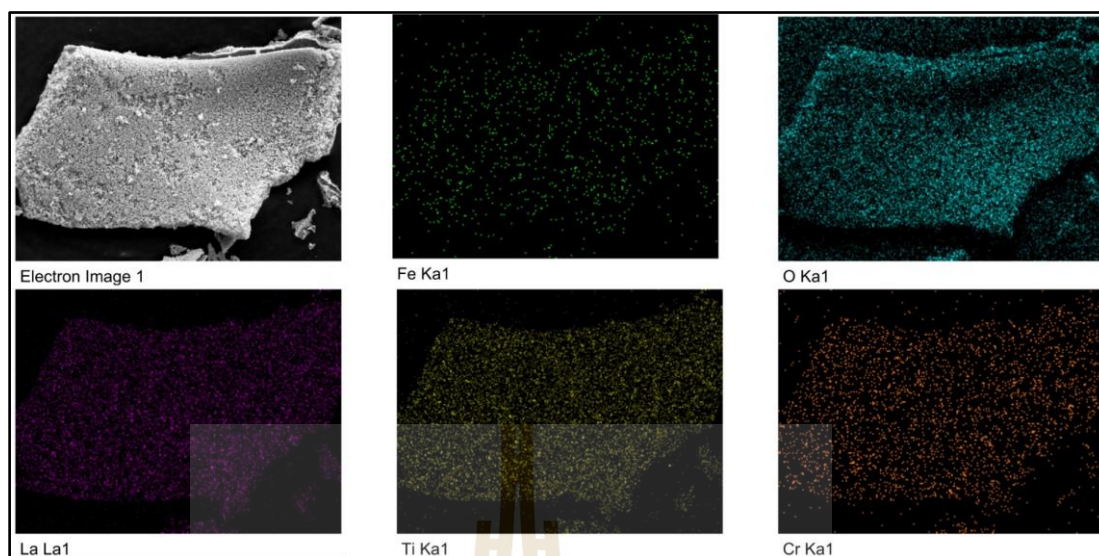
Figure A4 X-ray map composition of FeCrLTO(N) at 1150°C for 30h

Table A2 elemental composition of FeCrLTO1150(N)_30h

Sample	Elemental composition (% mass relative)				
	O	Ti	La	Fe	Cr
FeCrLTO1150(N)_30h	22.77	12.77	48.82	1.74	13.90
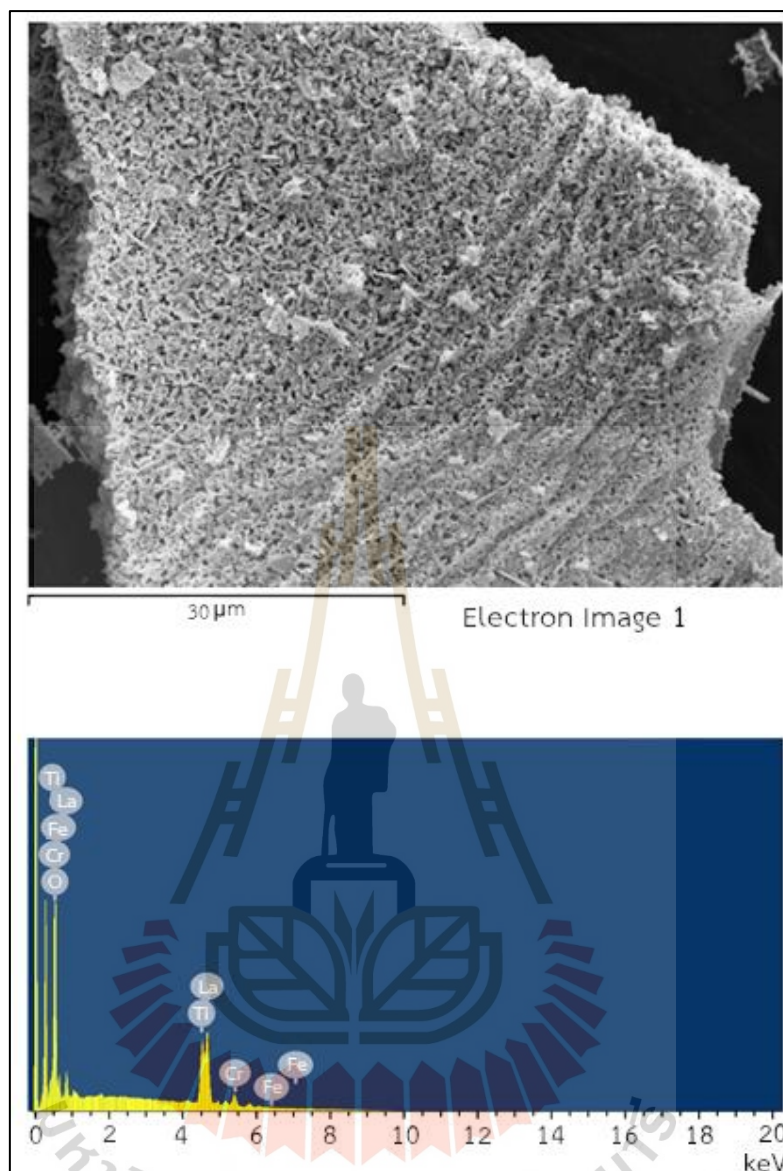
Figure A5 FE-SEM using EDS technique of FeCrLTO(N) at 1250°C for 18h
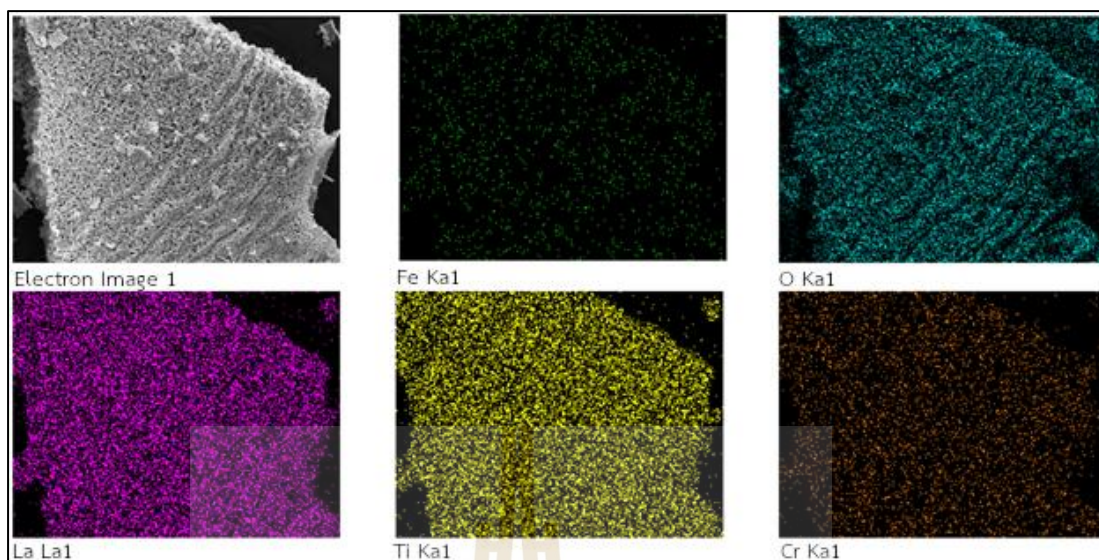
Figure A6 X-ray map composition of FeCrLTO(N) at 1250°C for 18h

Table A3 elemental composition of FeCrLTO1250(N)_18h

Sample	Elemental composition (% mass relative)				
	O	Ti	La	Fe	Cr
FeCrLTO1250(N)_18h	19.58	14.64	54.56	1.73	9.49
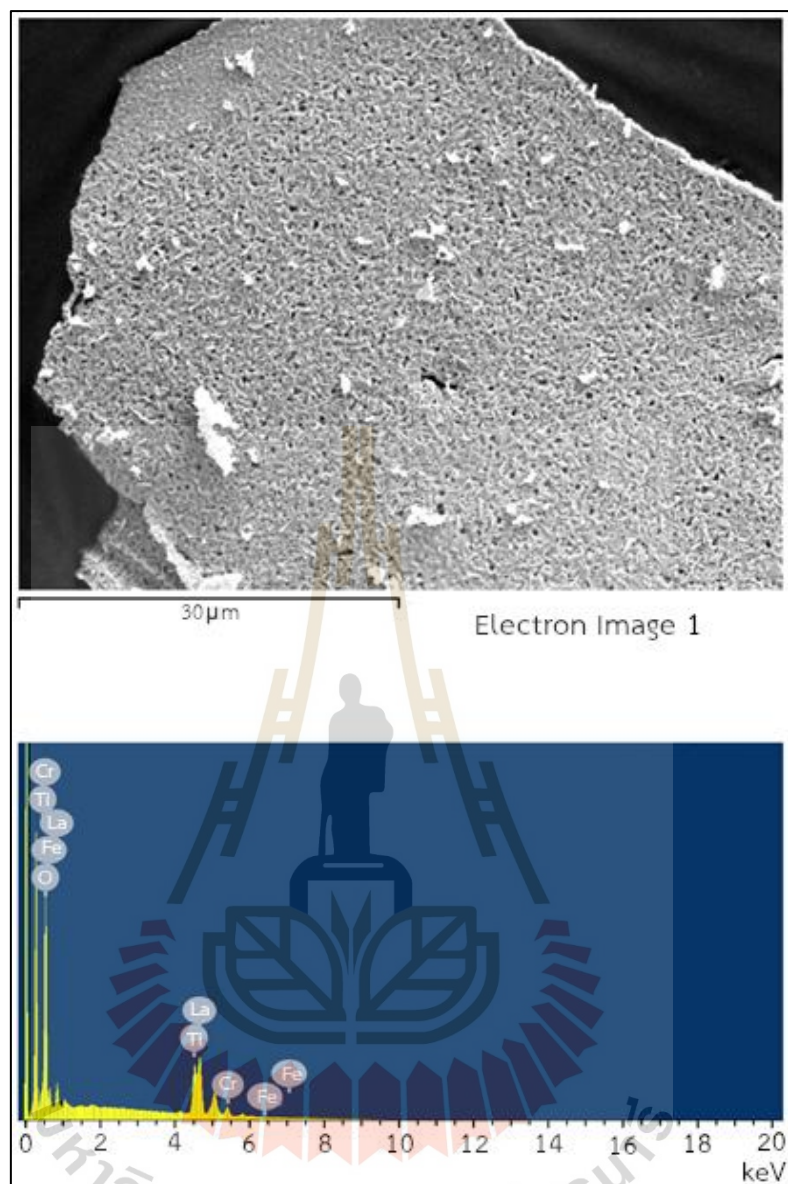
Figure A7 FE-SEM using EDS technique of FeCrLTO(N) at 1250°C for 24h
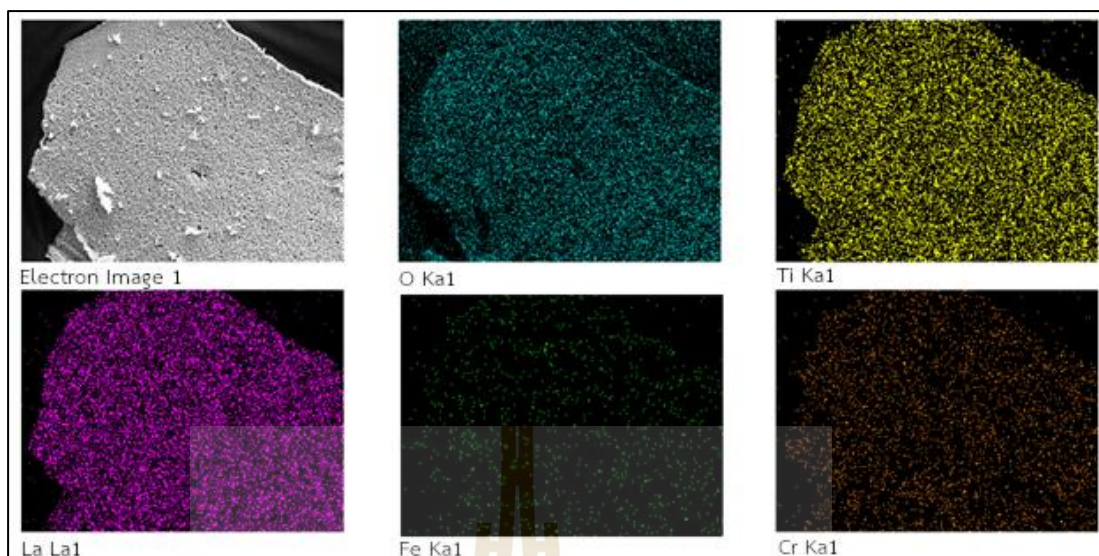
Figure A8 X-ray map composition of FeCrLTO(N) at 1250°C for 24h

Table A4 elemental composition of FeCrLTO1250(N)_24h

Sample	Elemental composition (% mass relative)				
	O	Ti	La	Fe	Cr
FeCrLTO1250(N)_24h	26.61	12.06	46.11	2.01	13.22
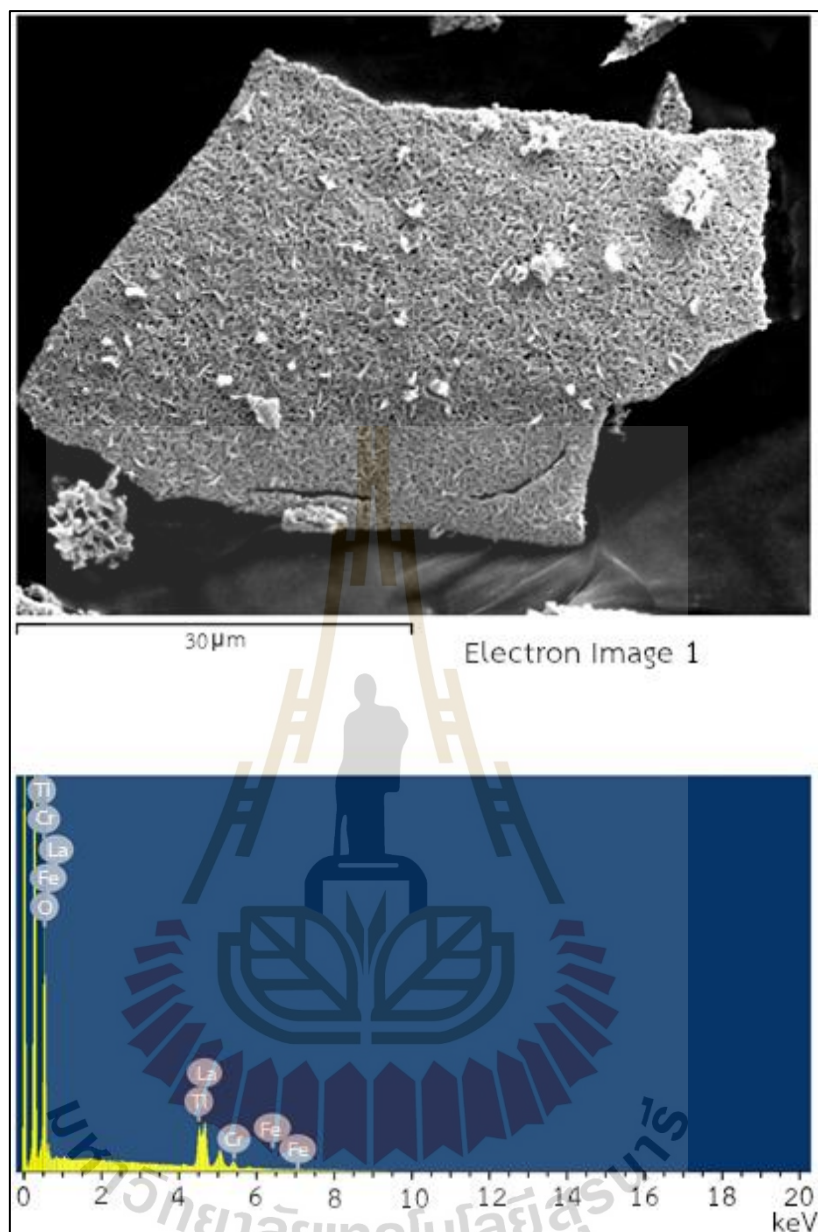
Figure A9 FE-SEM using EDS technique of FeCrLTO(N) at 1250°C for 30h
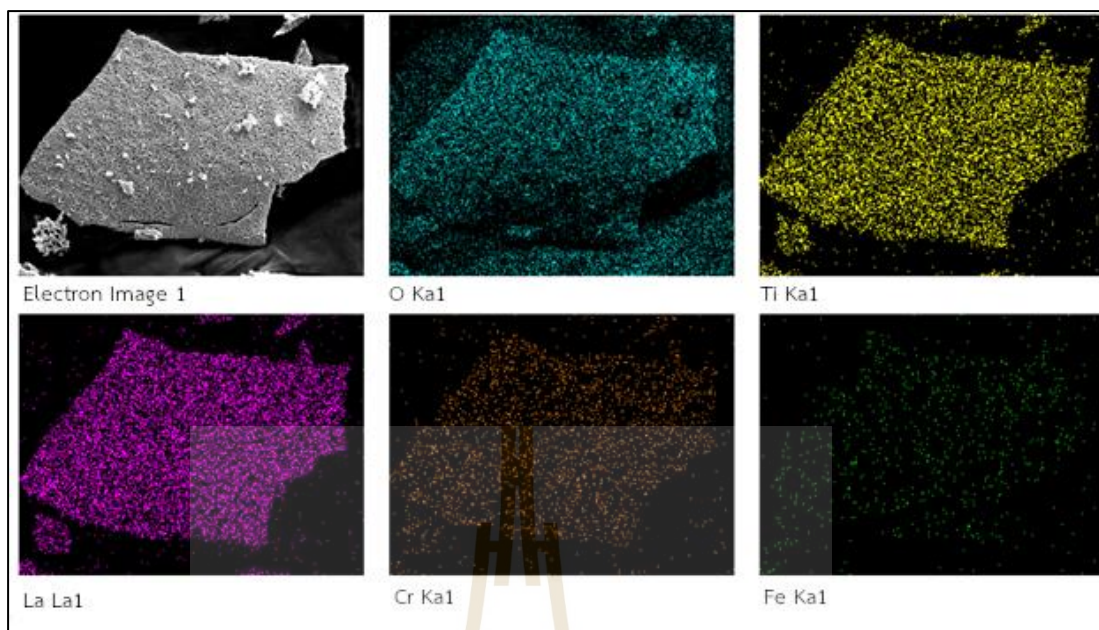
Figure A10 X-ray map composition of FeCrLTO(N) at 1250°C for 30h

Table A5 elemental composition of FeCrLTO1250(N)_30h

Sample	Elemental composition (% mass relative)				
	O	Ti	La	Fe	Cr
FeCrLTO1250(N)_30h	23.43	11.44	45.99	1.63	17.21
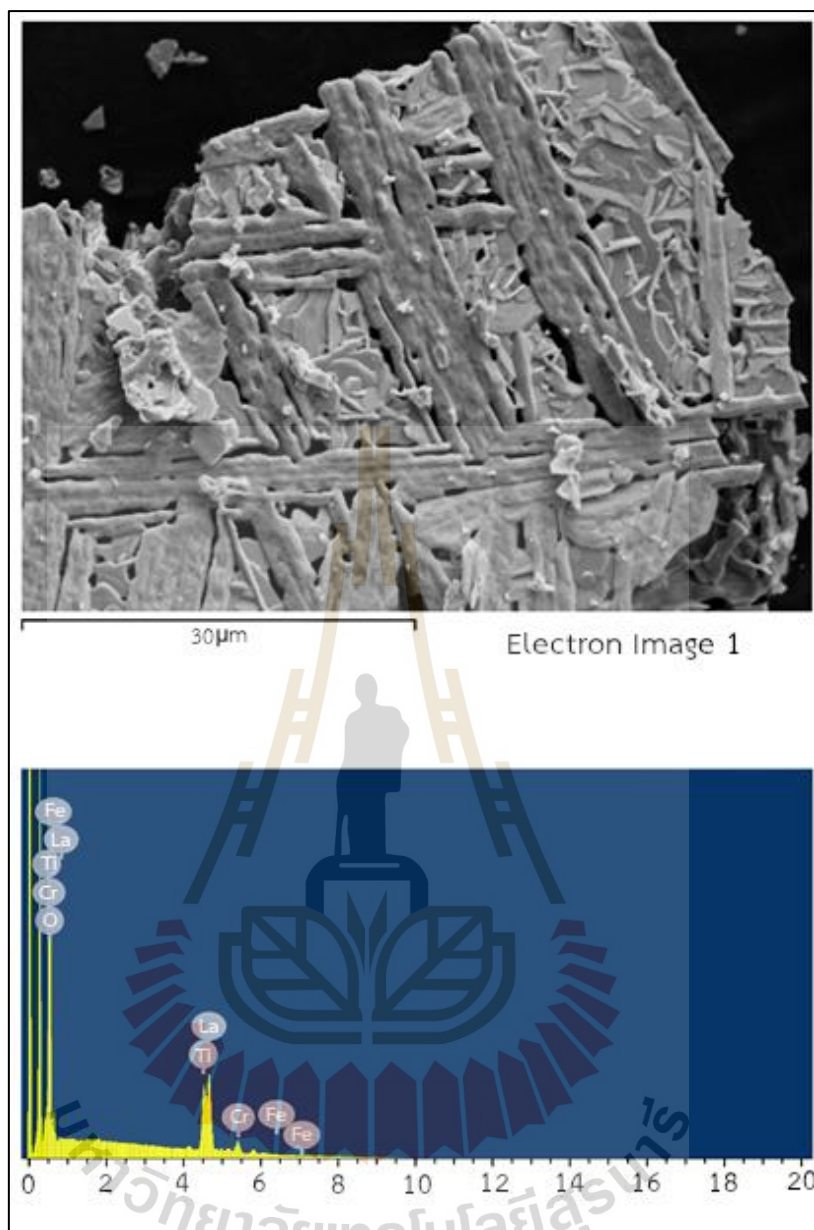
Figure A11 FE-SEM using EDS technique of FeCrLTO(N) at 1350°C for 18h
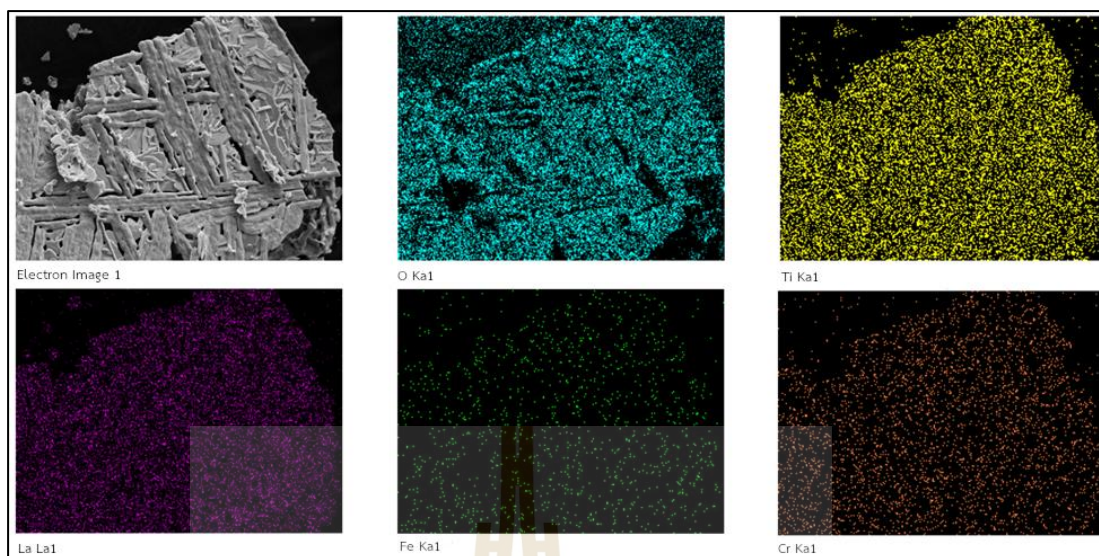
Figure A12 X-ray map composition of FeCrLTO(N) at 1350°C for 18h

Table A6 elemental composition of FeCrLTO1350(N)_18h

Sample	Elemental composition (% mass relative)				
	O	Ti	La	Fe	Cr
FeCrLTO1350(N)_30h	22.65	12.72	48.19	0.91	15.53
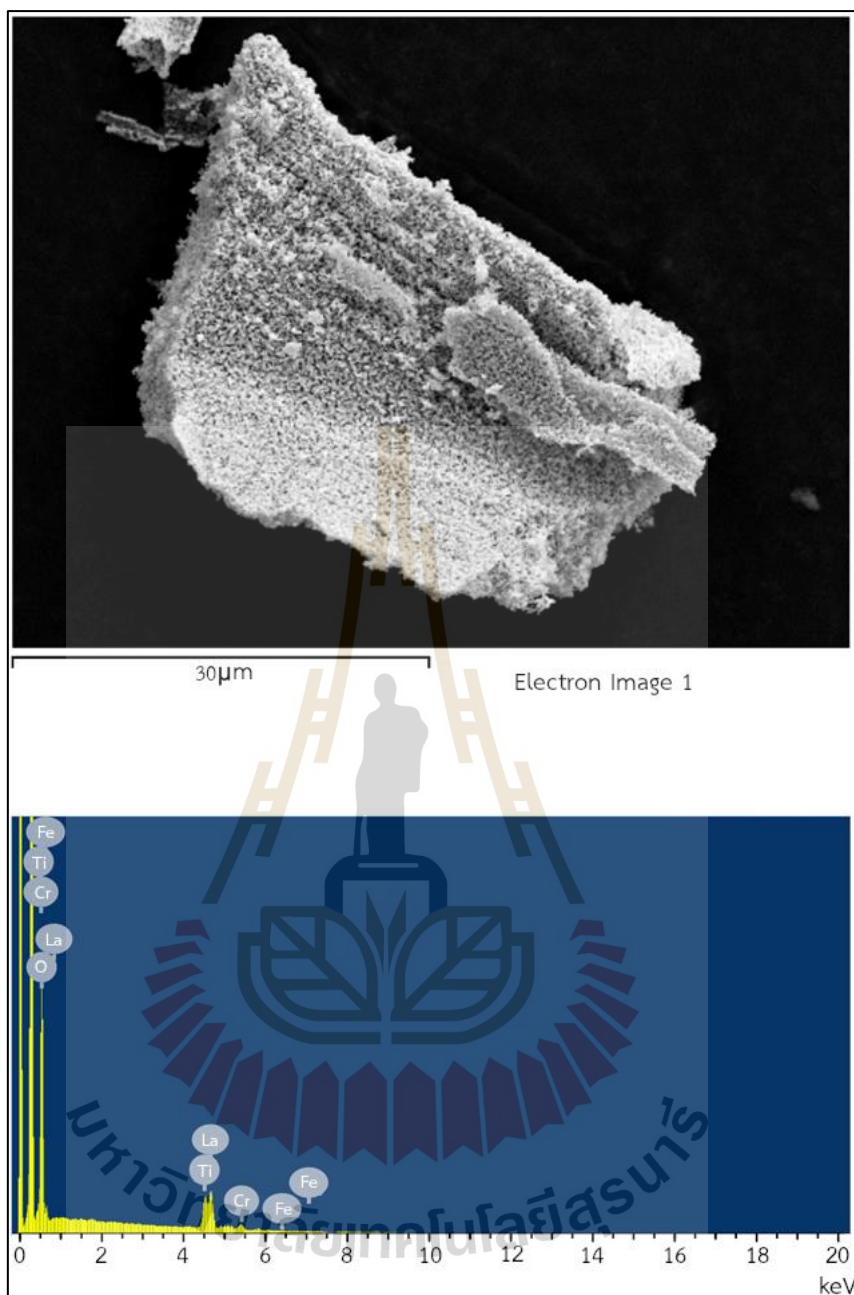
Figure A13 FE-SEM using EDS technique of FeCrLTO(N) at 1350°C for 30h
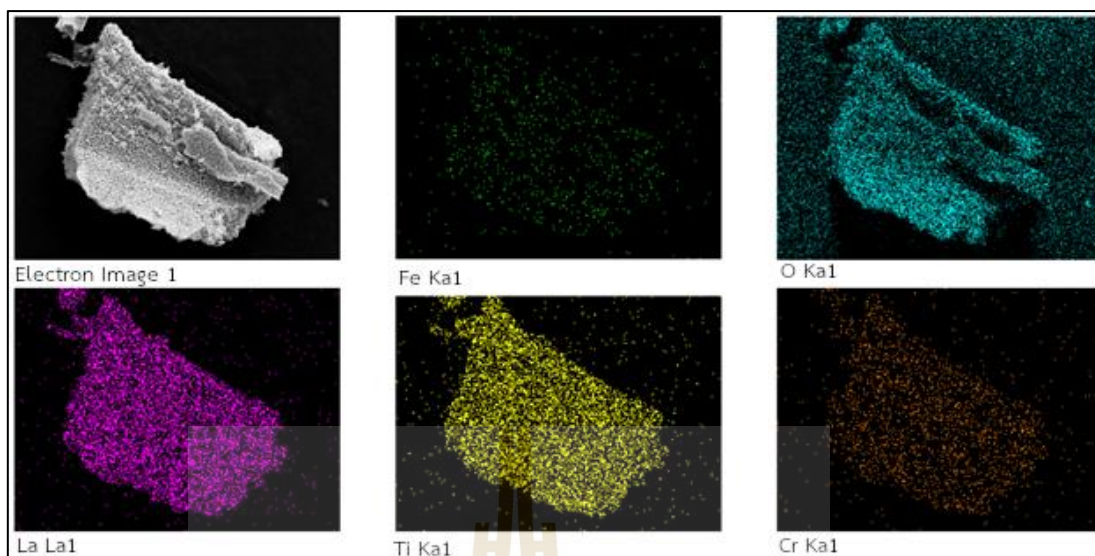
Figure A14 X-ray map composition of FeCrLTO(N) at 1350°C for 24h

Table A7 elemental composition of FeCrLTO1350(N)_24h

Sample	Elemental composition (% mass relative)				
	O	Ti	La	Fe	Cr
FeCrLTO1350(N)_24h	26.25	11.08	43.53	1.01	18.13
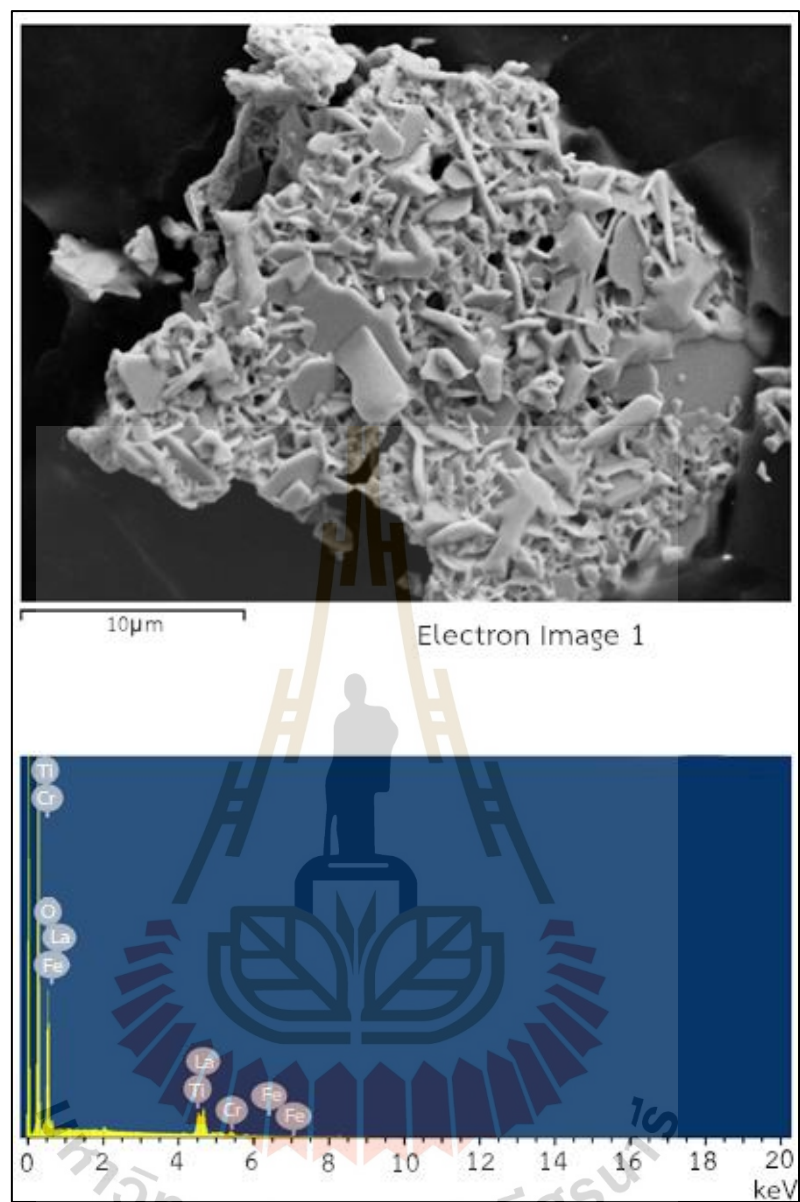
Figure 4.15 FE-SEM using EDS technique of FeCrLTO(N) at 1250°C for 30h
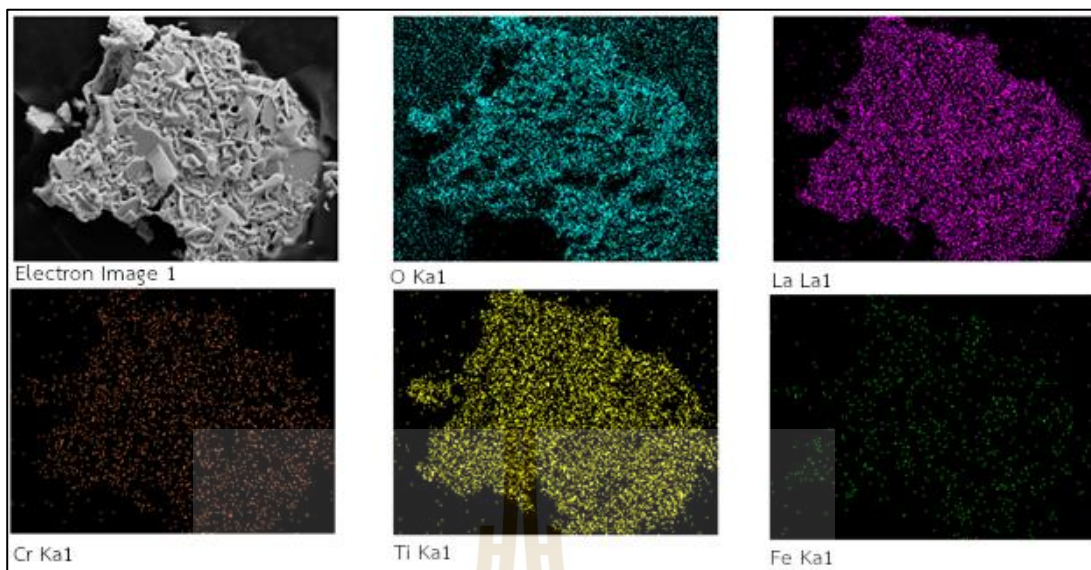
Figure A16 X-ray map composition of FeCrLTO(N) at 1350°C for 30h

Table A8 elemental composition of FeCrLTO1350(N)_30h

Sample	Elemental composition (% mass relative)				
	O	Ti	La	Fe	Cr
FeCrLTO1350(N)_30h	24.03	12.31	47.80	1.30	14.56

APPENDIX B

XPS analysis
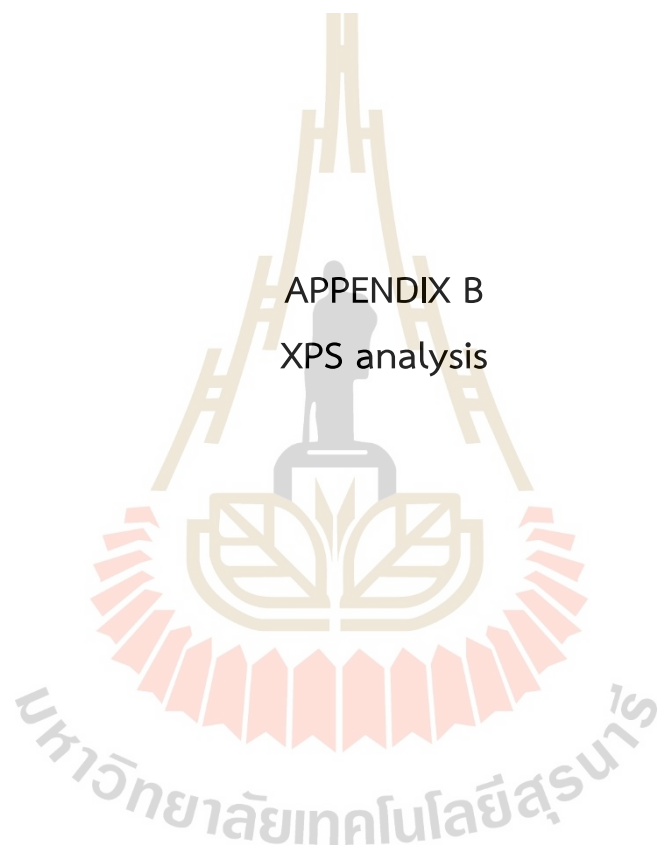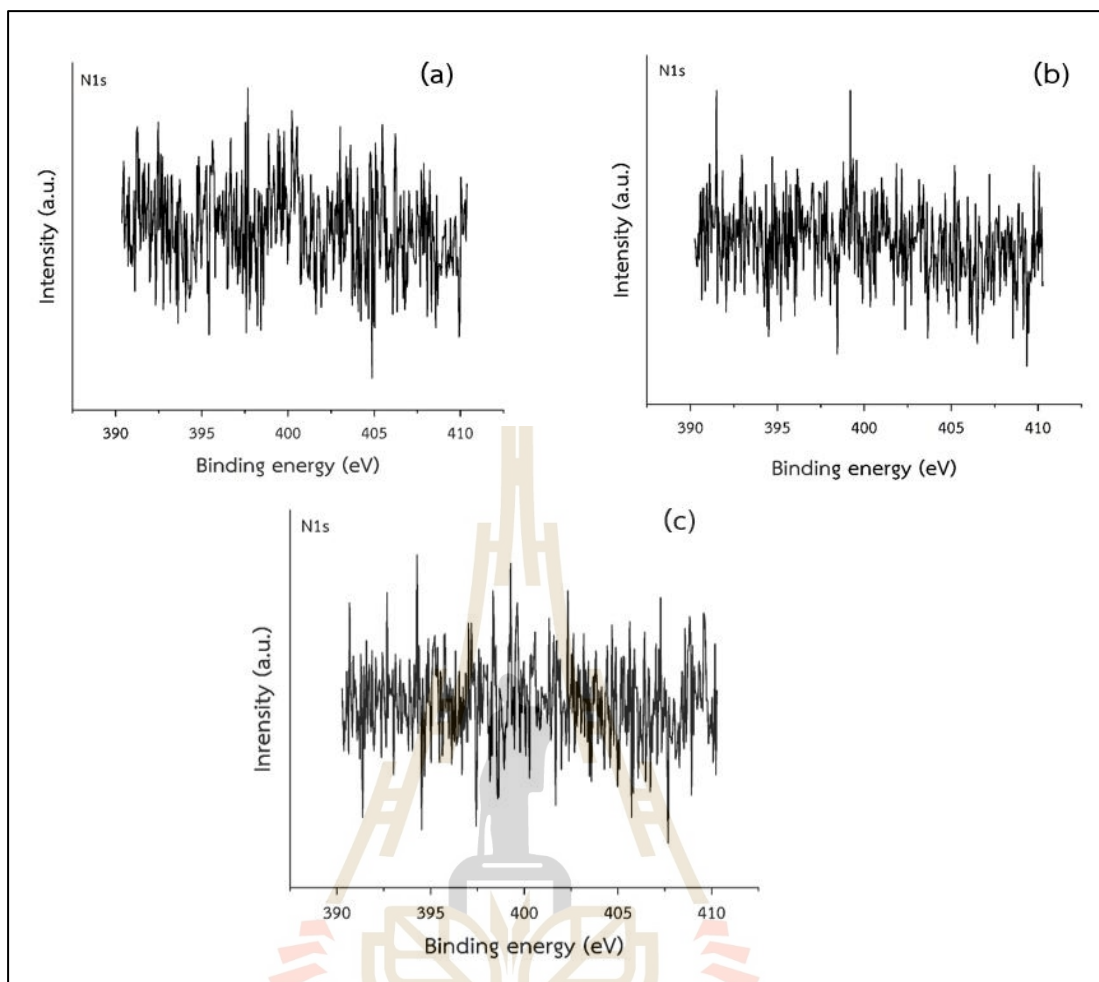
Figure B1 XPS N1s analysis of calcination temperature at 1150 ℃ (a) 18h, (b) 24h and (c) 30h
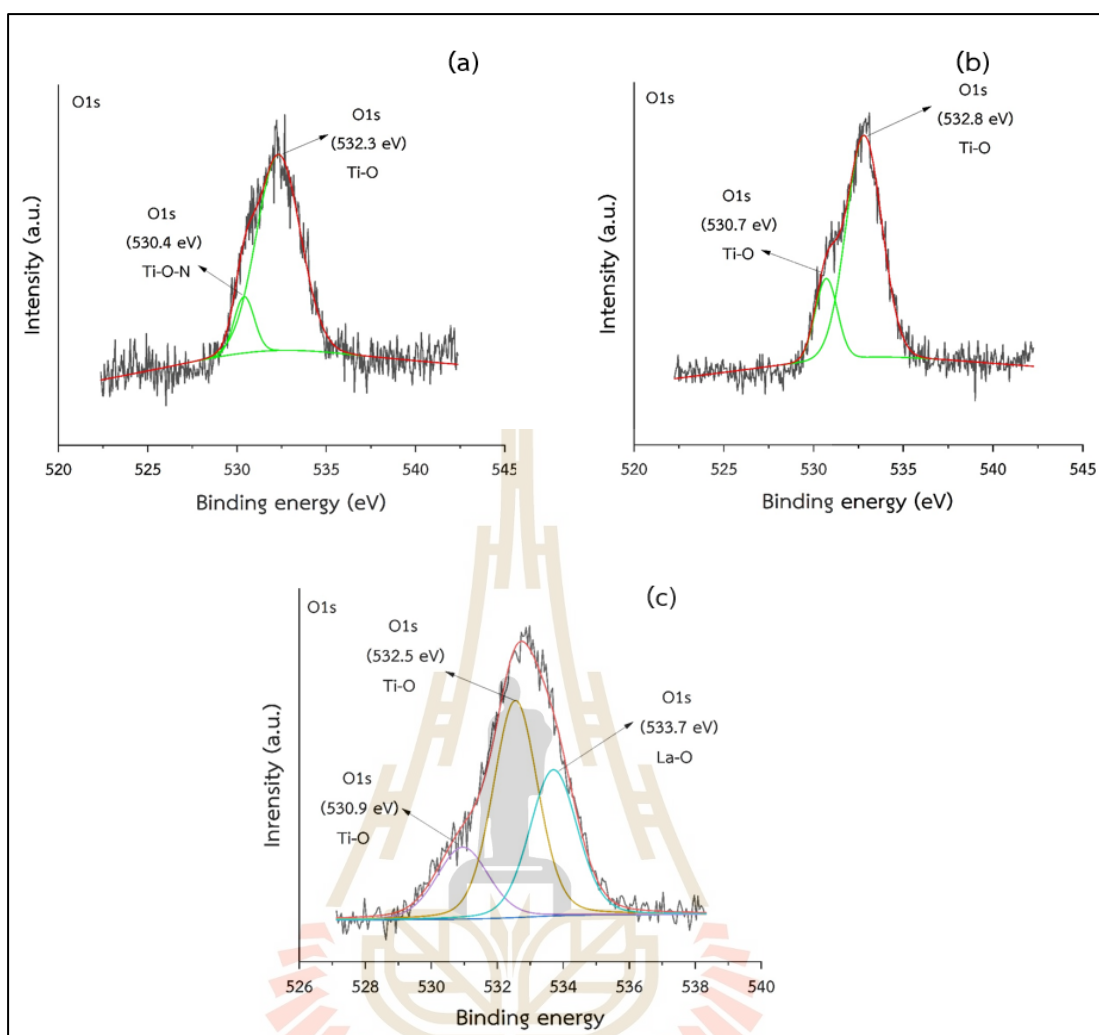
Figure B2 XPS O1s analysis of calcination temperature at 1150 ℃ (a) 18h, (b) 24h and (c) 30h
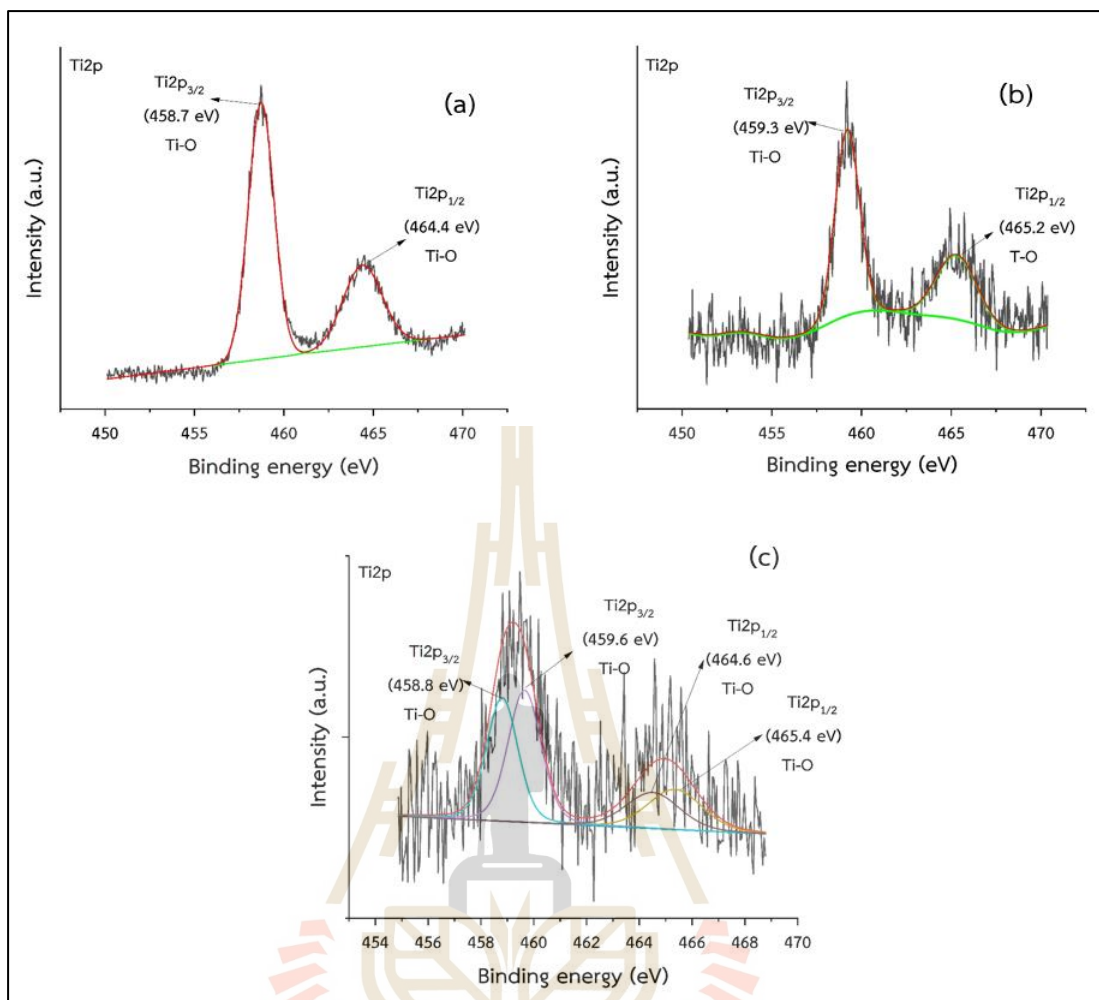
Figure B3 XPS Ti2p analysis of calcination temperature at 1150 ℃ (a) 18h, (b) 24h and (c) 30h
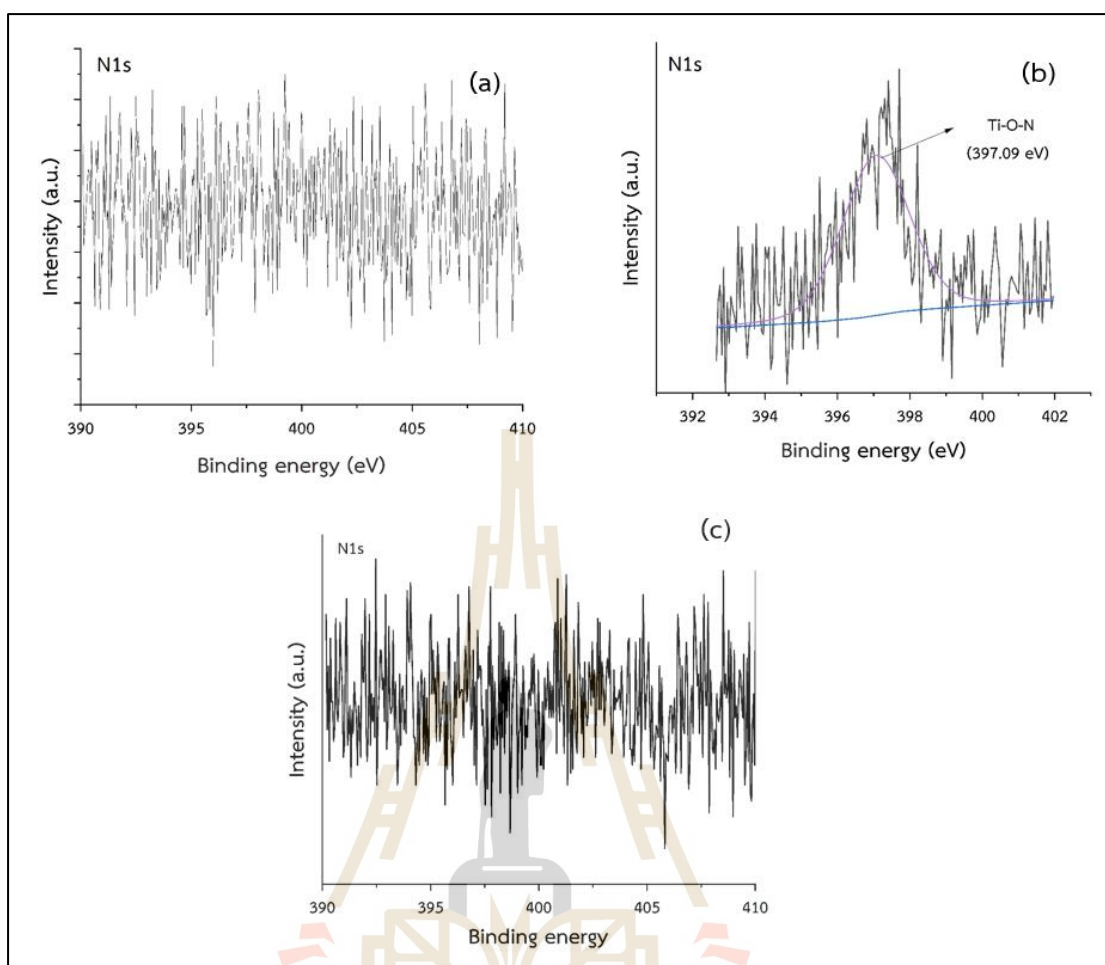
Figure B4 XPS N1s analysis of calcination temperature at 1250 ℃ (a) 18h, (b) 24h and (c) 30h

Figure B5 XPS O1s analysis of calcination temperature at 1250 ℃ (a) 18h, (b) 24h and (c) 30h

Figure B7 XPS Ti2p analysis of calcination temperature at 1250 °C (a) 18h, (b) 24h and (c) 30h
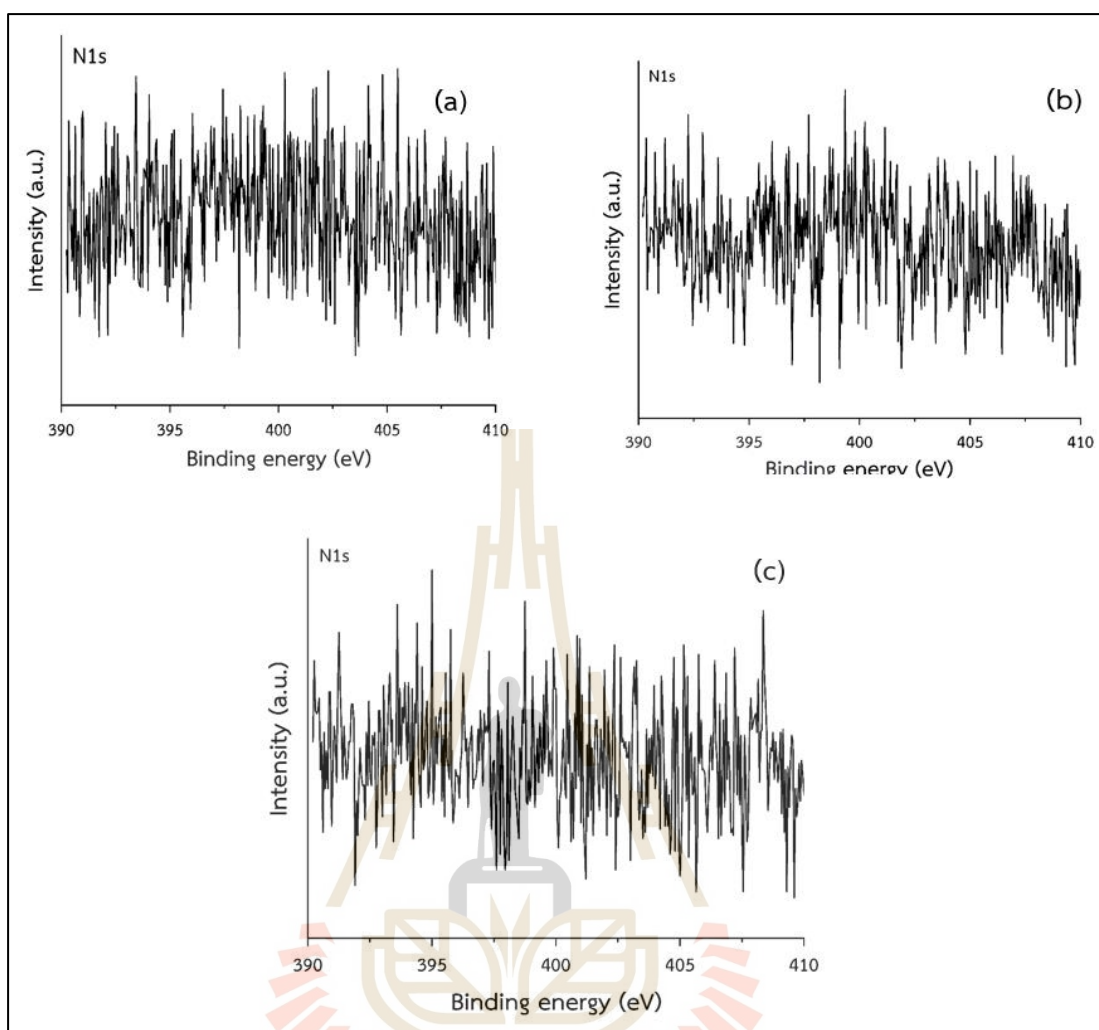
Figure B8 XPS N1s analysis of calcination temperature at 1350 ℃ (a) 18h, (b) 24h and (c) 30h
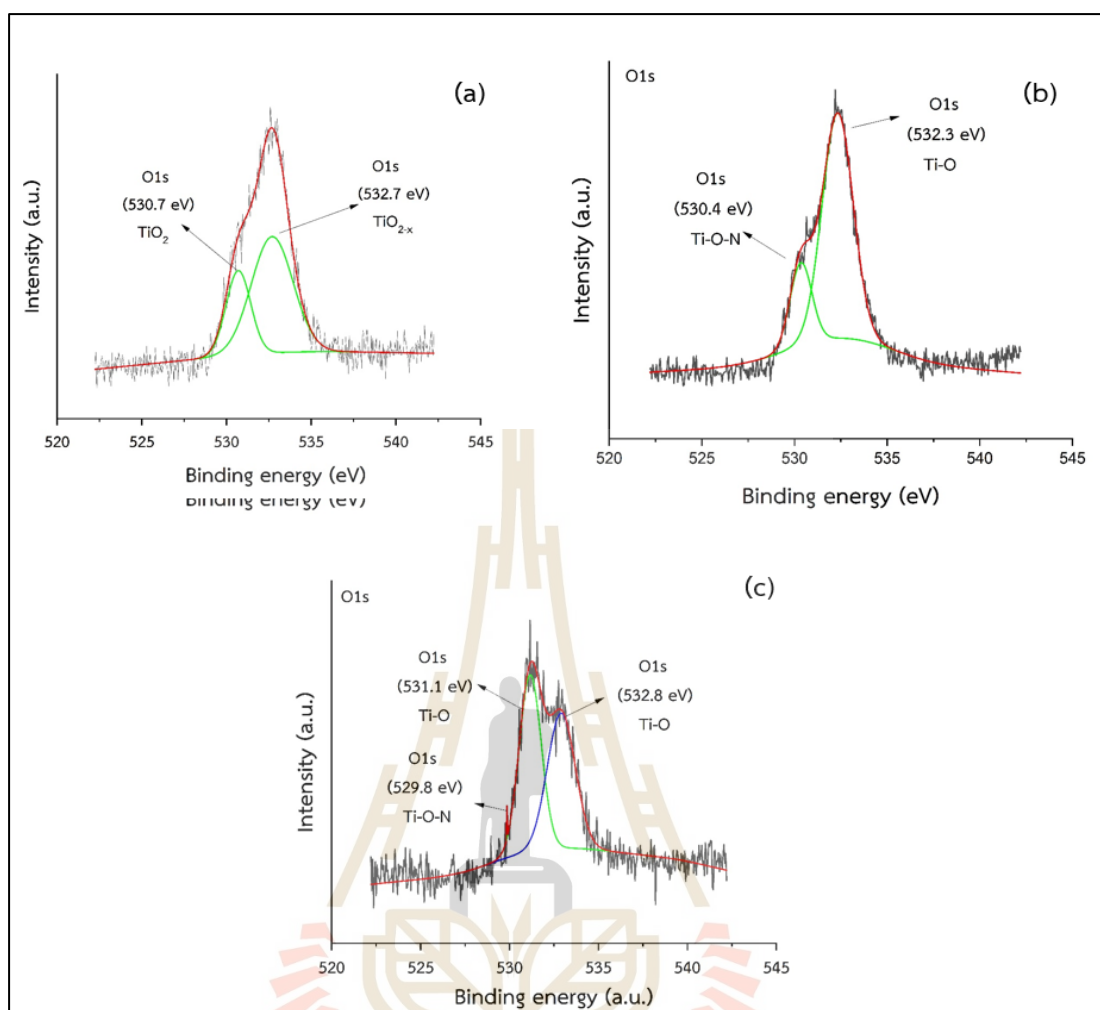
Figure B9 XPS O1s analysis of calcination temperature at 1350 ℃ (a) 18h, (b) 24h and (c) 30h
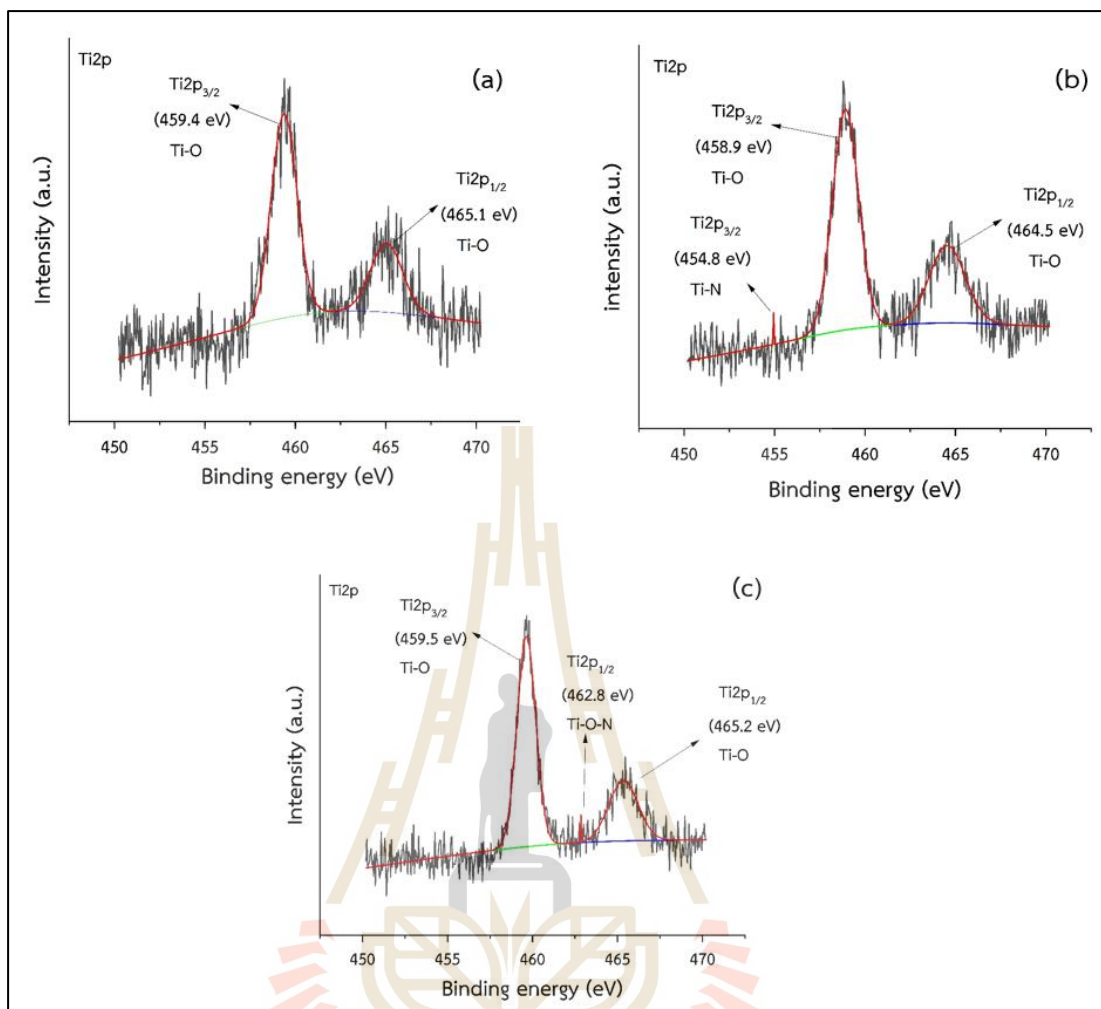
Figure B10 XPS Ti2p analysis of calcination temperature at 1350 ℃ (a) 18h, (b) 24h and (c) 30h

APPENDIX C

PUBLICATION
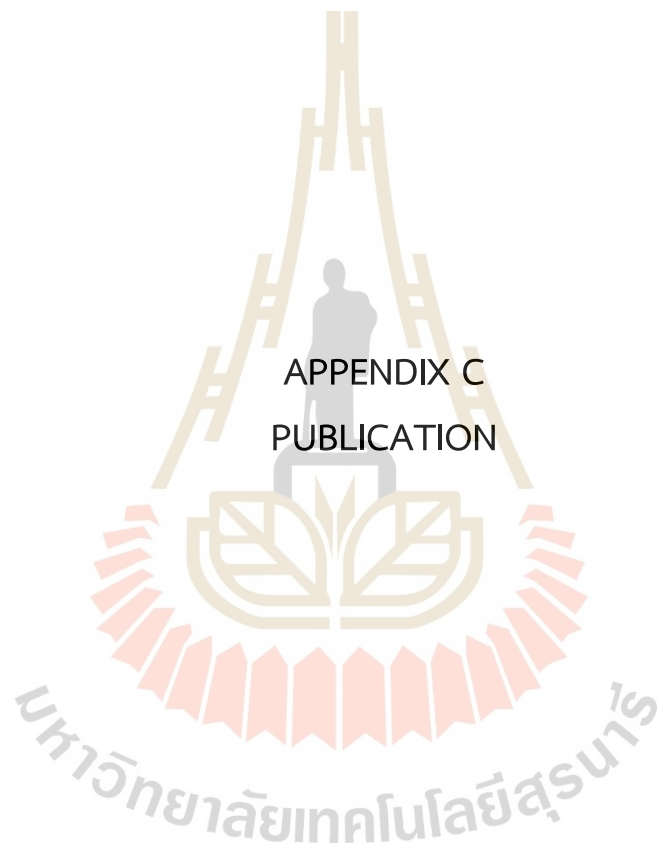
BCREC

Research Article

Investigate the Function and Structure of (Fe,Cr) La₂Ti₂O₇ Photocatalyst Calcined under the Nitrogen Atmosphere

Hussanai Luangthanarak[1], Ratchadaporn Supruangnet[2], Waraporn Tanthanuch[2],, Sukasem Watcharamaisakul[1],***

[1]School of Ceramic Engineering, Institute of Engineering, Suranaree University of Technology, Nakhon Ratchasima, Thailand.
[2]Synchrotron Light Research Institute (Public organization), Nakhon Ratchasima, Thailand.

Abstract

Extensive research has been conducted on enhancing the photocatalytic activity of Lanthanum titanium oxide ($La_2Ti_2O_7$) based photocatalysts. However, these photocatalysts were found to be inactive under visible light. To address this limitation, a modification was developed by co-doping Fe and Cr on $La_2Ti_2O_7$ to enable visible light driven photocatalytic response. The calcination of (Fe,Cr) $La_2Ti_2O_7$ was carried out under nitrogen atmosphere at various temperatures for 24 h. The results showed that the (Fe,Cr)-$La_2Ti_2O_7$ calcined at 1250 °C for 24 h exhibited the highest methylene blue degradation under visible light. Synchrotron X-ray absorption spectroscopy indicated that Fe and Cr were substitutionally located adjacent to the Ti atom within the $La_2Ti_2O_7$ structure. This metal substitutionally facilitated electron transfer and perturbed the *p-d* hybridization by modifying the local electronic structure of the surrounding oxygen atoms and transition metal ions, thereby reducing the band gap energy and enhancing the photocatalytic capability.

1. Introduction

The use of photocatalysts in various applications related to the environment and energy has been widely researched for decades due to its prominent property of photocatalytic activity [1]. The number of publications in this field continues to rise each year, with over 1000 peer-reviewed publications per year. One of the main areas of focus in renewable and sustainable energy is solar energy, which relies on the photo-

catalytic process for efficient conversion [2,3]. Typically, photocatalytic efficiency is active under Ultraviolet (UV) region due the high energy in this region can excite electrons from the valence band to the conduction band, which initiates a redox reaction. The excited electrons (e^-_{CB}) in the conduction band react with oxygen (O_2), for the valence band has left the positive holes (h^+_{VB}) obtaining water oxidation as the formation of active species: hydroxyl radical (OH·), hydrogen peroxide, superoxide ($O_2^-·$), *etc*. [4−7]. The layered perovskite structure, which has a general formula of $A_2B_2O_7$, possesses a unique electronic configuration that allows

Corresponding Author.
 *Email: sukasem@sut.ac.th (S. Watcharamaisakul);
 **Email: waraporn@slri.or.th (W. Tanthanuch);

it to exhibit photocatalytic performance when highly donor-doped. This structure is also highly stable and can participate in redox reactions. One notable member of this structure is $La_2Ti_2O_7$, which has demonstrated high efficiency in photocatalytic water splitting to produce H_2 and O_2. Furthermore, various applications of $La_2Ti_2O_7$ are used: decomposed isopropyl alcohol, decomposition of harmful organics, evolution of H_2 from water-ethanol solution, *etc.* Moreover, $La_2Ti_2O_7$ contains hypervalent La atoms within its layered perovskite structure. It is worth noting that $La_2Ti_2O_7$ exhibits efficient photocatalytic activity under the UV region, as it has a large band gap energy of approximately 3.8 eV [8−13].

Researchers are attempting to enhance the photocatalytic properties of $La_2Ti_2O_7$ in the visible light region by introducing cationic doping with transition metals. This process can extend the electronic configuration of $La_2Ti_2O_7$ towards band-edge photoresponse and narrow the band gap energy for visible light irradiation [14,15]. However, the incorporation of a single cation into a crystal structure has limitations in reducing the band gap energy due to the existence of an unoccupied impurity state. To overcome this limitation, scientists have resorted to codoping, a method that involves the simultaneous doping of two cations into the crystal structure. Codoping has been shown to enhance photocatalytic activity by maintaining charge balance, facilitating high carrier mobility, and achieving a desirable degree of band gap narrowing [16,17]. Fe and Cr codoping is a promising candidate for enhancing the photocatalytic activity of visible light driven $La_2Ti_2O_7$ through cation doping [18]. High purity $La_2Ti_2O_7$ was prepared by sol-gel method [19,20] with Fe and Cr being doped as cations during the initial preparation. Calcination was performed at different temperatures under a nitrogen atmosphere. The photocatalytic activity was analyzed using UV-Vis spectroscopy to investigate the degradation of methyl blue (MB). The synchrotron technique of Extended X-ray Absorption Fine Structure (EXAFS) was used for determine the neighbor atoms in the $La_2Ti_2O_7$ lattice structure.

2. Materials and Methods

2.1 Preparation of Photocatalytic Powder by Sol-gel Method

Photocatalytic powders ($La_2Ti_2O_7$) were prepared by sol-gel method [21] as following step. Firstly, preparation of the precursor solution by dissolve 0.476 g of titaniumbutoxide ($C_6H_{36}O_4Ti$, Sigma-Aldrich) in 31.002 g of ethylene glycol ($C_2H_6O_2$, QreC), Solution A. Solution B was prepared by dissolving 29.283 g of citric acid ($C_6H_8O_7$, Sigma-Aldrich) into 28 mL of di-water. Then solution A and B were mixed together by continuous stirring at 50 °C for 2 h to obtain solution C. Next, 0.0286 g of the iron (III) nitrate ($Fe(NO_3)_3.9H_2O$, Sigma-Aldrich), 6.1247 g of Lanthanum(III) nitrate hexahydrate ($La(NO_3)_3.6H_2O$, Sigma-Aldrich) and 0.0283 g of Chromium(III) nitrate ($Cr(NO_3)_3.9H_2O$, Sigma-Aldrich) were added into solution C and the mixture was heated to 130 °C for 8 h, resulting in the formation of a gel. The molar percent of Cr and Fe corresponding to Ti presented in the reaction are 0.005% Fe and 0.005% Cr. The calcination temperature of the obtained gel was increased gradually up to 350 °C and held for 2 h, followed by heating up to 1150 °C at a rate of 5 °C/min and holding for 2 h. In this state, the powder turned into a pale pink color, which is referred to as FeCrLTO. To investigate the effect of calcination temperature on the properties of FeCrLTO, the powder was subjected to calcination in a tube furnace under a nitrogen atmosphere (flow rate 1000 mL/min) for 24 h at different temperatures: 1150 °C (FeCrLTO1150_24h), 1250 °C (FeCrLTO1250_24h), and 1350 °C (FeCrLTO1350_24h). For comparison, control samples were calcined at 1150 °C for 2 h under ambient atmosphere, using the same chemical composition as the experimental samples (referred to FeCrLTO1150_2h), and without the addition of Iron(III) nitrate and Chromium(III) nitrate (referred to as LTO1150_2h).

2.2 X-Ray Powder Diffraction (XRD)

The crystal structure of the synthesized photocatalysts were determined by X-ray diffraction (XRD, BRUKER D2 PHASER). The characterized conditions used for analysis are as follows: Cu-Kα radiation (λ = 1.5406 Å) at 40 kV, 40 mA, scanning range 20.70° degree (2θ) with 0.02° step size, and a counting time of 0.2 s/step. Data manipulation and XRD pattern fitting were performed using Origin Pro 2023 version 10.0.0.154 (Learning Edition)

2.3 Photocatalytic activity

The degradation of photocatalytic activity was analyzed using methylene blue (MB). The MB solution was prepared at a concentration of 1.8×10^{-4} M. For each measurement, 0.01 g of the synthesized photocatalysts powder was added to 50 mL of the MB solution [22]. The re-

action was performed in a black box with continuous stirring while exposed to LED light (EVE panel square, 18 W, Kenko L41 super pro (W) filter: light wavelength >400 nm) for a total of 180 min [23,24]. The photocatalytic activity was determined by measuring the MB degradation using UV-Vis spectroscopy (UV-Vis, model: CARY 300) equipped with a tungsten lamp as the light source. The wavelength range of the analysis was set between 300 and 700 nm. Measurement was done in a transmittance mode.

Energy band gap (E_g) was evaluated by Tauc's plot which is relative with absorbance and energy, $(\alpha h\upsilon)^2$ versus E_g. Additionally, Tauc's equation calculated E_g, shown as equation (1):

$$\left(\alpha h\upsilon\right)^2 = k\left(h\upsilon - E_g\right) \qquad (1)$$

where, E_g is the optical energy gap value between the valence band and the conduction band, α is the absorption coefficient from the optical absorption spectrum using the Beer–Lambert's relation, $h\upsilon$ is the absorption energy (h-Planck constant, υ-incident frequency), k is the band tailing parameter [25].

The percentage of MB degradation was determined value of degradation, show as equation (2):

$$\%Degradation = \left(1 - absorbance\right) \times 100 \qquad (2)$$

where, absorbance is the highest intensity of UV-Vis analysis at 664 nm.

2.4 X-Ray Absorption Spectroscopy (XAS)

X-ray absorption measurements were carried out at the SUT-NANOTEC-SLRI XAS beamline (BL5.2) of the Synchrotron Light Research Institute (Public Organization) (SLRI), Nakhon Ratchasima, Thailand. The synchrotron light provides electron energy of 1.2 GeV; bending magnet; beam current 80-50 mA. The beam line optics of BL5.2 is equipped with a double crystal, fixed exit, Ge (220) monochromator. The beamline possesses an energy range of 1810-3000 eV, a photon flux of 108-1010 photons/s/100mA. For Ti K-edge measurement, a Ti foil was used for energy calibration at 4966 eV on a transmission mode. For La L-edge measurement, V foil was used for energy calibration at E_0 of 5465 eV in transmission mode. Samples were measured La L-edge X-ray Absorption Near Edge Spectroscopy (XANES) and Extended X-ray Absorption Fine Structure (EXAFS) in fluorescence-mode at E_0 of 5483 eV. XANES measurements were performed in the rage of −30 eV to 80 eV of E_0, while EXAFS

measurement, the photon energy scan was set up in a range of −150 eV, −10 eV, 30 , and 12k of E_0 with the photon energy step of 5 eV, 0.3 eV, and 0.05k. Samples were measured up to 4 scans. The normalized absorption data were processed after background subtraction in the pre-edge and post-edge region, then EXAFS fitting was performed using Athena and Artemis program in Demeter (version 0.9.26) Athena [26].

2.5 Field Emission Scanning Electron Microscopy (FE-SEM)

The crystal structure was analyzed by a field-emission scanning electron microscope (FE-SEM) from Carl Zeiss (model: AURIGA). The FE-SEM images revealed the shapes and pores in the crystal structure, and the analysis was performed with an acceleration voltage of 50 kV, a working distance (WD) of 6.5 mm, and a magnification of 30k. The identified elements were analyzed using energy dispersive spectroscopy (EDS).

3. Result and Discussion

The crystal phases of synthesized photocatalysts show in Figure 1 revealing that all samples exhibit the $La_2Ti_2O_7$ crystal phase as the dominant phase, and no impurities are detected (PDF 81-1066). It is apparent that the $La_2Ti_2O_7$ crystal started forming after being calcined at 1150 °C for 2 h under ambient atmosphere. The complete $La_2Ti_2O_7$ crystal was found in FeCrLTO1150_24h and FeCrLTO1250_24h, which obtained monoclinic (P1) of $La_2Ti_2O_7$. However, FeCrLTO1350_24h
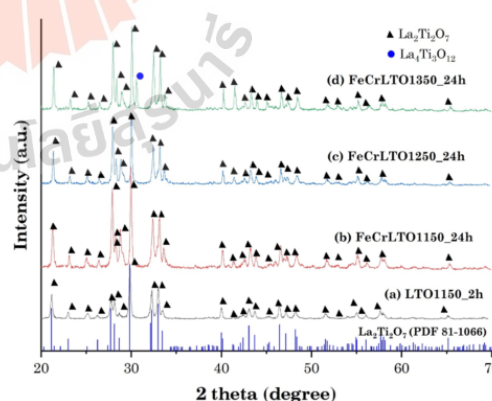
Figure 1. X-ray diffraction patterns of synthetic photocatalytic powder calcinated for 24 h under nitrogen atmosphere at different temperature; 1150 °C (a), 1250 °C (b), and 1350 °C (c).

found an extra peak of La$_4$Ti$_3$O$_{12}$ at 2θ of 30.255° (PDF 89-4520), suggesting that higher temperature induce decomposition or phase transformation from La$_2$Ti$_2$O$_7$ into mix phase of La$_2$Ti$_2$O$_7$ + La$_4$Ti$_3$O$_{12}$ [10−13]. In addition, the co-doping of Fe and Cr did not reveal any impurity phases, suggesting that the Fe and Cr cations were possibly integrated into the La$_2$Ti$_2$O$_7$ lattice [21].

The crystal morphologies of the synthesized photocatalysts were observed using FE-SEM.

The sample calcined at 1150 °C (FeCr1150_24h) was found to have the smallest grain size (Figure 2(a)). As the temperature increased up to 1250 °C (FeCr1250_24h), the crystal structure became larger and the grain edges became sharper. In contrast, the sample calcined at 1350 °C (FeCr1350_24h) showed disappearing gain edges, which resulted in the large grain size connecting with the adjacent grains. The results suggest that changes in the morphology of co-doped FeCrLTO are induced
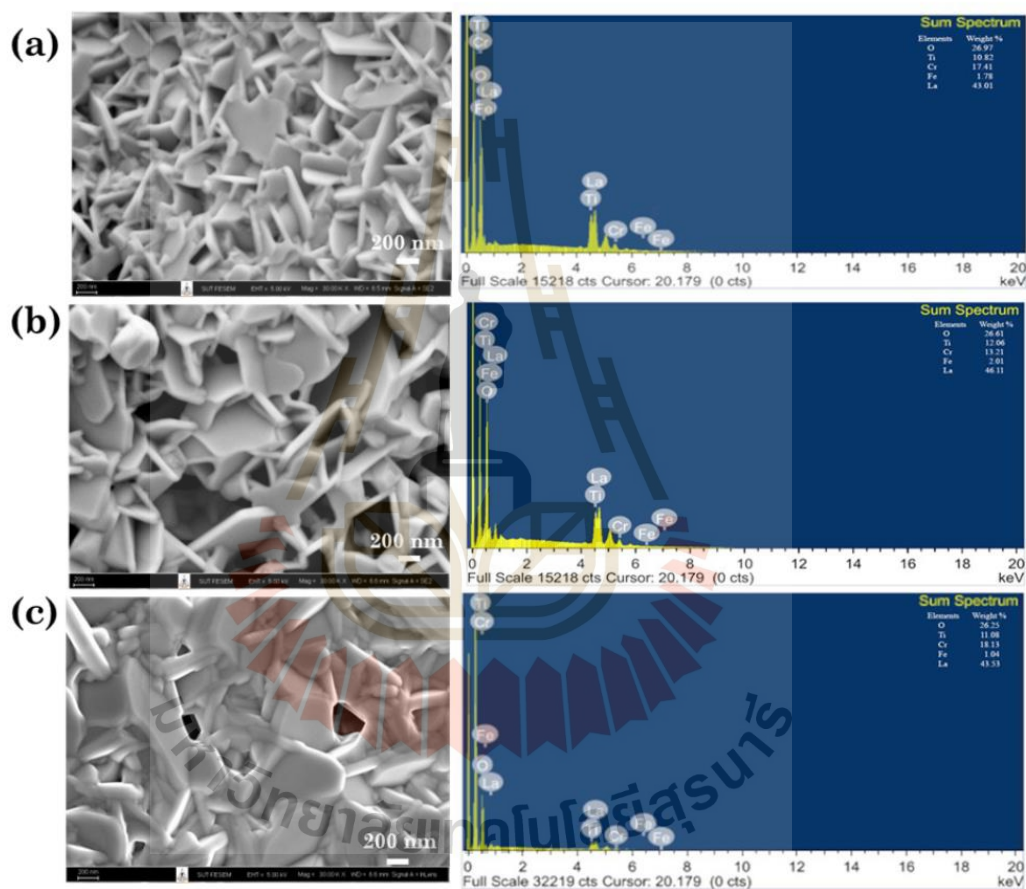
Figure 2. The FE-SEM image (left panel) and energy-dispersive X-ray (EDX) (right panel) of the synthesized photocatalysts calcined under nitrogen atmosphere for 24 h at different temperatures; 1150 °C (FeCrLTO1150_24h) (a), 1250 °C (FeCrLTO1250_24h) (b), 1350 °C (FeCrLTO1350_24h) (c).

Table 1. Elemental composition of synthesized photocatalysts examined by analyzed by FE-SEM using Energy-Dispersive X-ray (EDX) technique.

Sample	Elemental composition (% mass relative)				
	O	Ti	La	Fe	Cr
FeCr1150_24h	26.97	10.82	43.01	1.78	17.41
FeCr1250_24h	26.61	12.06	46.11	2.01	13.21
FeCr1350_24h	26.25	11.08	43.53	1.01	18.13

by the calcination temperature. Although higher temperatures are more favored for the formation of perovskite-type crystalline grains [27], but the temperature should not exceed 1250 °C to avoid adverse effects on the crystallinity.

The elemental compositions of synthesized photocatalysts were analyzed by FE-SEM using Energy-Dispersive X-ray (EDX) technique. The EDX spectra of all samples are shown in Figure 2 (right panel), and the percentage of mass relative to each element is summarized in Table 1. There was no contamination of the samples with other elements, as indicated by the peaks corresponding to O, Ti, La, Fe, and Cr. Moreover, the results confirm that Fe and Cr are incorporated into the crystal structure of $La_2Ti_2O_7$. Although the content of O and Ti was similar across all samples, there were slight variations in the contents of La, Fe, and Cr. Specifically, the FeCr1250_24h sample exhibited the highest levels of both La and Fe.

The photocatalytic efficiency of the synthesized photocatalysts was evaluated using the MB degradation method. Visible light was irradiated onto the reaction mixture for 180min, and changes in MB concentration were monitored using UV-Vis spectroscopy at a wavelength range of 300-700 nm. The highest peak of MB can be observed clearly at 664nm. The results showed that FeCrLTO1250_24h exhibited the highest degradation efficiency, showing lower peak absorption compared to other samples. The degradation efficiency of the FeCrLTO1350_24h that underwent calcination at 1350 °C was found to be lower than that of the catalysts calcinated at other temperatures. This finding aligns with the XRD pattern observed for the FeCrLTO1350_24h photocatalyst, as shown in Figure 3(a). The effeicent dagradation of MB found that FeCrLTO1250_24h increased upto 42.8%, which was highest dagradation of MB, for FeCrLTO1350_24h, FeCrLTO1150_24h, FeCrLTO1150_2h and LTO were 38.48%, 31.25%, 15.75% and 10.9%. In adddition, FeCrLTO1250_24h, FeCrLTO1350_24h, FeCrLTO1150_24h were still higher efficiency than LTO and FeCrLTO1150_2h, see Figure 3(b).

Figure 4 shows Tauc's plot extrapolation used to determine the optical bandgap energy (E_g) of the synthesized photocatalysts. The FeCrLTO1250_24h photocatalyst has the lowest E_g value (2.31 eV), followed by the FeCrLTO1150_24h (2.39 eV) and FeCrLTO1350_24h (2.48 eV), respectively. According to a previous report [21], the pure $La_2Ti_2O_7$ photocatalyst

Figure 3. UV-VIS spectra of MB degradation in 180 min by synthesized photocatalysts. (a) Methylene blue degradation; (b) Degradation efficiency of catalysts.
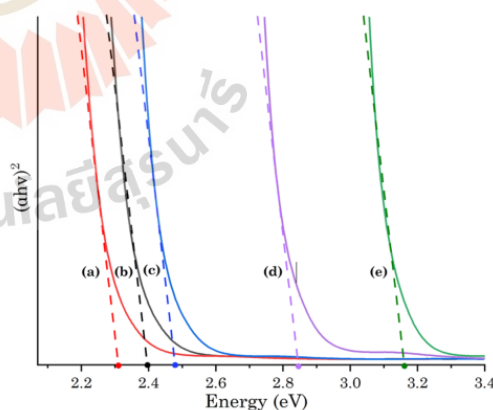
Figure 4. The optical bandgap energy (E_g) presented in Tauc's plot extrapolation of FeCrLTO1250_24h (E_g = 2.31) (a), FeCrLTO1150_24h (E_g = 2.39) (b), FeCrLTO1350_24h (E_g = 2.48) (c), FeCrLTO1150_2h (E_g = 2.84) (d), and LTO1150_2h (E_g = 3.18) (e).

has a large band gap energy of approximately 3.8 eV, which is activated by UV irradiation. The results of this study suggest that co-doping Fe and Cr into $La_2Ti_2O_7$ and calcinating the material at a high temperature under a nitrogen atmosphere for 24 h can reduce the band gap energy by more than 1 eV. This reduction in band gap energy allows the material to be activated under visible light. Additionally, previous studies have reported that the band gap energy of $La_4Ti_3O_{12}$ is 4.09 eV [28,29]. As the FeCrLTO1350_24h photocatalyst contains a mixed phase of both $La_2Ti_2O_7$ and $La_4Ti_3O_{12}$, it exhibits a higher E_g value than the other samples. Successful co-dope of Cr and Fe into photocatalyst was reported to increase catalytic activities [21,30].

XAS measurement was performed to investigate the electronic structure and local structure of synthesized $La_2Ti_2O_7$ photocatalysts.

The XANES spectra of La L_3-edge of all samples show similar feature but different in terms of peak height (Figure 5). The white line (5490.82 eV) observed in the La L_3-edge spectra describes the origin of electric transition of $2p_{3/2}$ electrons to the 5p or 5d state. The strong and symmetrical white line indicates that there was no deformation of the local structure. The EXAFS k^2 weight spectra (Figure 5(b)) supported the XANES results, demonstrating a similar k^2 weight patterns. The FeCrLTO1150_2h sample had the highest white line intensity (Figure 5(b), while the FeCrLTO1250_24h and FeCrLTO1150_24h had the lowest intensity. These findings imply that the co-doping of Fe and Cr in the $La_2Ti_2O_7$ structure in different temperature can impact the p-d hybridization by modifying the local electronic structure of the surrounding oxygen atoms and transition metal ions.

Figure 5. La L_3-edge XANES spectra of synthesized photocatalysts and the magnification of the white line region (a). The unsmoothed k^3-weighted of La L_3-edge EXAFS of synthesized photocatalysts (b).
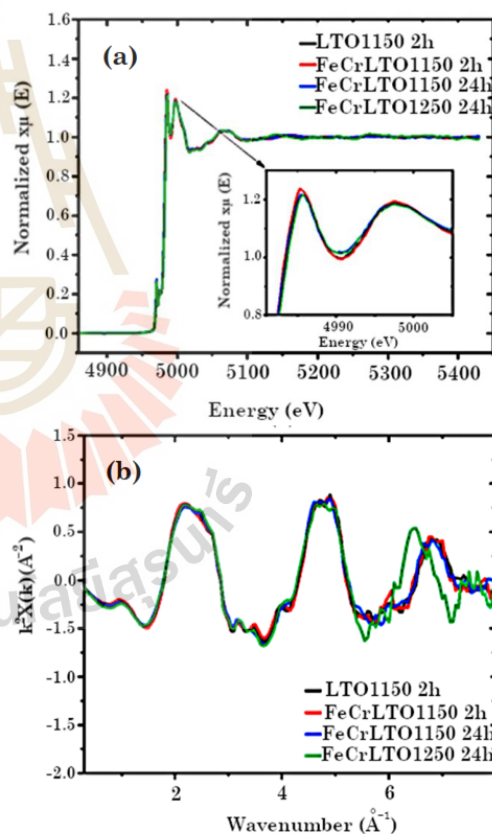
Figure 6. Ti K-edge XANES spectra of synthesized photocatalysts (a) and the magnification of the white line region. The unsmoothed k^3-weighted of Ti K-edge EXAFS of synthesized photocatalysts (b).

Ti K-edge spectrum of all synthesized $La_2Ti_2O_7$ photocatalysts show similar spectrum feature. The absorption edge position (4981.91 eV) remained unchanged, signifying that the valence state of Ti did not alter as a consequence of calcination process. The oxidation state of all samples is in the form of Ti^{4+}. All samples shared the same white line position of 4985.37 eV attributing to the 1s to 3p (or 4p) states dipole transitions. The height of this peak is generally related to the unoccupied orbital. FeCrLTO1150_2h sample showed highest intensity, which means the highest unoccupied p orbital, while FeCrLTO1250_24h had the lowest intensity. This suggests that doping Fe and Cr into $La_2Ti_2O_7$ at 1250 °C in an N_2 atmosphere may have perturbed the occupancy of the electron p orbital (Figure 6). The Ti K-edge EXAFS functions in the K space and R space of synthesized photocatalysts are mostly aligned at the same position, except FeCrLTO1250_24h which showed peak shift in k^2 weight space

(Figure 6). These findings demonstrate a transformation of the local structures of Ti atoms in $FeCrLa_2Ti_2O_7$ structure.

Since the XRD patterns of the synthesized photocatalysts predominantly exhibited the $La_2Ti_2O_7$ structure, this structure was employed for the EXAFS fitting. The EXAFS best-fit parameters of LTO samples to $La_2Ti_2O_7$ were listed in Table 2. The nearest neighbour atom of Ti corresponded to the oxygen in Ti−O shells with 6 coordination. The Ti−La shells also contained 6 coordinated atoms. The R space (Figure 7) identified 3 peak positions: (Peak 1) Ti−O(1-3) (~2 Å), (Peak 2): Ti−O(4-5) (~2.3-2.5 Å), (Peak 3) Ti−La (~3.3-3.7 Å). It is noteworthy that the intensity of Peak 2 in FeCrLTO1250_24h was higher than that of Peak 3, which differed from the other samples. Therefore, EXAFS fitting cannot be wholly matched with $La_2Ti_2O_7$ structure. The extra paths of Ti−Fe and Ti−Cr were introduced to $La_2Ti_2O_7$ structure for EXAFS fitting. The perfect fitting

Table 2. The EXAFS best-fit parameters of LTO samples.

	Fit parameter		LTO1150 2h	FeCrLTO1150 2h	FeCrLTO1150 24h	FeCrLTO1250 24h
	R factor		0.00682	0.0080399	0.0080399	0.0081609
	SO_2		0.873	0.873	0.873	0.814
	Delta E_0		1.5534	0.978	0.978	2.032
R (A)	Ti−O1	N = 1	1.97097	1.98446	1.98861	2.02939
	Ti−O2	N = 1	2.14025	2.1525	2.12481	1.98773
	Ti−O3	N = 2	1.90673	1.90367	1.89527	1.94938
	Ti−O4	N = 1	2.29333	2.33259	2.33259	2.29319
	Ti−O5	N = 1	2.4969	2.53234	2.53304	2.47567
	Ti−La1	N = 1	3.42331	3.4337	3.46541	3.3569
	Ti−La2	N = 2	3.70544	3.53227	3.55604	3.73304
	Ti−La3	N = 1	3.48902	3.6486	3.6786	3.54595
	Ti−La4	N = 1	3.61854	3.43632	3.41716	3.36572
	Ti−La5	N = 1	3.3877	3.30016	3.28831	3.10888
	Ti−Fe	N=0.372	-	-	-	2.66832
	Ti−Cr	N=0.744	-	-	-	2.63988
$\sigma2$	Ti−O1	N = 1	0.00286	0.00286	0.00286	0.002
	Ti−O2	N = 1	0.00634	0.00634	0.00634	0.0634
	Ti−O3	N = 2	0.00554	0.00554	0.00554	0.00554
	Ti−O4	N = 1	0.00554	0.00554	0.00554	0.00554
	Ti−O5	N = 1	0.00443	0.00211	0.00211	0.0078
	Ti−La1	N = 1	0.00228	0.00027	0.00027	0.0034
	Ti−La2	N = 2	0.00645	0.0069	0.0069	0.00137
	Ti−La3	N = 1	0.00144	0.00645	0.00645	0.00399
	Ti−La4	N = 1	0.0069	0.00144	0.00144	0.00183
	Ti−La5	N = 1	0.00576	0.0069	0.0069	0.00003
	Ti−Fe	N=0.372	-	-	-	0.00555
	Ti−Cr	N=0.744	-	-	-	0.00842

was exhibited in the Ti−Fe degeneracy of 0.372 and Ti−Cr degeneracy of 0.744. The interatomic distance of Ti−Fe and Ti−Cr are 2.67 Å and 2.64 Å, respectively. The evidence implied that the substituted Fe and Cr atom was positioned adjacent to the Ti atom in $La_2Ti_2O_7$ structure but not the La atom. In $La_2Ti_2O_7$, the Ti atom acts as the photoactive center, absorbing photons and promoting electrons to higher energy levels. The presence of substituted Fe and Cr atoms adjacent to the Ti atom can induce electron transfer from these metal atoms to the Ti atom, thus facilitating the separation of electron-hole pairs and improving the photocatalytic efficiency.

The substituted doping of Cr and Fe in the $La_2Ti_2O_7$ structure can affect the *p-d* hybridization between the oxygen 2p orbitals and the transition metal 3d orbitals, as indicated by the XANES results. The 3d orbitals of Cr and Fe have partially filled electrons that can interact with the 2p orbitals of the surrounding oxygen atoms, leading to hybridization between these orbitals. This interaction can then cause changes in the electronic structure of the nearby oxygen atoms and Ti ions, ultimately affecting the *p-d* hybridization. Therefore, substituted doping of Cr and Fe in the $La_2Ti_2O_7$ struc-

Scheme 1. Model of photocatalytic activities of synthesized FeCrLTO and FeCrLTO under nitrogen atmosphere for waste water treatment.
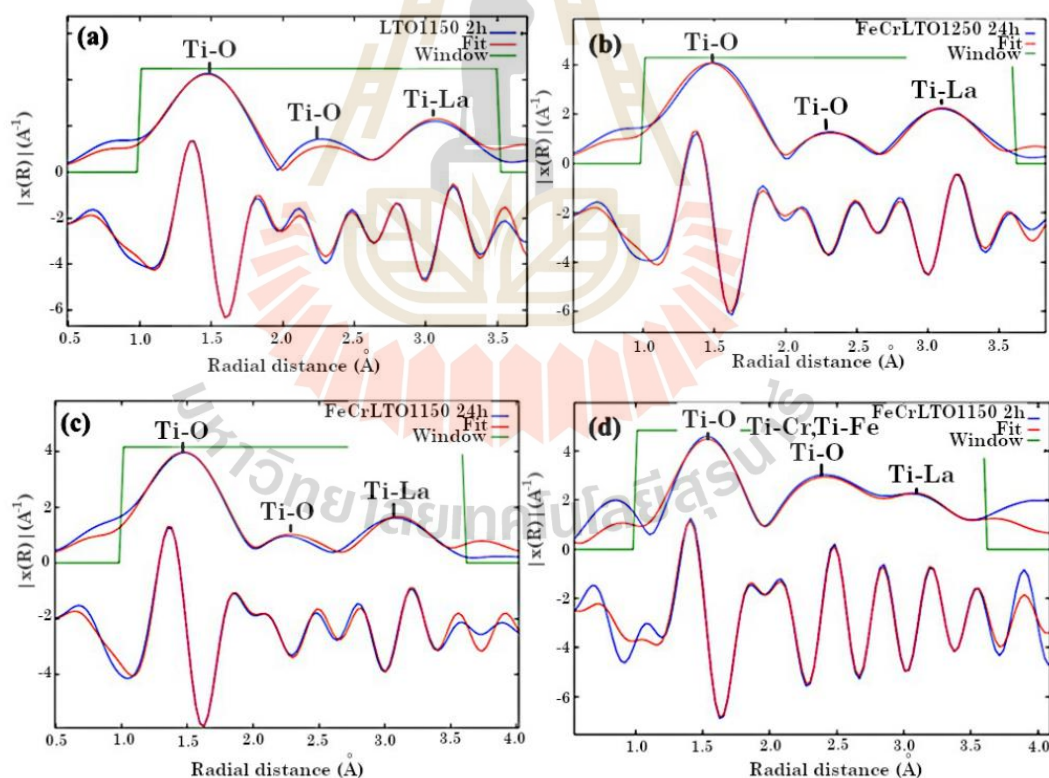
Figure 7. Ti K-edge EXAFS of synthesized photocatalysts with fits taken from the $La_2Ti_2O_7$ model. (a) LTO1150_2h, (b) FeCrLTO1150_2h, (c) FeCrLTO1150_24h, (d) FeCrLTO1250_24h. Upper graph is the k^3-weighted EXAFS. Lower graph is the Fourier transforms of the EXAFS signals in R space. Phase shifts were not corrected.

ture can lead to changes in their optical and photocatalytic properties (Scheme 1). These changes reduce the band gap of the photocatalysts, causing their absorption spectrum to shift and ultimately improve their photocatalytic performance. Extensive research has been conducted on the use of orbital hybridization to regulate the electronic structures and surface chemisorption properties of transition metals in order to enhance the performance of catalysts [31]. Moreover, calcination under a N_2 atmosphere can be used to control the oxygen content of the material and to prevent oxidation or reduction reactions that could alter the electronic properties of (Fe,Cr) co-doping $La_2Ti_2O_7$.

4. Conclusion

The sol-gel method is appropriate preparation for $La_2Ti_2O_7$-based photocatalysts that can be activated by visible light, the optimal approach with co-doping of Fe and Cr at the concentration of 0.005 molar percent corresponding to Ti atom. The calcination process was carried out under an N_2 atmosphere to control the oxygen concentration of the material and prevent the oxidation and reduction reactions that could modify the electronic characteristics of the (Fe,Cr) co-doped $La_2Ti_2O_7$. The heating temperature of 1250 °C for 24 h was provided the best photocatalytic efficiency. Fe and Cr was found to be substituted into the lattice sites of the photocatalysts. The Fe and Cr substitution leads to the transfer of electrons from Fe and Cr metal atoms to the Ti atom, thus facilitating the separation of electron-hole pairs and improving the photocatalytic efficiency. Additionally, Fe and Cr alter the p-d hybridization within the $La_2Ti_2O_7$ lattice, resulting in a reduction of the band gap and the absorption of lower energy.

Acknowledgments

CRedit Author Statement

Authors contributions are as follows. Sukasem Watcharamaisakul conceived conceptualization and planned the experiments, review and editing the manuscript. Hussanai Luangthsanarak, author, performed methodology, formal analysis, investigation, validation and writing- original draft. Waraporn Tanthanuch and Ratchadaporn Supruangnet contributed for the XAS experimental plan, measurement, data analysis and draft the manuscript on XAS part. Ratchadaporn Supruangnet contributed on experimental plan and revised the manuscript.

References

[1] Nakata, K., Fujishima, A. (2012). TiO_2 photocatalysis: Design and applications. *Journal of Photochemistry and Photobiology C: Photochemistry Reviews*, 13, 169-189. DOI: 10.1016/j.jphotochemrev.2012.06.001.

[2] Shaham-Waldmann, N., Paz, Y. (2016). Away from TiO_2: A critical minireview on the developing of new photocatalysts for degradation of contaminants in water. *Materials Science in Semiconductor Processing*, 42, 72-80. DOI: 10.1016/j.mssp.2015.06.068.

[3] Spasiano, D., Marotta, R., Malato, S., Fernandez-Ibañez, P., Di Somma, I. (2015). Solar photocatalysis: Materials, reactors, some commercial, and pre-industrialized applications. A comprehensive approach. *Applied Catalysis B: Environmental*, 170-171, 90-123. DOI: 10.1016/j.apcatb.2014.12.050.

[4] Banerjee, S., Dionysiou, D.D., Pillai, S.C. (2015). Self-cleaning applications of TiO_2 by photo-induced hydrophilicity and photocatalysis. *Applied Catalysis B: Environmental*, 176-177, 396-428. DOI: 10.1016/j.apcatb.2015.03.058.

[5] Gerischer, H., Heller, A. (1991). The role of oxygen in photooxidation of organic molecules on semiconductor particles. *The Journal of Physical Chemistry*, 95(13), 5261-5267. DOI: 10.1021/j100166a063.

[6] Shemer, G., Paz, Y. (2011). Interdigitated Electrophotocatalytic Cell for Water Purification. *International Journal of Photoenergy*, 2011, 596710. DOI: 10.1155/2011/596710.

[7] Batzill, M. (2011). Fundamental aspects of surface engineering of transition metal oxide photocatalysts. *Energy & Environmental Science*, 4(9), 3275-3286. DOI: 10.1039/C1EE01577J.

[8] Hwang, D.W., Cha, K.Y., Kim, J., Kim, H.G., Bae, S.W., Lee, J.S. (2003). Photocatalytic Degradation of CH3Cl over a Nickel-Loaded Layered Perovskite. *Industrial & Engineering Chemistry Research*, 42(6), 1184-1189. DOI: 10.1021/ie020457c.

[9] Hwang, D.W., Kim, H.G., Kim, J., Cha, K.Y., Kim, Y.G., Lee, J.S. (2000). Photocatalytic Water Splitting over Highly Donor-Doped (110) Layered Perovskites. *Journal of Catalysis*, 193(1), 40-48. DOI: 10.1006/jcat.2000.2875.

[10] Kim, J., Hwang, D.W., Kim, H.-G., Bae, S.W., Ji, S.M., Lee, J.S. (2002). Nickel-loaded La2Ti2O7 as a bifunctional photocatalyst. *Chemical Communications*, (21), 2488-2489. DOI: 10.1039/B208092C.

[11] Ku, Y., Wang, L.C., Ma, C.M. (2007). Photocatalytic Oxidation of Isopropanol in Aqueous Solution Using Perovskite-Structured La2Ti2O7. *Chemical Engineering & Technology*, 30(7), 895-900. DOI: 10.1002/ceat.200700071.

[12] Wang, R., Xu, D., Liu, J., Li, K., Wang, H. (2011). Preparation and photocatalytic properties of CdS/La2Ti2O7 nanocomposites under visible light. *Chemical Engineering Journal*, 168(1), 455-460. DOI: 10.1016/j.cej.2011.01.035.

[13] Wang, Q., An, N., Chen, W., Wang, R., Wang, F., Lei, Z., Shangguan, W. (2012). Photocatalytic water splitting into hydrogen and research on synergistic of Bi/Sm with solid solution of Bi-Sm-V photocatalyst. *International Journal of Hydrogen Energy*, 37(17), 12886-12892. DOI: 10.1016/j.ijhydene.2012.05.080.

[14] Borgarello, E., Kiwi, J., Graetzel, M., Pelizzetti, E., Visca, M. (1982). Visible light induced water cleavage in colloidal solutions of chromium-doped titanium dioxide particles. *Journal of the American Chemical Society*, 104(11), 2996-3002. DOI: 10.1021/ja00375a010.

[15] Lin, L., Chai, Y., Yang, Y., Wang, X., He, D., Tang, Q., Ghoshroy, S. (2013). Hierarchical Gd-La codoped TiO2 microspheres as robust photocatalysts. *International Journal of Hydrogen Energy*, 38(6), 2634-2640. DOI: 10.1016/j.ijhydene.2012.11.100.

[16] Lin, Y., Jiang, Z., Zhu, C., Hu, X., Zhu, H., Zhang, X., Fan, J., Lin, S.H. (2013). The optical absorption and hydrogen production by water splitting of (Si,Fe)-codoped anatase TiO2 photocatalyst. *International Journal of Hydrogen Energy*, 38(13), 5209-5214. DOI: 10.1016/j.ijhydene.2013.02.079.

[17] Long, R., English, N.J. (2011). Band gap engineering of double-cation-impurity-doped anatase-titania for visible-light photocatalysts: a hybrid density functional theory approach. *Physical Chemistry Chemical Physics*, 13(30), 13698-13703. DOI: 10.1039/C1CP21454C.

[18] Zhang, J., Tse, K., Wong, M., Zhang, Y., Zhu, J. (2016). A brief review of co-doping. *Frontiers of Physics*, 11(6), 117405. DOI: 10.1007/s11467-016-0577-2.

[19] Sharma, M., Pathak, M., Kapoor, P.N. (2018). The sol-gel method: pathway to ultrapure and homogeneous mixed metal oxide nanoparticles. *Asian Journal of Chemistry*, 30(7), 1405-1412. DOI: 10.14233/ajchem.2018.20845.

[20] Venkatachalam, N., Palanichamy, M., Murugesan, V. (2007). Sol-gel preparation and characterization of nanosize TiO2: Its photocatalytic performance. *Materials Chemistry and Physics*, 104(2-3), 454-459. DOI: 10.1016/j.matchemphys.2007.04.003.

[21] Hu, S., Jia, L., Chi, B., Pu, J., Jian, L. (2014). Visible light driven (Fe,Cr)-codoped La2Ti2O7 photocatalyst for efficient photocatalytic hydrogen production. *Journal of Power Sources*, 266, 304-312. DOI: 10.1016/j.jpowsour.2014.05.054.

[22] Jin, M., Nagaoka, Y., Nishi, K., Ogawa, K., Nagahata, S., Horikawa, T., Katoh, M., Hayashi, J. (2008). Adsorption properties and photocatalytic activity of TiO2 and La-doped TiO2. *Adsorption*, 14(2), 257-263. DOI: 10.1007/s10450-007-9095-4

[23] Turon, V., Anxionnaz-Minvielle, Z., Willison, J.C. (2018). Replacing incandescent lamps with an LED panel for hydrogen production by photofermentation: Visible and NIR wavelength requirements. *International Journal of Hydrogen Energy*, 43(16), 7784-7794. DOI: 10.1016/j.ijhydene.2018.03.019.

[24] Claypool, N.B., Lieth, J.H. (2020). Physiological responses of pepper seedlings to various ratios of blue, green, and red light using LED lamps. *Scientia Horticulturae*, 268, 109371. DOI: 10.1016/j.scienta.2020.109371.

[25] Etacheri, V., Geiger, U., Gofer, Y., Roberts, G.A., Stefan, I.C., Fasching, R., Aurbach, D. (2012). Exceptional Electrochemical Performance of Si-Nanowires in 1,3-Dioxolane Solutions: A Surface Chemical Investigation. *Langmuir*, 28(14), 6175-6184. DOI: 10.1021/la300306v.

[26] Ravel, B., Newville, M., (2005). ATHENA, ARTEMIS, HEPHAESTUS: data analysis for X-ray absorption spectroscopy using IFEF-FIT. *Journal of Synchrotron Radiation,* 12, 537-541. DOI: 10.1107/S0909049505012719.

[27] Pillai, S.C., Periyat, P., George, R., McCormack, D.E., Seery, M.K., Hayden, H., Colreavy, J., Corr, D., Hinder, S.J. (2007). Synthesis of High-Temperature Stable Anatase TiO_2 Photocatalyst. *The Journal of Physical Chemistry C*, 111(4), 1605-1611. DOI: 10.1021/jp065933h.

[28] Ma, Z., Wu, K., Sa, R., Li, Q., He, C., Yi, Z. (2015). Mechanism of enhanced photocatalytic activities on N-doped $La_2Ti_2O_7$: An insight from density-functional calculations. *International Journal of Hydrogen Energy*, 40(2), 980-989. DOI: 10.1016/j.ijhydene.2014.11.088.

[29] Low, J., Yu, J., Jaroniec, M., Wageh, S., Al-Ghamdi, A.A. (2017). Heterojunction Photocatalysts. *Advanved Materials*, 29(20), 1601694. DOI: 10.1002/adma.201601694.

[30] Lin, N., Gong, Y., Wang, R., Wang, Y., Zhang, X. (2022). Critical review of perovskite-based materials in advanced oxidation system for wastewater treatment: Design, applications and mechanisms. *Journal of Hazardous Materials*, 424, 127637. DOI: 10.1016/j.jhazmat.2021.127637.

[31] Chen, H., Wu, Q., Wang, Y., Zhao, Q., Ai, X., Shen, Y., Zou, X. (2022). d–sp orbital hybridization: a strategy for activity improvement of transition metal catalysts. *Chemical Communications*, 58(56), 7730-7740. DOI: 10.1039/D2CC02299K.

BIOGRAPHY

Mr. Hussanai Luangthanarak was born on Thursday, April 16th, 1981, in Wang-luk sub-district, Samchuk district, Suphan Buri province. He completed his primary education at Jirasadwittaya School in 1991. He then pursued his secondary education at Piya Maharaj Rommaniyakhet in Sai yok Sub-district, Sai yok District, Kanchanaburi Province, and completed his high school education in 1997.

Mr. Hussanai went on to pursue his higher education at Suranaree University of Technology, where obtained a Bachelor's degree in Ceramic Engineering in 2003 and obtained a Master's degree in Ceramic Engineering in 2010. His research focused on "Fabrication of Al_2O_3-SiC composite using SiC nanopowder synthesized by mechanical alloying method".

After completing his Master's degree studies, he continued his education at the same university to pursue a Doctoral degree in Materials Engineering. He received a scholarship from the Research and Development Fund (OROG), which was an external research funding source, to support his graduate studies. His research focused on "STUDY ON VISIBLE LIGHT RESPONSE OF $La_2(Ti_{1.9998}$ $Fe_{0.0001}$ $Cr_{0.0001})O_{7-n}$ N_n PHOTOCATALYST." He has also